THE UNIVERSITY *of* EDINBURGH

Hyaluronic Acid from Ophthalmic Viscosurgical Devices Interacting with Biomimetic Substrates

Eugénia Delacou

Doctor of Philosophy
The University of Edinburgh
August 2024

Abstract

Complex fluids are used in a variety of surgical procedures. In particular, cataract surgery widely uses viscoelastic fluids named Ophthalmic Viscosurgical Devices (OVDs), which contain high molecular weight polymers such as hyaluronic acid (HA). OVDs fulfil a dual role: maintaining volume in the anterior chamber and protecting the cellular structure from accidental damage. They are classified into two categories: cohesive OVDs have a higher viscosity at rest and are removed as a blob, whilst dispersive OVDs spread on the cells to act as a protective cushion.

The main surgical risk associated with OVDs occurs if they remain in the eye at the end of the operation. If not properly removed, they can obstruct the flow of aqueous humour through the trabecular mesh-work, which in turn increases the intraocular pressure. Although rheological characterisation of OVDs is routinely performed, their surface interaction with biological tissues has been less studied. In particular, the mechanics of polymer adsorption and subsequent desorption is of great interest to better understand the differences between the two classes of OVDs in the levels of protection they confer and their ease of removal during aspiration at the end of surgery.

In order to study adsorption, we used Quartz Crystal Microbalance with Dissipation monitoring (QCM-D) and phase modulation ellipsometry. After a polymer layer had formed, we injected a rinsing solution to mimic the irrigation/aspiration device used by surgeons in cataract surgery and gain insight on the desorption process. In addition to gold-coated QCM-D sensors, we used sensors functionalised with mucin to better mimic the surface properties of corneal endothelial cells.

Adsorption and desorption of polyvinylpyrrolidone (PVP) was first investigated as a model system, as described in Chapter 3. In Chapter 4, the same approach

was applied to HA from diluted OVD solutions Although the adsorption of cohesive and dispersive OVDs is comparable in the dilute and semi-dilute regimes, a difference emerges in the entangled regime.

It appears that on adsorption of the dispersive OVD, which is formulated from lower molecular weight HA, more of the entanglements are broken than when adsorption is from the longer chain cohesive OVD. In a surgical context, the structure of the adsorbed layer resulting in a higher dissipation could explain the medical observation that the dispersive OVD confers greater protection to the corneal endothelium.

Colloidal Probe Atomic Force Microscopy (AFM) was used to quantify the force associated with pulling off HA from a range of biomimetic surfaces exhibiting different surface charges (Chapter 5). The results are consistent with HA molecules from dispersive OVDs detaching by the simultaneous rupture of multiple anchoring points on the surface. On the other hand, it appears that HA molecules from cohesive OVDs sequentially break individual attachments, resulting in a higher work of adhesion. In a surgical context, it could be that this greater work of adhesion translates into more damage at the corneal endothelium when the OVD is aspirated.

The results we obtain with simple model substrates suggest that surface properties likely play a role, which merits future investigation.

Lay Summary

Cataract is a condition characterised by the clouding of the ocular lens, leading to a blurred vision. It is commonly treated by an outpatient surgery, in which gels called Ophthalmic Viscosurgical Devices (OVDs) are injected into the eye by the surgeon. These gels must be completely removed at the end of the surgery to avoid post-operative complications.

OVDs are categorised into two types based on their behaviour when the surgeon removes them at the end of the procedure. Cohesive OVDs are very efficient at maintaining the shape of the eye during the procedure, and they are removed as a single mass. Dispersive OVDs provide better protection to the outer layer of corneal cells, but usually take longer to remove because they break apart during removal. Although the efficacy of OVDs has been established, the exact mechanisms by which they confer protection remain unclear, as do the reasons for the differences between the two types.

Our results indicate that the way both classes of OVDs interact with the interior of the eye is different. The network of dispersive OVDs breaks down upon contact with solid surfaces. This allows the molecules to rearrange and form a film which is able to dissipate more energy, thereby offering an enhanced protection compared to cohesive OVDs, which remain entangled as they adsorb.

Additionally, their desorption behaviour differ. Detaching cohesive OVDs dissipates more energy than dispersive OVDs, which could cause more insult to the delicate cellular structure. A painful analogy would be to stretch an elastic band before cutting it with scissors. In that situation, the two halves of the band would snap back on the hand, releasing far more energy than that needed to clip the band.

Declaration

I declare that this thesis was composed by myself, that the work contained herein is my own except where explicitly stated otherwise in the text, and that this work has not been submitted for any other degree or professional qualification except as specified.

Dr Walter Hama provided guidance on how to perform the ellipsometry measurements. Dr Andreia Silva obtained the shear rheology on OVDs. Dr Laura Charlton offered instructions on how to use the AFM. Dr Fraser Laidlaw assisted with sample preparation and image acquisition for SEM and Cryo-SEM.

(*Eugénia Delacou, August 2024*)

Acknowledgements

I would like to express my gratitude to everyone who helped me navigate through this PhD. Many thanks to my supervisor Dr Simon Titmuss for his invaluable support and understanding over the years. I am also grateful to my industrial supervisor, Dr. Michael Haisch from Hyaltech Ltd, for entrusting me with this project and providing financial support. I extend my appreciation to my other supervisors, Prof. Alex Lips and Prof. Wilson Poon for insightful discussions on polymer physics. I address special thanks to Dr. Laura Charlton, Dr Andreia Silva, Dr. Fraser Laidlaw, Dr. Walter Hama and Dr. Andrew Schofield for their invaluable assistance with AFM, rheology, SEM, ellipsometry and lab queries. I am also grateful to Prof. Colin Bain from Durham University, who allowed me to perform ellipsometry experiments there.

This PhD would not have been possible without the support of EPSRC and the SOFI^2 CDT (EP/S023631/1), which inspired me to move to a new country and enabled me to forge wonderful friendships, especially vital during the challenging COVID times. Sometimes, a game of DnD is all it takes to brighten a dull day. I am also grateful to my colleagues from the School of Physics and Astronomy, for their support, their friendship and the good laughs along the way. Thank you for the Cake Clubs, the Bananagram lunches, and the Arts and Crafts nights.

I owe a debt of gratitude to my other friends for their continuous support, advice and enthusiasm: Tiffol, Marie, le Brest Crew, Anth, Jamie, le Trio Infernal... The list goes on. Janey, thank you for everything. I would not have finished this PhD without you.

I am immensely thankful to my partner Lucas, for standing by me all along and helping me get through the difficulties, the stress and the general grumpiness that comes with doing a PhD. Thank you for being my Number One supporter, together with Newton of course.

Last, but certainly not least, I would like to thank my loving family, who has always been there, either to celebrate during the good times or to support me during the hard times. To my Grandpa, to my parents, to Joseph, Justine, Victor, Augustin, you are my rock.

Contents

List of Figures

List of Tables

Chapter 1

Introduction

1.1 Relevant Eye Anatomy

Cataract is a degenerative condition characterised by a progressive diminishing and blurring of sight. It is the first cause of blindness worldwide, although it can be reversed through a surgical operation. This outpatient surgery is the most performed operation worldwide, which makes cataract a major topic in public health [1]. The aim of this section is to introduce some elements of eye anatomy which are important when considering cataract surgery.

Cataract is caused by a malfunction of the eye crystalline lens, a transparent biconvex structure found behind the iris which focuses the incoming light onto the retina, see Figure 1.1. The lens is able to change shapes though the contraction of the ciliary body muscles. This allows the vision to accommodate and focus on objects at different distances. In cataract, the structural proteins of the lens, crystallins, start to aggregate, which results in an opacification of the lens [2]. This can be caused by a multitude of factors, although the most common is ageing.

The lens is situated in the anterior cavity of the eye, a segment which encompasses the cornea, the iris and the ciliary body. This cavity is composed of two chambers: the anterior chamber, which typically has a volume of 250 µL, is situated between the iris and the cornea, whilst the posterior chamber lies between the iris and the back of the lens. Both of these chambers are filled with aqueous humour, a low

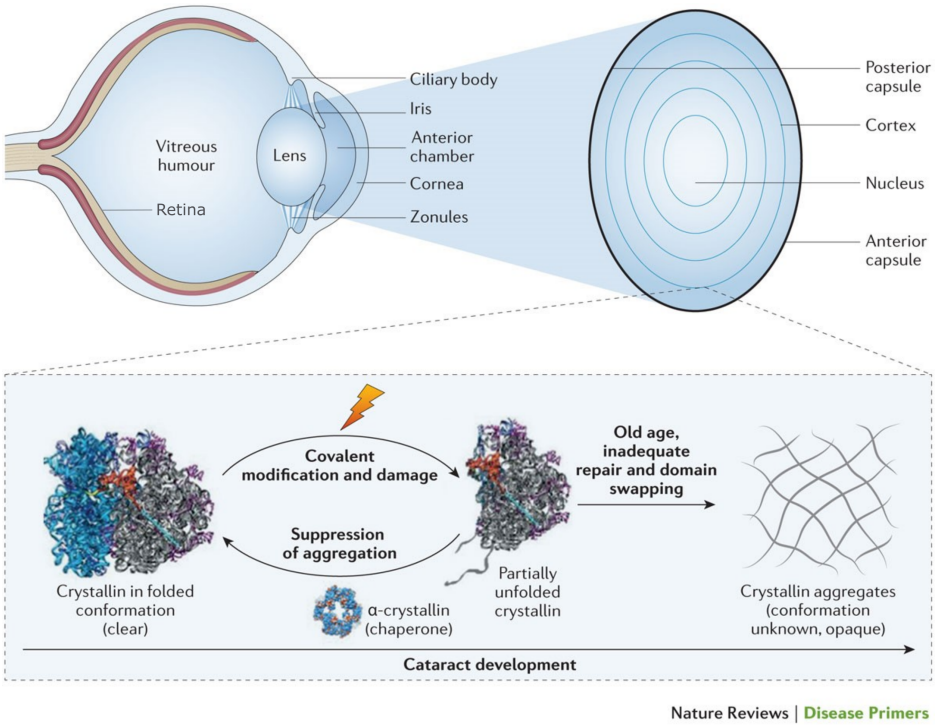

Figure 1.1 *A schematic representation of the ocular cavity. In cataract, the lens progressively becomes cloudy due to the aggregation of crystallin proteins, which results in a blurry vision. Adapted from [2].*

viscosity fluid which contains various ions and nutrients. Most of the tissues found in the eye need to be transparent in order to allow light to travel through. As a result, they do not contain a vascular system. Instead, the aqueous humour plays a similar role to blood by transporting essential nutrients and removing waste products [3]. The posterior cavity is filled with vitreous humour, a viscous transparent gel which maintains the structure of the eye.

Cataract surgery requires an incision through the cornea, which is a transparent oval tissue located on the outer layer of the eye. Its roles are to refract the incoming light to the interior of the eye and to act as a protective membrane. The cornea is approximately 550 µm thick and 12 mm in diameter [4]. It is composed of a succession of layers, as represented in Figure 1.2. Surface epithelial cells lie on the collagen Bowman's membrane. The stroma, which is the thickest layer, is delimited on the inner side by the Descemet's membrane. The innermost layer of the cornea is composed of a monolayer of hexagonal cells called the endothelium. The corneal endothelium plays a critical role in the transparency of the cornea by pumping out the excess fluid from the stroma [5]. Unlike the epithelium, endothelial cells do not regenerate in the event of a trauma [6, 7]. In case of cell

loss, the adjacent cells migrate and enlarge in order to bridge the newly-formed gap. As a result, endothelial cell loss is a serious condition which cannot be easily treated, and may result in irreversible vision loss [8].

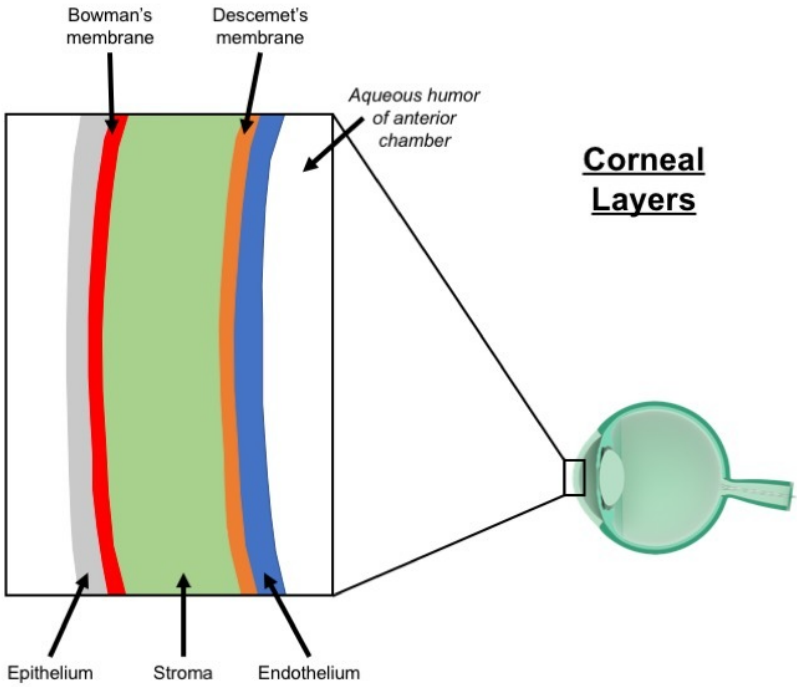

Figure 1.2 *A schematic representation of the layers forming the cornea. Endothelium protection is critical during cataract surgery, as these cells do not regenerate. Taken from [5].*

The corneal epithelium surface is covered by an aqueous coat named the tear film, which is an additional protective barrier against damage and infection and provides lubrication [9]. This film is composed of three layers: the outer part of the film mostly contains lipids, the core of the film is an aqueous phase, and the inner part is composed of mucins. The latter are high molecular-weight glycoproteins which are anchored to the surface of the corneal epithelium and ensure lubrication of the ocular surface.

The corneal epithelium and endothelium are covered by a viscoelastic glycocalyx, which is composed of a mixture of polysaccharides, proteins and lipids [10]. Several types of membrane-bound mucins have been identified, as well as a range of cellular receptors [11]. In particular, the receptors CD44 and RHAMM bind the endogenous hyaluronic acid (HA), which is a negatively-charged biopolymer widely used as a compound in cataract surgery [12, 13].

1.2 Cataract Surgery: Procedure and Challenges

The main procedure used to treat cataract is phacoemulsification [14]. It uses an ultrasound probe (also called a phaco probe) to break the defective lens into pieces through a small incision on the side of the cornea. An irrigation/aspiration device is used to balance the flow of aqueous solution in the eye to prevent a collapse of the anterior chamber of the eye, and to remove the lens debris. An artificial intraocular lens (IOL) is then inserted in the ocular cavity to replace the previous cloudy lens.

Although phacoemulsification is performed routinely with a good outcome for the patient, some complications may occur. Corneal endothelial cell loss has been described as a possible side-effect of cataract surgery [15–17]. As described in Section 1.1, a significant cellular loss on the endothelium is a risk because of its poor regenerative ability. The phacoemulsification procedure generates an significant shear stress in the anterior chamber, and accidental contact from the surgical equipment or the lens debris may induce damage to the delicate inner structures of the eye [18]. Thermal damage and free radical production have also been reported to result from use of the ultrasound probe.

Cataract surgeons use viscoelastic polymer gels called Ophthalmic Viscosurgical Devices (OVDs) in order to minimise the risks associated with the procedure. OVDs have a high viscosity at rest, whilst their shear-thinning characteristic facilitates their injection through small-gauge cannula. Their role is to maintain volume and pressure in the anterior chamber. They also provide a protection for endothelial cells. The main risk associated with OVDs is their remaining in the eye at the end of the operation. If not properly removed, they can obstruct the flow of aqueous humour through the trabecular mesh-work, increasing the intraocular pressure (IOP) [19]. Removing OVDs is thus a crucial step in the procedure. The composition and classification of these gels will be detailed in Section 1.3.

1.3 Ophthalmic Viscosurgical Devices: Composition and Classification

The classification of OVDs has changed throughout the years, adapting to the release of new products. In this section, we will discuss the composition of OVDs and detail their classifications based on rheological properties.

The first commercial OVD (Healon®) was introduced in 1984 [20]. It contains hyaluronic acid, or hyaluronan (HA), which is a linear, negatively-charged polysaccharide composed of two monosaccharides, namely β-D-N-acetyl-galactosamine and β-D-glucuronic acid. HA was first isolated in 1934 from bovine vitreous humour [21], and was later identified as an ubiquitous component of the extracellular matrix [13, 22]. It is also present in both the human aqueous and vitreous humours. It is generally produced by bacterial fermentation, but can be extracted from rooster combs in order to get a higher molecular weight if required. It has been shown that corneal endothelial cells have specific receptors for HA [23] and are endogenously coated with a layer of HA [24]. OVDs can contain a variety of polymers other than HA, such as hydroxypropylmethyl cellulose (HPMC) and chondroitin sulfate (CS). In this thesis, we will focus on OVDs containing HA, as this polymer's versatile properties can be tuned to formulate several classes of OVDs.

In the early days of OVDs, the classification was based on zero-shear viscosity η_0 only. When Healon5® was released in 2001, the classification was revised, as this product was the first to display a behaviour described as viscoadaptive. Although very viscous at rest, it fractures into small droplets under the stress applied during aspiration, unlike other viscous OVDs, which could be removed as a single bolus [25]. This led the biomedical industry to switch to a new classification, categorising OVDs based on their behaviour upon aspiration: dispersive or cohesive.

Dispersive OVDs have a lower elasticity, which results in the polymer network fracturing upon removal by aspiration. Conversely, cohesive OVDs display a high degree of polymer entanglement, allowing the entire network to be aspirated as one [26]. This difference in behaviour is a result of a balance between molecular weight and concentration: cohesive OVDs are composed of long-chain polymers

and therefore display a high molecular weight, in the range of several MDa. On the other hand, dispersive OVDs typically have a lower molecular weight (several hundreds kDa) [27], but contain polymers at a higher mass concentration than cohesive OVDs.

From a surgeon's perspective, dispersive OVDs provide a better endothelial protection, and they are more retained in the anterior chamber than cohesive ones, but they are less efficient in maintaining space and more difficult to aspirate [26, 28, 29]. The use of one type over the other mostly depends on the surgeon's preference, and the potential difficulties encountered during the procedure. Both types can also be used at different stages of the operation [30]. A method aiming to exploit the best of both categories of OVDs whilst getting rid of the setbacks was proposed in 1999: the soft-shell technique [31]. It relies on the sequential injection of both types of OVDs in adjacent spaces. Prior to phacoemulsification, the dispersive OVD should be injected before the cohesive OVD, whereas the order is reversed for the insertion of the IOL. Some OVD manufacturers produce dual syringes containing unmixed dispersive and cohesive OVDs in the same device to facilitate this sequential injection. Although the soft-shell technique may have an interest for complicated cases, it requires a longer operating time and a greater quantity of OVDs. As pointed out in [19], a longer operating time implies more intraocular manipulations and fluid flow, which can increase the overall risk of complications. It also makes it more difficult to entirely remove the fluid. On a more practical point of view, surgeons usually prefer to operate each patient in the most time-efficient way possible, in order to maximise the number of operations they can perform in one day.

In this work, we used cohesive (Hyaplus, Hyalock) and dispersive (Hyadel) OVDs kindly provided by Hyaltech Ltd [32]. A schematic summarising their respective concentrations and molecular weights is available in Figure 4.1.

1.4 Relevant Timescales

In order to compare our experimental results with surgeons' observations, it is important to keep in mind some of the timescales involved in phacoemulsification surgery. The surgery itself is rapid: between 5 and 10 minutes are typically required for each eye [19].

The ultrasound phaco probe vibrates at a frequency between 25 and 60 kHz, which can either be delivered in a continuous or intermittent fashion. Several articles have attempted to calculate the velocity of the resulting turbulent flow, with results ranging from 3.74 to 20 mm.s^{-1} [33, 34]. The total phacoemulsification time has been estimated to be between 25 s and several minutes [18, 19, 35].

The fluid flow rate from the irrigation/aspiration probe can be adjusted by the surgeons, and is typically close to 40 mL.min^{-1}. Likewise, the vacuum settings vary from 200 to 600 mm.Hg [29, 36–39]. OVD syringes contain approximately 1 mL of solution. As discussed before, the removal of dispersive OVDs tends to require a longer time than for cohesive OVDs. Values reported in the literature range from 10 to 30 s for cohesive OVDs, and from 30 to 210 s for dispersive OVDs [26, 28, 40].

As discussed in Section 1.2, the main risk associated with OVDs is the spikes in IOP, which can result from an incomplete removal of OVDs altering the flow of aqueous humour. IOP peaks after 5 to 7 hours following the operation, returning to baseline levels after a few days, possibly with the help of medication [41]. Aqueous humour is continuously produced, normally at a rate of 2 to 3 µL.min^{-1} [3, 42], resulting in a renewal rate of 2 hours in normal conditions.

1.5 Approach Adopted in this Work

Although articles from the literature widely describe the coating ability [43–45] and adherence of OVDs on endothelial cells [30, 43, 46, 47], the formation of an adsorbed surface layer which might exert an influence beyond viscoelastic bulk effects has not been clearly established so far. Yet the presence of an endogenous HA layer [24] and HA-binding receptors [23] on the corneal endothelium imply the possibility of an attractive interaction that might mediate the formation of such a layer. This effect has been exploited in the formulation of HA-coated niosomes, which have been reported to display an enhanced interaction with the cornea [48].

In this thesis, we use Quartz Crystal Microbalance with Dissipation monitoring (QCM-D) and phase modulation ellipsometry on a variety of solid substrates. Our

investigation starts with dilute solutions of polyvinylpyrrolidone (PVP), which flow as a Newtonian fluid, and a gold-coated substrate. We then progress to using solutions formulated from both cohesive and dispersive OVDs that span HA concentrations from the dilute to the entangled regimes. We then functionalise the solid substrates in an effort to mimic some of the functionalised groups that might be expected to be found at the surface of the corneal endothelium. In all cases, we examine the behaviour of any polymer layers that have formed under rinsing, to provide insight into what might happen in the aspiration step that follows phacoemulsification.

We go on to use colloidal probe Atomic Force Microscopy (AFM) to directly measure the interactions between a colloidal probe functionalised with HA from the two categories of OVDs and solid substrates functionalised with a range of biopolymers chosen to mimic the molecules found at the surface of the corneal endothelium. We use these measurements to attempt to rationalise the adsorption and the rinsing behaviours seen in our QCM-D experiments and the experience of the surgeons when using the two types of OVDs. We will not be using any cells in this work, as this would require equipment and expertise which are beyond the scope of this PhD.

Chapter 2

Methods

2.1 Quartz Crystal Microbalance with Dissipation Monitoring (QCM-D)

2.1.1 Theory

QCM-D relies on the reverse piezoelectricity of quartz. When subject to a voltage, the quartz sensor undergoes a shear deformation causing it to oscillate at a resonant frequency determined by its thickness. Any mass adsorbed on the sensor surface as well as viscoelastic coupling with either the ambient fluid or the layer will induce changes in the resonant frequency (Δf) and dissipation (ΔD). The latter is defined as the reciprocal of the Q factor, or the ratio of the energy dissipated to the energy stored during one oscillation. It is obtained in a ring-down measurement by measuring the exponential decay of the amplitude after the voltage is turned off. The values of Δf and ΔD are recorded for the fundamental as well as 3rd, 5th, 7th, 9th, 11th and 13th overtone. Each overtone has a different penetration depth: a higher overtone with a higher frequency will probe a smaller depth. We will now describe the different models that can be used to translate the time-dependent values of Δf and ΔD into surface excess and viscoelastic parameters. These models are represented in Figure 2.1.

2.1.2 Data Analysis: Modelling the Physical System

Sauerbrey Model

Sauerbrey introduced the first QCM-D model in 1959 [49]. For a thin, rigid layer in vacuum or in air, it predicts a linear relationship between the frequency shift of overtone n, Δf_n, and the mass adsorbed per unit area, φ (equation 2.1):

$$\frac{\Delta f_n}{n} = -\frac{f_0\ \varphi}{\rho_Q\ h_Q} = -\frac{f_0^2\ \varphi}{N\ h_Q} \tag{2.1}$$

where f_0 is the resonant frequency of the unloaded crystal in air, h_Q and ρ_Q are the quartz thickness and density, N is the frequency constant, and φ is the surface excess, which corresponds to the mass adsorbed per unit area.

This model makes several assumptions: the film must be homogeneous and rigid to let the acoustic wave propagate elastically without energy loss. It must be thin enough that it can be treated as an extension of the quartz, meaning the wave velocity is the same as in the crystal.

In practice, the film is considered thin enough if the frequency decrease is less than 2%, and rigid if the ratio $\frac{\Delta D}{\Delta f} << \ 4\ \cdot\ 10^{-7}$ Hz^{-1} or if the dissipation is less than 1 ppm. Another indicator that the layer is sufficiently rigid for the Sauerbrey assumption to be met is that $\frac{\Delta f_n}{n}$ is independent of the overtone n. Equation 2.1 and the uncertainties associated will be derived below.

As a QCM-D quartz crystal is free to oscillate on both faces, there is an anti-node on the surface, and the thickness corresponds to half a wavelength, which induces a resonance phenomenon. The corresponding frequency f_0 of the oscillating quartz crystal can be calculated by equation 2.2:

$$f_0 = \frac{f_n}{n} = \frac{v_{tr}}{2\ h_Q} = \frac{N}{h_Q} \tag{2.2}$$

where v_{tr} is the speed of a transverse wave propagating in the quartz crystal, and N is the frequency constant, which is $1670 \cdot 10^2 \pm 1\%$ Hz.cm for an AT-cut crystal with a ratio of diameter (Θ) and thickness (h_Q) higher than 20. With the

crystal used in this experiment, $\frac{\Theta}{h_Q} = \frac{14}{0.300} = 46$. AT-cut refers to the geometry of the quartz, which is cut with a 35° angle from the vertical axis. This type of crystal is commonly used for its precision and temperature stability.

The deformation arising from an ideal shear oscillation in a plane is expected to propagate in the vertical direction, with no impact of the deformation of the slices inside the material. This implies that if a surface layer is thin enough, the frequency will be impacted by its added mass only, and not its viscoelasticity. As a result, the layer can be approximated as being an extension of the quartz itself. Equation 2.2 can be differentiated to obtain equation 2.3.

$$-\frac{\Delta f_n}{n\ f_0} = \frac{\Delta h_Q}{h_Q} \tag{2.3}$$

If the density is evenly distributed across the layer, the added mass per unit area is a product of the added thickness and the density, which yields equation 2.4:

$$-\frac{\Delta f_n}{n\ f_0} = \frac{\Delta m}{A\ \rho_Q\ h_Q} = \frac{\varphi}{\rho_Q\ h_Q} \tag{2.4}$$

where Δm is the mass adsorbed, ρ_Q is the density of quartz (2.65 g.cm^{-3}), A is the sensor area and φ is the mass adsorbed per unit area. This is equivalent to equation 2.1, and can be rearranged into equation 2.5:

$$\varphi = -\frac{\Delta f_n}{n}\ \frac{\rho_Q\ h_Q}{f_0} = -\frac{\Delta f_n}{n}\ \frac{\rho_Q\ N}{f_0^2} = -\frac{\Delta f_n}{n}\ C_f \tag{2.5}$$

where C_f is a constant depending on the quartz properties only, sometimes referred to as the sensitivity constant. It follows that in the Sauerbrey model, the slope of Δf_n plotted against n corresponds to -$\frac{\varphi}{C_f}$, and one expects all overtones to yield the same value of φ. It follows that the value of C_f is:

$$C_f = \frac{\rho_Q\ N}{f_0^2} = 18.06(41)\ \text{ng.cm}^{-2}.\text{Hz}^{-1} \tag{2.6}$$

The uncertainty ΔC_f is calculated using error propagation in Appendix A.

Kanazawa-Gordon Model

Kanazawa and Gordon adapted the approach for use in liquids by taking into account the coupling of the shear wave in the sensor with the Newtonian fluid it is immersed in [50]. From there, the changes in frequency and dissipation upon immersion can be calculated with equations 2.7 and 2.8 [51],

$$\Delta f_n = -\frac{1}{C_f}\sqrt{\frac{n\ \rho_l\ \eta_l}{2\ \omega_F}} \tag{2.7}$$

$$\Delta D_n = -2\ \frac{\Delta f_n}{f_n} \tag{2.8}$$

where ρ_l and η_l are the ambient density and viscosity of the liquid, and ω_F is the angular fundamental resonance frequency.

Voinova Model

The Voinova model treats the system as a Voigt element, comprising an elastic spring and a viscous dash pot connected in parallel [52]. It takes into consideration the coupling of the shear wave with both the adsorbed layer, which can be viscoelastic, and the ambient Newtonian fluid. It adds information about the layer's viscoelastic parameters, making QCM-D a high frequency rheometer. However, one should keep in mind that the parameters are correlated in the equations. Ideally, one would use another independent technique to get a measurement of one of the parameters, for instance layer thickness or surface excess, otherwise the output will be a composite parameter.

The frequency and dissipation shifts of the layer can be calculated using equations 2.9 and 2.10:

$$\Delta f \approx -\frac{1}{2\pi\rho_Q h_Q}\left\{\frac{\eta_{fluid}}{\delta} + \left[h_{layer}\rho_{layer}\omega - 2h_{layer}\left(\frac{\eta_{fluid}}{\delta}\right)^2 \frac{G''_{layer}\omega}{{G'_{layer}}^2 + {G''_{layer}}^2}\right]\right\} \tag{2.9}$$

$$\Delta D \approx \frac{1}{2\pi f \rho_Q h_Q} \left\{ \frac{\eta_{fluid}}{\delta} + \left[2h_{layer} \left(\frac{\eta_{fluid}}{\delta} \right)^2 \frac{G'_{layer}\omega}{{G'_{layer}}^2 + {G''_{layer}}^2} \right] \right\} \tag{2.10}$$

where η_{fluid} is the bulk fluid viscosity, δ is the shear wave viscous penetration depth, h_{layer} and ρ_{layer} are the layer thickness and density, ω is the angular frequency, and G'_{layer} and G''_{layer} are the layer storage and loss moduli.

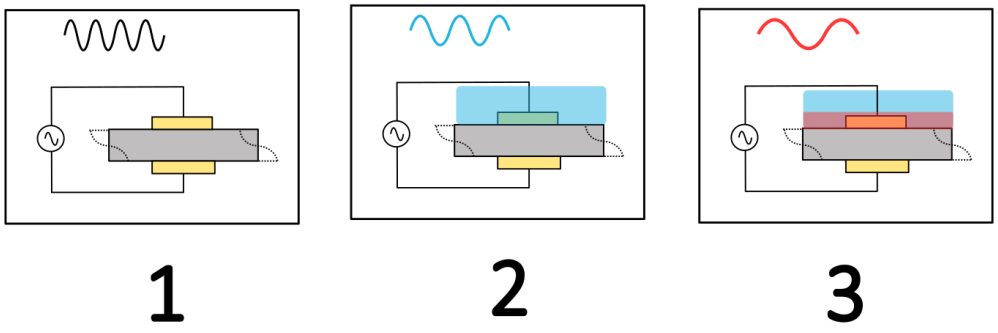

Figure 2.1 *A schematic of the QCM-D sensor in air/vacuum (1), in liquid (2) or in liquid with an adsorbed layer (3). The corresponding oscillation frequency decreases at each step. (2) can be described by the Kanazawa-Gordon model and (3) by either the Sauerbrey or Voinova model depending on the rigidity of the layer.*

2.1.3 Experimental Protocol

In Chapters 3 and 4, QCM-D is used to monitor the adsorption of the polymers PVP and HA respectively. The common elements of the experimental protocol are described here.

PVP 360 kDa was purchased from Sigma Aldrich (St. Louis, MO, USA), and the OVD solutions were kindly provided by Hyaltech. Solutions were prepared in advance and diluted at the desired concentration. They were degassed in vacuum for at least 1h before every measurement in order to avoid the formation of air bubbles.

The adsorption of polymers on gold and other functionalised gold surfaces was monitored using a QSense Explorer QCM-D from Biolin Scientific (Sweden). The QSX 301 AT-cut gold sensors used were 14 mm in diameter, 330 µm thick and

had a fundamental shear resonant frequency of 4.95 MHz when unloaded in air. The sensors were cleaned before each experiment using the following protocol: after a 30-minute sonication in a 2% v/v solution of Hellmanex-II, and a 10-minute sonication in distilled water, the sensors were dried with an inert 2,3,3,3-tetrafluoropropene gas and left for one to three hours in a UV-Ozone ProCleaner Plus (Bioforce Nanosciences).

Each measurement began by pumping either distilled water or phosphate buffer saline (PBS) at 20°C (RT = 21°C) through the sensor chamber for at least 25 minutes using a peristaltic pump with a flowrate set at 100 µL.min^{-1} to get a stable baseline. The baseline was considered stable when the frequency shift of the third overtone was drifting by less than 0.2 Hz during a 10-minute period. The chosen polymer solution was then pumped through the sensor chamber at 100 µL.min^{-1} for the desired time, typically 50 minutes, followed by a subsequent rinsing with distilled water or PBS until the frequency and dissipation reached a plateau. The changes in frequency (Δf) and dissipation (ΔD) were recorded for the fundamental as well as the 3rd, 5th, 7th, 9th, 11th and 13th overtones. As the overtone number increases, the shear wave penetration depth decreases. The third overtone provides the best signal-to-noise ratio and was used as a default if not specified otherwise. The fundamental frequency is typically discarded as it is very sensitive to flow effects in the sensor chamber, yielding a noisy signal. A schematic of the setup is given in Figure 2.2. The solution of interest has to flow through various geometric boundary conditions, which correspond to different shear rates and stresses. Tables summarising these regimes can be found in Appendix C. It is worth noticing that the shear rates encountered are in the same range as the frequency of the ultrasound probe used in phacoemulsification, which are reported in Section 1.4.

2.2 Phase Modulation Ellipsometry

The ellipsometry measurements were done at Durham University, in Prof. Colin Bain's group. The measurements were done with Dr Walter Hama, who also helped with data analysis, in particular by providing some of his own data to test the efficiency of a Python software I wrote (Appendix D).

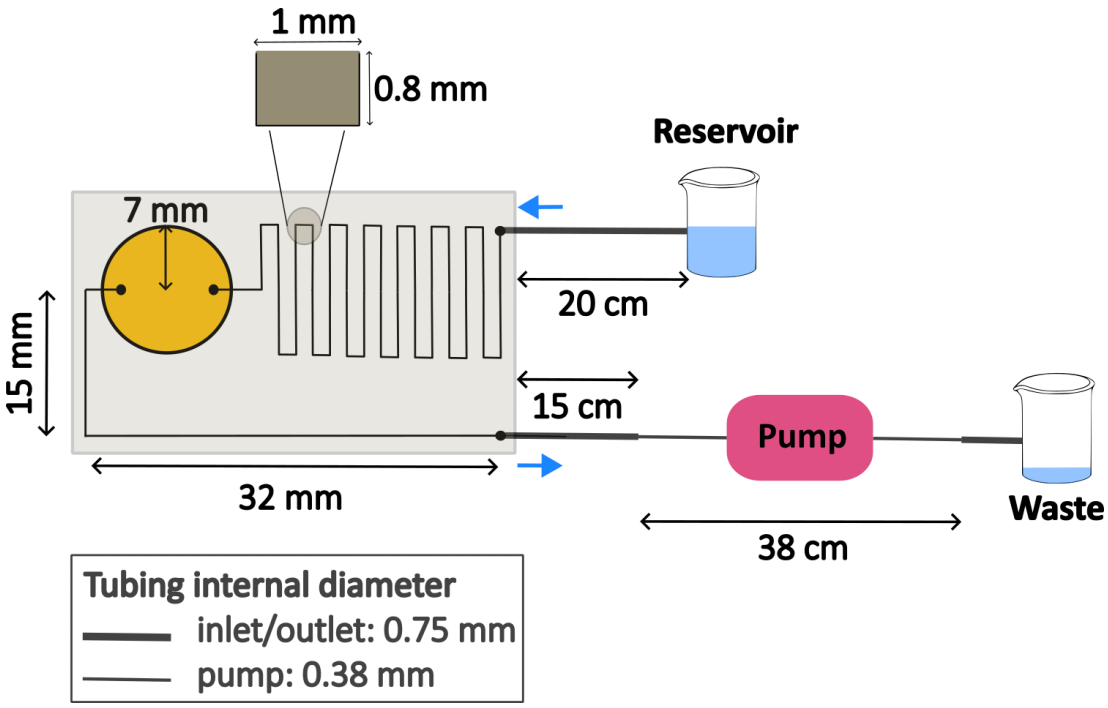

Figure 2.2 *A schematic of the QCM-D experimental setup (not to scale). A peristaltic pump was used to pull the solution through the QCM-D flow-cell, which contains the 7 mm radius sensor. The solution had to go through a serpentine before reaching the sensor, allowing it enough time to reach the set temperature of the sensor.*

2.2.1 Theory and Data Analysis

Ellipsometry is an optical technique based on the change in polarisation of an incident light beam upon reflection from a sample. The ratio ρ of the reflectance of the p- and s- components can be characterised by an amplitude ratio, $\tan(\psi)$, and a phase angle Δ (equation 2.11).

$$\frac{R^p}{R^s} = Re(\rho) + i\ Im(\rho) = \tan(\psi)\ \exp(i\Delta) \tag{2.11}$$

The reflectances can be calculated by using the Fresnel equations applied to stacks of layers characterised by the optical parameters given in Table 2.1, which are also schematised in Figure 2.3 b. The refractive index corresponds to a ratio of the speed of light in air and in the material of interest.

The angle of incidence θ_j at each interface j was determined using Snell's Law (equation 2.12) where n_j^* is the complex refractive index $n_j^* = n_j - ik_j$.

Material:	j	n	k	d (nm)
Air	-	1	0	∞
Glass window	-	1.46	0	$2 \cdot 10^6$
Distilled water	0	1.33	0	∞
PVP	1	1.51	0	h_1
HA	1	1.563	0	h_1
Gold	2	0.166	3.15	8000

Table 2.1 *Optical model used to calculate PVP or HA layer thickness.*

$$n_j^* \sin\theta_j = n_{j+1}^* \sin\theta_{j+1} \tag{2.12}$$

The p- and s- Fresnel reflection coefficients at each interface are calculated using equations 2.13 and 2.14.

$$r_{j(j+1)}^p = \frac{n_{j+1}^* \cos\theta_j - n_j^* \cos\theta_{j+1}}{n_{j+1}^* \cos\theta_j + n_j^* \cos\theta_{j+1}} \tag{2.13}$$

$$r_{j(j+1)}^s = \frac{n_j^* \cos\theta_j - n_{j+1}^* \cos\theta_{j+1}}{n_j^* \cos\theta_j + n_{j+1}^* \cos\theta_{j+1}} \tag{2.14}$$

The overall reflection coefficients R^p and R^s were subsequently calculated following equation 2.15, where x is either p or s [53]:

$$R^x = \frac{r_{01}^x + r_{12}^x \exp(-2i\delta_1)}{1 + r_{01}^x r_{12}^x \exp(-2i\delta_1)} \tag{2.15}$$

where the phase shift δ_1 induced by the polymer layer is calculated for a range of layer thicknesses h_1, using:

$$\delta_1 = \frac{2\pi}{\lambda} n_1 \; h_1 \cos\theta_1 \tag{2.16}$$

The experimental data measured in air was first fitted to the closest values of n and k for gold, using a custom Python code to minimise the difference between the experimental and calculated values of $\mathrm{Re}(\rho)$ and $\mathrm{Im}(\rho)$. The code, which I wrote for this analysis, is included in Appendix D. We checked that the values of n and k obtained from this fit were close to those expected from the literature for a gold surface, which are displayed in Table 2.1.

In the case of ultrathin polymer layers, it is not possible to separately fit Re(ρ) to the film refractive index n. The value of 1.51 chosen corresponds to that of dry PVP. We used 1.563 as the refractive index for HA [54]. The experimental data points of Im(ρ) obtained when pumping the polymer solution in the ellipsometry measurement chamber were fitted to values of layer thickness for the growing polymer layer. The same procedure was applied when injecting the rinsing solution in the flow cell.

2.2.2 Experimental Protocol

Phase modulation kinetic ellipsometry measurements were done using a Beaglehole Instrument equipped with a 632.8 nm HeNe laser and a laminar flow cell, as shown on Figure 2.3 a. The angle of incidence of light on the flow cell was 60°, which is reasonably close to the Brewster angle for the system (75°).

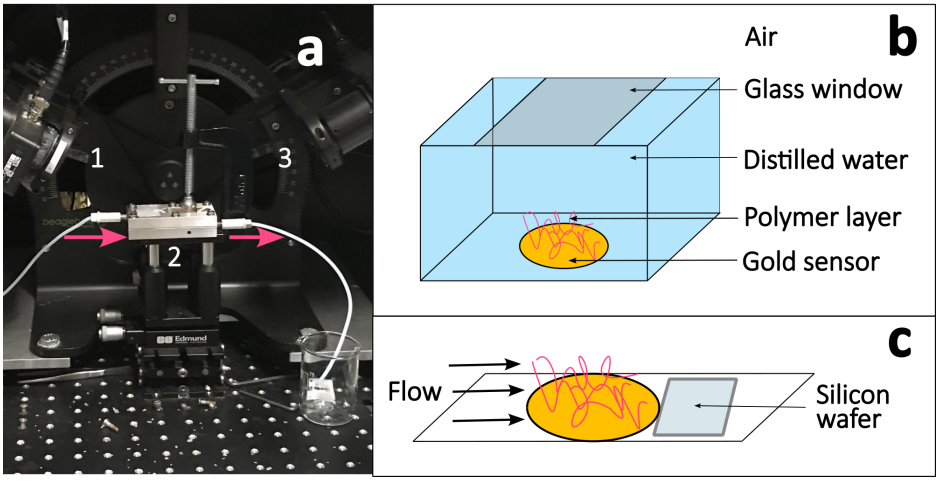

Figure 2.3 *Picture of the ellipsometry experimental set-up (a), comprising 1: a 632.8 nm HeNe laser, 2: a laminar flow cell and 3: a split photo-detector. The pink arrows indicate the direction of the flow. Schematic representation of the optical model (b). When monitoring the formation of an HA layer from an entangled OVD solution, a piece of silicon wafer was added downstream of the sensor to prevent it from being displaced by the flow of the viscoelastic solution (c).*

Unlike QCM-D, the adsorbed mass determined by ellipsometry is not affected by any coupling of the adsorbed layer to the surrounding fluid, although approximations have to be made about the refractive index of the polymer layer.

Polymer adsorption was monitored *in situ* on the gold surface of the QCM-D sensors mounted in the ellipsometry flow cell. Prior to each measurement, the following cleaning procedure was used: after a 30-minute sonication in 2% Hellmanex II, the sensors were rinsed, sonicated for 10 minutes in milliQ water and dried with nitrogen. When using OVD solutions diluted in distilled water by a factor of two, they were degassed in a desiccator under vacuum to avoid the formation of air bubbles. A piece of silicon wafer was placed downstream of the sensor to prevent it from being displaced by flow of the viscous OVD solution.

A measurement was first performed in air for one minute to ensure a stable initial baseline, then milliQ water was injected using the same peristaltic pump as in the QCM-D experiment at a flow rate of 100 µL.min^{-1}. Once the sensor was covered in water, the polymer solution was injected at the same flow rate for an hour. Afterwards, the sensor was rinsed with distilled water for 10 minutes at the same flow rate to see if any desorption occurred.

2.3 Interfacial Tensiometry

Interfacial tensiometry is used to provide information on the interfacial activity of the polymer solutions used in this thesis. The pendant drop method yields information on the air-liquid surface tension. The shape of the interface at equilibrium can be predicted using the Young-Laplace equation 2.17:

$$\Delta P \;=\; P_{in} \;-\; P_{out} \;=\; \gamma_{LG}\left(\frac{1}{R_1}+\frac{1}{R_2}\right) \tag{2.17}$$

.

where ΔP is the pressure difference between the inside (P_{in}) and the outside of the droplet (P_{out}), and γ_{LG} is the liquid-gas surface tension. R_1 and R_2 are the radii of curvature, as represented on Figure 2.4 a.

On the other hand, the sessile drop method is mostly used to characterise the substrate wettability by the solutions. The boundary conditions for thermodynamic equilibrium between the three phases are predicted by the Young-Dupré equation 2.18:

$$\gamma_{LG}\cos\theta = \gamma_{SG} - \gamma_{SL} \tag{2.18}$$

where γ_{LG}, γ_{SG} and γ_{SL} respectively refer to the liquid-gas, solid-gas and solid-liquid surface tensions, and θ refers to the contact angle that the liquid forms with the solid surface, as represented on Figure 2.4 b.

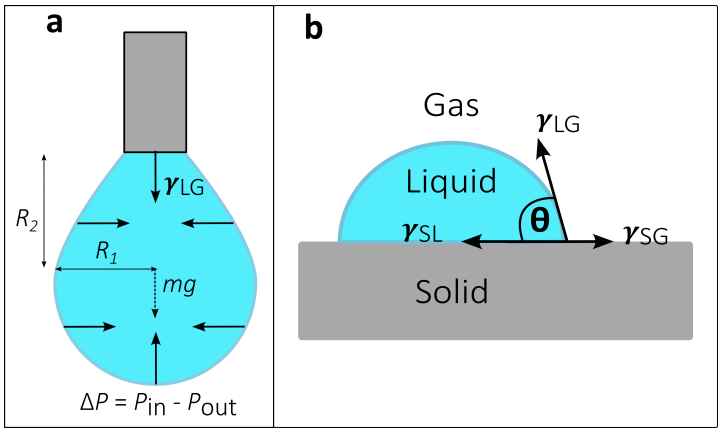

Figure 2.4 *A schematic representation of (a) a pendant and (b) a sessile drop studied with interfacial tensiometry. The shape of a pendant drop is described by the Young-Laplace equation, where R_1 and R_2 are the radii of curvature. mg represents the weight of the droplet. The sessile drop is a Young-Dupré system where a droplet of liquid is in thermodynamic equilibrium with a solid and the ambient gas, forming a contact angle Θ with the underlying substrate. γ_{LG}, γ_{SL} and γ_{SG} correspond to the interfacial tension at the liquid-gas, solid-liquid and solid-gas interface.*

2.4 Colloidal Probe Atomic Force Microscopy

2.4.1 Introduction

Atomic Force Microscopy (AFM) is a scanning probe microscopy method based on the interaction force between an oscillating cantilever with a nanoscopic tip and a surface. The desired tip-surface interaction force is chosen prior to measurement, and is referred to as the setpoint. As the tip approaches the surface, the bending of the cantilever is measured by means of an optical system comprising a laser diode and a split photo-detector. The difference between the amplitude measured and the amplitude of the setpoint is recorded as an error signal. This signal is fed into a feedback loop, which automatically adjusts the height of the cantilever through a piezoelectric element in the vertical direction.

This yields information on both the surface topography and the tip-substrate

interaction force. AFM can therefore be used for either imaging or force spectroscopy. In addition to its versatility and molecular scale resolution, AFM can be used in solution, which is of great interest for the study of soft matter and biological systems.

Several imaging methods exist, and differ based on how the tip interacts with the substrate. In contact mode, the tip stays in contact with the substrate, whereas in non-contact mode, it oscillates above the surface without touching it. We used the tapping, or intermittent mode, where the cantilever tip periodically comes into contact with the substrate. This method allows high-resolution imaging whilst minimising damage on the substrate.

To measure force curves, the cantilever approaches the substrate in the normal direction, until contact. It then needs to overcome the adhesion force F_{adh} between the tip of the probe and the substrate in order to retract away from the surface [55]. The cantilever deflection is translated into a force by multiplying by the spring constant.

Colloidal probe AFM uses a tipless cantilever to which a colloidal particle has been attached. In that situation, one can use the Derjaguin approximation to obtain the energy per unit area U_A between a microsphere of radius R and a flat surface.

$$U_A = \frac{F}{2\pi\ R} \tag{2.19}$$

It follows from equation 2.19 that the ratio $\frac{F}{R}$ corresponds to $2\pi\ U_A$, which is why this variable is typically plotted against the distance between the probe and the surface.

Colloidal probe AFM offers several advantages. The particle radius is typically known with a great precision, which allows quantitative force measurements with a great repeatability compared to other AFM tips of various shapes and dimensions. The particles can also be functionalised to study specific interactions. We used this technique to measure the force between a silica particle coated with HA and biomimetic surfaces, which were also imaged topographically with AFM.

2.4.2 Experimental Protocol: Colloid and Substrate Functionalisation

For imaging the samples, we used a Bruker JPK NanoWizard 4XP AFM head, whilst the force curves were obtained with a Bruker JPK Cellhesion200, which is a type of head optimised for measuring data at large tip-sample separation, up to 100 µm. The relevant head was mounted on an inverted Zeiss Axio Observer optical microscope with a precision motorised stage. A Cytosurge FluidFM (Fluidic Force Microscopy) micropipette with a 2 µm aperture and a 0.3 $N.m^{-1}$ spring constant allowed us to pick up individual colloids and use them as a tip for force measurements. The spring constant was calibrated using the Sader contact-free method [56].

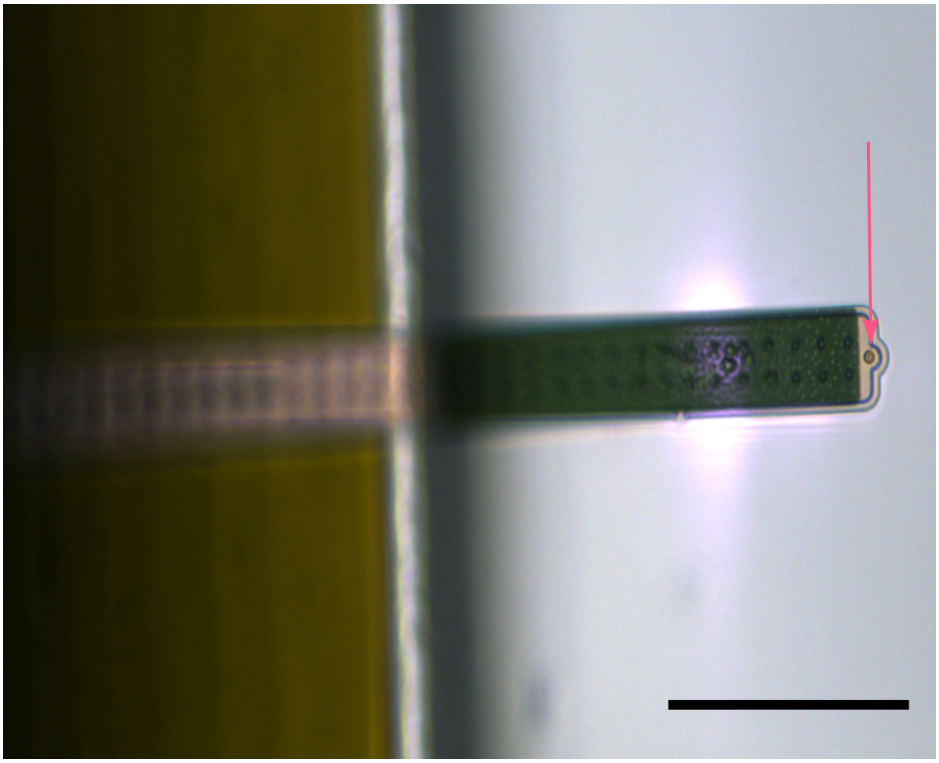

Figure 2.5 *A FluidFM micropipette was used to pick up a silica particle functionalised with HA which was then used as an AFM tip (arrow). Scale bar is 100 µm.*

We bought 4.48 µm diameter SiO_2 particles suspended in aqueous solution from microParticles GmbH. Our functionalising protocol was inspired by Jiang *et al.* [57]. A 100 µL aliquot of solution was placed in the UV-Ozone cleaner for 30 minutes in order to create surface silanol groups. We centrifuged the particles for 5 minutes at 2500 rpm and redispersed them in a 1:9 v/v

solution of 3-aminopropyltriethoxysilane (APTES) in ethanol overnight at room temperature under gentle stirring. During this silanisation step, an APTES self-assembled monolayer (SAM) formed on the particle surface, as confirmed by AFM topography imaging in Section 5.3.1. The particles were centrifuged three times in pure ethanol to remove any unattached APTES molecule and break any silane networks.

The next step involved creating a chemical crosslink between the APTES SAM and HA from the OVDs provided by Hyaltech. We employed the widely used 1-ethyl-3-(-3-dimethylaminopropyl) carbodiimide hydrochloride/N-hydroxysuccinimide (EDC/NHS) coupling. This works by converting carboxylic acid functional groups in HA into an NHS-ester intermediate. The latter reacts with the amine group of the APTES SAM on the particle surface, forming a peptide/amide bond. A schematic of the experimental design can be found in Figure 5.1.

To a solution containing 2 mM EDC and 5 mM NHS, we added 1 mL of an OVD solution diluted to 1 mg.mL^{-1} HA in PBS (pH 7, 144 mM NaCl). After 5 minutes, we immersed the APTES-coated particles in this coupling solution and left it under gentle stirring overnight. Afterwards, we rinsed the particles in distilled water three times to hydrolyse back any residual ester groups back to the native carboxylic acid groups of HA. The solutions were diluted by a factor of 10 in distilled water before use.

On two separate occasions, due to a shortage in the FluidFM micropipette, a silica particle was glued to the cantilever using a microscope and we functionalised the whole cantilever instead[1]. The centrifuging steps were replaced by rinsing three times. The force profiles were similar to those obtained with FluidFM.

The substrates were functionalised as follows: microscope glass slides were cleaned by sonication in a 2% Decon solution for 30 minutes, rinsed with distilled water and ethanol, dried with air and placed 1h in UV/Ozone. They were then either immersed for 5 minutes in a 0.1 mg.mL^{-1} PLGA or PLL solution, or for 90 minutes in a 1 mg.mL^{-1} mucin solution. Lastly, they were thoroughly rinsed with distilled water and stored in PBS until use. The HA-functionalised substrates were prepared by adapting the protocol used for the particles by

[1]The gluing step was performed by Dr Laura Charlton

replacing the centrifuging steps with a thorough rinse in the appropriate solvent (ethanol for the silanisation step and distilled water for the coupling step).

2.4.3 Data Analysis: Worm-like Chain Model

Flexible linear polymers exhibit a random coil configuration [58, 59]. Assuming the end-to-end distance follows a Gaussian distribution, the restoring force that would act on a retracting cantilever would be proportional to polymer extension. However, such a linear response is only observed for small extensions. The reason is that the effective end-to-end distance cannot physically be longer than the contour length, which is the length at maximum extension, which is not captured by the Gaussian distribution.

Polymer physics models have been developed to overcome this caveat, and give a more appropriate description of the mechanics of macromolecules. The most widely used models are the freely-jointed chain (FJC) and worm-like chain (WLC). The former describes the polymer as independent discrete segments only able to rotate with respect to one another. The latter, which we have used in our analysis, describes the polymer as a semi-flexible isotropic rod. In this model, the polymer behaves rigidly over short distances, following the linear relation described in Hooke's law for spring deformation, but it gains some flexibility at a larger extension, deviating from the linear behaviour. The force F corresponding to end-to-end extension x is given by equation 2.20:

$$F = \frac{k_B T}{b} \left(\frac{1}{4\ (1 - \frac{x}{L})^2 - \frac{1}{4} + \frac{x}{L}} \right) \tag{2.20}$$

where b is the persistence length and L is the contour length.

2.5 Scanning Electron Microscopy

2.5.1 Introduction

SEM is a non-optical microscopy technique using a beam of electrons to generate high-resolution images. Vacuum is required in order to prevent electrical

discharge and avoid beam attenuation. As the beam reaches the sample surface, some electrons are reflected back to the detector (back-scattered electrons, ESB detector). These low-energy electrons (< 50 eV) provide information on elemental composition, as heavier elements yield more back-scattered electrons and therefore appear as brighter on the image [60].

In parallel, the equipment also detects secondary electrons generated by inelastic scattering at the interface (SESI and Inlens detectors). Unlike back-scattered electrons, these do not penetrate the sample, which makes them more surface-sensitive. They provide the best topological resolution [61].

Another feature of SEM is the ability to produce elemental mapping of the substrate using Energy Dispersive X-ray spectroscopy (EDX). As the sample is hit by the electron beam, it emits X-rays with an energy defined by the atomic structure of the elements present. However, one must keep in mind that elements of low atomic number such as carbon ($Z = 6$) are difficult to detect with EDX because the X-rays they produce are low in energy and can be absorbed by the sample [62].

A drawback of SEM is the need for vacuum, which requires dry samples. Cryogenic SEM (Cryo-SEM) was developed as a way to work around this issue. The Cryo-SEM samples are flash-frozen in liquid nitrogen, turning the liquid water into vitreous ice. The ice surface is then fractured, revealing the internal structure effectively fixed in its hydrated configuration when a high pressure freezer is used [63, 64]. As we did not have access to a high pressure freezer, some ice damage did occur, and this effect will be discussed later.

2.5.2 Sample Preparation

Colloids were functionalised using the procedure described in Section 2.4.2. Control particles were prepared by replacing the OVD solution with pure PBS, and APTES with pure ethanol. After functionalisation, the solutions were centrifuged to increase the effective particle concentration. For regular SEM, droplets of solution were put on a silicon wafer, dried on a 150°C plate for a few minutes and coated with platinum to ensure good conductivity. We chose platinum over gold because it has a far smaller grain size. We used a field emission gun electron source, which allows for high magnification imaging, where the gold coating would have been visible.

For Cryo-SEM, a droplet of solution was placed on a brass hollow rivet. The system was immersed into slush nitrogen to enable fast freezing. It was then transferred to a preparation chamber under vacuum set at -140°C, to prevent any amorphous ice from crystallising. After chopping off the ice from the top of the frozen droplet, we increased the temperature to 90°C for 5 minutes to sublime a thin layer of ice from the sample surface, and coated it with platinum unless stated otherwise.

Chapter 3

Model System: PVP Adsorption and Desorption from Solid/Liquid Interfaces

3.1 Introduction: Rationale for Using PVP

The fundamental differences between dispersive and cohesive OVDs lie in their spreading ability and their behaviour upon aspiration from the corneal endothelium, as described in Chapter 1. In a nutshell, dispersive OVDs provide a better coating, but their removal is more challenging than their cohesive counterpart, although complete removal is necessary in order to avoid post-operative complications.

The ability of OVDs to coat the endothelium [43, 65] and their retention time in the anterior chamber [29, 40, 66, 67] have both been characterised before. However, the literature lacks a quantitative measurement of polymer adsorption from OVD solutions. We used QCM-D and ellipsometry to monitor the formation of adsorbed polymer layers from solution. We also probed the resistance of the layer to solvent rinsing. This type of flow-induced desorption can happen *in vivo* both as a consequence of the turbulent flow originating from the ultrasound phaco probe or when the surgeons actively attempt to remove OVDs using an irrigation-aspiration device.

These two *in situ* techniques offer an interesting comparison: QCM-D is sensitive to the viscoelastic coupling of the layer to the surrounding solvent, which is why the surface excess obtained with QCM-D is often referred to as a wet mass [68, 69]. On the other hand, ellipsometry measures the reflection of a light beam on the layer, which makes it sensitive to the layer thickness but not to its viscoelasticity [70, 71]. The result obtained from ellipsometry and other optical techniques is therefore qualified as a dry thickness, even though the measurement can be done in solution and does not require air or vacuum [70, 71].

Despite being a powerful technique to simultaneously probe polymer adsorption and film viscoelasticity, QCM-D is typically used for dilute low viscosity solutions. OVDs, on the contrary, are complex shear-thinning viscoelastic fluids with a high zero-shear viscosity. For this reason, we decided to start our study using a well-characterised low concentration polymer solution for which the solution viscosity is close to that of water and Newtonian [72]. This polymer will later be used as a starting point to compare OVDs with in Chapter 4.

Polyvinylpyrrolidone (PVP) is a synthetic linear non-ionic amphiphilic polymer. It is used in various industrial applications ranging from food stabilisers to cosmetic creams owing to to its good biocompatibility and relatively low cost. As a consequence, its properties have been described quite extensively in the literature, sometimes in conjunction with HA [73, 74]. More pertinently, PVP is also commonly used in ocular applications. It is a candidate of choice to treat dry eye syndrome thanks to its lubricating properties. It is a component of artificial tears, as it bears a resemblance to the glycoproteins which constitute the mucin layer of the tear film, as described in Chapter 1. Specifically, chemisorbed layers of high molecular weight PVP ($\geq$ 360 kDa) have been found to be excellent at reducing the coefficient of friction (CoF $\leq$ 0.01) due to their hydrophilicity and water retention ability [75]. Contact lenses have also been formulated to progressively release PVP in the eye, either for therapeutic applications or simply optimised comfort [76].

Water is expected to be a Θ solvent for PVP at room temperature [77]. In theta conditions, the attractive contributions arising from excluded volume, which typically result in polymer expansion, exactly cancels out the repulsive contributions. This results in a net zero excluded volume [78], meaning that the intermolecular affinity of PVP is equivalent to its affinity for water. This

implies that the polymer chains should be relatively swollen in water, and are not expected to form dense globules.

In addition to characterising the interaction of PVP with a bare gold sensor surface, we use a mucin layer physisorbed on the gold surface as a biomimetic substrate. The literature describes the existence of a 0.5 µm thick mucinous layer on the endothelial surface [79]. This layer is highly hydrophilic and possesses a net negative charge at physiological pH due to the presence of sialic acid and sulfonic acid residues. The term mucinous is somewhat misleading, as it has been used as a generic term to describe a viscous gel before actually determining if the layer contained any mucins. The latter, also called mucoproteins, are high molecular weight glycoproteins, 21 of which were identified in humans [80, 81]. Although most studies focus on the corneal epithelium, where the mucins MUC1, MUC4 and MUC16 are expressed [11], the presence of MUC1 on the corneal endothelium has also been highlighted, as well as some other macromolecules, including HA [82]. Based on that information, we concluded that mucin functionalisation from solution was suitable to mimic the properties of the endothelial surface.

3.2 Polymer Adsorption Kinetics: Theory

The kinetics of polymer adsorption have been described in [83, 84]. At the very early stages of adsorption, the kinetics differ based on the adsorption mechanism: chemisorption or physisorption. In the former case, the polymer has to overcome an energy barrier to create a covalent bond with the surface, and one expects an initial linear increase of the surface excess φ with respect to time. In the latter case, the rate-limiting step is the diffusion of polymer chains to the solid interface, and φ increases linearly with the square root of time, as described in the work of Weber and Morris on adsorption kinetics of organic compounds onto porous carbon [85]. This simple model yields equation 3.1, where φ is the adsorbed quantity, k is the diffusion rate constant and C represents the boundary effect.

$$\varphi(t) = k\ \sqrt{t}\ +\ C \tag{3.1}$$

The addition of a new chain to an adsorbed layer follows a two-step process, whereby the chain first enters the layer, and subsequently spreads on the surface, creating multiple adsorption sites per chain. As the film builds up, the polymer

chains adopt a self-similar concentration profile as described by de Gennes, with some long segments in contact with the surface (trains), some dangling segments between two contact points (loops) and some unattached ends (tails) [86], as illustrated in Figure 3.1. Once saturation has been reached, and the substrate is covered in polymer, the adsorption enters a slower stage. Any new chain has to overcome an energy barrier arising from the excluded volume of the previously adsorbed chains.

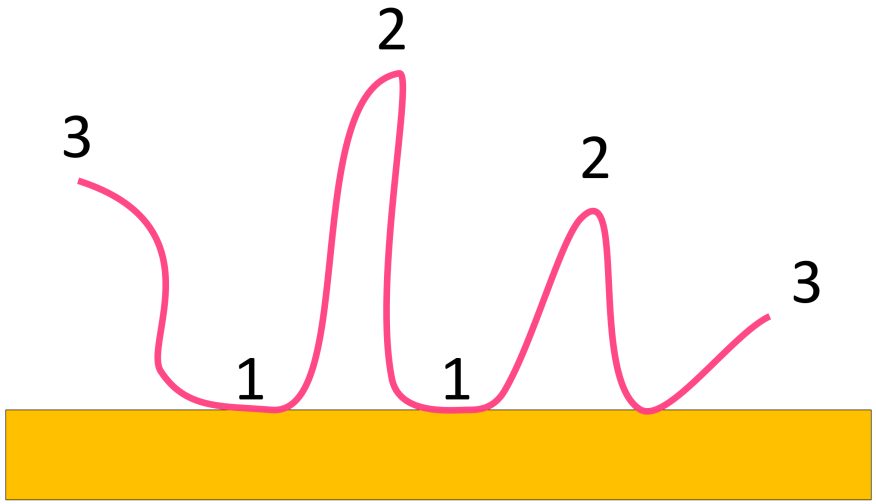

Figure 3.1 *Adsorbed polymers typically adopt a configuration where some segments are in close contact with the surface (trains, 1), whilst some dangling segments (loops, 2) and unattached ends (tails, 3) extend into solution [86].*

Complete removal of an adsorbed polymer layer by washing with pure solvent is not observed on measurable timescales. However, exchange between adsorbed polymers and free chains in solution is quicker than desorption and can be observed experimentally [87]. The rate-limiting step to the desorption of an adsorbed polymer chain can either be the energy required to break adsorption sites or the diffusion of all surface-bound segments through the adsorbed layer [88]. In the latter case, polymer desorption follows extremely slow kinetics. Undersaturated starved layers can be obtained if the layer is in equilibrium with a highly dilute polymer solution [89].

3.3 Adsorption From a Highly Dilute Solution

3.3.1 Validity of the Initial Baseline Approximation

As described in Chapter 2, QCM-D was initially developed for use in air or vacuum. It was adapted to the use in liquids by Kanazawa and Gordon [50], who proposed a model to account for the damping of the shear wave in a quartz immersed in a Newtonian fluid. In order to check that our initial baseline was in line with the values expected from the Kanazawa-Gordon model, we recorded the frequency shifts at all overtones when the sensor was immersed in distilled water at 20°C ($\eta_l = 1.0016$ mPa.s, $\rho_l = 0.9982$ g.cm^{-3}). The values stabilised in a flow of distilled water at 100 µL.min^{-1} for 25 minutes at room temperature. We also plotted the difference between the value observed and the one expected from the Kanazawa-Gordon model (residuals plot) to estimate the validity of the fit and the error estimation. Figure 3.2 (upper left) shows the frequency shifts measured and calculated using the Kanazawa-Gordon model. From the residuals shown in the upper right it can be seen that there is a systematic deviation.

Despite a systematic deviation from the model as the overtone number increased, which could be due to the decrease in the wave penetration depth and in the increase in signal-to-noise ratio, the recorded frequency shifts were close to the values expected from the model, with a linear dependence on the overtone number. The error bars were calculated according to the formula for error propagation, which is detailed in Appendix A. They expand with the overtone number, which is expected as we are plotting Δf_n, and not $\frac{\Delta f_n}{n}$, as a function of n. In the rest of the thesis, the frequency will be plotted as $\frac{\Delta f_n}{n}$.

The dissipation shifts were also close to the model, with the exception of the fundamental, which is known to experience a significant noise due to its high sensitivity. As for ΔD, the data points appear to be more scattered, however only 2/7 points lie within one error bar of the x axis, which suggests the error bars were somewhat underestimated.

Based on this information, we determined it was reasonable to use this signal in distilled water as an initial baseline. Additional changes in frequency and dissipation when injecting a PVP solution will be attributed to polymer layer formation.

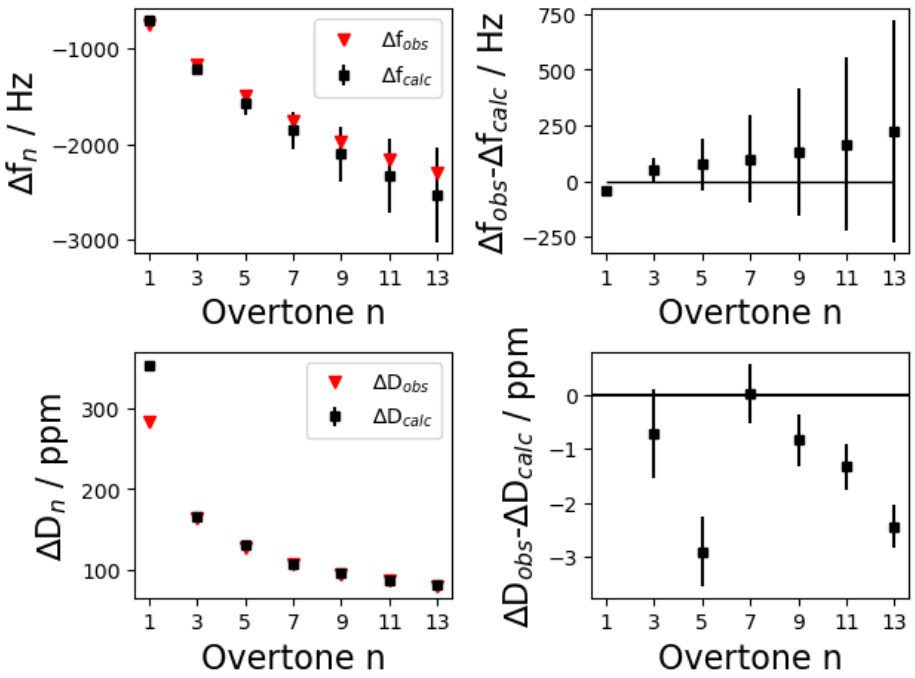

Figure 3.2 *The frequency (upper left) and dissipation shifts (lower left) expected for the sensor going from air to distilled water was calculated using the Kanazawa-Gordon model (Δf_{calc}, ΔD_{calc}, black squares) and compared to the experimental values (Δf_{obs}, ΔD_{obs}, red triangles). The residuals were plotted to estimate the fitness of error estimation (upper right, lower right). The fundamental was omitted for ΔD for clarity. The error bars were calculated from error propagation with the instrument specifications, as detailed in Appendix A.*

3.3.2 Formation of a Starved PVP layer

Figure 3.3 shows the change in the resonant frequency and dissipation measured for the third overtone during adsorption from a highly dilute 1 ppm (w/v) solution of 360 kDa PVP in distilled water. The experimental protocol is detailed in Section 2.1.3.

Injecting the PVP solution in the sensor chamber resulted in a rapid decrease in frequency, which reached a plateau after 30 minutes. In parallel, the dissipation increased, whilst staying at a low value (less than 1 ppm). Rinsing with distilled water had no effect on Δf, which suggests the layer was sufficiently strongly attached to the gold surface to resist desorption. ΔD slightly decreased, which is characteristic of a layer becoming more rigid. Flowing an alkaline detergent (2% Hellmanex II) for 30 minutes and then rinsing with distilled water at 150 µL.min^{-1} for two hours was sufficient to desorb the layer, as seen by the

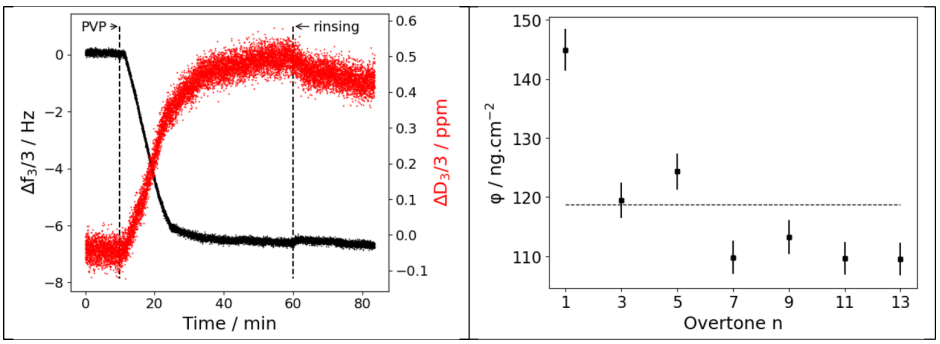

Figure 3.3 *(Left panel) Time-dependent changes in resonant frequency (black diamonds) and dissipation (red squares) measured with QCM-D for the third overtone. (Right panel) Sauerbrey analysis of the PVP surface mass adsorbed after flowing a 1 ppm solution for 1h (from the fundamental to the thirteenth overtone). The dotted line represents the average value. The error bars were calculated using the error propagation described in Appendix A.*

signal returning to the original baseline (see Figure B.1 in the Appendix). The frequency and dissipation shifts values lie within the same range as the ones reported in the literature for PVP adsorption onto a silica-coated sensor [72].

Based on Figure 3.2, and the low dissipation value shown in Figure 3.3 typically associated with a rigid polymer layer, the Sauerbrey model is a good approximation here. The resulting surface excess values obtained are presented in Figure 3.3.

The surface excess calculated with the Sauerbrey model displayed a decrease as the overtone number increased. However, all values were in the same order of magnitude, close to 120 ng.cm^{-2} and with some error bars overlapping. The average value from the third to the thirteenth overtone was determined from 4 independent measurements and yielded $\varphi = 114(5)$ ng.cm^{-2}. As explained earlier, the Sauerbrey model is used for dense rigid layers, with a volume fraction close to 1, so in calculating the surface excess it is appropriate to assume the layer density can be approximated by the dry polymer density ($\rho_{PVP} = 1.2$ g.cm^{-3}). Dividing the surface excess φ by the dry PVP density yields a value of layer thickness close to 1 nm. This can be seen as a measure of the bound material, which contribute to a change in Δf. The formation of loops is sensed through the changes in ΔD.

The Kanazawa-Gordon model described in Section 3.3.1 predicts that a difference between the ambient fluid density and viscosity compared to the baseline buffer

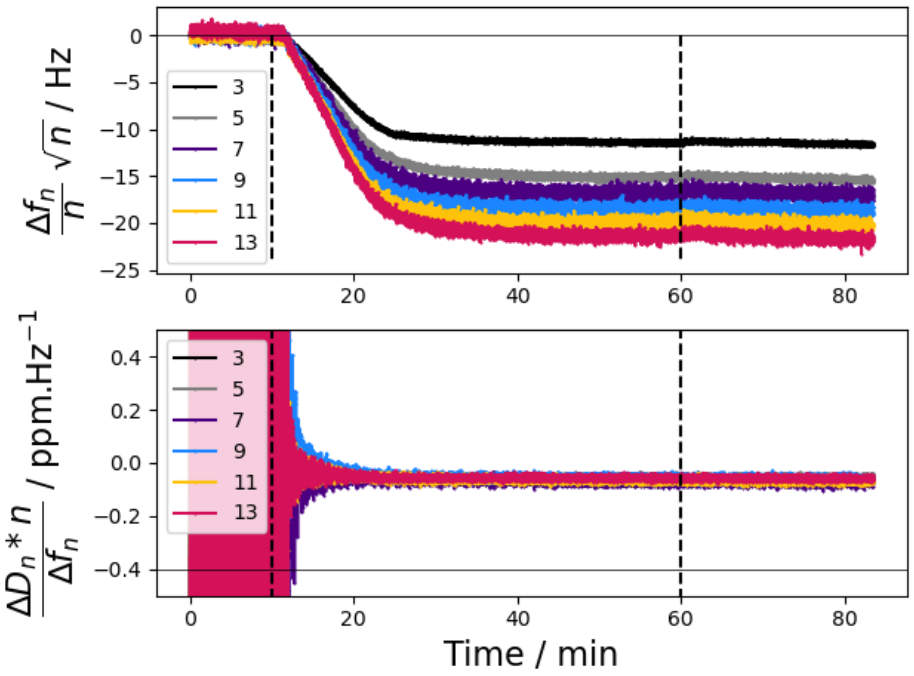

Figure 3.4 *(Upper panel) Time-dependent changes in* $\frac{\Delta f_n}{n}\sqrt{n}$ *for all overtones. (Lower panel) Time-dependent ratio of* ΔD *and* $\Delta f_n/n$*. Both these features are representative of polymer adsorption as opposed to bulk shift. The vertical dotted lines correspond to PVP injection and rinsing. The vertical axis minimum in the lower panel was set at -0.5 ppm.Hz*$^{-1}$ *to only reflect the values which were in the range of interest despite a spiky signal.*

should also result in a shift in frequency and dissipation, which is referred to as bulk shift. In that situation, one would expect $\frac{\Delta f_n}{n}$ to be proportional to $\frac{1}{\sqrt{n}}$, and the acoustic ratio $\frac{\Delta D_n\ n}{\Delta f_n}$ to have a constant value of -0.4 ppm.Hz^{-1}. In the case of PVP, neither condition is met, Figure 3.4, so we can be confident that the shifts observed can be attributed to adsorption rather than bulk shift.

3.3.3 Phase Modulation Ellipsometry: Comparison with QCM-D

Kinetic ellipsometry was used to monitor the adsorption of PVP onto the gold surface of a QCM-D sensor *in situ* from a dilute 1 ppm solution in the same way as QCM-D. The procedure is detailed in Section 2.2.2. Getting an independent measurement of layer thickness is of interest to confirm the validity of the Sauerbrey model. Besides, ellipsometry is an optical technique which is sensitive to the total layer thickness but not to polymer reorganisation or coupling with

the ambient fluid, unlike QCM-D. It is common in the literature to refer to the thickness obtained with optical techniques as dry thickness for this reason [70, 71]. On the other hand, conformational changes can be spotted on QCM-D if the frequency stays constant whilst the dissipation changes. The layer thickness obtained with the Sauerbrey model was compared with the result obtained with ellipsometry and is shown on Figure 3.5. The values for the layer density and refractive index were respectively 1.2 g.cm^{-3} and 1.51, which both correspond to the values for dry PVP.

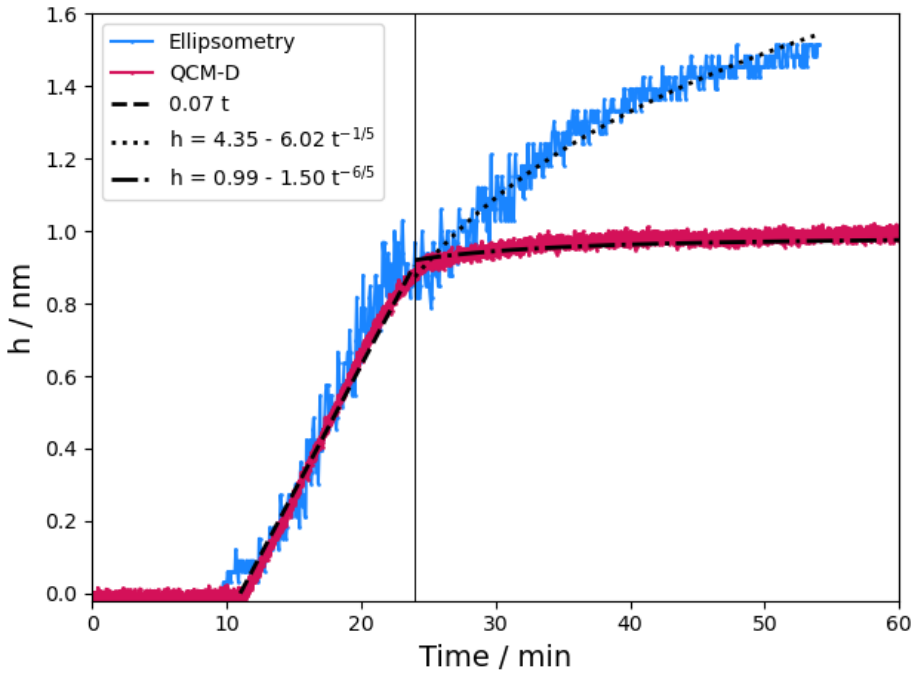

Figure 3.5 *Layer thickness h obtained with the Sauerbrey model from QCM-D results (3rd overtone) assuming a layer density ρ_{layer} = 1.2 g.cm^{-3} (pink) compared with ellipsometry results assuming a refractive index n_{layer} = 1.51 (blue), which both correspond to dry PVP. The data was fitted to chemisorption kinetics, with a first linear stage between 11 and 24 minutes (dashed black line) followed by a slower stage between 24 and 60 minutes with a $t^{-1/5}$ dependence for ellipsometry (dotted black line) and a $t^{-6/5}$ dependence for QCM-D (dash-dot black line).*

O'Shaughnessy and Vavylonis have proposed kinetic models for irreversible adsorption from dilute polymer solutions [84]. For chemisorption, in which there is an energetic adsorption barrier, they identify a linear dependence for surface excess up to monolayer formation. Beyond that, they predict that further adsorption of surface-bound segments has a $t^{-\frac{6}{5}}$ dependence whilst all segments in the diffuse layer comprising the loops, referred to as a total mass, build up

with a $t^{-\frac{1}{5}}$ dependence.

The values of layer thickness found with both techniques were remarkably close for the first 24 minutes. In that initial stage, the layer grew linearly with time (11 to 24 minutes, dashed line), as expected for monolayer formation. The low dissipation upon adsorption recorded with QCM-D (Figure 3.3) associated with this similarity of layer thickness measured with ellipsometry (a technique which is not affected by the potential elasticity of the layer) shows that the layer displays a negligible elasticity at that stage. This would be the case for a flat configuration with mostly tails adsorbed, allowing the polymer chains to make multiple contact points on the surface.

After 24 minutes, the signals started to deviate, with the thickness determined by QCM-D increasing less rapidly than that determined by ellipsometry. This corresponds to the slower stage described earlier, once the surface reached saturation. In this second stage, $\Delta h \approx t^{-6/5}$ (dash-dot line) for QCM-D whilst $\Delta h \approx t^{-1/5}$ for ellipsometry (dotted line). Our interpretation is that after 24 minutes, the film started to rearrange from a mostly trains configuration to the formation of some loops which, while only leading to a minor frequency change in QCM-D, was detected in a more significant fashion by ellipsometry. In other words, frequency shifts in QCM-D would probe the mass of polymer segments effectively bound to the sensor surface (1 in Figure 3.1), whilst ellipsometry would be sensitive to the total surface excess, regardless of whether the segments are bound to the sensor or in loops/tails (1, 2, 3 in Figure 3.1). This would also be compatible with the slight increase in dissipation between 25 and 50 minutes, which can be seen on Figure 3.3, and indicates the formation of a more diffuse layer.

There are examples of experiments in the literature where an adsorbed layer of relatively short polymer chains is exposed to a solution containing larger chains, which progressively displace the shorter ones [90–92]. In the context of these measurements, if PVP is polydisperse, shorter, faster-diffusing chains might adsorb first. They could then be replaced by longer chains, creating a fluffy layer detected by ellipsometry, but missed by QCM-D.

We have shown in this section that the kinetic evolution of the experimental values of layer thickness determined by QCM-D and ellipsometry can be explained by

a kinetic model for chemisorption of a polymer from a dilute solution. This chemisorption may occur from electronic interactions between gold and the pyrrolidone ring. Rinsing with distilled water did not result in any significant polymer desorption, which points out to a strong attachment of the PVP layer to the gold surface, as expected from a chemisorption process.

3.4 PVP Interaction with a Solid Substrate: Concentration Dependence

As discussed, OVDs have concentrations which are several orders of magnitude higher than the 1 ppm concentration studied so far. They are typically well above the overlap concentration c^*, where polymer coils start to interact in solution, marking the crossover from the dilute to the semi-dilute regime. This will be discussed in more detail in Chapter 4. For this reason, we decided to also investigate the influence of concentration on the adsorption of our PVP system. We recorded the QCM-D response to flowing PVP solutions of increasing concentrations which span from the dilute regime up to 11000 ppm. The latter is equal to twice the overlap concentration [93] and thus corresponds to the semi-dilute regime. The results are presented on Figure 3.6.

All polymer concentrations exhibited some similarities upon adsorption as the 1 ppm solution: Δf decreased upon injection of the polymer solution before rapidly reaching a plateau, with a simultaneous increase in ΔD. Both the frequency and dissipation shifts at equilibrium increased with concentration, which suggests a higher bulk concentration lead to the formation of a thicker, softer layer. The frequency signal obtained with the 1000 ppm solution had a slightly different profile, with a shoulder forming after a few minutes, and a longer time needed to reach a stable value. This suggests the layer formation was kinetically slower.

As described in Section 3.3.1, the frequency shift expected for a bulk shift effect can be calculated from the change in density and viscosity of the bulk solution. Furthermore, at low concentrations, the dynamic viscosity η of a polymer solution can be predicted using equation 3.2:

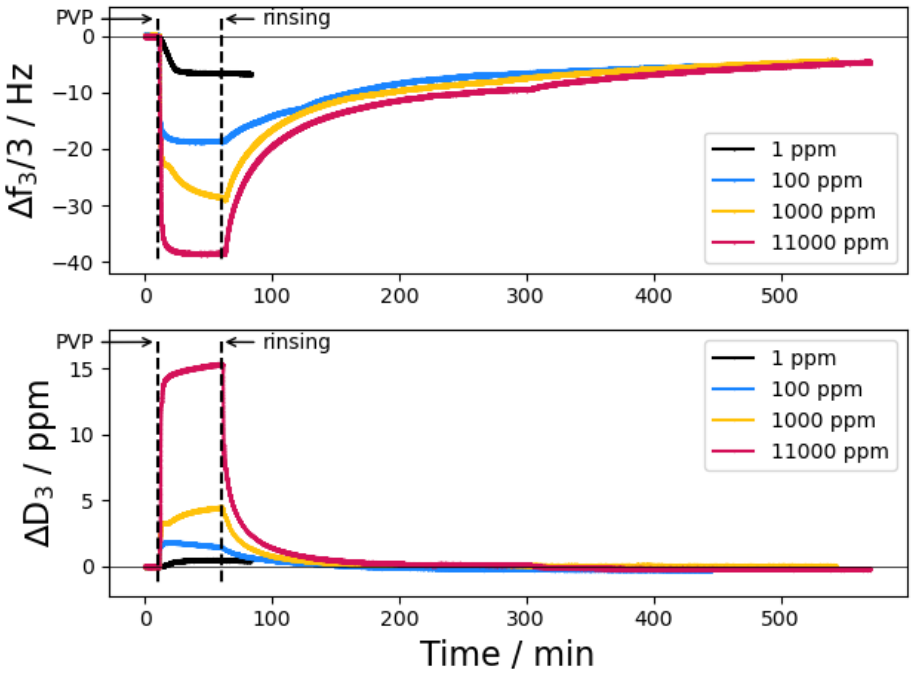

Figure 3.6 *Time-dependent changes in resonant frequency (upper panel) and dissipation (lower panel) measured for the third overtone at different PVP concentrations (black: 1 ppm, blue: 100 ppm, yellow: 1000 ppm, pink: 11000 ppm). The frequency and dissipation shifts increased with concentration. The kinetics of desorption were slow and a residual layer stayed on even after rinsing for several hours.*

$$\eta = \eta_s \, (1 + [\eta]c + k_H[\eta]^2 c^2) \tag{3.2}$$

where c is the bulk concentration, η_s is the solvent dynamic viscosity, $[\eta]$ is the intrinsic viscosity, and k_H is the Huggins coefficient. $[\eta]$ and k_H are both concentration-independent parameters, and have been determined for 360 kDa PVP in [93]. Using this viscosity parameterisation, we calculated the expected frequency shift for each PVP concentration used in Figure 3.6 compared to pure solvent. The results are summarised in Table 3.1.

This shows that the frequency shift arising from the difference in viscosity between the bulk polymer solution and the solvent is insignificant for 1 ppm and 100 ppm. Bulk effects start to become noticeable at 1000 ppm, however the Δf measured is significantly larger, which confirms it is largely arising from polymer adsorption. Bulk effects in the semi-dilute regime (11000 ppm) could not be predicted from the virial expansion used in equation 3.2, as this model is limited to dilute solutions.

PVP concentration	η / mPa.s	ρ / g.cm^{-3}	Δf_3 / Hz
0	1.0016	0.9982	0
1 ppm	1.0018	0.9982	-0.0036
100 ppm	1.02016	0.9983	-0.36
1000 ppm	1.1988	0.9992	-3.66

Table 3.1 *The frequency shifts predicted for the third overtone from a bulk shift effect were calculated using equations 2.7 and 2.8 resulting from the Kanazawa-Gordon model. The viscosity was calculated using equation 3.2.*

A similar analysis as the one presented on Figure 3.4 also confirmed the change in Δf and ΔD was representative of polymer adsorption rather than bulk shift for all concentrations.

As for 1 ppm PVP, the kinetics were fitted to a linear dependence on t during the initial phase of adsorption, which happened over a very short timescale only (typically less than a minute). The results for frequency (k_{f3}) and dissipation (k_{D3}) are presented on Table 3.2.

Concentration:	k_{f3} / Hz.min^{-1}	k_{D3} / ppm.min^{-1}
1 ppm	-0.7(2)	0.025(5)
100 ppm	-27(4)	1.10(8)
1000 ppm	-28(6)	2.0(9)
11000 ppm	-20.86(13)	14(2)

Table 3.2 *The experimental QCM-D data was fitted to chemisorption kinetics during the initial phase, both for frequency k_{f3} and dissipation k_{D3}. The uncertainty corresponds to the standard error of the mean taken over several independent measurements.*

The absolute values of k_{f3} increasing with concentration suggests the monolayer builds up faster in a more concentrated solution, which makes sense for a diffusion-limited process. The largest concentration, 11000 ppm, was an exception to this rule. Polymer overlap in this semi-dilute solution ($c > c^*$) may have slowed the diffusion of the polymer coils. The linear dependency of Δf occurred over a significantly shorter time, and the kinetics were not as clearly compatible with chemisorption as with the 1 ppm case. It is possible that here, the adsorption process was not purely chemisorption, but rather a mixture of chemisorption and physisorption.

On increasing concentration by a factor of 100, the gradient of the initial linear region of Δf_3 increased by a factor of 38. It is less than would be predicted from O'Shaughnessy and Vavylonis for a constant monolayer-surface contact rate [84]. This is however reasonable, as their model does not take into account any energy barrier associated with incoming chains having to penetrate the diffuse outer region of the adsorbed polymer layer. As the solution concentration increases, a higher number of polymers make contact with the surface simultaneously. In a crowded system, there is little space available for new segments to make contact. There is a higher energy barrier to cross in order for the polymer to make multiple contact points with the substrate, which results in a higher grafting density. As the latter increases, the polymer coils sequentially go from a flat (or pancake) configuration with mostly trains adsorbed to an intermediate mushroom configuration, and finally form extended polymer segments with large loops and long tails at high grafting density [94]. Following Guiselin's terminology, we will refer to this configuration as brush-like [95]. This terminology indicates that the polymer is not necessarily adsorbed on its extremity, distinguishing it from end-grafted polymer brushes and avoiding potential confusion. Physisorption becomes more likely than chemisorption, as it is a kinetically faster process.

The gradient of ΔD_3, k_{D3}, also increased by a factor of 44 during this initial period. This indicates an enhanced coupling of the polymer layer with the surrounding solution, which is characteristic of a more diffuse layer involving loops and tails extending into the bulk phase. Unlike the frequency gradient k_{f3}, which did not significantly change beyond 100 ppm, the dissipation gradient kept steadily increasing up to 11000 ppm.

As the dissipation was significant for all concentrations above 1 ppm, the Sauerbrey model was no longer valid. We therefore applied the Voinova model for viscoelastic layers instead. The average value of layer thickness h_{layer}, viscosity η_{layer} and elasticity μ_{layer} over 5 minutes before rinsing are included in Table 3.3.

The results suggest that the layer formed becomes increasingly thick as the concentration increases, which is compatible with the diffuse layer we described earlier. At the highest concentration, which is in the semi-dilute regime, h_{layer} reaches a much larger magnitude than at the other concentrations. This value is close to the radius of gyration R_g, which is expected to be 56 nm at this molecular weight [93]. The layer viscosity decreased as its elastic modulus increased, which

Concentration:	h_{layer} / nm	η_{layer} / mPa.s	μ_{layer} / kPa
100 ppm	9.8(4)	1.238(15)	5.2(2)
1000 ppm	16.87(12)	1.121(2)	6.90(7)
11000 ppm	46.2(3)	1.0439(4)	14.51(7)

Table 3.3 *The layer thickness h_{layer}, viscosity η_{layer} and elastic modulus μ_{layer} before rinsing were obtained using the Voinova model with the third to the thirteenth overtone. The uncertainty corresponds to the standard error of the mean taken over several independent measurements.*

suggests a rather tight packing of the polymer coils compatible with a brush-like configuration, as described by Guiselin [95]. The formation of a polymer layer from solution of increasing concentrations is represented in Figure 3.7.

3.5 PVP Rinsing Behaviour: Concentration Dependence

An interesting difference between the 1 ppm and the more concentrated solutions was the behaviour upon rinsing with distilled water. Whilst the former saw no desorption upon rinsing, the latter exhibited a kinetically slow desorption showcased by an increase in Δf over several hours. The value reached was not quite equal to the original baseline in water, but remarkably close to the plateau obtained with the 1 ppm solution. The rinsing time needed to reach this limit increased with concentration, as shown in Table 3.4. The dissipation displayed the same concentration dependence, albeit the timescale was significantly quicker.

Concentration:	Δt_f / min	Δt_D / min
100 ppm	244	64
1000 ppm	304	86
11000 ppm	371	104

Table 3.4 *Time needed for the frequency Δt_f and dissipation Δt_D to return to the ultrathin layer formed from a 1 ppm solution and shown in Figure 3.3. The rinsing step started at 60 minutes.*

These results show that thicker layers initially formed when the sensor was in contact with more concentrated solutions, possibly brush-like based on the dissipation values. Upon rinsing, these brush-like polymers are exposed to a larger drag force than the flat layer formed from the 1 ppm solution, as they have

loops and tails extending further into the bulk. This larger shear stress leads to a slow desorption of the segments, until only a residual, strongly attached flat layer is left. This behaviour has been highlighted on other polymer systems in the literature [96]. The faster shift in dissipation compared to frequency suggests that a rapid reorganisation of polymer chains took place in the layer exposed to rinsing. Every time a chain is pulled out of the layer, the corresponding volume is liberated, which leaves some space for the remaining chains to spread on the surface. Large loops are progressively replaced by trains. Trains have a limited mobility due to constraints on the surface, which restraints their diffusion through the polymer layer. A schematic representation of the polymer layer forming on the sensor and being rinsed off with solvent can be found in Figure 3.7.

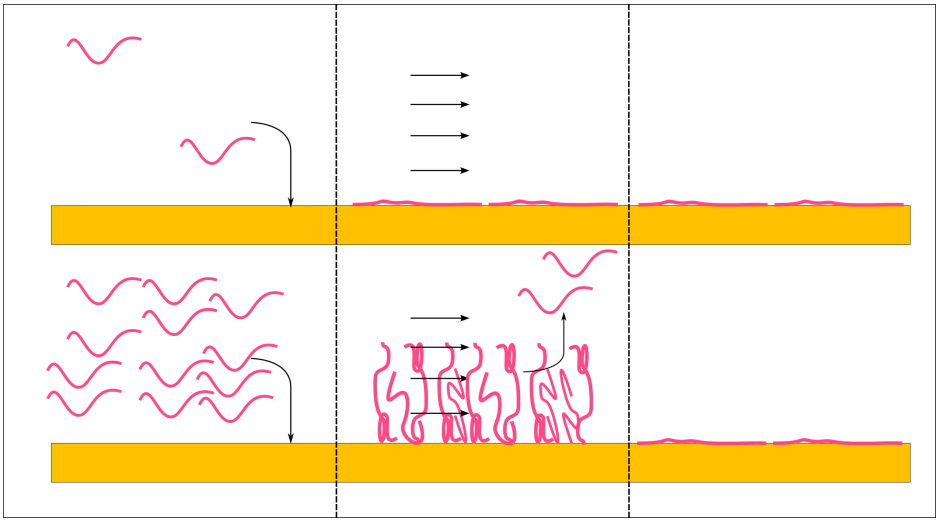

Figure 3.7 *Schematic representation of a dilute (upper panel) or semi-dilute (lower panel) PVP solution being pumped in the QCM-D chamber (left panel). The polymers adsorb as a flat layer from a dilute solution and as a Guiselin brush-like layer from a semi-dilute solution (middle panel). After rinsing, a starved flat layer is left in both cases (right panel).*

3.6 PVP Adsorption on Mucin from a Dilute Solution

As our system of interest is OVDs in the anterior segment of the eye, and in particular how they interact with the corneal endothelium, we designed a protocol to modify the surface of the QCM-D gold sensor, so that it would better resemble the corneal endothelium, described in Chapter 1. The plasma

membranes of epithelial and endothelial cells are covered by a viscoelastic glycocalyx. The glycocalyx is made of polysaccharides which can be associated with lipids (glycolipids) or proteins (glycoproteins). This layer plays a role in cell signalling, but also protection against external damage.

Mucin is a family of endogenous high-molecular weight glycoproteins. 21 of them have been identified in humans, including several types associated with ocular membranes. We decided to use a commercially available mucin powder extracted from porcine stomach to make solutions to physisorb on the substrate, as a first model for the endothelial surface. Mucin adsorption on gold has been studied with QCM-D before [97, 98].

After establishing a stable baseline in distilled water, a 25 ppm mucin solution in distilled water was flowed through the sensor chamber for 50 minutes. Following this, the sensor was rinsed by flowing distilled water for 10 minutes to remove any loosely-bound molecules. Finally, a 100 ppm PVP solution was flowed through the sensor chamber for 50 minutes and then rinsed by flowing distilled water for another 30 minutes. The results are shown in Figure 3.8.

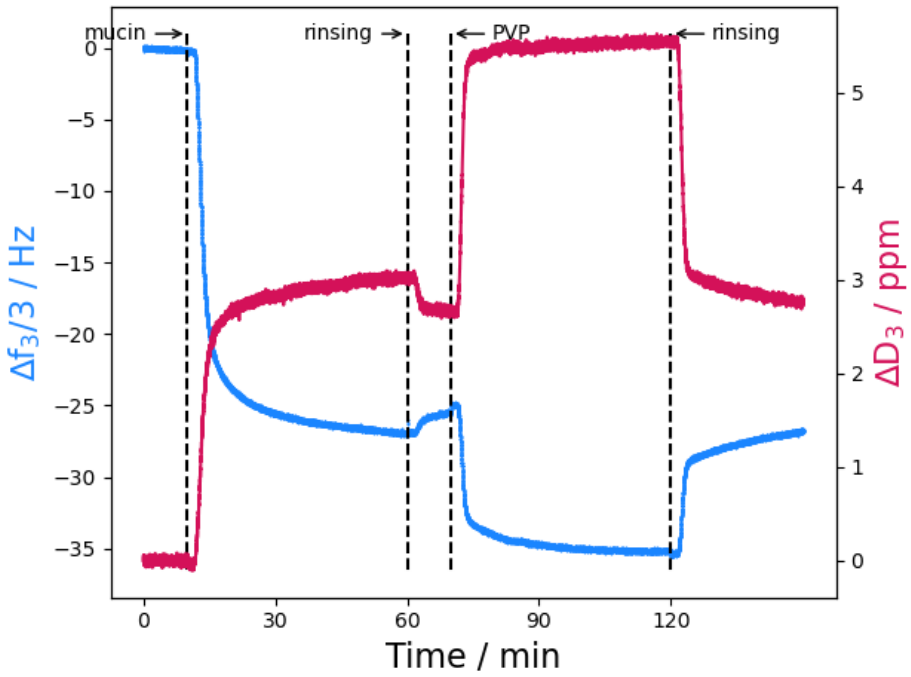

Figure 3.8 *Changes in frequency (blue) and dissipation (pink) for the third overtone observed with QCM-D when injecting a 25 ppm mucin solution and a 100 ppm 360 kDa PVP solution.*

Injecting mucin resulted in the formation of a viscoelastic layer, as shown by the

Substrate	$\Delta f_{monolayer}$ / Hz	$\Delta D_{monolayer}$ / ppm
Gold	-16.8(12)	1.56(6)
Mucin	-10.42	2.88

Table 3.5 *Table comparing the QCM-D signals for the third overtone for a PVP layer on gold and on mucin. The uncertainty for gold corresponds to the standard error of the mean taken over two independent measurements.*

rapid decrease in frequency and concomitant increase in dissipation. The minor changes on rinsing the layer show that it is strongly attached to the QCM-D sensor. Mucin displays some cysteine-rich regions with disulfide bonds, which could break to form thiol bonds with the gold surface. Injecting a 100 ppm PVP solution lead to an additional decrease in Δf and increase in ΔD. Performing an analysis similar to the one presented on Figure 3.4 revealed that these shifts could not be attributed to a bulk shift effect, but to the formation of an additional ad-layer. The frequency shift accompanying the flow of a 100 ppm PVP solution (Δf = -10.42 Hz) was smaller than observed for the bare gold surface, but the increase in dissipation (ΔD = 2.88 ppm) was larger, see Table 3.5. This implies the film formed on mucin had a lower surface excess and was less rigid than the one on the bare gold sensor. It was also easier to desorb, as the signal was already relatively close to the mucin baseline after rinsing for 30 minutes.

The weaker interaction of PVP with mucin than gold was to be expected. The presence of mucin constitutes a steric barrier which partially hinders the formation of an additional PVP ad-layer. The mucin layer, on the other side, appears to be strongly attached to the gold surface, which makes it a good biomimetic substrate. We will discuss its viscoelastic properties in Chapter 4 and compare them with the literature.

3.7 Conclusions

The PVP system showed us how polymer adsorption can be monitored over time using QCM-D. When the gold sensor was in contact with an extremely dilute 1 ppm PVP solution, the polymer chains formed an ultrathin rigid layer for which the Sauerbrey model can be used to monitor the surface bound polymer. We find that the kinetics of the adsorption process are consistent with a model

for polymer chemisorption. The layer attachment was sufficiently strong to resist any desorption upon rinsing with distilled water.

Increasing the solution concentration to up to twice the overlap concentration lead to the quick formation of increasing thick and soft layers, compatible with brush-like polymers. These, however, were partially desorbed upon rinsing, leaving a starved layer behind, similar to the film formed in the 1 ppm solution, which suggests it is a limiting case of undersaturated layer.

We also characterised the adsorption of PVP on a mucin-coated layer, in a first attempt to make a biomimetic substrate. The affinity of PVP for this substrate was lower than for the bare gold sensor, but the attachment of mucin was strong enough to resist desorption, which makes it a good model to further study the adsorption of HA from OVDs, and attempt to draw conclusions on the adsorption on the corneal endothelium.

This low-viscosity PVP model system will be compared with OVDs on Chapter 4.

Chapter 4

Adsorption and Desorption of OVDs from Solid Interfaces

The shear rheology data included in Section 4.5 was obtained by Dr Andreia Silva.

4.1 Introduction

There is great interest in optimising OVDs to ensure effective endothelial protection, whilst minimising the time for complete removal [30, 99]. Cohesive and dispersive OVDs have been reported to exhibit contrasting behaviours upon removal by aspiration. The former is aspirated as a bolus, which can be compared to the adhesive fracture of a polymer coating, whereby the detachment happens at the interface between the polymer coils and the substrate. As the latter is aspirated, it experiences an internal rupture of the polymer network, resembling a cohesive fracture process. However, there is little information in the literature about the adsorption of HA from OVD solutions at a solid interface. The aspiration properties of OVDs are usually attributed to bulk viscoelasticity, ignoring the potential interface effects.

In Chapter 3, we established a model of polymer adsorption and desorption using QCM-D and ellipsometry, which we will use as a base for comparison in this chapter. Although distilled water is a good solvent for HA, the 144 mM PBS

used in these experiment will screen the negative backbone charges, decreasing the solvent quality. We will consider PBS as a Θ solvent for HA [100].

OVDs contain HA at a concentration well above the overlap concentration c^*, where polymer coils start to interact in solution, and above the entanglement concentration c_e (see Section 4.4.1 for the calculations). As a consequence, OVD solutions have a high viscosity at rest, and do not behave as Newtonian fluids. When subject to a shear stress, polymer chains can disentangle and align with the orientation of the deformation, resulting in a decrease in viscosity, which is referred to as a shear-thinning behaviour.

To decrease the impact of the solution viscoelasticity, we started by focusing on highly dilute 1 ppm solutions of both cohesive and dispersive OVDs to gather information on diffusion-limited adsorption, and then progressively increased the concentration to those used in phacoemulsification. Previous studies have shown that HA was able to form three-dimensional networks even from 1 ppm solutions [101]. It is therefore interesting to compare how adhesive and cohesive OVDs interact with a solid interface in these extremely dilute solutions. The low concentrations are also a good model for residual OVDs which may be left behind after aspiration. Additionally, 1 ppm corresponds to the concentration of endogenous HA in the aqueous humour [102]. A summary of the relevant concentrations and molecular weights of HA in the in the OVDs used in this thesis and how they map onto polymer solution regimes can be found on Figure 4.1.

The objectives of this analysis were to monitor the formation of HA layers on gold and on a mucin-coated sensors, to characterise its viscoelasticity at high shear rates, paying attention to the effect of solution concentration, and to probe its desorption behaviour when rinsed. In particular, we wanted to see if we could observe a difference in rinsing behaviour between cohesive and dispersive OVDs, and relate it to the properties of the polymer solutions.

The main cohesive OVD used in this chapter was Hyaplus. Due to a shortage, it was replaced with Hyalock in the ellipsometry experiment, and when probing the effect of salt with QCM-D. Hyalock has the same molecular weight as Hyaplus, and was diluted to the same concentration. The only dispersive OVD we used was Hyadel.

Note that strictly speaking, it is the HA molecules from the OVD solutions which

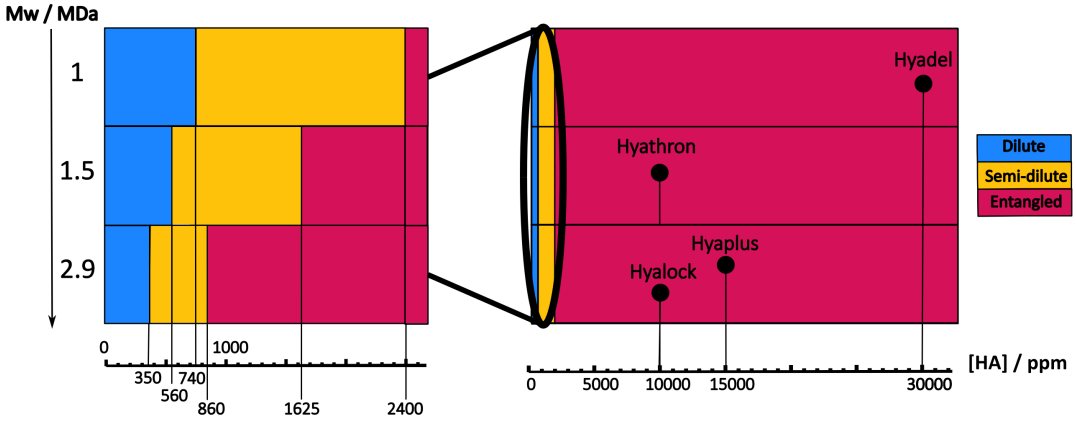

Figure 4.1 *Summary of the different concentration regimes of HA in PBS: dilute (blue), semi-dilute (yellow) and entangled (pink) for the cohesive OVDs Hyalock and Hyaplus, viscosupplement Hyathron (not used in this thesis, but included for completeness) and dispersive OVD Hyadel. The overlap concentration c^* was calculated using the Mark-Houwink equation (see Section 4.4.1). The entanglement concentration c_e at 1 MDa was taken from [103] and calculated for the other molecular weights in Section 4.4.1.*

adsorb on the sensor to form a polymer layer. To improve readability, we will sometimes use terms such as OVD layers, or the configuration of an OVD on the surface.

4.2 Adsorption From a Highly Dilute Solution

4.2.1 QCM-D

We diluted OVD solutions to a HA concentration of 1 ppm in PBS similar to the OVD solvent (1.55 mM Na_2HPO_4, 0.42 mM NaH_2PO_4, 144 mM NaCl) and isotonic to the aqueous humour found in the anterior chamber [104]. We then followed the experimental protocol described in Section 2.1.3 using PBS as the baseline and rinsing solution. The results for the cohesive Hyaplus and the dispersive Hyadel are presented on Figure 4.2.

The results display some similarity with the PVP studied in Chapter 3 (refer to Figure 3.3). The frequency decreased upon injection of the polymer solution, whilst the dissipation increased. The magnitude of the ΔD shift was similar to the former case of 1 ppm PVP, which suggests the layer formed was rigid

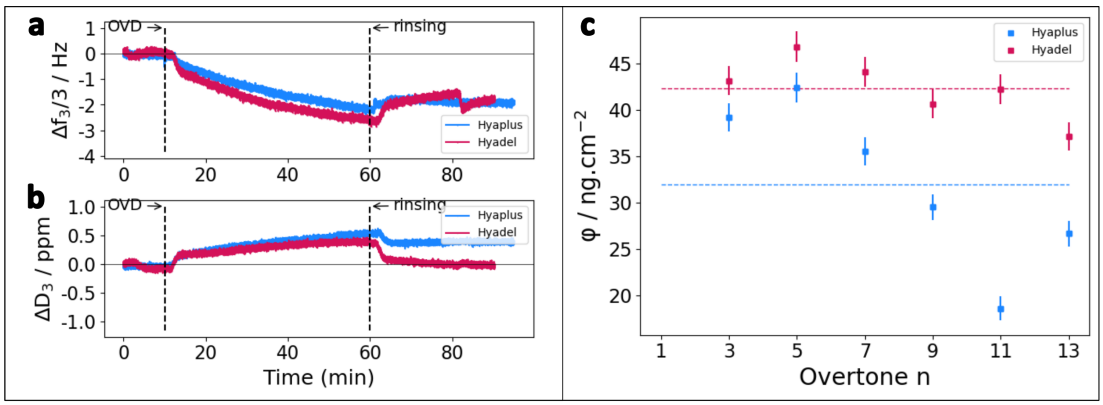

d

OVD	Surface excess φ / ng.cm^{-2}	Overtone distribution / ng.cm^{-2}
Hyaplus	27(16)	4.4
Hyadel	43(26)	1.9

Figure 4.2 *(a) Time-dependent changes in resonant frequency and (b) dissipation for cohesive Hyaplus (blue) and dispersive Hyadel (pink) measured with QCM-D for the third overtone. (c) Sauerbrey analysis of the HA mass adsorbed after flowing a 1 ppm solution for 1h (third to thirteenth overtone). The dashed line is the average value. The error bars were calculated using the error propagation described in Section 2.1.2. (d) Table summarising the average surface excess obtained from three independent measurements. The uncertainty is the standard deviation across three repeat measurements. The standard deviation across overtones is also displayed, as the overtone distribution.*

enough to justify the use of the Sauerbrey model. The Δf shift was however significantly smaller than for PVP, which points to a small value of surface excess. This agrees well with the ellipsometry results of Sterner *et al.* [75]. HA and the gold surface both possess negative charges, which could explain a relatively weak surface attraction.

The average value of Sauerbrey surface excess obtained from three independent measurements was higher for Hyadel than for Hyaplus, despite a relatively high standard deviation. Additionally, the distribution across the overtones was narrower for the dispersive OVD. Lower frequency overtones have a larger penetration depth, and therefore probe the layer further away to the surface. This observation suggests that the Hyadel layer was denser and more even across the sensor surface, which can be interpreted as Hyaplus forming a few loops whilst Hyadel is distributed closer to the surface.

For Hyadel, the rinsing step led to a small increase in frequency whilst the

dissipation went to zero, which can be attributed to a complete flattening of the adsorbed polymer segments. The Hyaplus signal experienced a similar evolution but with a lesser magnitude, which suggests a few loops remained after rinsing. In both cases, the minor increase in frequency upon rinsing indicates that the majority of the adsorbed polymer coils were not desorbed, as with the low concentration PVP. The tendency of adsorbed polymers to resist desorption on rinsing is well known [90], and has been explained to be a consequence of the low mobility of surface bound segments resulting in a lower diffusive flux from the layer [105].

As discussed in Chapter 3, a flatter configuration of the polymer coils like the one we have highlighted for Hyadel grants the adsorbed layer a higher resistance to the shear stress induced by rinsing with solvent. These observations could explain the better coating ability and higher retention time of dispersive OVDs reported by cataract surgeons.

When monitoring PVP adsorption with QCM-D in Chapter 3, we were able to highlight a second adsorption regime after 25 minutes, where the chemisorbed polymers started to rearrange from a flat to a more diffuse configuration once a monolayer had been formed. This behaviour was not observed with HA, which followed the same time dependency throughout the whole measurement, and followed a physisorption kinetic model which will be detailed in Section 4.2.2.

4.2.2 Ellipsometry

Dilute OVD solutions were also studied following the same ellipsometry protocol as PVP, detailed in Section 2.2.2. Note that in contrast to the QCM-D experiments, we studied the adsorption of OVDs diluted in pure distilled water rather than in PBS containing 144 mM NaCl. Although cataract surgery requires the use of a solvent with 9 $g.L^{-1}$ physiological salinity, we are able to tune the solvent quality by varying the salt concentration, and observe the effect this has on the adsorption behaviour. Distilled water also provided the baseline, as in the case of the PVP experiment. As stated in Section 4.1, the presence of salts in solution lowers the charge density along the polymer backbone, screening the intermolecular repulsive interaction, decreasing solvent quality.

Due to a shortage, the cohesive OVD solution tested with ellipsometry was

Hyalock, and not Hyaplus like for the QCM-D presented in Section 4.2.1. As Hyalock and Hyaplus have the same molecular weight and the solutions were diluted to the same 1 ppm HA concentration in both experiments, this substitution should not be significant. The results are shown in Figure 4.3.

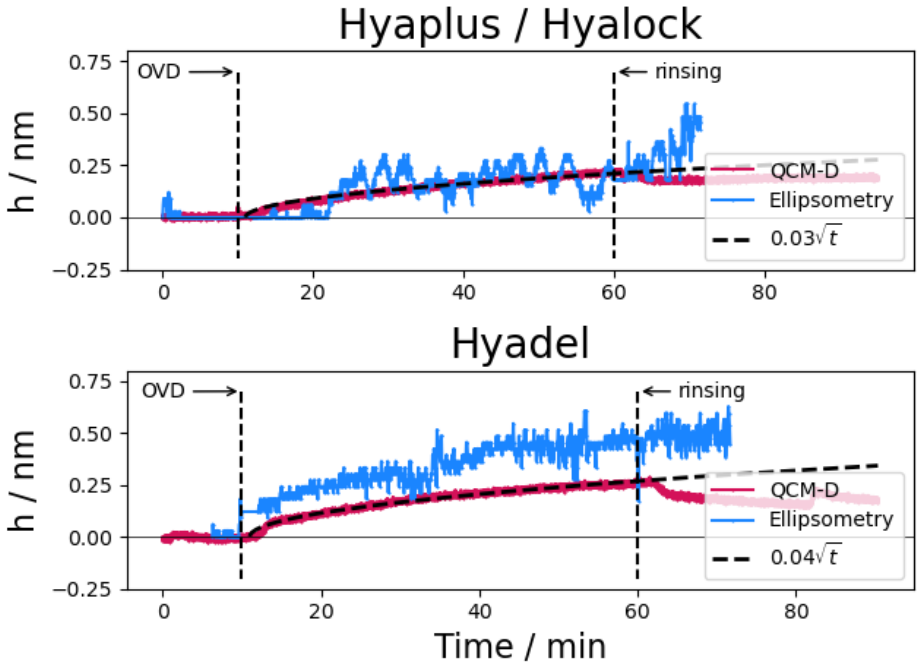

Figure 4.3 *Layer thickness h found with the Sauerbrey model from QCM-D results in PBS (3rd overtone) for Hyaplus (upper panel) and Hyadel (lower panel) assuming a layer density* $\rho_{layer} = 1.8\ g.cm^{-3}$ *(pink) compared with ellipsometry in distilled water for Hyalock (upper panel) and Hyadel (lower panel) assuming a refractive index* $n_{layer} = 1.563\ g.cm^{-3}$ *(blue). The QCM-D data was fitted to the Weber-Morris equation [85] between 11 and 60 minutes (dashed black line).*

For both OVDs, the signal observed with ellipsometry increased upon pumping the solution in the flow cell, albeit to a lesser extent than with 1 ppm PVP. Similarly to the QCM-D results from Section 4.2.1, this indicates that there was some adsorption occurring from both OVDs, but that the resulting HA layer was thinner than that formed from PVP.

The values of layer thickness obtained from QCM-D and ellipsometry for the cohesive OVDs were very close, which means that the change in solvent quality did not impact the coupling of the layer with the surrounding solvent. As discussed in Section 4.2.1, the overtone distribution observed with Hyaplus suggests that a few loops were formed in the Θ solvent PBS, and there was no further expansion

of the polymer segments when replacing the solvent with distilled water.

In the case of Hyadel, ellipsometry yields a higher value of layer thickness than QCM-D. This indicates that the polymer segments were more swollen in distilled water, which is a better solvent. This results in a higher coupling of the polymer layer with the surrounding solvent.

Rinsing for 10 minutes had no effect on the Hyadel layer, and led to an increase in signal for Hyaplus, possibly showing a rearrangement of adsorbed chains. It is however worth noting that the ellipsometry signal was quite noisy. Moreover, the surface area probed with ellipsometry is only as large as the width of the laser, which is about 1 mm^2. For this reason, it is more difficult to extract meaningful information about the polymer configuration within the layer from ellipsometry compared to QCM-D.

We fitted the QCM-D data to the Weber-Morris equation for physisorption, described in Section 3.2, which led to a very good concordance throughout the whole adsorption process (11 to 60 minutes). This is different from the dilute PVP system, which followed chemisorption kinetics, and entered a slower stage of adsorption as the monolayer approached saturation after about 25 minutes (see Figure 3.5). We can infer from the absence of a second kinetic regime that a complete monolayer was not formed in the timescale of the observation. The rate of arrival was slow enough to allow a relatively flat configuration throughout the whole measurement, which can be explained by the extremely dilute concentration, coupled with the polymer's high molecular weight and the rather short residence time of the flowing solution at the sensor surface (calculated as 24 s, as detailed on Table C.1). The values of the diffusion-limited rate constant k was higher for Hyadel (0.04 VS 0.03 $nm.min^{-1/2}$), which is consistent with its smaller contour length compared to Hyaplus, resulting in a faster diffusion.

4.3 Impact of Solvent Salinity

We used QCM-D to monitor the adsorption of HA from solutions of cohesive OVD (Hyalock) diluted in pure distilled water, in order to further investigate the impact of solvent quality on the formation of polymer layers. As stated in Section 4.1, distilled water is a good solvent for HA, which adopts a more

extended configuration in solution than PBS. We started from solution diluted to a 1 ppm HA concentration, progressively increasing concentration, similarly to PVP in Chapter 3. The results are presented on Figure 4.4.

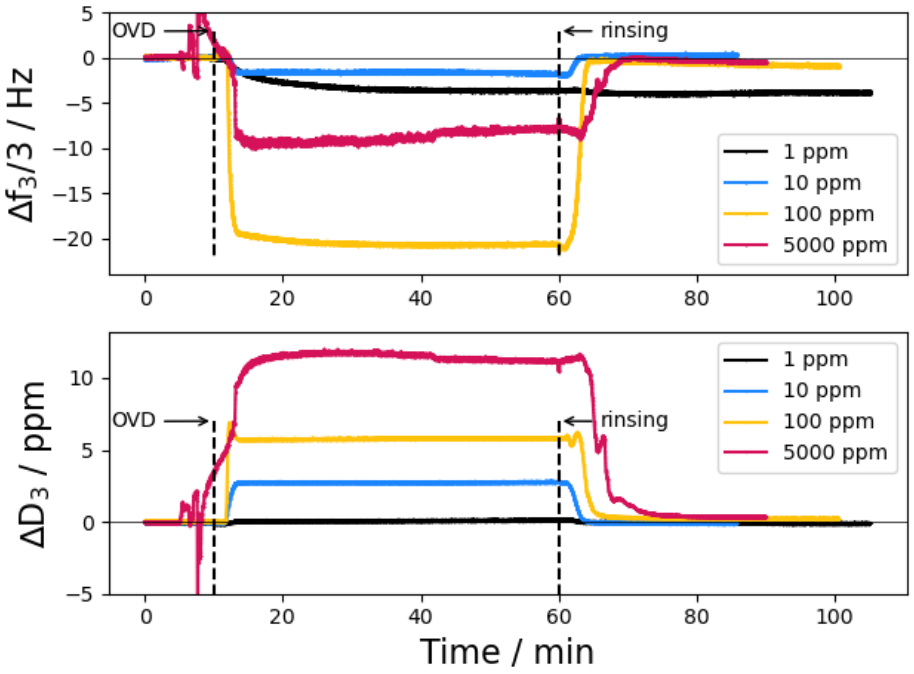

Figure 4.4 *Time-dependent changes in (upper panel) frequency and (lower panel) dissipation measured at the third overtone for the cohesive Hyalock diluted in pure distilled water from different concentrations: 1 ppm (black), 10 ppm (blue), 100 ppm (yellow), and 5000 ppm (pink).*

The measurement done using a 1 ppm concentration displays a similar behaviour to the measurement done in PBS (Figure 4.2), with a progressive decrease in Δf and a minor increase in ΔD, indicating the formation of an ultrathin flat layer. The signal saw no change upon rising. We propose that in this extremely dilute regime, the polymer is lying flat on the surface, which constraints the mobility of the individual segments and prevents desorption.

The responses to injection of Hyalock in salt-free solvent at all the other concentrations display some notable differences with the measurements done so far. Pumping the OVD solution to the sensor chamber resulted in an abrupt decrease in Δf and increase in ΔD. When rinsing with distilled water, the signals went back to the original baseline in a matter of minutes. This rapid and complete removal of the OVD from the QCM-D chamber suggests that the shifts in Δf and ΔD could potentially reflect bulk shift effects associated with the

viscosity of the solution rather than any specific adsorption on the gold sensor. In order to test this hypothesis, we plot $\frac{\Delta f_n}{n}\sqrt{n}$ and $\frac{\Delta D_n * n}{\Delta f_n}$ against time in Figure 4.5.

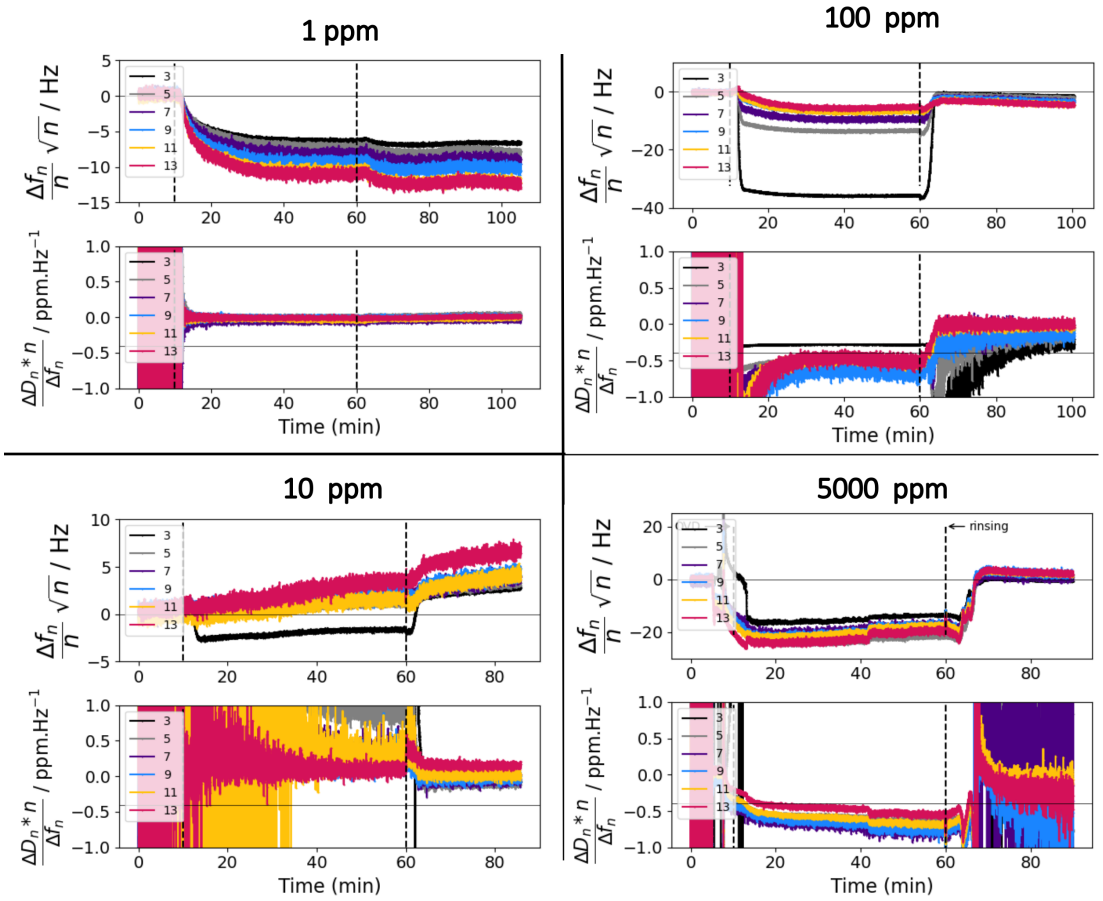

Figure 4.5 *HA in a salt-free solvent presents some features suggesting bulk shift over adsorption at certain concentrations (upper panel: constant value of* $\frac{\Delta f_n}{n}\sqrt{n}$ *for all overtones and lower panel: ratio* $\frac{\Delta D_n * n}{\Delta f_n}$ *= -0.4 ppm.Hz*$^{-1}$*). The vertical dotted lines correspond to OVD injection and rinsing. The vertical axis minimum in the lower panel was set at -1.0 ppm.Hz*$^{-1}$ *to only reflect the values which were in the range of interest despite a spiky signal. Note the difference in y-scale between the different concentrations for the* $\frac{\Delta f_n}{n}\sqrt{n}$ *plots.*

This analysis confirms that for the 1 ppm case, the shifts in Δf and ΔD do not meet the criteria for a bulk shift effect, but rather indicate the adsorption of HA at the sensor surface.

As the bulk concentration increases to 10 ppm, the value of $\frac{\Delta f_n}{n}\sqrt{n}$ appear to be mostly constant over the different overtones, which is a feature of a bulk shift effect, although this is less true for the third overtone. However, the ratio of ΔD_n

and $\frac{\Delta f_n}{n}$ is different from -0.4 ppm.Hz^{-1}. This suggests that bulk shift does not account for all the signal measured with QCM-D, which would indeed be unlikely from the minor change in solution viscosity at this low concentration. We propose instead that HA adsorbs on the quartz sensor at this concentration. The increased solvent quality of distilled water compared to PBS leads to a greater proportion of loops, which results in a thicker layer more easily desorbed upon rinsing.

In the 100 ppm case, $\frac{\Delta f_n}{n}\sqrt{n}$ is not constant across the overtones, but the ratio of ΔD_n and $\frac{\Delta f_n}{n}$ is close to -0.4 ppm.Hz^{-1}. It is possible that at this concentration, an adsorbed layer initially forms, and that some unattached polymers from the flowing solution get entangled within the layer. This adsorption-entanglement phenomenon has been described in [106, 107]. As pure distilled water is injected into the QCM-D chamber during the rinsing step, the entangled polymers drag the adsorbed segments along, which results in a complete removal of the layer.

At 5000 ppm, the ratio of dissipation and frequency is close to -0.4 ppm.Hz^{-1}, and the values of $\frac{\Delta f_n}{n}\sqrt{n}$ overlap for some of the overtones. Both these criteria are representative of a bulk shift effect. However, the prediction of frequency and dissipation associated with a bulk shift does not take into consideration the elasticity of the solution. At this concentration, polymer entanglements in bulk solution are expected, and the elasticity is likely to be significant. Additionally, the 5000 ppm solution displayed spikes of negative values of ΔD upon injection. Dissipation being a ratio of the energy stored to the energy lost at each oscillation, this negative ΔD can reflect a sudden increase in the energy stored resulting from the elasticity of the OVD solution. In parallel, the injection of the 5000 ppm solution led to spikes of positive values of Δf, which we attribute to the instability which was created when injecting the high viscosity polymer solution into the flow cell, previously filled with distilled water.

These results show that in this situation, HA does not adsorb as strongly on the gold sensor. Entanglements between the bulk solution and the adsorbed layer appear to play a role, and to facilitate desorption. This is different from the adsorption behaviour observed with PVP in Chapter 3, where Guiselin brush-like layers were formed when flushing solutions of increasing polymer concentrations. This weaker adsorption may be driven by the solvent quality, and in Section 4.4, PBS will be used as the solvent again. As the salt concentration increases, the polymer network collapses. The solution displays a lower viscosity, leading to a

less dampened sensor [108].

4.4 Increasing Concentration: Effect on the Adsorption (QCM-D)

4.4.1 1000 ppm OVD solutions

The 1 ppm solutions in PBS studied in Section 4.2 were limiting cases of extremely dilute systems. In reality, OVD solutions contain HA at a much higher concentration where polymer segments can interact with neighbouring coils and entanglement process become important; Figure 4.1 summarises the different concentration regimes. The overlap concentrations of our solutions were calculated as respectively 350 and 740 ppm for Hyaplus and Hyadel using the reciprocal of the Mark-Houwink equation:

$$[\eta] = KM^{\alpha} = \frac{1}{c^*} \tag{4.1}$$

where $[\eta]$ is the intrinsic viscosity, K and α are parameters related to the polymer and solvent, which are respectively $9.78 \cdot 10^{-2}$ $\mathrm{cm}^3.\mathrm{g}^{-1}$ and 0.69, and M is the molecular weight [109].

The entanglement concentration c_e for an HA solution at a 1 MDa concentration was taken from the literature [103] as 2400 ppm. We estimated values of c_e at the other molecular weights using equation 4.2 [110], which is appropriate for Θ solvents. As explained in Section 4.1, water is a good solvent for HA, whilst PBS displays a lower solvent quality. We will therefore describe it as a Θ solvent [100]:

$$\frac{c_e}{c^*} = \frac{[Ne(1)]^{\frac{3}{4}}}{N^{\frac{1}{4}}} \tag{4.2}$$

where $Ne(1)$ is the number of Kuhn monomers in an entanglement strand in the melt, which was considered to be independent of the molecular weight, and N is the number of monomers per polymer chain.
This equation yields values of c_e equal to 1625 ppm for Hyathron and 860 ppm

for both Hyalock and Hyaplus.

In a similar approach to the one used in Chapter 3, we compared the QCM-D signals of the highly diluted 1 ppm with solutions 1000 times more concentrated, which were in the semi-dilute regime for Hyadel and just in the entangled regime for Hyaplus. The results are presented on Figure 4.6.

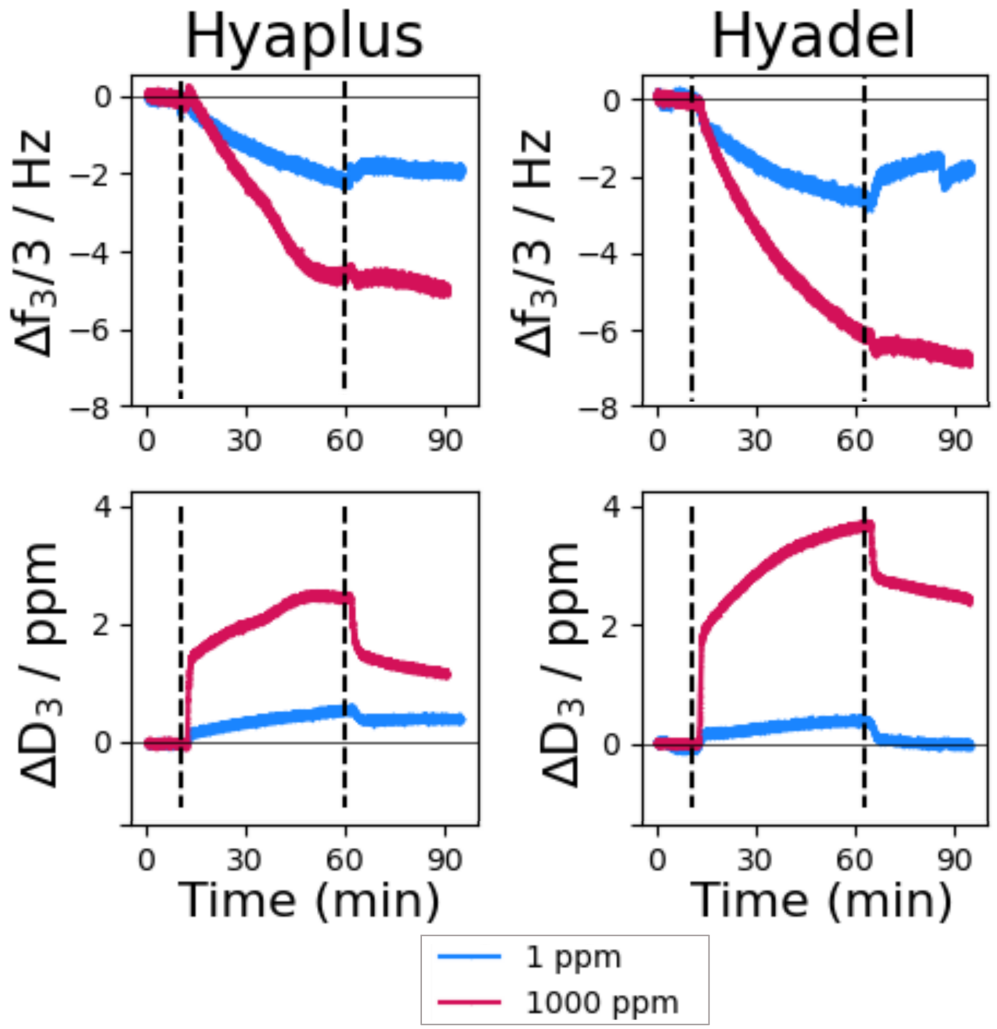

Figure 4.6 *Time-dependent changes in resonant frequency and dissipation for cohesive Hyaplus (left panel) and dispersive Hyadel (right panel) measured with QCM-D for the third overtone from 1 ppm (blue) or 1000 ppm solutions (pink). The dashed lines correspond to the injection of OVD and rinsing steps.*

Injecting the 1000 ppm OVD solutions led to an immediate step increase in ΔD, with a similar step decrease observed when rinsing with PBS. We attribute this sudden change to the arrival of the OVD solution in the sensor chamber, and the resulting bulk shift effect, accompanying the increase in solution viscosity. Unlike the behaviour observed in Section 4.3, the dissipation kept increasing as the solution was pumped through the sensor chamber. During that time, Δf was also continuously decreasing, which points towards polymer adsorption on the gold sensor and coupling of the resulting layer to the ambient solution. We therefore attribute the absence of polymer adsorption observed in Section 4.3 to the enhanced solvent quality. The importance of salinity is important to keep in mind, and one should be careful when comparing experimental results with articles from the literature using a different solvent salinity.

Increasing the solution concentration leads for both OVDs to a larger decrease in Δf and increase in ΔD. This is similar to what was observed with PVP in Chapter 3 and points towards the formation of a thicker layer with a higher coupling with the ambient solution, which results in more energy being dissipated. However, the Δf decrease was smaller than with 1 ppm PVP even when using a 1000 ppm HA solution. This suggests that HA forms significantly thinner layers than PVP during this timescale, which could be due to its larger size leading to a slower diffusion to the solid interface. We calculated the diffusion coefficient D of PVP and HA from OVDs using equation 4.3:

$$D = \frac{k_B\ T}{6\pi\ \eta\ R_g} \tag{4.3}$$

where k_B is the Boltzmann constant, T is the temperature, $\eta = 0.89$ mPa.s is the solution viscosity and R_g is the radius of gyration, which was taken as 56 nm for 360 kDa PVP [93], compared to 126 nm and 258 nm for 1 MDa and 3 MDa HA [111], respectively. The resulting values of D were $4 \cdot 10^{-12}$ m^2.s^{-1} for PVP and $2 \cdot 10^{-12}$ m^2.s^{-1} for Hyadel. It follows that in a diffusion-limited system, the formation of a complete monolayer would be twice as long for Hyadel than it is for PVP, and even longer for Hyaplus which contains longer chains and yields $D = 9 \cdot 10^{-13}$ m^2.s^{-1}.

Likewise, the dissipation observed in Figure 4.6 remained smaller than PVP when considering the 1000 ppm solutions, which is typical of a more rigid layer. We can infer from this that HA preferentially adsorbs as trains rather than forming

large loops, possibly owing to the repulsive interaction between neighbouring coils. This would also be consistent with previous measurements showing HA adsorbing as long filaments on solid mica substrates [101].

In contrast to the layer formed from concentrated PVP, rinsing the layer formed from 1000 ppm HA with solvent did not increase the frequency shift back to the baseline, which suggests there was no desorption upon rinsing. As stated previously, resistance to desorption is typically associated with a low mobility of polymer chains. For polymer coils laying flat on the surface, one would expect a limited diffusion through the polymer layer and very slow kinetics of desorption. The dissipation decreased, which could reveal some rearrangement on the surface.

Following the approach adopted in Figure 4.5 for solutions diluted in distilled water, we have checked that the changes in frequency and dissipation are not entirely associated with bulk shifts. This information and the small values of dissipation encouraged us to use the Sauerbrey model to calculate the values of surface excess for both OVDs. The results are shown in Table 4.1.

OVD	Surface excess φ / ng.cm^{-2}	Overtone distribution / ng.cm^{-2}
Hyaplus	80 ± 17	3.8
Hyadel	76 ± 10	10.7

Table 4.1 *Table summarising the average Sauerbrey surface excess for 1000 ppm OVD solutions obtained from 3 independent measurements for the third overtone. The uncertainty is the standard deviation across the repeat measurements.*

The surface excess values were comparable for both OVDs in this regime. The overtone distribution was lower for Hyaplus at this concentration, which suggests that the polymer configuration was flatter on average, contrary to the observation made at 1 ppm (see Figure 4.2 d). As discussed earlier, Hyadel is in the semi-dilute regime at this 1000 ppm concentration, whereas Hyaplus is already in the entangled regime. Entanglements add additional constraints to the chains of the cohesive OVD, which may contribute to the polymers flatter configuration on the surface, which is reflected by the lower value of ΔD. Regarding the kinetics of adsorption, we used the Weber-Morris equation to calculate the values of the adsorption rate constants k for both OVDs. The results are shown on Table 4.2.

Like PVP, both OVDs saw faster kinetics as the concentration increased, as one

Concentration	k Hyaplus (nm.min$^{-1/2}$)	k Hyadel (nm.min$^{-1/2}$)
1 ppm	0.03	0.04
1000 ppm	0.09	0.10

Table 4.2 *Table summarising the adsorption rate constants k (nm.min$^{-1/2}$) obtained from the Weber-Morris equation.*

expects. The formation of a layer from a Hyadel solution was slightly faster than it was for Hyaplus, just like it was at 1 ppm. This can be related to its smaller length resulting in a faster diffusion. We also noted that just like the dilute OVDs, the adsorption followed the Weber-Morris equation throughout the whole time. This suggests that the adsorption did not enter a second stage, in which there is a slow rearrangement of chains on the surface once saturation is reached.

In conclusion, shifting from the dilute to the semi-dilute regime did not fundamentally change the adsorption behaviour of the OVDs on gold. The kinetics were faster due to the higher polymer concentration, but they remained apparently too slow to form a complete monolayer. Unlike PVP, the layer formed from 1000 ppm solutions did not desorb upon rinsing, which suggests it remained flat on the gold sensor and did not adopt an extended brush-like configuration allowing the segments to diffuse away through the layer. This would be consistent with the flat filament network which has been described in the literature [101].

4.4.2 Entanglement Effects: 7500 and 15000 ppm

To provide a better comparison with the behaviour of OVDs used in phacoemulsification, we further increased the concentration of the solutions to above the entanglement concentration (see Figure 4.1 for a summary of the different concentration regimes). In order for the solutions to be able to flow through the 0.38 mm diameter tubing, it was necessary to dilute the native OVDs by a factor of two, yielding final concentrations of 15000 ppm and 7500 ppm for Hyadel and Hyaplus respectively. A change in the ambient fluid density and viscosity leads to a change in both frequency and dissipation. This is referred to as a bulk shift effect, the magnitude of which can be calculated using the Kanazawa-Gordon model. In that case, one expects the overtones to yield a constant value of $\frac{\Delta f_n}{n}\sqrt{n}$, and the ratio of ΔD_n over $\frac{\Delta f_n}{n}$ should reach a value close to -0.4 ppm.Hz^{-1} for all overtones. The possibility of a bulk shift effect is investigated in Figure 4.7.

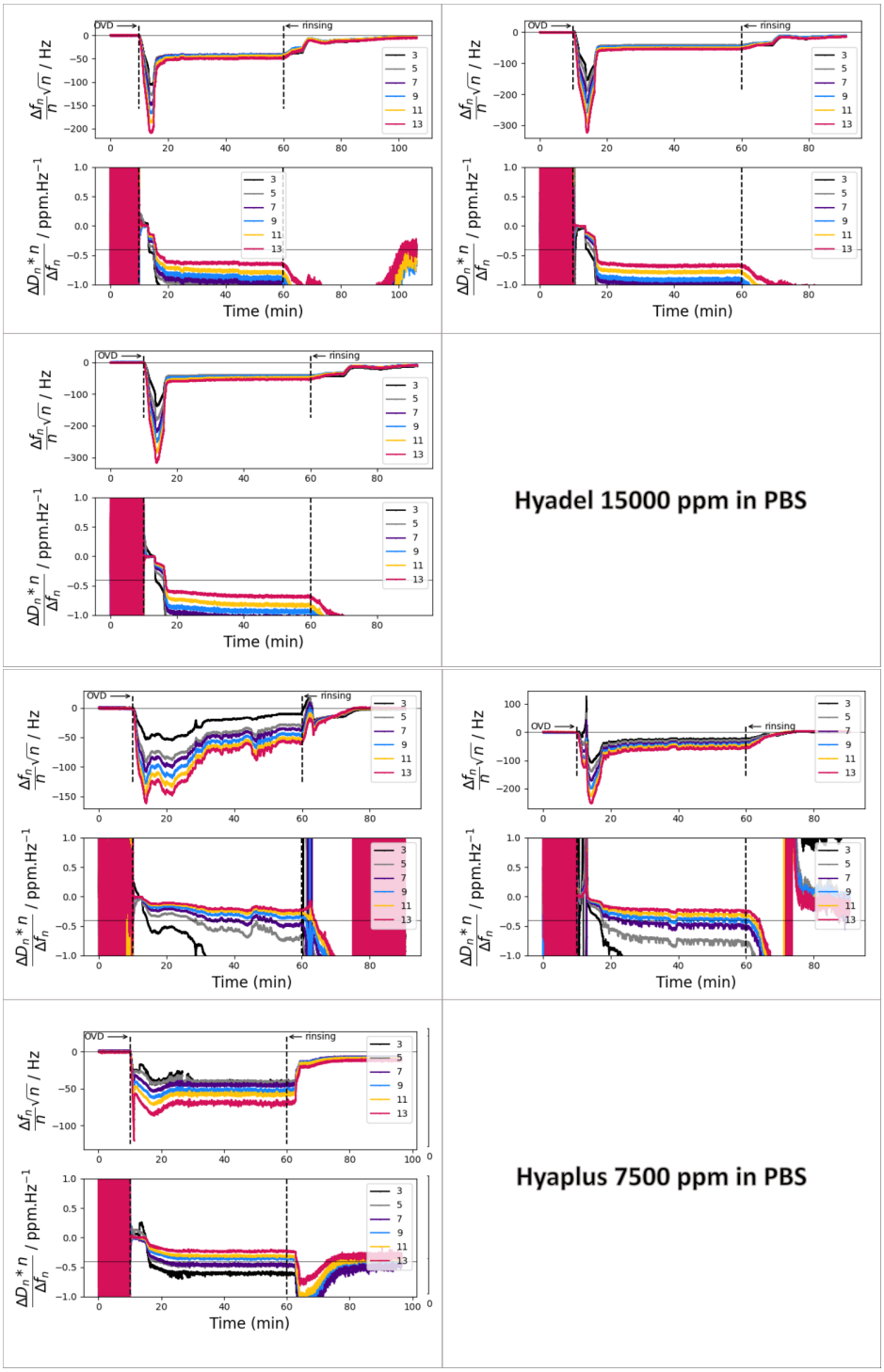

Figure 4.7 *The presence of a bulk shift effect was investigated for solutions of Hyadel at 15000 ppm (upper panel) and Hyaplus at 7500 ppm (lower panel) on three separate measurements. A bulk shift effect would be expected to yield a constant value of* $\frac{\Delta f_n}{n}\sqrt{n}$ *for all overtones and the ratio of* ΔD_n *and* $\frac{\Delta f_n}{n}$ *to be close to -0.4* $ppm.Hz^{-1}$. *The vertical axis minimum in the lower panel was set at -1.0* $ppm.Hz^{-1}$ *to only reflect the values which were in the range of interest despite a spiky signal.*

In the case of Hyadel, the overtones appear to yield comparable values of $\frac{\Delta f_n}{n}\sqrt{n}$, but the ratio $\frac{\Delta D_n\ n}{\Delta f_n}$ is different from -0.4 ppm.Hz^{-1}, which suggests that the shifts in Δf and ΔD cannot be entirely attributed to a bulk shift effect, and that there is some adsorption happening. For Hyaplus, the overtones do not overlap in Figure 4.7, which again points to polymer adsorption. Nevertheless, the ratio of ΔD_n and $\frac{\Delta f_n}{n}$ is very close to -0.4 ppm.Hz^{-1}. This suggests that the viscosity of the layer formed from the cohesive OVD is comparable to that of the ambient OVD solution. This would be the case if the structure of the adsorbed layer was being dictated by the same entanglement length as in the bulk solution. Conversely, the dispersive OVD layer comparatively dissipates more energy. This layer would lead to energy being dissipated on the layer rather than on the endothelium, which is consistent with the superior protective ability reported by surgeons in the literature.

In contrast with the dilute and semi-dilute regimes, where individual polymer chains could adsorb on the sensor, we expect that in the entangled regime, the polymer coils adsorb from a network of intertwined polymer segments, as represented by the reduced opacity segments in Figure 4.11. The results are shown in Figure 4.8 for Hyadel and Figure 4.9 for Hyaplus.

Upon injection of the Hyadel solution, the QCM-D sensor experienced an abrupt downward spike in frequency (arrows in Figure 4.8) before reaching a plateau value at a smaller magnitude of Δf. During that time, the dissipation increased to reach a plateau. In contrast to the lower concentrations (1 and 1000 ppm), there was no $\sqrt{t}$ kinetic variation, which suggests that HA does not follow a diffusion-limited physisorption process on the gold sensor at this concentration. The observation of a downward spike followed by a plateau in Δf is similar to what is observed during vesicle adsorption, where the downward spike in frequency corresponds to the mass uptake caused by the adsorption of intact vesicles, followed by vesicle rupture and bilayer formation, resulting in a loss of entrapped water [112, 113]. This pattern has rarely been reported for polymers in the literature [114, 115].

We attribute the downward spike in frequency to the adsorption from an entangled polymer network. We suggest that the subsequent increase corresponds to the network breaking down as the HA chains make multiple contact points with the gold surface, releasing some of the constraints on chains in the network due to entanglements. Notably, the increase in Δf during the adsorption process was

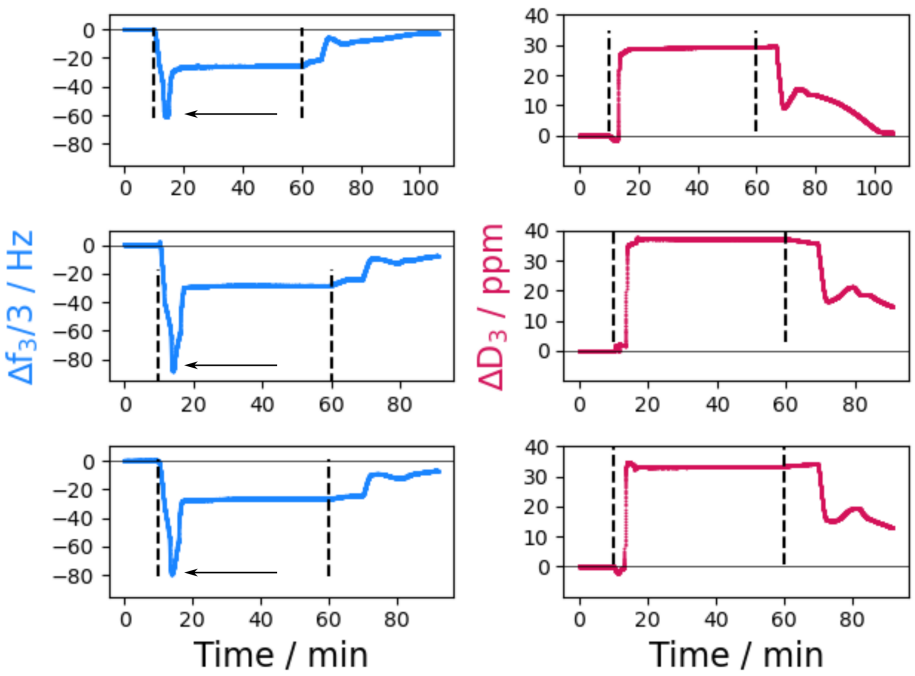

Figure 4.8 *Time-dependent changes in resonant frequency (left panel) and dissipation (right panel) for dispersive Hyadel measured with QCM-D for the third overtone from pure OVDs diluted by a factor of 2, yielding a concentration of 15000 ppm. The dashed lines correspond to the injection of OVD and rinsing steps. The arrows point towards a downward spike in frequency. The three data sets plotted are repeats of the same experiment.*

not coupled with a decrease in ΔD. This provides evidence that the rupture of the polymer network did not lead to structural collapse. We attribute this effect to a strong coupling with solvent. HA is a glycosaminoglycan, a family of biopolymers characterised by their water retention ability.

Rinsing for 30 minutes led to an increase in Δf coupled with a decrease in ΔD, which shows that the polymer layer was partially desorbed, however the signals did not revert back to the baseline in this timescale, which suggests some polymers remain adsorbed at the surface.

Several differences can be noted between the two OVDs. The dispersive OVD, as shown on Figure 4.8, led to a remarkably consistent behaviour whereby the frequency experienced an initial drop before reaching a plateau after 20 minutes. The cohesive OVD displayed more variability between experiments, as can be seen from Figure 4.9. Additionally, the downward spike observed with Hyadel was recorded on one occasion only with Hyaplus. This can be explained as follows:

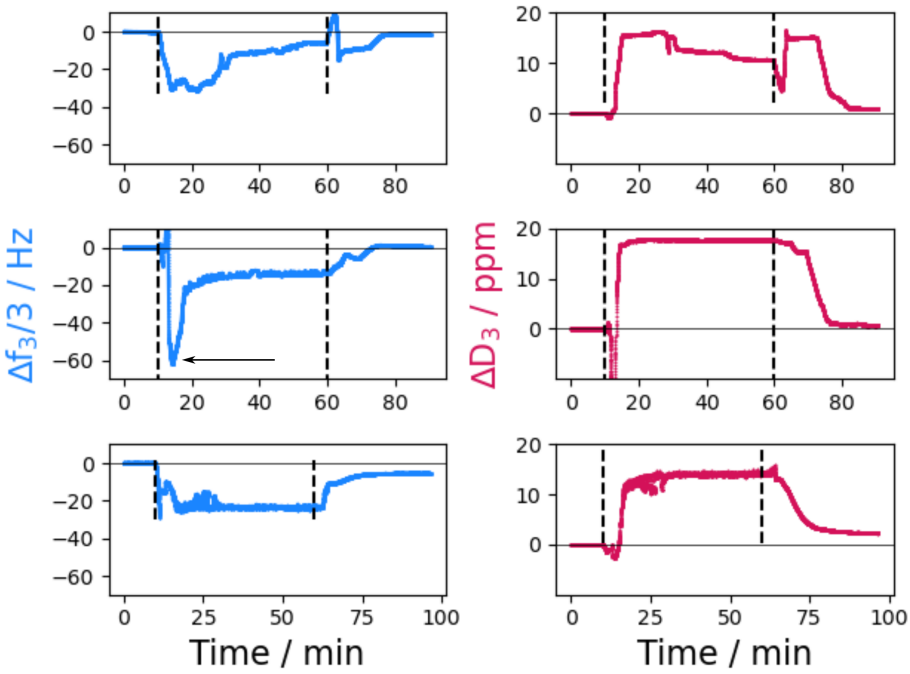

Figure 4.9 *Time-dependent changes in resonant frequency (left panel) and dissipation (right panel) for cohesive Hyaplus measured with QCM-D for the third overtone from pure OVDs diluted by a factor of 2, yielding a concentration of 7500 ppm. The dashed lines correspond to the injection of OVD and rinsing steps. The arrow points towards a downward spike in frequency. Note the difference in y-scale with the Hyadel plots from Figure 4.8, indicating a difference in the adsorption behaviour. The three data sets plotted are repeats of the same experiment.*

Hyadel, which has a lower molecular weight, contains shorter polymer chains than Hyaplus. As a result, the number of entanglements per chain is lower, making it easier for the gel to break down as it adsorbs as a surface layer. On the other hand, Hyaplus does not break down as easily upon adsorption.

The Δf shift upon adsorption of Hyaplus was on average lower than for Hyadel, which suggests that the surface excess was lower. It can be related to its lower bulk concentration, and lower chain mobility polymer density at the surface [94]. The ΔD shift was also lower for Hyaplus, which can again be explained by its lower concentration at the surface. The entanglements are separated further apart for the cohesive OVD, which results in a lower energy dissipation.

For the cohesive OVD, 10 minutes of rinsing was sufficient for the frequency and dissipation shifts to return to the limiting value observed following adsorption and

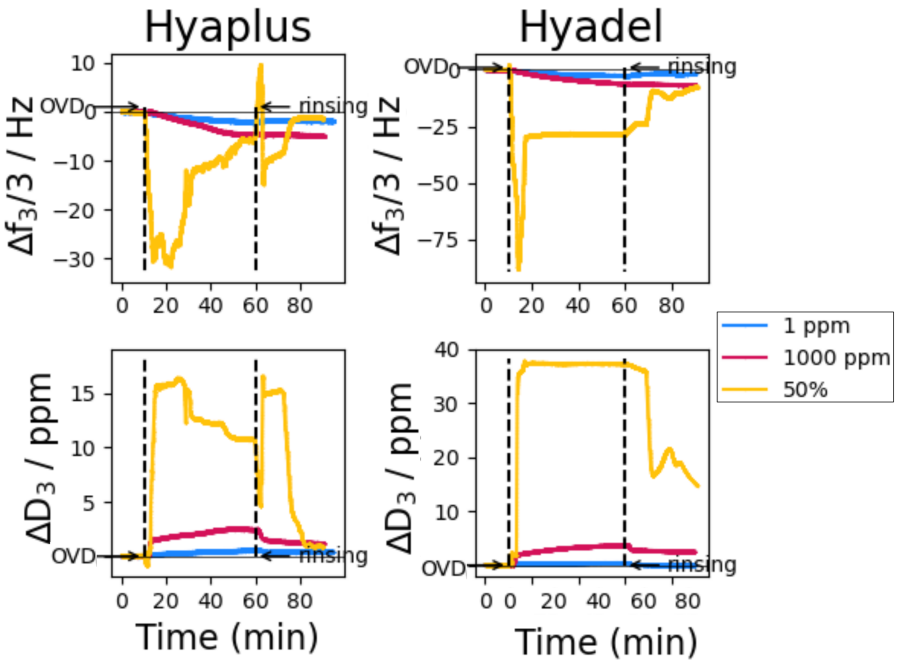

Figure 4.10 *Time-dependent changes in resonant frequency (upper panel) and dissipation (lower panel) for cohesive Hyaplus (left panel) and dispersive Hyadel (right panel) measured with QCM-D for the third overtone from 1 ppm (blue), 1000 ppm solutions (pink) or pure OVDs diluted by a factor of 2, yielding 7500 ppm for Hyaplus and 15000 ppm for Hyadel (yellow). The dashed lines correspond to the injection of OVD and rinsing steps. Note the difference in y-scale between the Hyadel and Hyaplus plots, indicating difference in the adsorption behaviour.*

rinsing from a 1 ppm solution. For the dispersive OVD, even after 30 minutes of rinsing the frequency shift only returned to the value observed following adsorption and rising for a 1000 ppm solution, which corresponds to a higher residual polymer excess. The dissipation shift remained five times higher than it was in the 1000 ppm case, as shown on Figure 4.10. This high dissipation suggests that the Hyadel layer does not collapse easily upon rinsing, but remains highly hydrated instead.

The higher concentration of dispersive OVDs leads to a high degree of polymer entanglement within the layer, which makes it more resistant to rinsing. The lag time and incomplete desorption seen with the dispersive OVD also makes sense with regard to the behaviour observed after phacoemulsification. Surgeons report that the dispersive OVD network gradually breaks up upon aspiration,

resulting in a longer removal time. In Chapter 5, we will relate this resistance to rinsing to a detachment mechanism, whereby pulling off the dispersive OVD requires the simultaneous rupture of multiple anchoring points on the surface, which represents a high energy barrier. In contrast, cohesive OVDs detach by a sequential rupture of tethering points.

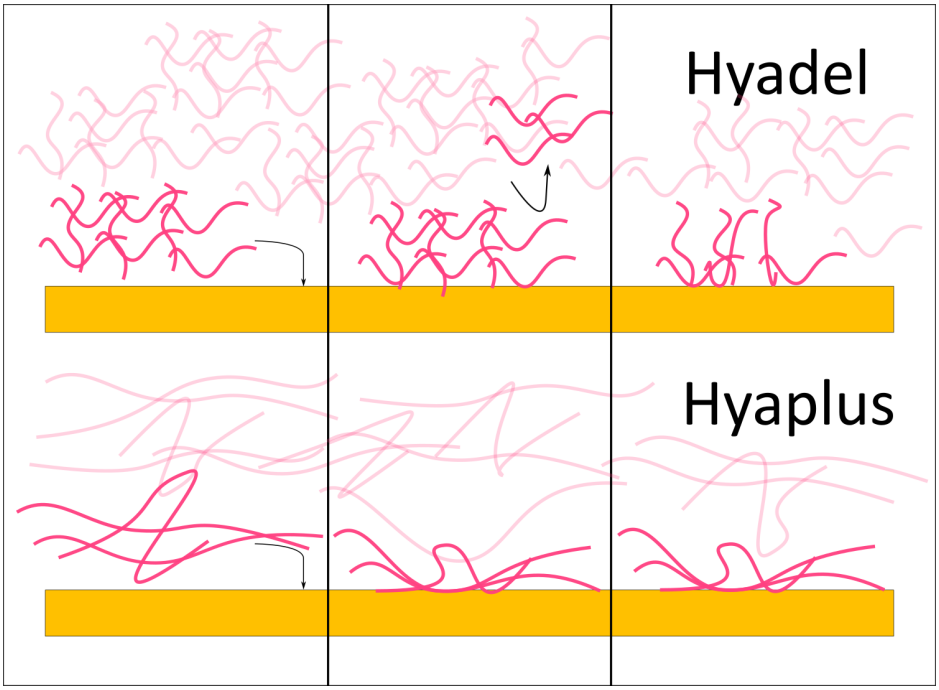

Figure 4.11 *Schematic depiction of the adsorption mechanism of both OVDs on the QCM-D sensor from entangled solutions. Hyadel is more concentrated, and adsorbs as a network which immediately ruptures to create a polymer layer with a high density. Hyaplus has longer chains, and so more entanglements per chain. As a result, it does not break down as easily and forms a more dilute layer which is less dissipative in QCM-D. Polymer segments with a reduced opacity present the existence of an entanglement network in the bulk, as discussed in [106, 107]*

.

Adsorbed polymer layers are commonly used to provide lubrication of a substrate of interest [72, 116]. Densely grafted polymer brushes offer a resistance to compression because of the steric hindrance they provide. As a result, if a deformation occurs in the bulk, the stress will be partially absorbed by the layer, shifting the shear plane away from the substrate. In particular, the ability of the layer to entrap solvent under applied load is critical for lubrication, which can be seen from an increase in the coefficient of friction above a certain load threshold [75]. In that regard, the consistent ability of Hyadel to remain swollen by the solvent when adsorbing on the QCM-D sensor and when rinsing with

solvent can be related to its better protective ability.

4.5 High Shear Rheology from the Voinova Model

Applying the Voinova model to the previous measurements in Section 4.4.2, we find a similar average value of layer viscosity and elastic modulus for both OVDs, with $\eta_{layer} = 1.1$ mPa.s, slightly higher than the viscosity of water. Crucially, the layer thickness obtained for both OVDs are significantly higher than the values estimated so far from more dilute systems. These length scales are relevant to endothelial cells: for instance the CD44 HA receptor has a diameter close to 25 nm [117], and the gap between the tight junctions of adjacent cells is about 15 nm wide [118]. The results are shown in Figure 4.12, and the average values between 10 and 60 minutes from three independent measurements is displayed in Table 4.4. The values of Δf and ΔD calculated from the fit compared to the experimental values are also plotted in Figures E.1 and E.2.

OVD	Thickness h_{layer} / nm	Viscosity η_{layer} / mPa.s	Elastic modulus μ_{layer} / kPa
Hyadel	68(12)	1.1(2)	28(6)
Hyaplus	29(5)	1.1(2)	23(8)

Table 4.3 *Average values of the layer thickness, viscosity and elastic modulus of layers formed in OVD solutions diluted by a factor of two, using the Voinova model on 3 independent measurements. The uncertainty corresponds to the standard error of the mean.*

Additionally, the HA layer formed in presence of the dispersive OVD was twice as thick as the one obtained from the cohesive OVD (60 nm and 30 nm respectively). This can be interpreted as the Hyadel surface layer having a stronger coupling with the ambient solution, possibly forming larger loops. This result is significant with regards to cataract surgery, as dispersive OVDs were reported to have a better resistance to the shear induced during phacoemulsification.

We include the value of the viscosity determined by application of the Voinova model to the QCM-D data to a plot of the shear rate dependence of the viscosities of Hyadel and Hyaplus measured using shear rheology in Figure 4.13.

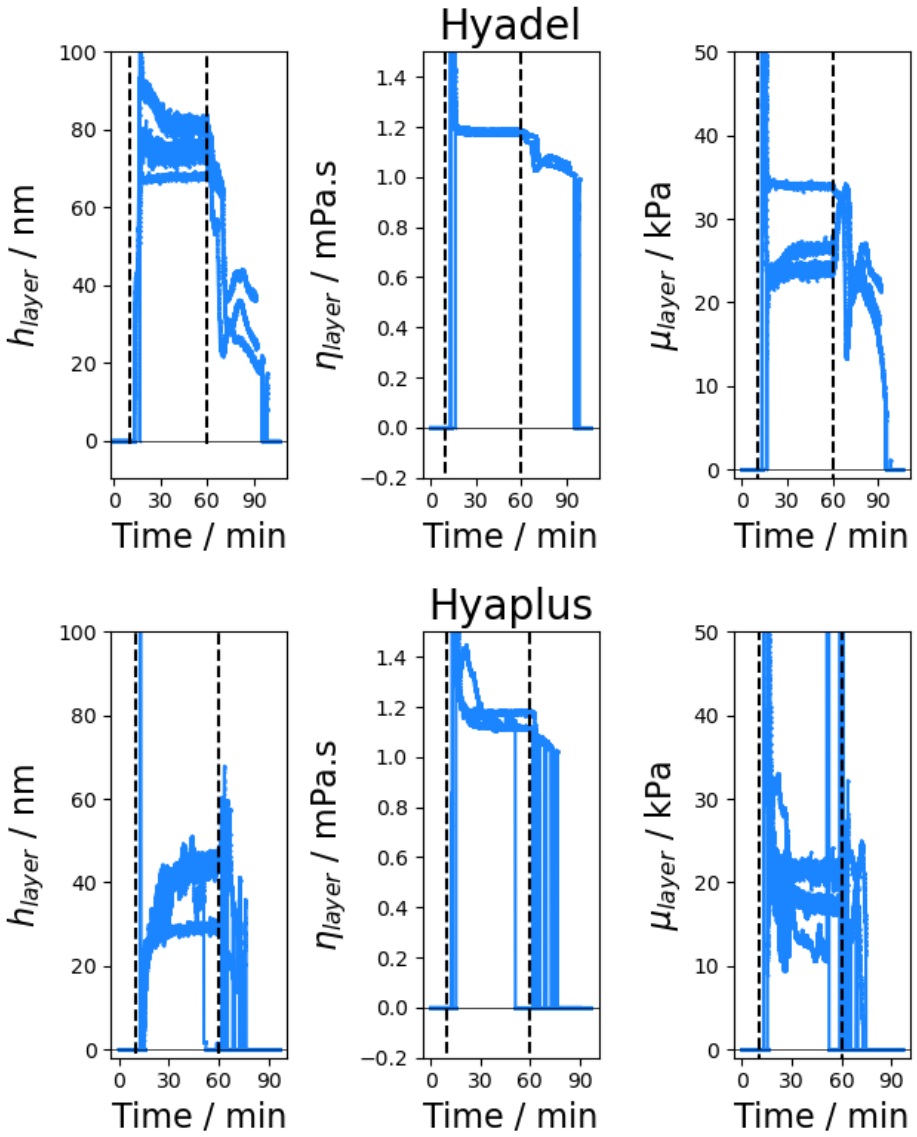

Figure 4.12 *The Voinova model for viscoelastic layers was applied to the layers formed from Hyadel (upper panel) and Hyaplus (lower panel) solutions diluted by a factor of two for three independent measurements from Figures 4.8 and 4.9. We obtain values of the thickness h_{layer}, viscosity η_{layer} and elastic modulus μ_{layer}. The input parameters were layer density ρ_{layer} = 1000 $g.L^{-1}$, buffer density and viscosity respectively ρ_{fluid} = 1006 $g.L^{-1}$ and η_{fluid} = 1.03 mPa.s. The dashed lines correspond to the injection of OVD and rinsing steps, respectively.*

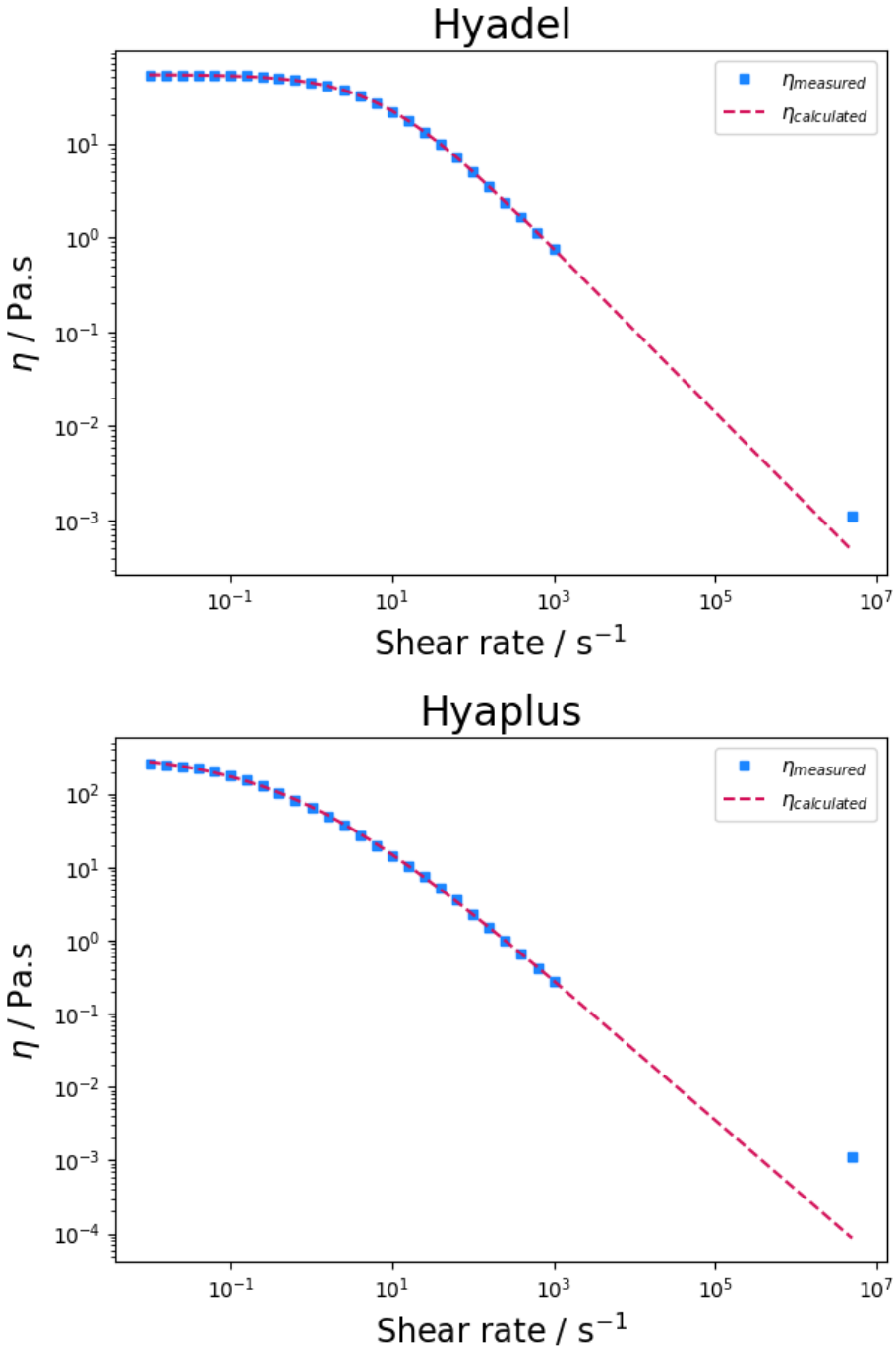

Figure 4.13 *Comparing the high shear rheology obtained with QCM-D for Hyadel (upper panel) and Hyaplus (lower panel) with the results from shear rheology at lower shear rates. The measured values are represented by blue squares and the pink dashed line represents the Carreau-Yasuda fit obtained with shear rheology. Note the difference in y-scale between the Hyadel and Hyaplus plots, indicating differences in the magnitude of viscosity and shear-thinning ability.*

Using the Carreau-Yasuda model to extrapolate the measured viscosities to

the frequency relevant to QCM-D (pink dashed line in Figure 4.13) led to an overestimation of the viscosity obtained with QCM-D from the Voinova model. This can be explained by the limitations of this model, which include microstructural changes, viscoelastic effects like stress relaxation, and high shear rates effects such as shear banding [119]. The Voinova model also has limitations, such as the homogeneous film assumption which may overlook deviations arising from film roughness. However, the values obtained with both methods are of a similar magnitude, although the shear rheology was performed on pure OVDs, whilst the solutions used in QCM-D were diluted by a factor of two. This shows that QCM-D is a promising technique for high-shear rheology, which is usually not accessible to most instruments. One could also probe the intermediate shear range with another technique such as capillary measurements. In phacoemulsification, the ultrasound probe vibrates at a frequency close to 40 kHz, which stands in that intermediate shear range.

4.6 Interaction of OVDs with a Biomimetic Layer: Mucin

After getting information about the interaction of OVDs with gold, we extended the investigation to a more biologically-relevant surface to better mimic the endothelial surface. As explained in Chapter 3, the endothelial surface is covered by a viscoelastic layer which contains mucoproteins, making mucin a good biomimetic model. Additionally, the adsorption of macromolecules on mucin has been studied with QCM-D before, providing a baseline for comparison [97, 98]. Although the commercially available mucin we used was extracted from porcine stomach, it shares some similarities with corneal endothelium, such as the presence of MUC1, as well as MUC4 which is expressed on the epithelium.

The experimental protocol was the same as the one used in Chapter 3, with the exception that the solvent used here was PBS instead of distilled water. The results are shown on Figure 4.14.

As we showed in Chapter 3, injecting the mucin solution led to a decrease in frequency accompanied by an increase in dissipation. Rinsing for 10 minutes with a buffer solution had a very limited impact on the signal, which suggests that a strongly attached layer of mucin formed on the sensor despite the increase

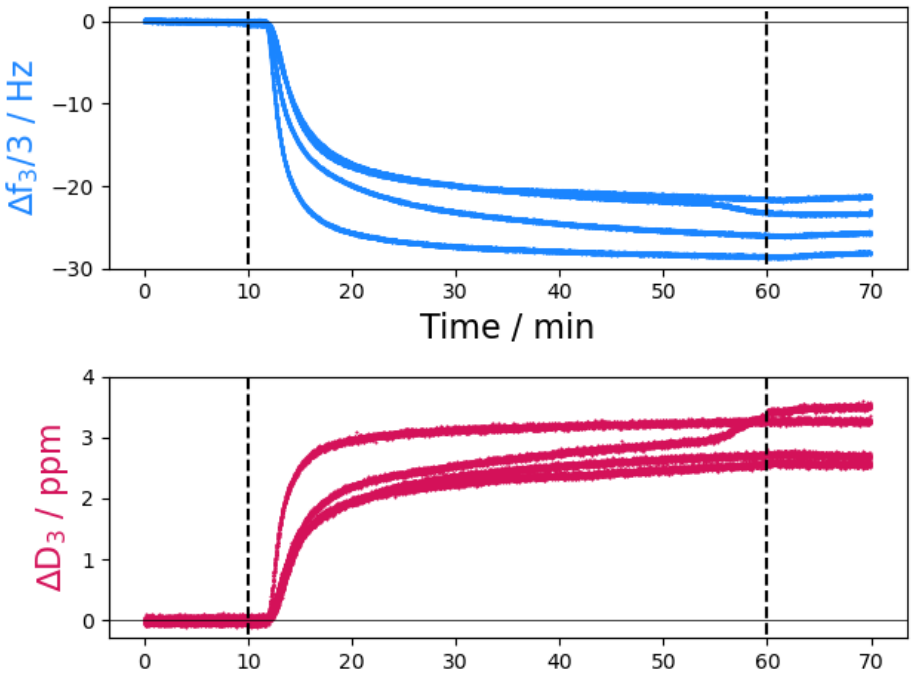

Figure 4.14 *A mucin layer was adsorbed from a 25 ppm solution in PBS and followed with QCM-D for the third overtone in four independent experiments. It was rinsed for 10 minutes to remove any free mucin and check the attachment was strong enough. The dashed lines correspond to mucin injection and PBS rinsing, respectively.*

in solvent salinity.

The dissipation was not negligible, so we did not use of the Sauerbrey model, which is only valid for thin, rigid layers. Instead, we used the Voinova model, which takes into account the viscoelastic coupling of the layer with the surrounding medium. The analysis was performed using the Biolin Dfind software using as input parameters a layer density $\rho_{layer} = 1050$ kg.m^{-3}, a buffer density and viscosity of $\rho_{fluid} = 1006$ kg.m^{-3} and $\eta_{fluid} = 1.03$ mPa.s, respectively. The results are presented on Figure 4.15, and the average values obtained after rinsing for 10 minutes are presented on Table 4.4. The values of Δf and ΔD calculated from the fit compared to the experimental values are also plotted in Figures E.3 and E.4.

We determined the layer to be relatively thicker and to have a lower elastic modulus than some results found in the literature [97, 120]. The lower elastic modulus may be a consequence of the higher pH used in our measurements [98, 121]. The layer was significantly thinner than the 0.5 µm endogenous

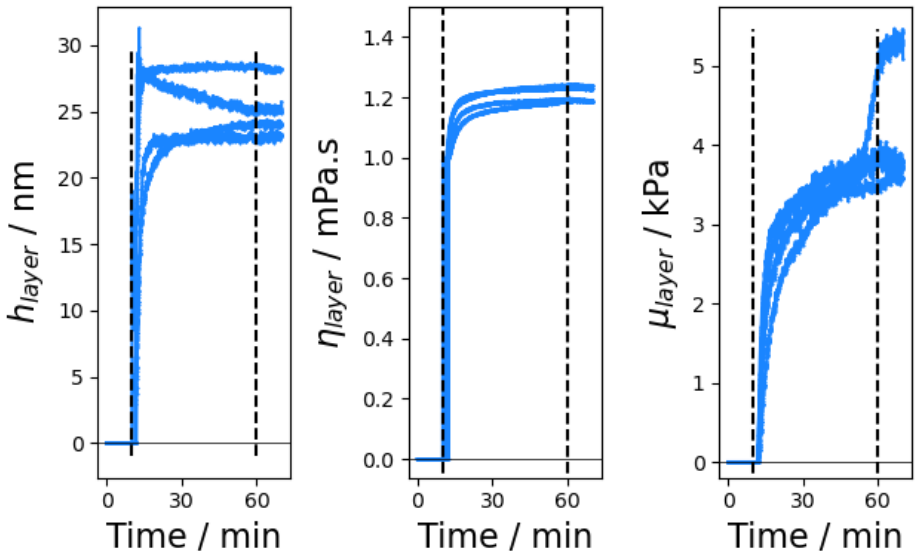

Figure 4.15 *The Voinova model for viscoelastic layers was applied to the mucin layer from the four different measurements from Figure 4.14 to get values of the thickness h_{layer}, viscosity η_{layer} and elastic modulus μ_{layer}. The input parameters were layer density $\rho_{layer} = 1050\ kg.m^{-3}$, buffer density and viscosity respectively $\rho_{fluid} = 1006\ kg.m^{-3}$ and $\eta_{fluid} = 1.03\ mPa.s$. The dashed lines correspond to mucin injection and PBS rinsing.*

Thickness h_{layer} / nm	Viscosity η_{layer} / mPa.s	Elastic modulus μ_{layer} / kPa
25(3)	1.211(10)	4.10(3)

Table 4.4 *Average values of the mucin layer thickness, viscosity and elastic modulus found using the Voinova model on 4 independent measurements. The uncertainty corresponds to the standard error of the mean.*

mucinous layer, but this should mean the interfacial properties are more representative of the corneal endothelium.

Once the mucin layer was formed, an OVD solution diluted by a factor of two with PBS (yielding 15000 ppm for Hyadel and 7500 ppm for Hyaplus) was then injected in the flow chamber for 50 minutes before rinsing with PBS. The results are presented on Figures 4.16 for Hyadel and 4.17 for Hyaplus.

Injection of both OVDs resulted in the same downward spike in Δf observed reproducibly with Hyadel on gold, which we associated with a breakdown of the network of HA as segments interacted with the substrate rather than other chains in the network.

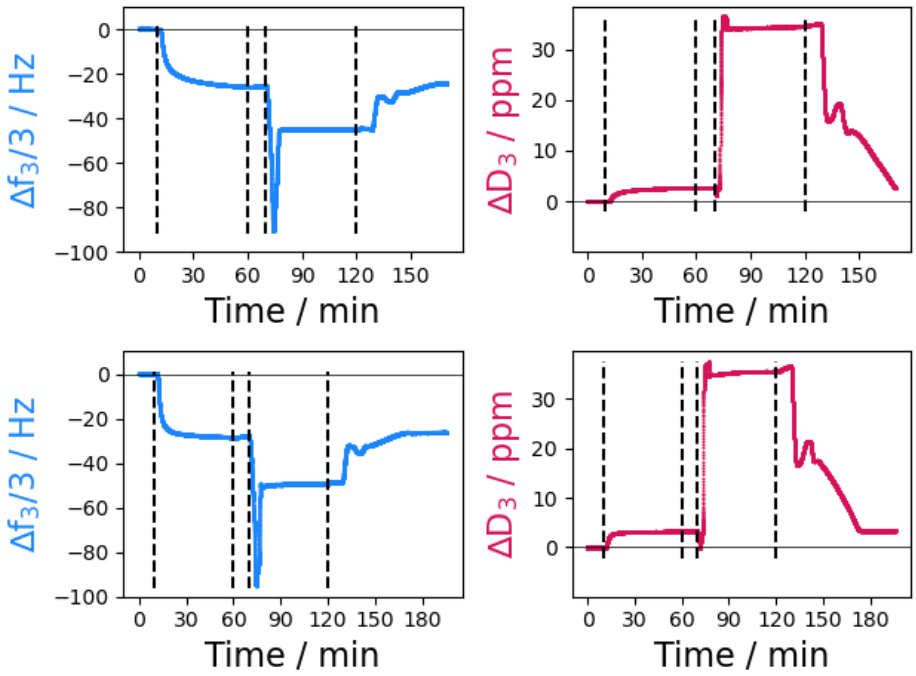

Figure 4.16 *A mucin layer was adsorbed from a 25 ppm solution in PBS and followed with QCM-D for the third overtone on two repeat measurements. A solution of Hyadel diluted by a factor of two was then injected. The dashed lines correspond to the successive injections of mucin, PBS, OVD and PBS.*

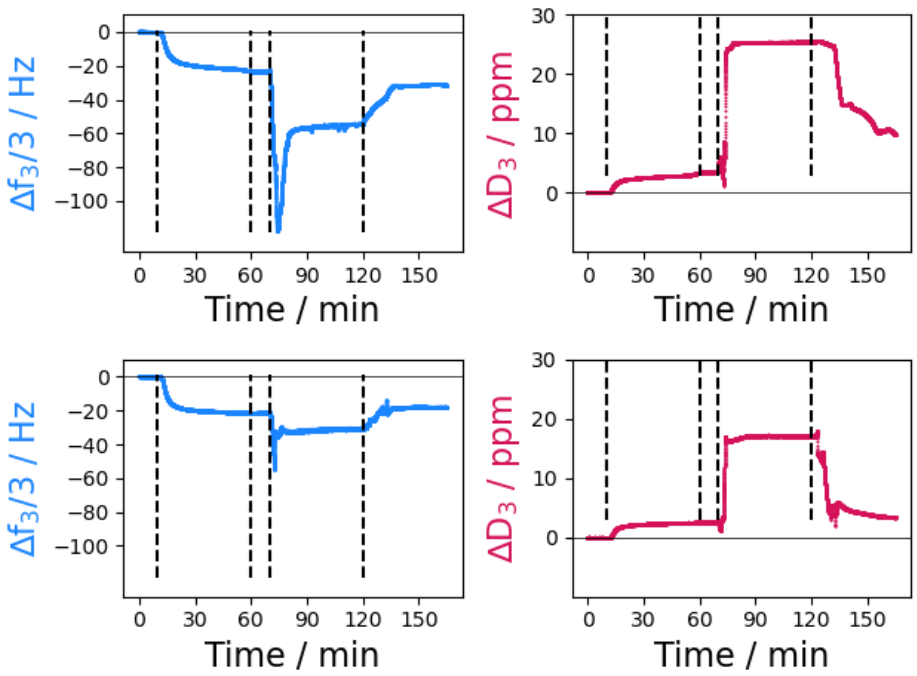

Figure 4.17 *A mucin layer was adsorbed from a 25 ppm solution in PBS and followed with QCM-D for the third overtone on two repeat measurements. A solution of Hyaplus diluted by a factor of two was then injected. The dashed lines correspond to the successive injections of mucin, PBS, OVD and PBS. Note the difference in y-scale with Hyadel plots from Figure 4.16, indicating a difference in the adsorption behaviour.*

Figures 4.18 and 4.19 compare the adsorption on gold obtained from Figures 4.8 and 4.9 with the adsorption on mucin obtained from Figures 4.16 and 4.17.

The frequency shift measured for Hyadel on gold was lower than on the mucin-coated sensor, which indicates that the presence of mucin decreased the amount of surface excess deposited from the Hyadel solution. We attribute this reduced adsorption to the steric hindrance arising from the mucin layer. This phenomenon has been well described before [122], and self-assembled monolayers are regularly used as coatings to minimise unspecific adsorption [123, 124].

Interestingly, Hyadel desorption followed the exact same pattern regardless of the substrate. This lack of sensitivity of the dispersive OVD to the interface it is desorbing from could be a sign of cohesive rather than adhesive failure, which would agree with phacoemulsification observations. It is more difficult to compare the Hyaplus results, as they lead to signals with a higher polydispersity between measurements.

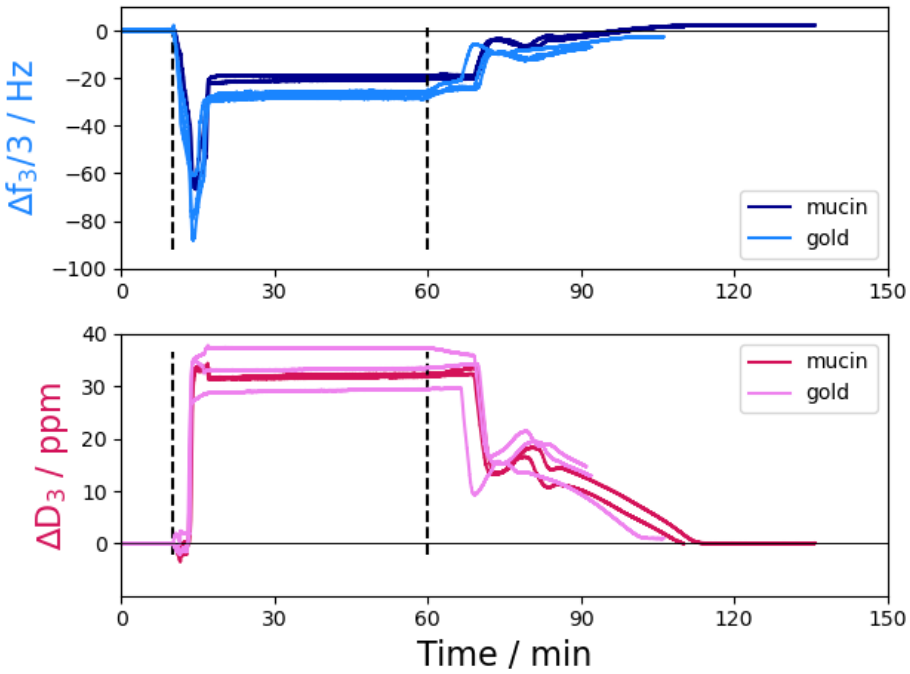

Figure 4.18 *Comparing the QCM-D signal of Hyadel adsorbing from a 25 ppm solution on a mucin layer (darker shade) or on gold (lighter shade).*

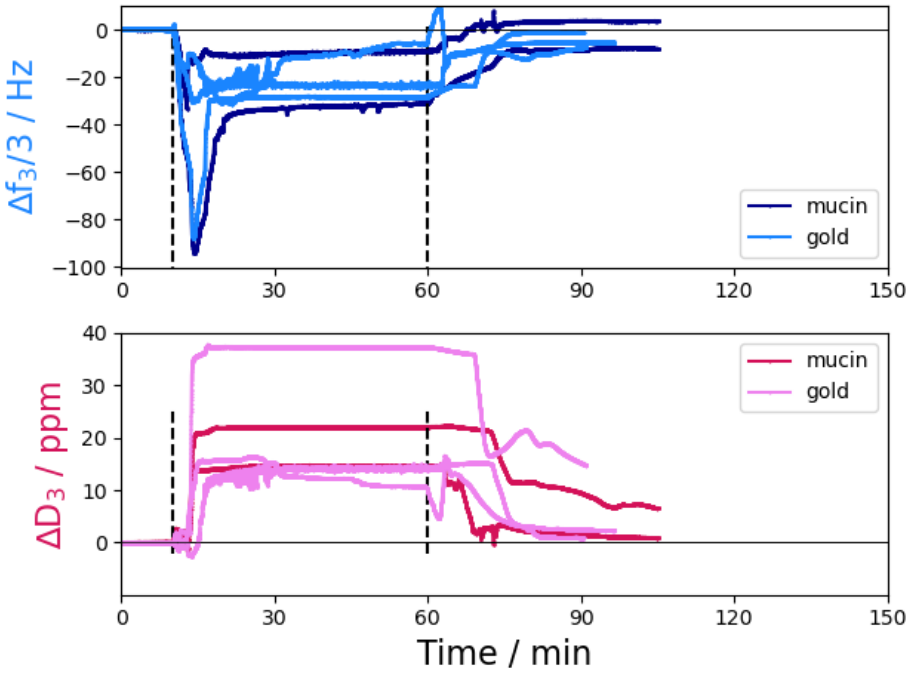

Figure 4.19 *Comparing the QCM-D signal of Hyaplus adsorbing from a 25 ppm solution on a mucin layer (darker shade) or on gold (lighter shade).*

4.7 Conclusions

In this chapter, we showed that in the dilute and semi-dilute regimes, both types of OVD solutions have a relatively similar adsorption mechanism from a Θ solvent, where they physisorb as thin flat layers, with a strong enough attachment to resist desorption upon rinsing. However, in the entangled regime, a divergence emerges. Dispersive OVDs consistently experience an instantaneous network rupture upon contact with the substrate. They form highly solvated polymer layers which exhibit a large dissipation in QCM-D, and are not easily washed out by rinsing. By contrast, the longer chain cohesive OVD, Hyaplus, appears to respond to rinsing in a manner which suggests that some entanglements are retained between the bulk network and the adsorbed layer. This implies that the layer breaks at the solid interface, which could be described as an adhesive failure. The presence of mucin on the gold sensor slightly decreased HA adsorption but overall led to similar results. The consistency of rinsing behaviour observed with the dispersive OVD regardless of the substrate, as well as the network rupture upon adsorption may be signs of cohesive failure.

The ability of dispersive OVDs to dissipate more energy is an encouraging result regarding the superior endothelial protection reported by cataract surgeons. The next chapter is going to be devoted to the measurement of adhesion forces of HA on biomimetic substrates. The results will help us determine whether the removal of OVDs - particularly cohesive OVDs - is likely to cause any damage to the underlying endothelium.

Chapter 5

Strength of the Interaction of OVDs with Biomimetic Surfaces

The AFM imaging and force maps measurements were done in collaboration with Dr Laura Charlton, who provided instruction in using the equipment. The SEM and Cryo-SEM was done with the help of Dr Fraser Laidlaw for sample preparation and image acquisition.

5.1 Introduction

The removal of OVDs at the end of phacoemulsification is crucial in order to avoid post-operative complications. A current consensus in the literature is that aspiration of cohesive and dispersive OVDs exhibit different kinetics and fracture mechanisms. Cataract surgeons report that cohesive OVDs are removed by a rapid bolus aspiration, which would imply a process which is similar to adhesive failure at the endothelial interface. Dispersive OVD experience a slower removal and break up upon aspiration, which could be likened to a cohesive failure process [125–127].

However, this mainly relies on observations at the macroscopic scale and bulk rheology studies. Despite providing useful information on the polymer configuration in solution, classical rheology is impacted by the presence of an interface. Surface phenomena such as polymer adsorption or steric hindrance

arising from excluded volume leads to localised accumulation or depletion of material, which may be overlooked in a rheology experiment. When an adsorbed polymer layer forms on a solid substrate, its volume fraction can be substantially higher than the solution concentration. In particular, adhesive fracture is localised at the endothelium interface, and in that regard surface interactions are key.

In Chapter 4, we demonstrated how HA from OVDs adsorb as thin, strongly-attached layers on a gold surface from dilute and semi-dilute solutions. We also showed that once the entanglement concentration is reached, viscoelastic contributions become important. Polymer coils still form adsorbed layers on the quartz sensor, but they are largely flushed out during rinsing, which could be linked to an adsorption-entanglement process. We witnessed slower desorption kinetics for dispersive OVDs, consistent with the experience of surgeons described in the literature. We also proposed a mechanism that included a release of constraints upon adsorption of the dispersive OVDs, which has some features in common with the fracture of polymer networks. This allows the polymer to rearrange to form a layer that is able to dissipate more energy and more resistant to rinsing than the cohesive OVDs. The desorption of dispersive OVD led to similar signals in QCM-D regardless of the presence of mucin on the gold sensor, which could be consistent with a cohesive fracture mechanism.

A question which remains unanswered is whether the detachment behaviour of dispersive OVDs, which fracture upon aspiration, could contribute to their superior protective ability. Our QCM-D results from Chapter 4 highlighted an attractive interaction between HA and biomimetic substrates resembling corneal endothelial cells. If such an interaction also exists between HA and the endothelium, detachment of the polymer coils may result in cellular damage. In order to test this hypothesis, we used colloidal probe AFM to study the detachment of OVDs. Our approach consists in investigating detachment of HA from biomimetic surfaces, and is inspired by the one used by Button *et al.* [128] when studying the role of mucus in cough clearance. They postulated that mucus clearance could either occur by adhesive failure (bonds breaking at the interface between cells and mucus), or cohesive failure. We hypothesised that the bolus aspiration experienced by cohesive OVDs, which resembles an adhesive fracture process as described in [128] could lead to a higher energy dissipation at the surface. This energy transfer to the surface would increase the risk of aspiration

trauma on the underlying corneal endothelium.

We did not use endothelial cells in this study, as cell culture requires technical knowledge and equipment which were out of the scope of this PhD. To mimic the endothelial cell surface and study adhesive failure, we functionalised glass slides with biopolymers bearing different surface charges: poly-L-glutamic acid (PLGA, -), poly-L-lysine (PLL, +) and mucin from porcine stomach, which has both positively and negatively charged regions, but is overall negatively charged. The functionalisation procedure is described in Section 2.4.2. The corneal endothelium, like all external layers of organs, is covered by a cellular coat called the glycocalyx. Sometimes referred to as a mucinous layer, it is a protective viscoelastic layer composed of high molecular weight polysacharrides associated with proteins or lipids, including endogenous HA and mucin glycoprotein MUC1. We therefore used a mucin coating to mimic the composition of the glycocalyx.

HA is likely to interact with a number of structures in the eye during phacoemulsification, such as aquaporins, which are transmembrane proteins involved in balancing the flux of water in the eye [129]. Two types of HA-binding receptors are also present on the corneal endothelium: CD44 and RHAMM. The binding to CD44 happens via a lysine residue [130, 131], whilst RHAMM is rich in both lysine and glutamic acid [13], the latter being key to HA binding [132]. For this reason, we used polymerised versions of these amino acids to mimic the composition of the receptors. We also functionalised slides with OVDs following the same protocol as the colloidal probe (see Figure 5.8) in an attempt to study cohesive failure. A schematic of the colloidal probe AFM experimental set-up is shown in Figure 5.1.

The two parameters used to tune the rheology of HA-based OVD formulation are polymer molecular weight and concentration. Cohesive OVDs usually display a higher molecular weight and a lower concentration than their dispersive counterparts. Molecular weight determines the contour length of each individual polymer chain, which in turn influences its radius of gyration and diffusion constant. Concentration impacts the local crowding and three-dimensional network. In our study, the concentration dependence was removed by functionalising the silica bead in solutions which contained the same mass concentration of HA. We will therefore attribute any difference spotted between cohesive and dispersive OVDs to a molecular weight dependence.

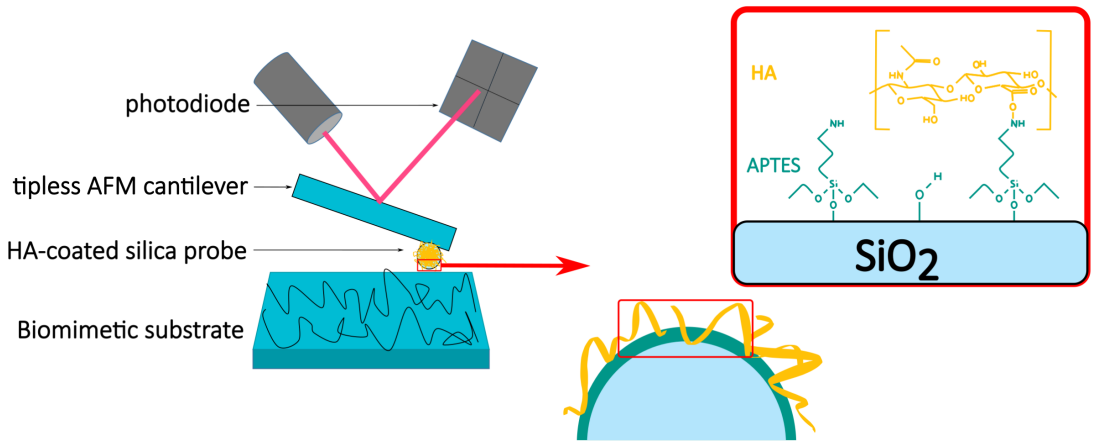

Figure 5.1 *Schematic of the colloidal probe AFM experiment. A 4.48 µm diameter silica particle coated with hyaluronic acid (HA) from ophthalmic viscosurgical devices (OVDs) was attached to a tipless cantilever and used as a force testing probe. The functionalisation involved a self-assembled monolayer of aminopropyltriethoxysilane (APTES) chemically linked to HA. The substrate was a glass slide functionalised with biological material: poly-L-lysine, poly-L-glutamic acid, mucin or hyaluronic acid.*

We first used contact angle measurements and AFM imaging to characterise the effect of the different substrate functionalisation protocols. We used AFM, SEM and Cryo-SEM to image the HA-functionalised colloids which were then used as a probe in the AFM adhesion force measurements. AFM yielded a quantitative measure of two parameters: the adhesion force and the energy released upon detachment of polymer chains. We considered the effect of probe speed and dwelling time on the surface. The worm-like chain model highlighted information on the polymer flexibility.

5.2 Characterisation of Biomimetic Substrates

Before the AFM study, it is important to characterise the functionalisation described in Section 2.4.2 of our biomimetic substrate. To do this, we used a range of different techniques, namely interfacial tensiometry, drop shape analysis and AFM imaging.

5.2.1 Interfacial Tensiometry

When studying the adsorption of polymers on a solid substrate, it is important to consider the energies at different interfaces. The balance of interfacial energies ultimately determines the affinity of the different phases for one another at thermodynamic equilibrium, which then determines the shape of the liquid droplet. The ability of a liquid to spread on a surface, or wettability, depends on the liquid and solid surface tensions: a liquid with a higher surface tension than the underlying substrate will minimise the contact area and form spherical droplets. On the contrary, a liquid with low surface tension will spread on the substrate. Dispersive OVDs like Hyadel have been reported to have a better coating ability *in vivo*. For this reason, they are often referred to as low surface tension solutions compared to cohesive OVDs [30, 43, 46].

In this work, we were interested in three interfaces. First of all, we measured the OVD-air interfacial tension by studying a pendant drop of pure OVD in air (Figure 5.2). Our objective was to characterise the intrinsic surface tension of a dispersive and a cohesive OVD, and to see if we measured a lower surface tension for the dispersive OVD, as inferred from observations by surgeons. One should keep in mind that in phacoemulsification, the ambient phase is the liquid aqueous humour and not air. The second interface of interest was between our functionalised biomimetic substrates and water. We also measured the contact angle of a sessile drop of distilled water on three surfaces: bare oxidised glass, or glass functionalised with either PLL or PLGA. This allowed us to show the effect of functionalisation on the substrate wettability (Figure 5.3). Lastly, we considered the substrate-OVD interface by measuring the contact angles of droplets of OVD on the three substrates (Figure 5.4). The aim was to compare the wettability of the different substrates by either OVD, and relate it with the pendant drop results. Each measurement was performed for a minimum of 10 minutes. It was not always long enough to reach thermodynamic equilibrium, however cataract operations are only a few minutes long, so phenomena occurring on longer timescales are outside the scope of interest of this study.

OVD-Air Interface

OVDs differ in terms of concentration and molecular weight, which can both impact surface tension. If the polymer adsorbs at the air/water interface, an

increase in concentration will typically decrease the surface tension [133, 134], although this decrease was reported to be weaker for high molecular weight polymers, such as we present in both OVDs. Surface tension also decreases with concentration according to a study from Silver *et al.* [135]. The authors determined the second virial coefficient of polysaccharides, a parameter which reflects the intermolecular repulsion between polymer chains. They stated that a higher molecular weight HA experiences an increased repulsion, resulting in a lower surface tension. It is enthalpically favourable for the polymer to adsorb on the surface rather than interacting with neighbouring chains. Cohesive OVDs have a higher molecular weight, but a lower concentration than dispersive OVDs, so predicting any differences in their surface tension is not a trivial problem.

The interfacial tensions of pendant droplets of OVDs in air are shown in Figure 5.2.

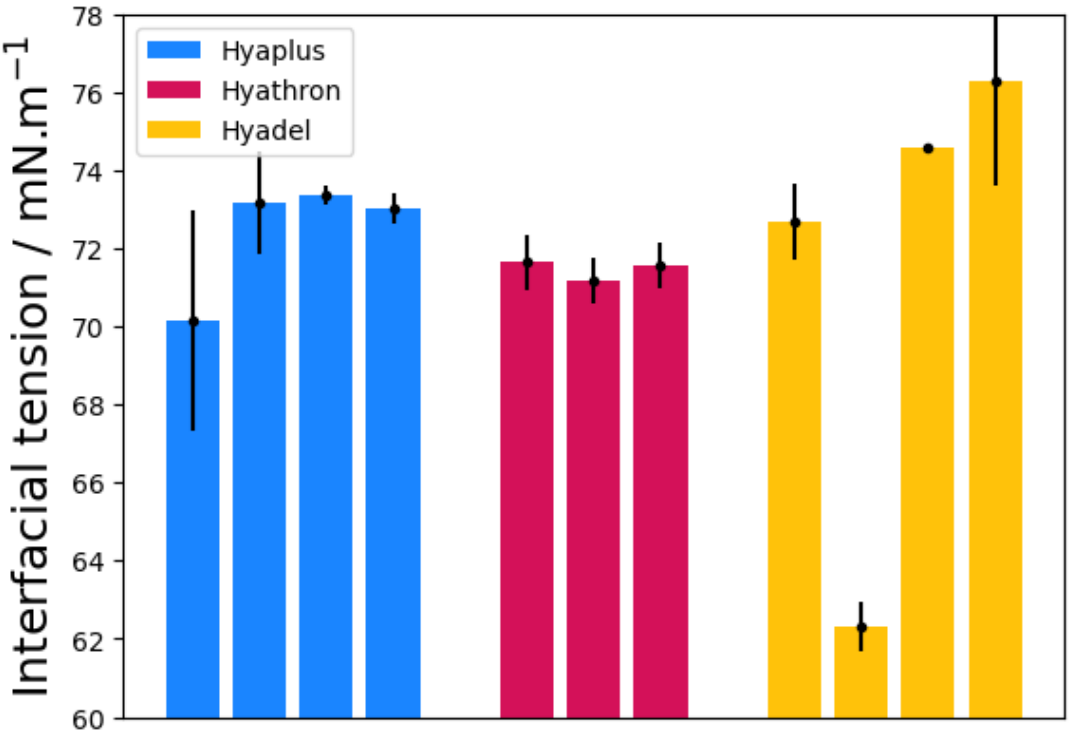

Figure 5.2 *Interfacial tension of a top-down droplet of cohesive Hyaplus (blue), viscosupplement Hyathron (pink, not used in the rest of this thesis, but included for completeness) and dispersive Hyadel (yellow) in air.*

The surface tensions we measured for both OVDs were fairly close, albeit with the values for Hyadel being more widely distributed. They were also close to the surface tension of water (72 mN.m^{-1}), and even higher on several occasions, which is not physically reasonable. This lack of a clear decrease in surface tension

for either OVD compared to distilled water suggests that there is no adsorption of HA at the air interface in the timeframe of the experiment. This is consistent with the heterodyne-detected vibrational sum-frequency generation spectroscopy (HD-VSFG) results from Moll *et al.*, who saw no adsorption of high molecular weight HA ($\geq$ 1 MDa) at the air interface even after several hours [136]. The adsorption was found to be highly dependant on molecular weight, which was attributed to polymer entanglements. In that regime, individual polymer segments have a limited mobility. As a result, the diffusion to the interface is too slow to be detected experimentally. Other authors have previously pointed out the difficulty in relating surface tension and adsorption in polyelectrolyte systems [134, 137].

An erratic behaviour was previously described at 2.4 mg.mL^{-1} for the surface tension of HA, where a large standard deviation was attributed to the start of the entanglement process [134]. As shown in Figure 4.1, both Hyaplus and Hyadel are well above the entanglement concentration c_e, with concentrations of 10 and 30 mg.mL^{-1}, respectively. The large distribution of interfacial tensions observed in our measurements agrees well with this erratic behaviour.

In the entangled regime, the shape of a pendant drop may not be easily correlated to interfacial tension using the Young-Laplace model described in Chapter 2. This model is based on the assumption that the droplet shape is determined by the balance between gravity and Laplace pressure, which is the pressure difference between the inside and the outside of the droplet. Although this model works well for simple polymer solutions, it does not take into account the viscoelasticity of OVD solutions. These viscoelastic contributions were also visible from sessile OVD droplets in Figure 5.5, which will be discussed later on.

Despite this deviation from simpler models, our measurements compared well with the results from Silver *et al.* for pure 2.1 MDa HA (70 mN.m^{-1}) [44]. The HA concentration used was not clearly stated in the article, but it is interesting to note that they did not see any significant change in surface tension with dilution from a factor 10 to 100,000. This is compatible with the three time difference of concentration between both our OVDs not resulting in a measurable difference in surface tension.

The same group also reported surface tensions of other OVDs, which differed largely from ours (43 mN.m^{-1} for dispersive Ocucoat, 62.7 mN.m^{-1} for cohesive

Healon) [135]. It is however difficult to compare Ocucoat, which contains HPMC, to the HA-based Hyadel. Another notable difference is that they diluted the OVD stock solutions by a factor of 10, perhaps as a way to minimise the viscoelastic contributions mentioned earlier.

Water-Substrate Interface

The contact angles measured for sessile drops of water on the various functionalised substrates are shown on Figure 5.3. Water displayed a different contact angle on each substrate, which is a first sign that our functionalisation protocol had an effect on the glass slide.

The bare glass slide had the highest hydrophilicity, as shown by the low contact angle ($\theta \sim 5°$). The UV-Ozone cleaning procedure created a high density of -OH groups on the surface able to form hydrogen bonds with the solvent. The lowest hydrophilicity was on the PLL-functionalised slide ($\theta \sim 40°$), whilst PLGA was intermediate ($\theta \sim 12°$). PLL has an amine function per residue from which hydrogen bonds may arise, whilst PLGA has a carboxylic acid, which may explain its higher hydrophilicity. The availability of surface groups may also be decreased in the case of PLL, as we expect an attractive Coulomb interaction between the positively-charged amino acid and the negative underlying glass. A high surface coverage could result in the polar functions being partially hidden from solvent molecules. This could also explain why the contact angle of distilled water on PLL continues to decrease overtime, whereas the other two substrates already reached thermodynamic equilibrium.

The corneal endothelium, which is our system of interest, is hydrophilic due to the presence of biopolysaccharides at the glycocalyx surface. However, it exhibits a hydrophobic behaviour upon removal of these polymers [138]. This makes both hydrophilic and hydrophobic surfaces relevant to our study.

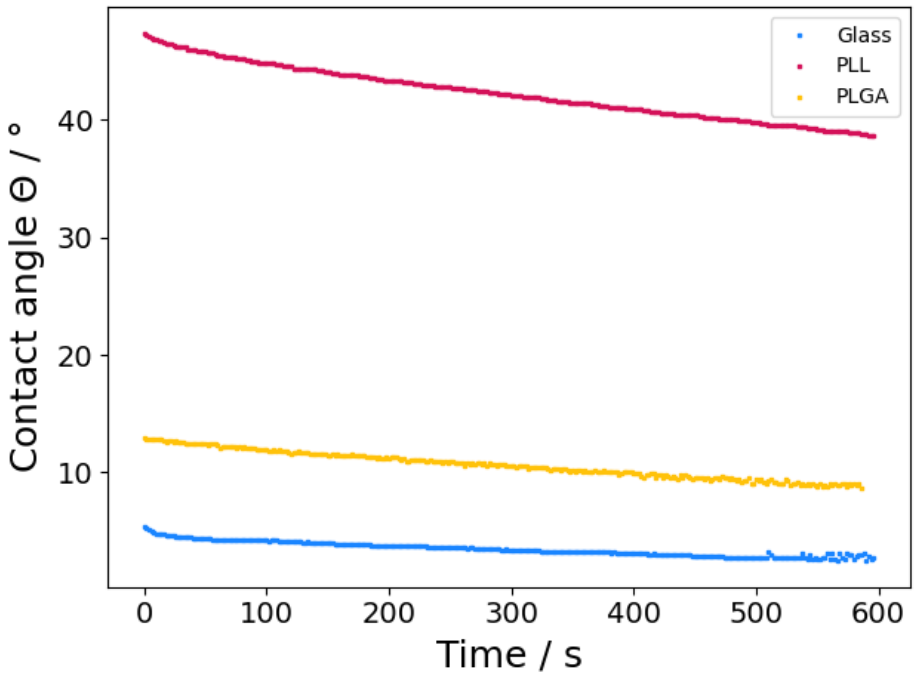

Figure 5.3 *Contact angles as a function of time for a droplet of water on bare oxidised glass (blue), poly-L-lysine (pink) and poly-L-glutamic acid (yellow). Hydrophilicity reflects the availability of surface groups and their ability to form hydrogen bonds.*

OVD-Substrate Interface

We then characterised the contact angle of OVDs on bare or functionalised glass slides. We wanted to see how they compared with the contact angle of water, and if the results would be consistent with the adsorption of OVDs to the corneal endothelium. The results are shown on Figure 5.4

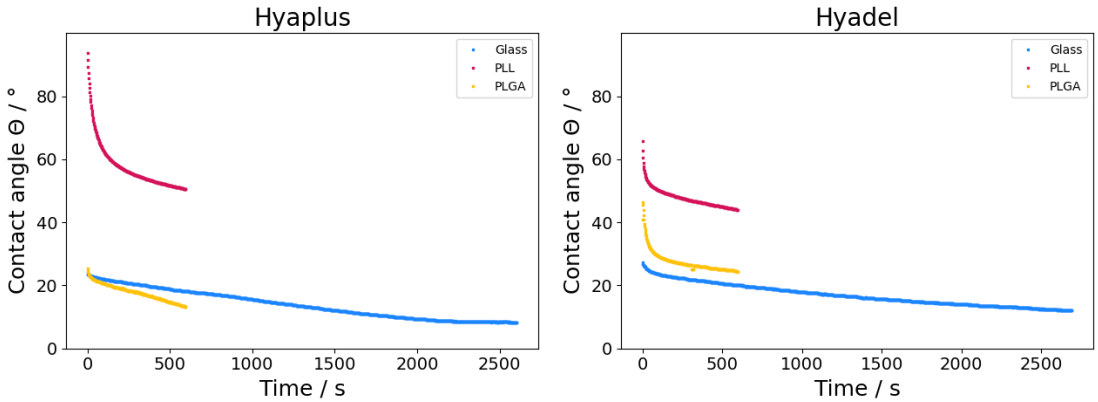

Figure 5.4 *Contact angle as a function of time for a droplet of cohesive Hyaplus (left panel) and dispersive Hyadel (right panel) on bare oxidised glass (blue), poly-L-lysine (pink) and poly-L-glutamic acid (yellow).*

A first observation is that the contact angle order observed with the water droplet on Figure 5.3 (Glass < PLGA < PLL) was mostly preserved with OVDs, which was expected as they are aqueous solutions. This contrasts with the similar values of interfacial tension observed for both OVDs in air in Figure 5.2. The contact angle of both OVD droplets was marginally higher than the one obtained with water droplets, which suggests the liquid surface tension of OVD solutions is slightly higher than distilled water.

Cataract surgeons describe a higher spreading ability of dispersive OVD solutions, which is commonly attributed to a lower surface tension. In our measurement, this was not systematically verified. Specifically, the contact angle on the PLL-functionalised surface was lower for the dispersive Hyadel, but on the PLGA surface, it was the cohesive Hyaplus which displayed a lower contact angle. Viscoelasticity is known to play a role in spreading, as described in [139]. To prepare the sessile droplets, OVD syringes were emptied in a vial. Another syringe, with the right dimensions for the equipment, was then filled with the corresponding solution. This procedure possibly put the viscoelastic solution through a deformation leading to shear-thinning. The variability in the contact angle measurements, which could arise from the deformation history of the gel, makes it difficult to clearly identify trends.

Figure 5.5 shows snapshots taken at different stages of the drop shape analysis measurement. Both OVDs had a tendency to spread overtime, which is both visible on the pictures from Figure 5.5 and by the contact angle rapid drop in the first seconds of the experiment on Figure 5.4. The non-spherical shape of the Hyaplus droplet on PLL at $t = 0$ can be related to the viscoelastic contributions discussed previously, which deviates from the Young-Laplace model. The OVDs represent a limiting case, where the forces in play are not only gravity and capillary force, but also internal elasticity spread throughout the bulk.

The droplets did not reach thermodynamic equilibrium in the timeframe of the experiment, as shown by the continuing contact angle decrease after several minutes on Figure 5.4. The high molecular weight of HA results in a very slow diffusion of the polymer chains to the solid interface. Moreover, the HA concentration (15 and 30 $g.L^{-1}$) is way above the entanglement limit of polymer chains (2.4 $mg.L^{-1}$ for 1 MDa HA [103, 140]), which greatly reduces the mobility of individual chains. Both these effects imply that very few segments are likely to be at the solid interface in the timeframe of the experiment.

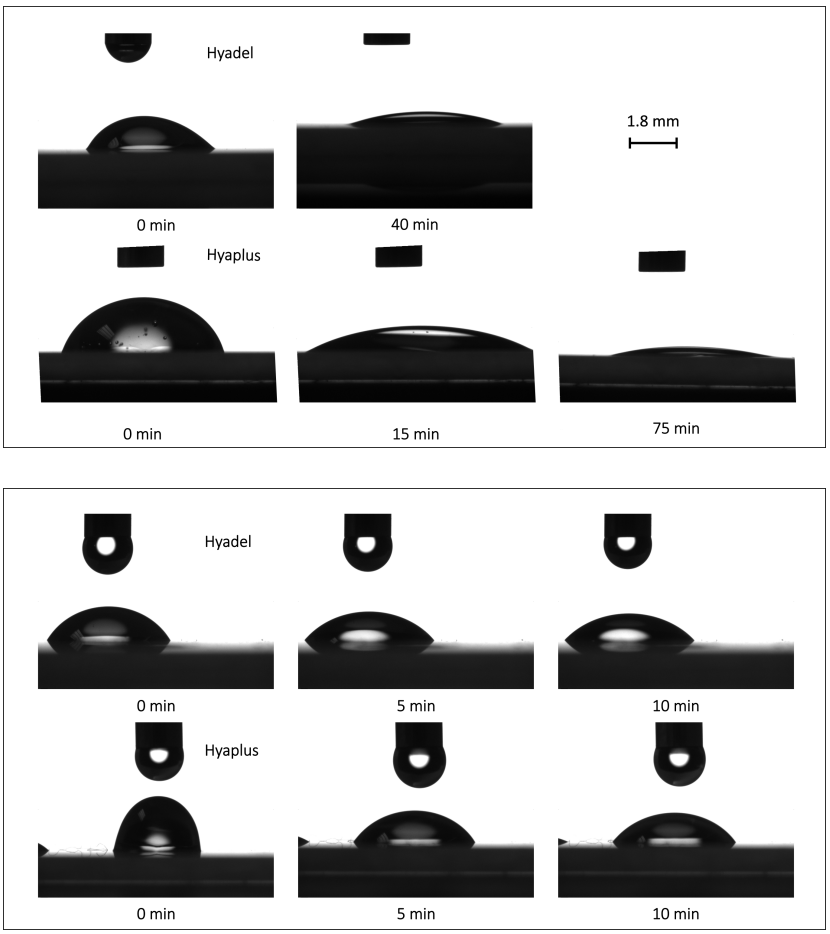

Figure 5.5 *Pictures of sessile drops of dispersive Hyadel and cohesive Hyaplus on bare oxidised glass (upper panel) or PLL-functionalised glass (lower panel) at different measurement times. The scalebar is similar in both panels.*

To conclude, the interfacial tensiometry and drop shape analysis revealed that the lower surface tension widely predicted for dispersive OVDs in the literature is not straightforward in practise. OVDs are complex solutions, and do not act as simple Newtonian liquids. This is due to their high molecular weight and concentration, and their resulting viscoelastic nature. The glass slide and both functionalised substrates had a visibly different hydrophilicity, which is an encouraging sign that the biopolymers were adsorbed on the substrate.

5.2.2 AFM Topography: A/C Imaging of the Substrate

Before using AFM to measure the adhesion strength of HA with our biomimetic substrates, the topography of the substrates was measured using dynamic mode

(A/C) AFM. The aims were to characterise the homogeneity of the coating and its roughness. Surface roughness could decrease the area available for contact with a colloidal probe, resulting in a weakened adhesion, so it is important to look for differences in roughness before studying AFM force profiles. The results are presented in Figure 5.6

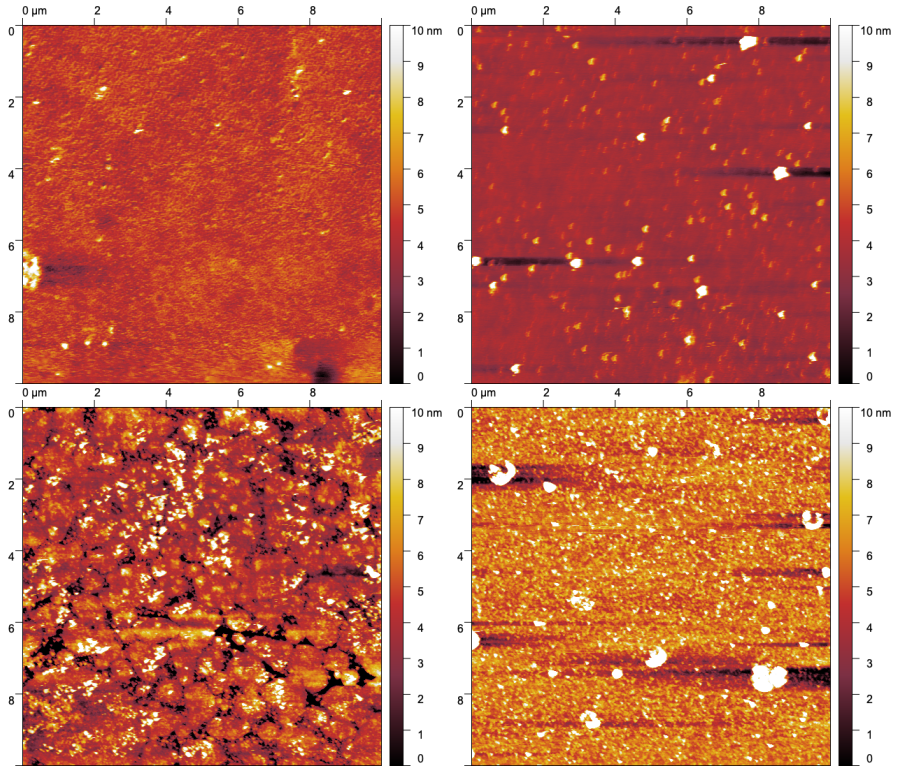

Glass	1.2 ± 0.4 nm
PLL	2.1 ± 1.5 nm
Mucin	2.5 ± 1.6 nm
PLGA	2.8 ± 1.6 nm

Figure 5.6 *Dynamic mode AFM images of the different substrates' topography in PBS: glass (top left), PLL (top right), mucin (bottom left) and PLGA (bottom right), and table summarising the root mean square roughness parameters for each substrate. The standard deviation from measuring different regions is displayed as uncertainty.*

The four substrates were visibly different, however they have relatively similar root mean square (RMS) roughness. The bare glass slide was the smoothest surface, as expected, with a RMS roughness close to a nanometer. It increased on all functionalised slides, with no significant difference between substrates. This gives us some confidence that any differences measured in adhesive strength between the colloidal probe and the different substrates can be related to the

strength of the interaction between HA and the substrate.

The coating was homogeneous on all functionalised slides, which suggests the coating protocol was efficient. The slides had all been rinsed thoroughly before imaging, which clearly did not completely remove the adsorbed material. This is particularly important to note for polymerised aminoacids, which had a short timescale of functionalisation (5 minutes only compared to 1h30 for mucin). The efficient functionalisation is consistent with the change in contact angle for PLL and PLGA compared to bare glass described in Section 5.2.1.

The reason for employing different functionalisation times were two-fold. First, mucins have a higher molecular weight (4000-5500 kDa) than PLL (70-150 kDa) or PLGA (50-100 kDa). For this reason, they are expected to diffuse more slowly in solution, justifying the need for a longer adsorption time. The second reason is that, as stated earlier, mucin is being used as a model for the overall glycocalyx layer, whereas poly-amino acids are meant to mimic localised structures such as HA-binding receptors. We therefore wanted to allow more time for a higher coverage, more extended layer to build up in the case of mucin.

Figure 5.8 summarises the different dimensions relevant to the experiment presented in this chapter.

Each AFM force map was measured on a 8 × 8 grid covering a 100 × 100 µm area (left panel). Each point on the map thus probed a 12.5 × 12.5 µm area, which is in the same range as both the the colloid diameter (4.48 µm) and the area imaged for the substrate coating on Figure 5.6 (10 × 10 µm, middle panel). The apparent coating homogeneity of the substrates on that scale led us to the conclusion that any large heterogeneity in the force maps could not be attributed to the coating itself.

5.3 Characterisation of the OVD-functionalised Silica

In this section, we will start by characterising the procedure used to functionalise the silica particles used as an AFM colloidal probe with OVDs. To do this, we imaged OVD-functionalised glass slides with AFM and whole OVD-functionalised silica colloids using SEM and Cryo-SEM. Once the presence of the HA coating

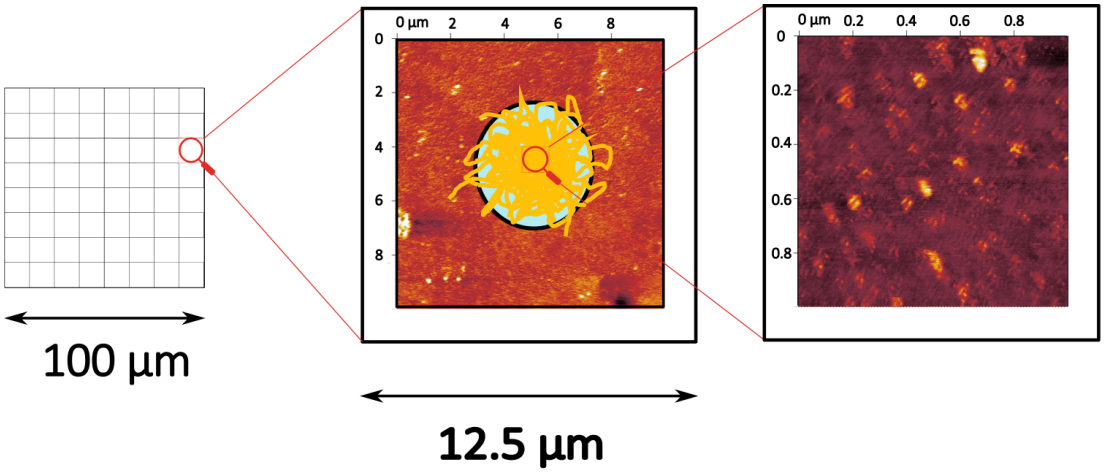

Figure 5.7 *Schematic of the dimensions relevant to the experiment. AFM force curves scanned an 8 × 8 point grid covering a square of side 100 µm (left panel). Each point on the map corresponds to a 12.5 × 12.5 µm square, which is comparable to the area imaged on Figure 5.6 for the substrate (middle panel). The HA-functionalised silica particle used as a probe (4.48 µm diameter) is also in the same length range, and is represented by the blue and yellow circle. Although the bead itself was not imaged with AFM, a glass slide functionalised with the same OVD coating was imaged on a 1 µm^2 area, see Figure 5.8 (right panel).*

has been established, we will move on to the AFM force measurements, and the information they provide on the strength of the interaction between cohesive and dispersive OVDs and a range of biomimetic substrates.

5.3.1 Imaging the Probe Coating: AFM

In order to gain some insight into the nature of the coating on the colloidal particle attached to the cantilever, a glass slide was functionalised using the same procedure, described in Section 2.4.2. This functionalised slide was imaged with AFM and the images are shown in Figure 5.8. Note that the area imaged here was 1 µm^2 to highlight small scale structures that will come into contact with the substrate when similarly functionalised colloidal probes are used in force profile measurements.

As with the images obtained on the substrates (Figure 5.6), we could see material adsorbed on all the functionalised slides. The slide coated with APTES presented

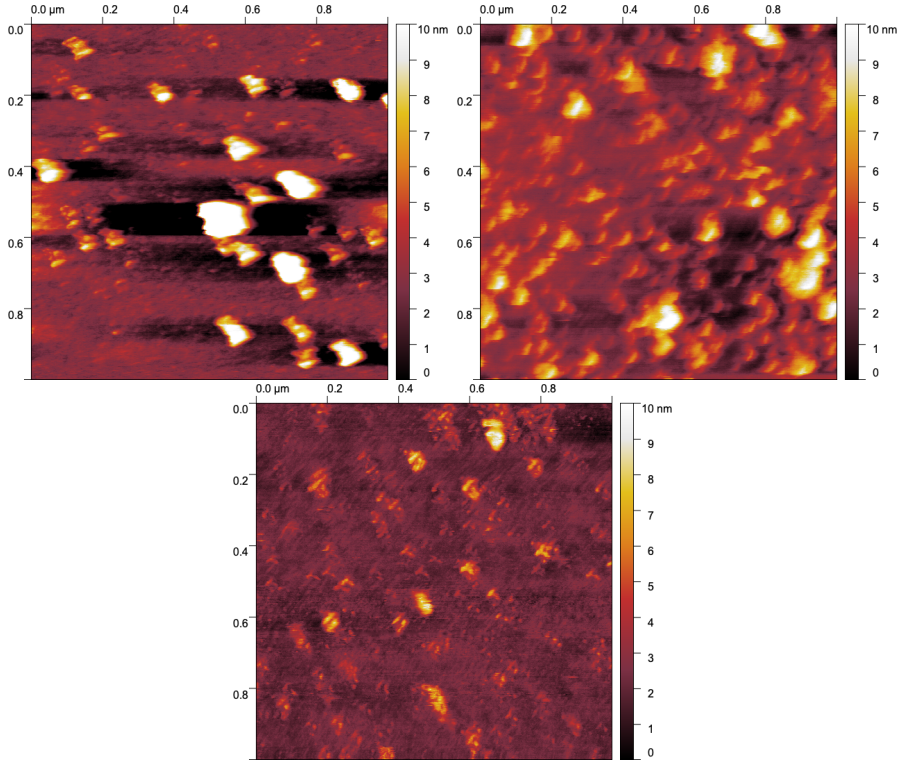

Figure 5.8 *Dynamic AFM topography images of a glass surface in PBS functionalised using the same protocol as the colloidal probe: APTES coating (upper left panel) and either Hyaplus (upper right panel) or Hyadel functionalisation (lower panel). The HA coating appears to be homogeneous in spite of the larger structures evident on the APTES coating surface.*

some spherical aggregates ($\approx$ 100 nm) which could be polymerised APTES nanoparticles, like those imaged in [141, 142]. A spontaneous polymerisation of aminosilane can arise from traces of water in the solvent. We used 99% anhydrous ethanol as solvent, however ambient humidity may decrease the solvent purity.

The apparent inhomogeneity of the APTES coating did not prevent HA from forming a homogeneous layer. Hyaplus appears to form globules with a dimension of 85 $\pm$ 31 nm. As for Hyadel, structural features (75 $\pm$ 25 nm) can be seen on the AFM images, but they are less pronounced. Our interpretation is that the globules and features correspond to single HA molecules. The radius of these items is smaller than the radius of gyration found in the literature for HA of similar molecular weights (126.1 nm for 1.06 MDa and 257.7 nm for 3.5 MDa according to [111]). These values are not conflicting, as AFM images reflect the density of polymer layers rather than their thickness, which can be estimated using the radius of gyration. The larger globules observed for the

cohesive OVD suggest that the attachment points to the surface are separated further apart, which implies there is a lower grafting density resulting in a configuration resembling collapsed mushrooms [143]. The higher distribution can be related to its higher polydispersity [109]. Conversely, the polymer layer formed from adsorbed Hyadel is compatible with an extended brush-like configuration. Although the polymers were chemically linked to the substrate in this procedure, and merely adsorbed in the experiments from Chapter 4, we can draw parallels between the results of both procedures. The layer formed in the presence of a dispersive OVD solution dissipated more energy in QCM-D than that formed from a cohesive OVD. We attributed this behaviour to a stronger coupling of the HA from dispersive OVD with the surrounding solvent, as would be expected from an extended brush-like configuration compared to collapsed mushrooms.

Note that in the APTES image, the globules all appear to have a doublet shape structure, and to be oriented in the same direction. This may result from a tip convolution, which could make the dimensions in the x-y plane unreliable. Despite this setback, the visible difference between the three types of functionalised slides, as well as the concordance with the structural configuration inferred from the QCM-D data in Chapter 4 provide some initial evidence for the attachment of HA to glass. Silica colloids functionalised with the same procedure will be imaged using SEM and Cryo-SEM in Section 5.3.2.

5.3.2 Imaging the Probe Coating: SEM and Cryo-SEM

In order to complement the information gathered from AFM measurements of topography, we imaged the colloidal probes with SEM and Cryo-SEM microscopy. In addition to allowing for direct imaging of the whole colloidal particle, Energy Dispersive X-Ray Analysis (EDX) provides information on the chemical composition of the coating and the underlying particle. The disadvantage is that the measurements are done in vacuum whereas AFM imaging was done in solution. Control particles, both unfunctionalised and partially functionalised with silane only were also imaged as a way to ensure we did not mistakenly attribute structural features arising from either the silane or the underlying silica particle to HA from OVDs.

The SEM image and EDX analysis for bare colloids can be found on Figure 5.9. The bare silica particles appear relatively smooth. EDX revealed an oxygen

signature on the particles, whilst the silicon signal was weaker than the silicon wafer background. This suggests the existence of an amorphous surface oxide layer. Carbon and platinum signals were equivalent to the background.

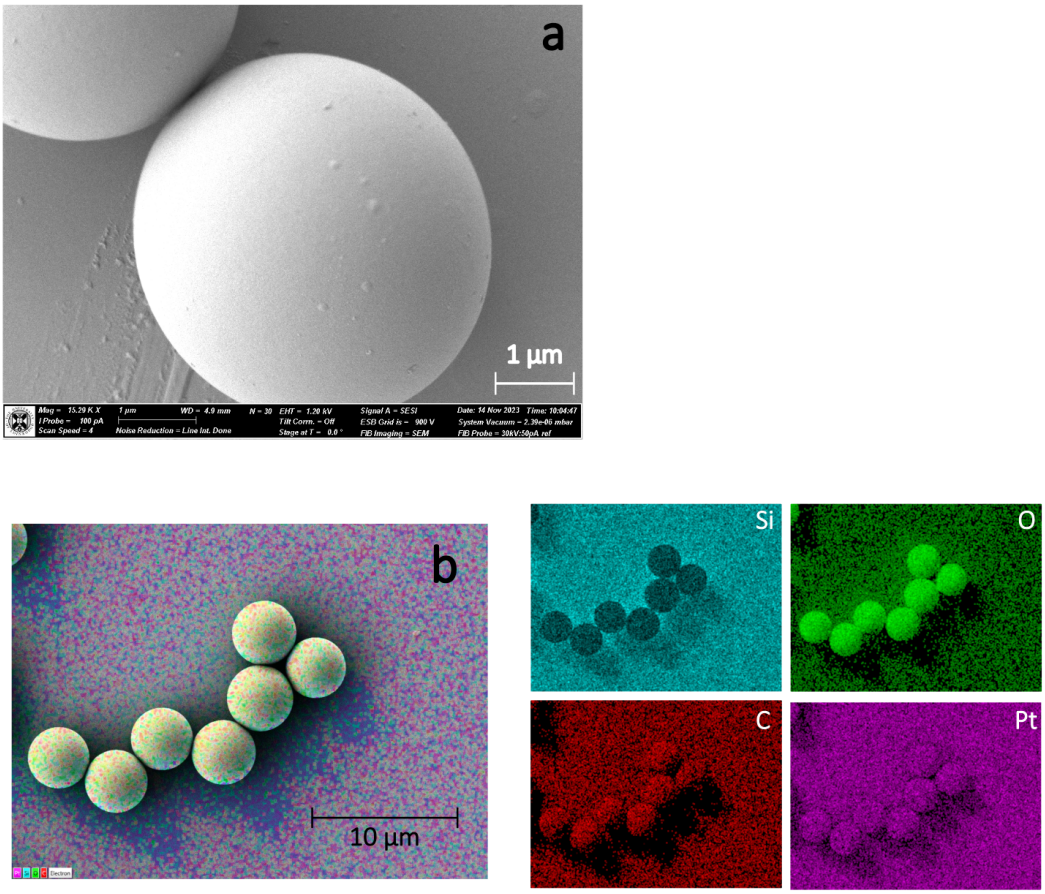

Figure 5.9 *SEM image of bare silica particles (a), and corresponding EDX element analysis (b) before any functionalisation. The right hand panel of (b) shows signal from Si (turquoise), O (green), C (red) and Pt (magenta). The left hand panel of (b) is a combination of all four. The particles were coated with platinum prior to imaging.*

The APTES-coated particles were visibly different from the bare colloids, and displayed a coating on the surface. The thicker structures (arrows on Figure 5.10 a) could be polymerised silane aggregates like those identified with AFM. Some fragmented coating was also visible at the interface between particles (arrows on Figure 5.10 b). The EDX signature was close to that of the bare particles, which suggests the APTES carbon backbone was not detected, perhaps because it was too thin to generate a measurable signal. It should also be kept

in mind that the carbon signal in EDX is not easy to detect. The reason for this is two-fold: carbon contamination is often observed in SEM, generating a background noise which lowers the resolution of the carbon signal. Additionally, carbon has a low atomic number ($Z = 6$), yielding low energy X-rays which are mostly absorbed by the sample [144].

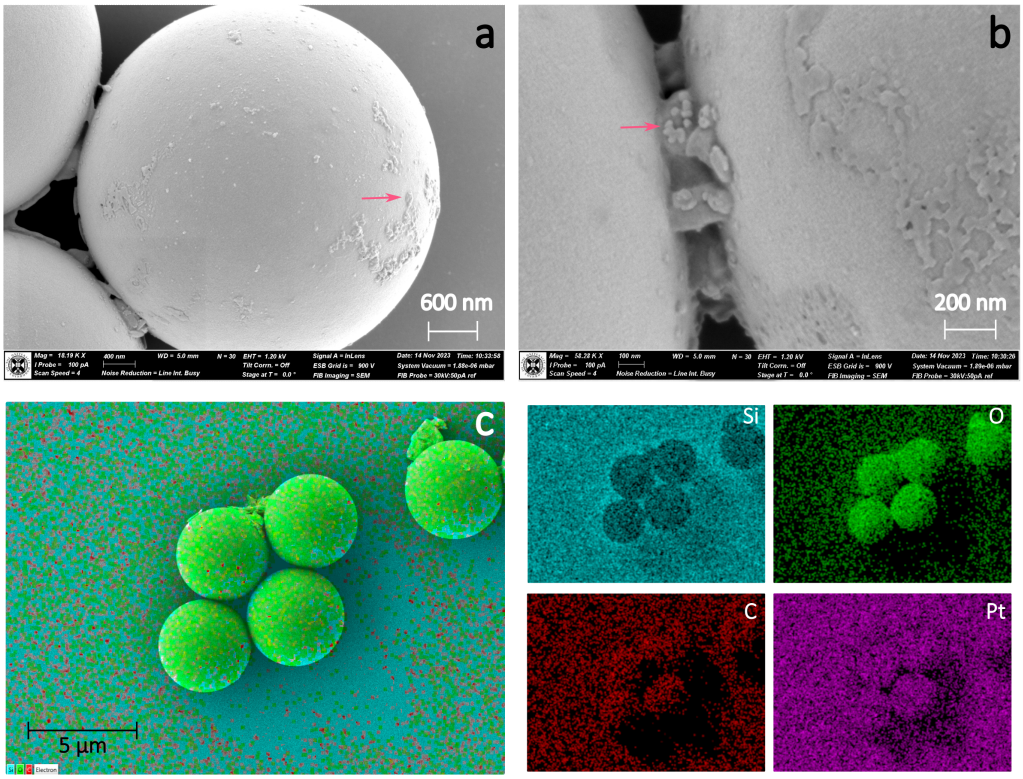

Figure 5.10 *SEM images of APTES-coated silica particles (a, b), and corresponding EDX element analysis (c) before any chemical linking to HA. The right hand panel of (c) shows signal from Si (turquoise), O (green), C (red) and Pt (magenta). The left hand panel of (c) is a combination of all four. Arrows point towards polymerised APTES. The particles were coated with platinum prior to imaging.*

SEM images of Hyadel-coated particles can be found on Figure 5.11. As can be seen on Figure 5.11 a, the surface of a Hyadel coated particle is different compared to either the bare particle (Figure 5.9) or the APTES-coated particle (Figure 5.10). The Hyadel-coated particle has a mesh-like surface topography, indicated by the arrows on Figure 5.11 a. Interestingly there is a clear accumulation of material at the interfaces formed between pairs of particles (Figure 5.11 b and c) and in the interstices within a group of five particles (Figure 5.11 d). Careful examination of Figure 5.11 d indicates that there is some deformation of the particles, indicating an adhesive interaction between them. Also visible in Figure 5.11 d is a relatively thick layer capping the particles. There appears to be some artefacts attributed to the drying process, specifically mounts and pits possibly arising from a coffee-ring effect like the one indicated by an arrow on Figure 5.11 b.

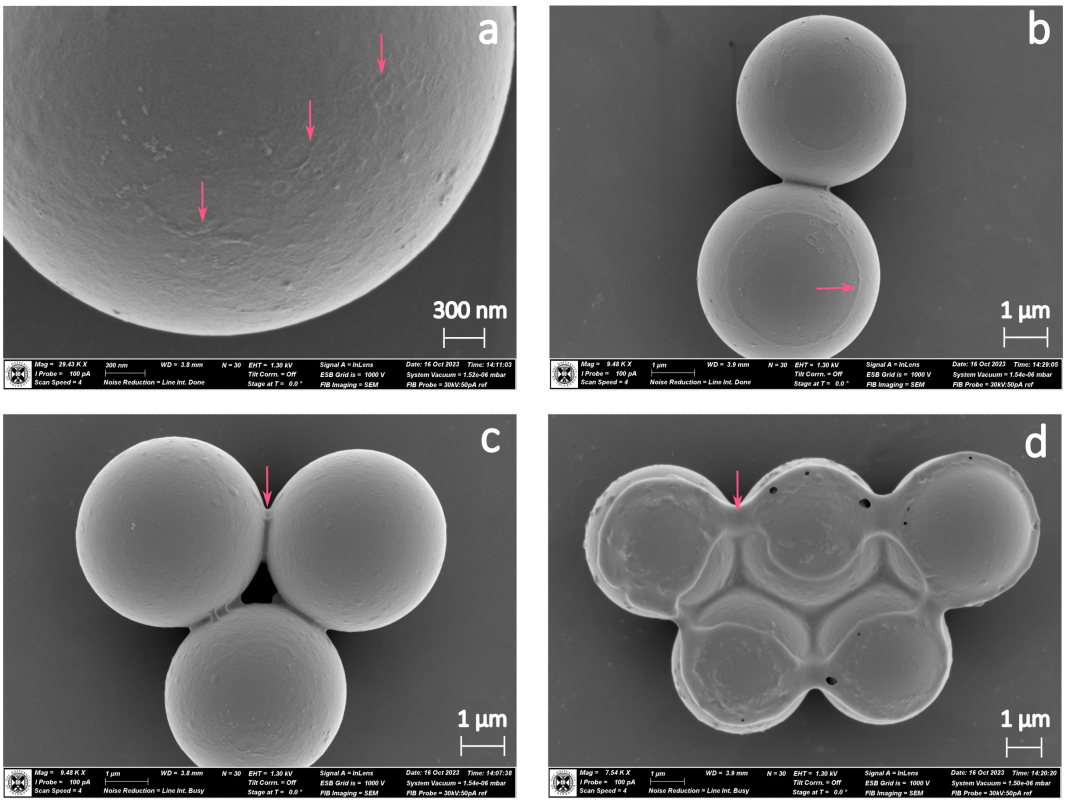

Figure 5.11 *SEM images of silica particles coated with Hyadel, a dispersive OVD. Arrows point towards the HA mesh structure (a), a coffee-ring effect attributed to the drying process (b), HA mediating an adhesive interaction at the interface between neighbouring particles (c), and a thick HA coating on top of the particles (d). The particles were coated with platinum prior to imaging.*

The SEM images of Hyaplus-coated particles visible in Figure 5.12 appear similar

to those of the Hyadel-coated particles. Both show the presence of mounts and pits, as well as a coffee-ring effect on top of the beads. Nearby particles appear to adhere by means of a filament-forming coating, as indicated by an arrow on Figure 5.12 b. This suggests the presence of a viscoelastic material at the interface between adjacent particles prior to imaging, which we attribute to HA from the OVDs. We did not observe the thick coating seen with Hyadel in Figure 5.11 d, which is consistent with the denser polymer layer inferred from the lower ΔD shifts observed for the cohesive OVD in the QCM-D experiments from Chapter 4. The EDX analysis, as with the control particles, displayed a weak silicon and a strong oxygen signal. In this case, a significant carbon signal was observed, which suggests the presence of a polymer coating.

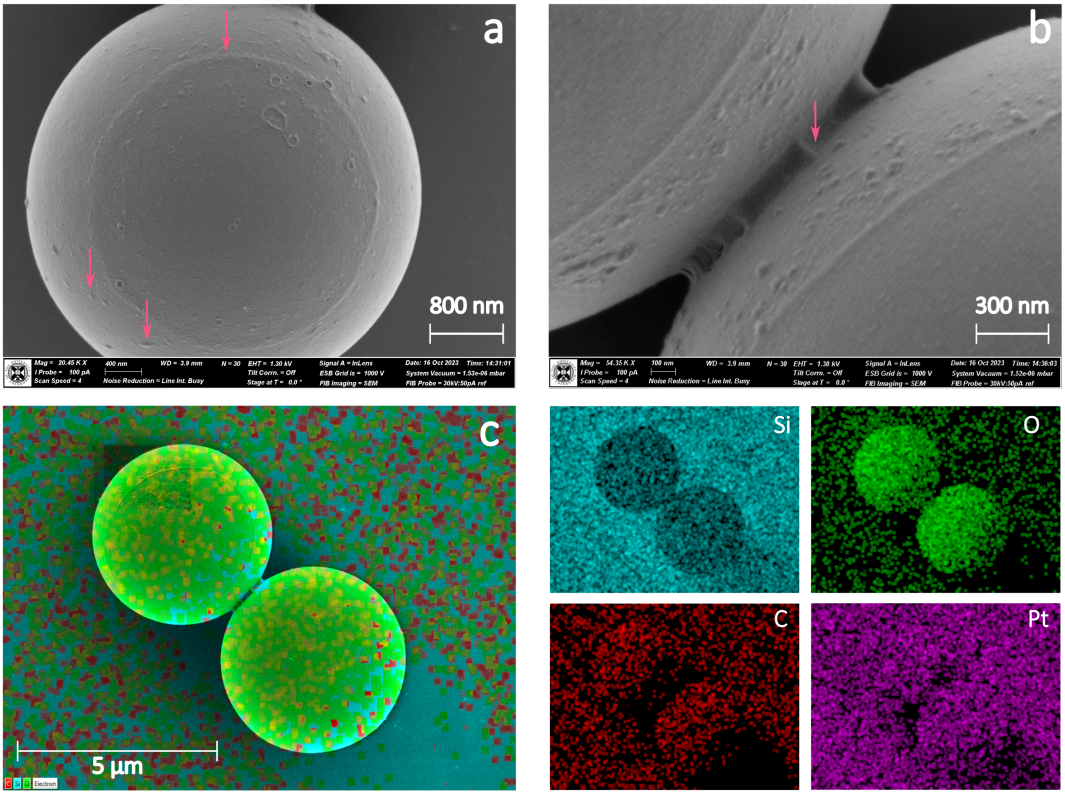

Figure 5.12 *SEM images (a, b) and EDX analysis (c) of silica particles coated with Hyaplus, a cohesive OVD. The right hand panel of (c) shows signal from Si (turquoise), O (green), C (red) and Pt (magenta). The left hand panel of (c) is a combination of all four. Arrows point towards globular structures similar to those observed with AFM and a coffee-ring effect attributed to the drying process (a), and HA acting as a glue at the interface between neighbouring particles (b). The particles were coated with platinum prior to imaging.*

The OVD coatings looked more similar under SEM than AFM. As explained in

Section 5.3.1, the AFM images may be convoluted due to a tip contamination. Additionally, in SEM, the drying process during sample preparation leads to a structural collapse. Conversely, AFM imaging is performed on hydrated polymer layers in solution, which maintain their structural integrity. We also imaged the particles using Cryo-SEM, which should provide more of an insight into the coating conformation in solution. The image of control particles (bare and APTES-coated) can be found on Figure 5.13.

As with SEM, the bare particles looked smooth in Cryo-SEM (Figure 5.13 a, b). The grains seen on the surface of the particles were attributed to the platinum coating. In addition to particles sticking out of the ice, some craters indicated where particles were before the ice was fractured as part of sample preparation, as indicated by an arrow in Figure 5.13 b.

Some APTES-coated particles displayed surface roughness (arrow in Figure 5.13 c) which could either be ice or aggregates of the coating itself. When left under the beam for a few seconds, whilst some of it appeared to be melting, the rest was not affected, which suggests there was more than just ice. The coating was not homogeneous, however it may have been partially ripped from the particle during sample preparation. The EDX silicon signal was strong with these particles (Figure 5.13 e), whereas it was weak when observed under classical SEM (Figure 5.10 c). The reason is that the background in this measurement was ice, which saturated the oxygen signal, whereas the sample holder for the latter was a silicon wafer. The carbon and platinum signals were both uniformly distributed, which suggests that the APTES coating may have again been too thin for EDX to pick up its carbon signal.

We then imaged the OVD-functionalised silica particles, starting with the dispersive OVD Hyadel (Figure 5.14).

Two types of structures were visible on the surface: spherical globules and linear filaments. We measured the radius of 50 globules from the image in Figure 5.14 a, and found an average value of 59 ± 15 nm, which is comparable to the 75 ± 25 nm features observed with AFM topography on Figure 5.8. Highly hydrated samples such as polymer hydrogels can experience ice damage during the freezing step of sample preparation [145]. High pressure freezing can avoid this phenomenon, but we did not have access to such an equipment. The growing ice crystals have the potential to expand and compress other structures such as polymers, which can

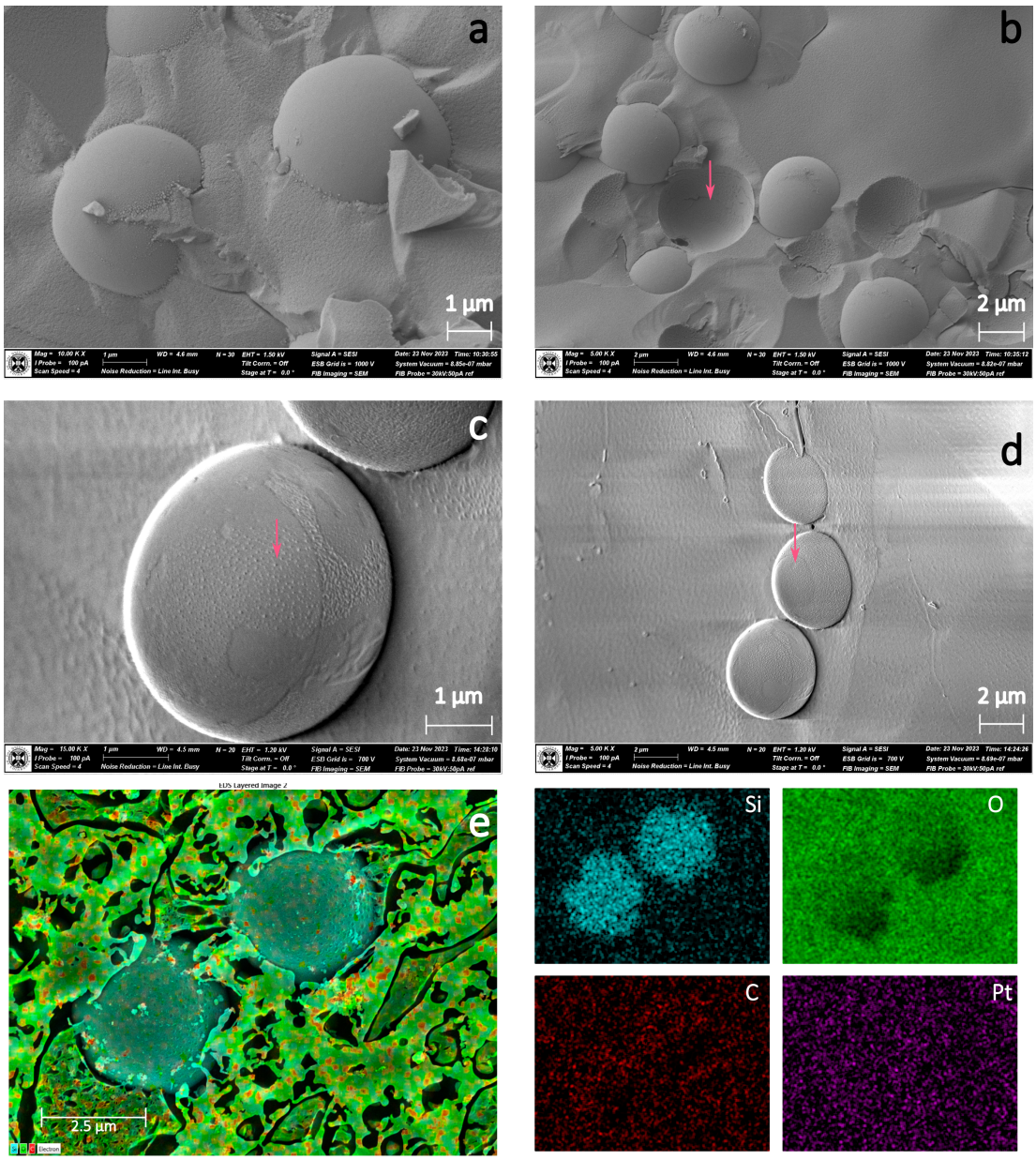

Figure 5.13 *Cryo-SEM images and EDX analysis of bare (a, b) or APTES-coated (c, d, e) silica particles. The right hand panel of (e) shows signal from Si (turquoise), O (green), C (red) and Pt (magenta). The left hand panel of (e) is a combination of all four. Arrows point towards a crater (b), the APTES coating (c), and a coffee-ring (d). The particles were coated with platinum prior to imaging.*

lead to the formation of dense globules, as if in a bad solvent. This effect explains the smaller size observed with CryoSEM compared to AFM. To get additional information on the nature of these structures, we beamed a section for several seconds (rectangle in Figure 5.14 b). Instead of melting, which would be expected if the structures were made of ice, we observed cracks and structural collapse.

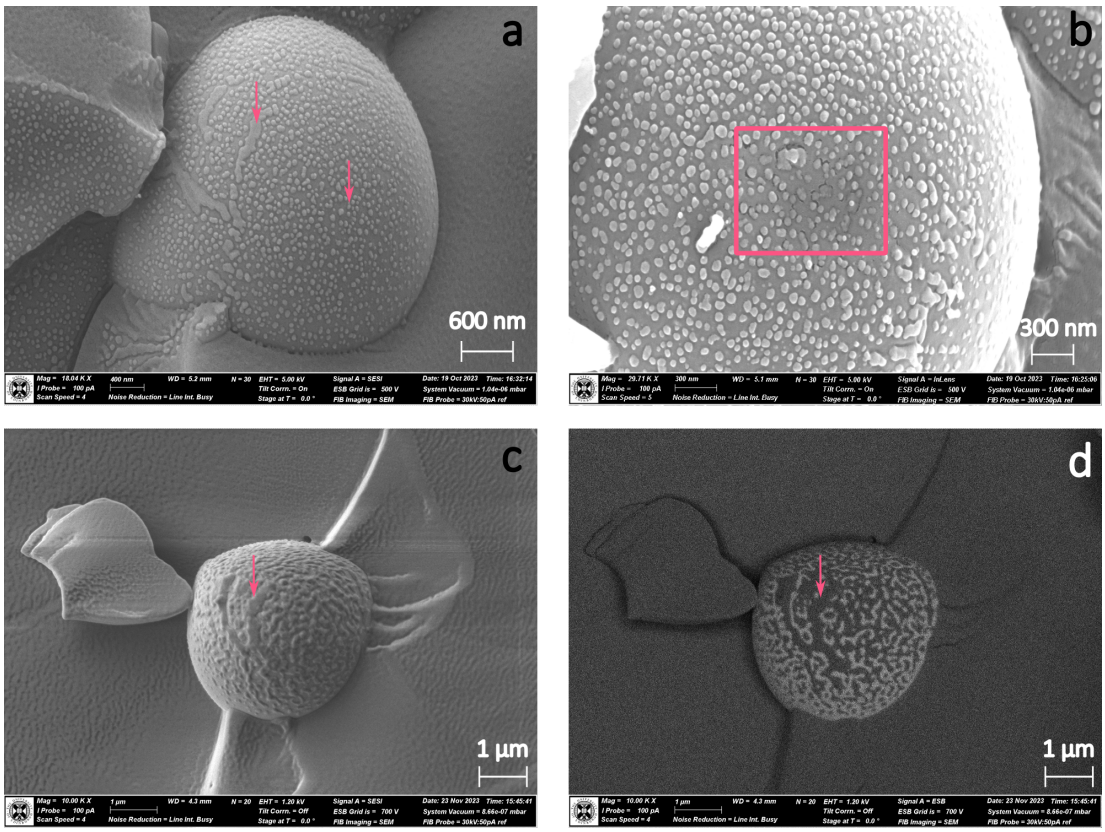

Figure 5.14 *Cryo-SEM images of silica particles coated with Hyadel, a dispersive OVD. The arrows point towards two types of surface nanostructures: HA globules and filaments (a, c, d). The rectangle in (b) is an area which was beamed for several seconds to check the structures were not purely ice. (c) and (d) were imaged without prior platinum coating of the sample in order to map their surface composition using back-scattered electrons.*

In a second measurement, we observed the beads without adding a platinum coating (Figure 5.14 c, d). Whilst the resolution was slightly worse due to electric charge build-up, it had the advantage of letting us use back-scattered electron imaging to highlight the difference in composition (Figure 5.14 d). Heavier elements appear lighter using this imaging mode: we can see the filamentous network was made of an element lighter than the underlying silicon, but close to the oxygen background arising from the ice. Carbon and oxygen have a close atomic number (6 and 8), so they are indistinguishable from each other in this imaging mode, however it did not rule out the presence of a carbon signature as expected from the polymer. A careful examination of the shade of grey displayed by the surface globular structures suggests they had the same composition as the filaments, which is compatible with our explanation that the filaments and

globules were both HA structures.

We have used the same protocol to image particles coated with Hyaplus, a cohesive OVD, see Figure 5.15.

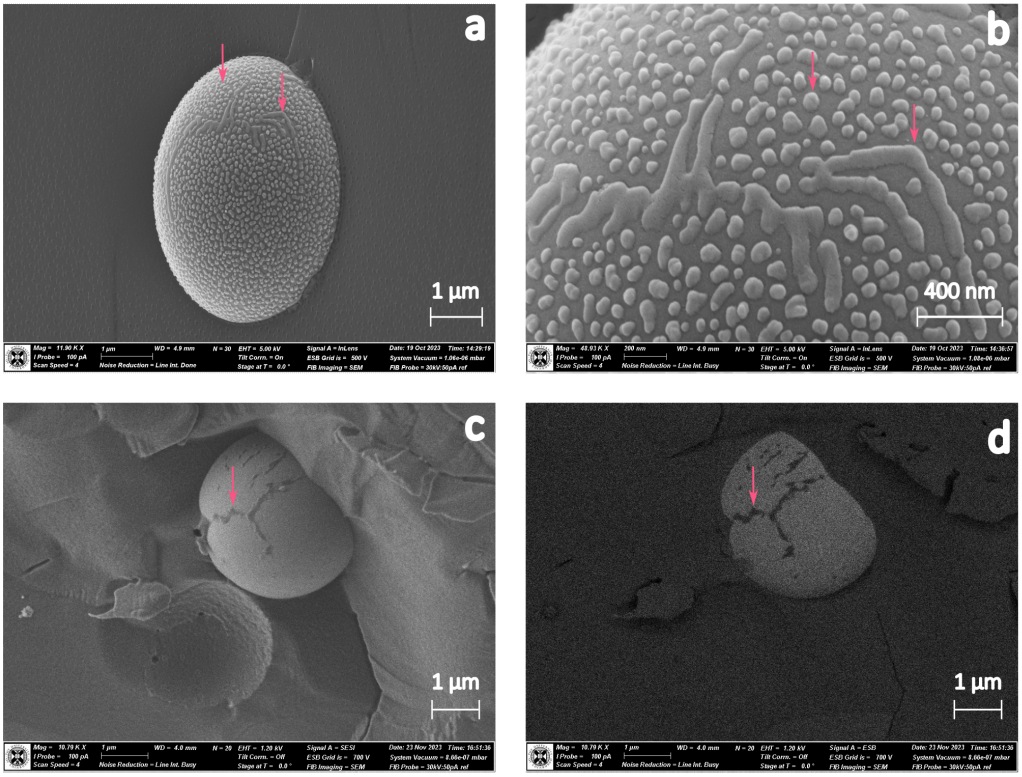

Figure 5.15 *Cryo-SEM images of silica particles coated with Hyaplus, a cohesive OVD. The arrows point towards two types of surface nanostructures: HA globules and filaments. (c) and (d) were imaged without prior platinum coating of the sample in order to map their surface composition using back-scattered electrons.*

Here again, we found similar patterns as we did with Hyaplus on Figure 5.14, with the particle surface presenting globules and filaments, indicated by arrows. The average radius of 50 globules from Figure 5.15 a was 85 $\pm$ 31 nm, which is remarkably consistent with the value obtained from AFM imaging in Figure 5.8. This is slightly higher than the radius of the globules identified in Figure 5.14, which is consistent with the three times higher molecular weight of the cohesive OVD. If we take the case where HA adsorbs as globules, as if in a bad solvent, the Flory theory of polymer chains predicts that $R_g \propto \sqrt[3]{M_w}$, where M_w is the molecular weight. Here, it is precisely the case as the ratio of R_g for Hyaplus and Hyadel is $\frac{85}{59} = 1.4 = \sqrt[3]{\frac{3}{1}}$.

When they were not coated with platinum (Figure 5.15 c, d), we imaged the particles with back-scattered electron, which revealed the filaments and the globules were composed of an element lighter than silicon, which could either be carbon (darker than the background) or oxygen (similar to the background).

To conclude, SEM and Cryo-SEM allowed us to check that the coating protocol allowed the attachment of HA to the silica particle, complementing the information gathered with AFM imaging. The OVD-functionalised particles were visibly different from control particles, either bare or coated with APTES. SEM revealed that HA had a tendency to accumulate at the interface between neighbouring particles, holding them together. Cryo-SEM allowed us to image the surface topography with an increased resolution. HA appeared to form either separated globules or longer filaments. Although the differences between both OVD coatings were subtle, we were able to identify a denser coating for Hyadel in SEM, whilst the globules observed with CryoSEM were smaller on average compared to the ones on the particle functionalised with Hyaplus. The main pitfall of this experiment is the fact that the sample preparation (drying, freezing, sublimation, fracture) had an impact on the particle surface.

5.4 Adhesion of the OVD Network to Biomimetic Substrates: Colloidal Probe AFM

Now that we have characterised both the biomimetic substrates and the OVD-functionalised silica, we can move on to the measurement of AFM force maps. This study aimed to investigate the strength of the interaction between OVDs and substrates functionalised with a variety of biopolymers, chosen to be representative of the functionalities found at the surface of corneal endothelium. We sought to relate these interaction strengths to the aspiration behaviour and protective ability of OVDs during phacoemulsification. The minimum in the force profiles, such as the ones presented in Figure 5.16, correspond to what we refer to as the adhesion force of the system (F_{adh}). By integrating the force with respect to the separation, we obtain the work of adhesion of the system (W_{adh}) , which is the work needed to completely separate the polymer-coated colloidal probe from the substrate. In this section, we will start by studying the different force profiles and the implications for the polymer detachment process. We will then apply the

worm-like chain (WLC) model to the results to get some more insight into the physical properties of the polymer. Lastly, we will compare the average values of F_{adh} and W_{adh} measured for the different substrates, as well as the impact of probe speed and dwelling time on the surface.

5.4.1 Force-Distance AFM Curves: Sawtooth-Pattern

We recorded AFM force curves between the OVD-functionalised colloidal probe and substrates with six different functionalities (gold, glass, PLGA, PLL, mucin and HA from OVDs) at four different probe speeds (1, 2.5, 5 and 10 µm.s^{-1}) and two residence times on the surface (0 or 1 s at 2.5 µm.s^{-1}). Each set of conditions was measured in triplicate. We noticed the existence of 3 identifiable patterns in these measurements. The patterns remained largely consistent over all force profiles within a given 8 × 8 map, which allows us to classify a whole map according to a type of profile. Example force curves following these patterns can be found on Figure 5.16 for dispersive Hyadel (a) and cohesive Hyaplus (b) on glass, as well as Hyadel on a Hyadel-functionalised slide (c).

In all cases, the interacting force between the approaching cantilever and the substrate is initially zero, until the cantilever experiences a hard wall repulsion upon contact, as seen on the approach curve. On the example shown on Figure 5.16 a, Hyadel displayed a wide, broad peak at low distance followed by an isolated spike of a lower magnitude at a higher distance, which are indicated by arrows. It can be noted that the wide peak is composed of several spikes. On the other hand, the Hyaplus example (Figure 5.16 b) displayed a succession of spikes of similar magnitudes, also indicated by an arrow. We will refer to each individual spike as an adhesion spike, and to both these profiles as sawtooth patterns. In addition to these sawtooth patterns, there were certain occasions where very little to no adhesion was seen the retract curve, like the one shown on Figure 5.16 c.

In the sawtooth pattern examples depicted in Figure 5.16 a and 5.16 b, the retract curve displays negative values, showing an attraction between the cantilever and the substrate. This attractive force was measured over a long range (several micrometers) upon retracting the probe. Interestingly, the range of the interaction is consistent with the polymer expected contour length (represented by the black dashed line) which can be easily calculated. The number of monomer units on a

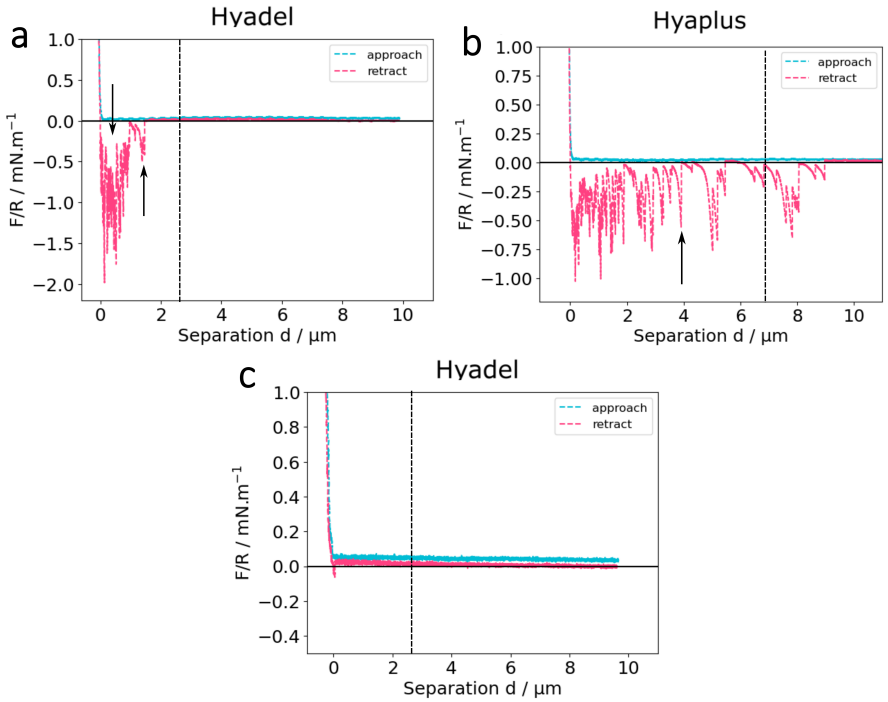

Figure 5.16 *AFM force curve of a colloidal probe functionalised with dispersive Hyadel (top left) or cohesive Hyaplus (top right) interacting with glass measured at a probe speed of 1 µm.s^{-1}. These profiles are referred to as type A and type B, respectively. Their origin is discussed in the text. The bottom curve corresponds to a limiting case (type C) where little to no adhesion was seen, this time for Hyadel on a Hyadel-functionalised slide at 5 µm.s^{-1}. The dotted line corresponds to the expected polymer contour length. The force profiles were normalised by dividing by the radius of the particle.*

polymer chain can be obtained by dividing the polymer molecular weight by that of the monomer unit (379 g.mol^{-1}). From there, as each monomer unit is about 1 nm long [146], we expect the extended polymer chain to be 2.6 µm long for Hyadel and 7.6 µm for Hyaplus. This is consistent with the interaction measured being indeed due to HA and not to the underlying silica particle nor the silane coating.

Sawtooth patterns have previously been observed for force profiles measured for biopolymers such as the protein titin [147]. In their work, Rief *et al.* attributed the existence of these highly non-linear dynamics to the unfolding of individual protein domains. In the case of HA, although it is a linear polymer unlikely to have a defined sequence of domains, it may have some localised folded structures or entanglement knots. In particular, several studies on HA highlight the formation of a macroscopic anti-parallel helix in solution, even from

low concentrations [140]. These knots would unravel as the probe stretches the polymer chain by moving away from the surface. This will be discussed further in Section 5.4.2.

The literature also mentions sawtooth profiles in the case of polymer chains, and suggests that each single spike corresponds to a monomer detachment from the surface, or specific adhesion, if the removal rate is significantly faster than the internal dynamics of the bond [148–150]. It follows that the higher number of individual spikes in the type B profile would point towards slower internal dynamics of the polymer chain. The distance between spikes was reported to correspond to the distance between anchoring sites on the surface. On the other hand, wider peaks such as the one identified on the Hyadel example were reported to correspond to an unspecific adhesion, whereby multiple polymer segments are detached at the same time. The sawtooth patterns are likely to reflect a combination of effects, where the detachment of anchoring points on the substrate leads to the unravelling of some supramolecular structures. We classified every force map, composed of 8×8 force profiles, into one of the three types described previously. The results are presented in Table 5.1.

Profile type	Hyadel	Hyaplus
Type A	47	24
Type B	32	41
Type C	11	17

Table 5.1 *All the AFM force maps were attributed one of the three typical profiles shown on Figure 5.16. The first one (Type A) corresponds to a wide proximal peak followed by occasional spikes of a lower magnitude, like the Hyadel example on Figure 5.16 a. Type B corresponds to a succession of spikes of a similar magnitude, like the Hyaplus example on Figure 5.16 b. Type C displayed less than two spikes and the force stayed close to zero throughout the whole extension of the probe, like the Hyadel example on Figure 5.16 c.*

The results in Table 5.1 reveal that although both type A and type B sawtooth patterns could be found for either OVD, Hyadel was more likely to follow a type A pattern. On the other hand, Hyaplus was more likely to follow a type B pattern. As noted earlier, this type of profile is expected for slower polymer dynamics, which is consistent with the slower relaxation time of Hyaplus (32 ms) compared to Hyadel (3.5 ms) measured by extension rheology [151]. This result suggests that the two OVDs follow different detachment dynamics: our interpretation

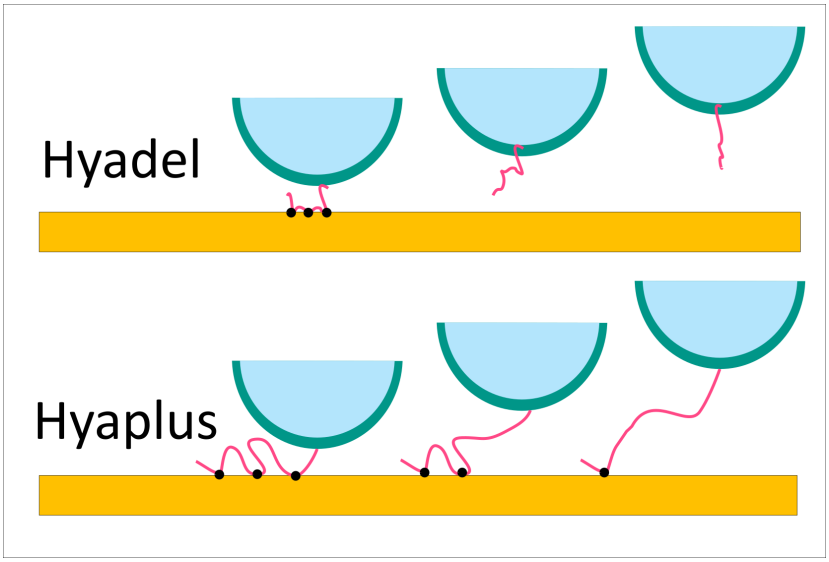

Figure 5.17 *Schematic representation of the type A AFM force profile in Figure 5.16 a and mostly observed for Hyadel (upper panel), compared to the type B AFM force profile in Figure 5.16 b and favoured by Hyaplus (lower panel). Type A corresponds to the simultaneous rupture of several attachment points on the surface whereas type B is the consecutive rupture of single attachment points.*

is that Hyadel desorption happens via the simultaneous rupture of multiple tethering points on the surface. This results in a wide proximal peak at low distances, which is a sum of the forces associated with the detachment of these tethering points. On the other hand, for Hyaplus, there is a release of tension at longer distances, such that the force goes to zero, which points towards a sequential rupture of individual anchoring points on the surface. This difference in behaviour is similar to the one observed for hydrolysed polyacrylamide on calcium carbonate [150], where the polymer went from a type A to a type B profile when increasing the molecular weight. This detachment mechanism is compatible with the adsorbed configuration proposed for entangled HA in Section 5.3.1. We suggested that cohesive OVDs adsorb as collapsed mushrooms, with anchoring points standing further apart from one another than dispersive OVDs, which adsorb in a brush-like configuration. In that situation, the cohesive OVD will be more likely to stretch between attachment points. This is represented on Figure 5.17.

Our AFM experiment consists in pulling off polymer coils from a substrate. It results that the bonds have to be broken at the surface rather than inside the polymer network, which is equivalent to forcing an adhesive failure mechanism. In

the case of Hyadel, which mostly follows a type A profile, this requires crossing an energy barrier corresponding to the work of adhesion of the proximal wide peak presented on Figure 5.16 a. Conversely, Hyaplus mostly follows a type B profile, which is composed of a succession of individual spikes, which individually represent a lesser work of adhesion. Because of this energy barrier, adhesive failure may not be the favoured mechanism in practise, which agrees well with the cohesive failure upon aspiration which has been reported by cataract surgeons.

The force curves measured on the OVD-functionalised glass slide predominantly followed the type C profile depicted in Figure 5.16, indicating a very weak interaction. Our interpretation is that the contact time between HA attached to the AFM probe and HA chemisorbed on the substrate was not long enough to allow any polymer entanglement. It would be interesting to extend the dwelling time on the surface in a future experiment. In this situation, retracting the probe would require breaking the internal bonds of the polymer network, which is comparable to a cohesive failure mechanism. Comparing the magnitude of the resulting F_{adh} and W_{adh} to the ones measured on other substrates could assess the likeliness of cohesive failure over adhesive failure, and see how it compares to the observations reported by surgeons.

Figure 5.18 a is a heatmap representing the number of adhesion spikes observed for each curve on a 8×8 AFM force map in the case of the type A Hyadel graph from Figure 5.16 a. Likewise, Figure 5.18 c is the equivalent for the type B Hyaplus graph from Figure 5.16 b. The corresponding F_{adh} and W_{adh} are plotted on Figure 5.18 b and Figure 5.18 d for each force curve on the map.

Despite some variability arising from the stochastic effects of surface roughness or polymer conformation, the number of spikes does not appear to be steadily decreasing over time as consecutive measurements are made across the grid. Likewise, the values of F_{adh} and W_{adh} stay consistent throughout the experiment. This suggests that the stretching deformation associated with retracting the probe at each point was reversible in the timeframe between measurements, and did not yield an irreversible plastic deformation. This is consistent with the polymer relaxation time ($\lambda \approx 3.5$ ms for Hyadel and $\lambda \approx 32$ ms for Hyaplus [151]) being quicker than the measurement repetition rate across the map. It is reasonable to infer that the polymers are adopting similar conformations on each subsequent measurement. For this reason, the assumption of each individual force curve on the map being independent from the previous ones, which we have made

throughout, is indeed justified. The analysis confirms the expectation from visual inspection of Figure 5.16 that a type A profile comprises fewer individual adhesion spikes. A comparison between both classes of OVDs will be discussed in Section 5.4.2 and Section 5.4.3.

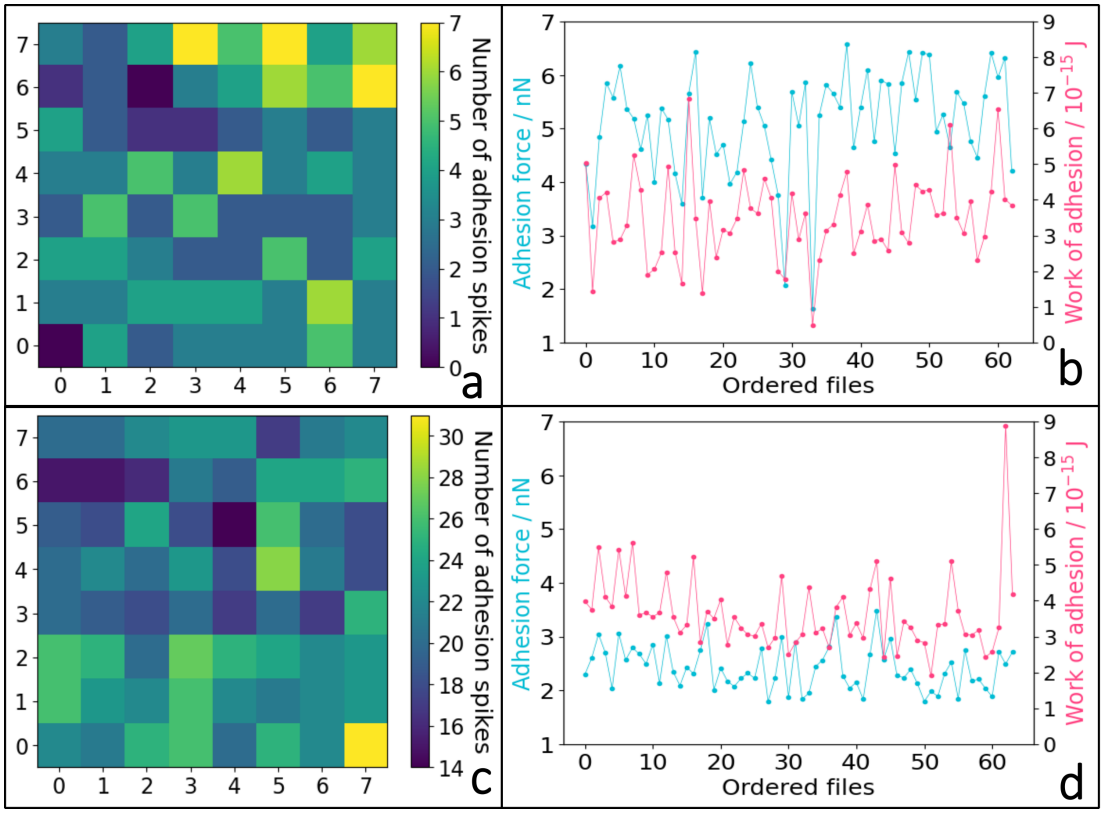

Figure 5.18 *Heatmap representing the number of adhesion spikes for each point on the force map (left panel) for Hyadel (a) and Hyaplus (c). Note the difference in scale between the Hyadel and Hyaplus plots, indicating a difference in the number of adhesion spikes. The map starts on the bottom left, then scans to the right, goes up to the second row which is scanned to the left, etc. The adhesion force (blue) and work of adhesion (pink) for each point on the map is plotted on the right panel for Hyadel (b) and Hyaplus (d).*

5.4.2 Worm-like Chain Model

Each of the adhesion spikes described in the previous section were fitted to a worm-like chain model (WLC), as shown in Figure 5.19 a. This mathematical model is used to predict the dynamics of a semi-flexible polymer behaving as a thin rod. It yields two parameters of interest, namely the contour length (L) and persistence length (b). The former is the length of the polymer chain at maximum extension, whilst the latter is the maximum length where the conformations of the first and last monomer are correlated (which is half the Kuhn length). The lower the persistence length, the higher the flexibility. We defined an adhesion spike (like the example on Figure 5.19 a) as a portion of the curve which is negative, contains at least 50 datapoints, and has a prominence of $\frac{F}{R} \geq 0.2$ mN.m^{-1} (the prominence being the amplitude between the lowest point and the highest point on the y axis), in order to overcome the noise level. We also checked that the force F obtained with the WLC fit (equation 2.20) was at least 0.03 nN in amplitude and did not go below -10 nN, as we found from examining hundreds of force profiles that taking these criteria allowed us to discard the most commonly observed poor fits. The corresponding Python code I wrote is included in Appendix D. As discussed for Figure 5.16 a, the wide proximal peak on the type A profile appear to be composed of a succession of individual WLC spikes, however it was not possible to use them in our fit because of the very low number of data points yielding a poor result.

The physical significance of the persistence and contour length obtained from the WLC fit needs to be considered. The physical behaviour of a polymer chain is more complex than the simple sum of the intrinsic mechanical properties of each monomer, and the mesoscale organisation is a determinant factor for the macroscopic properties. For instance here, even though HA is a linear polymer, the AFM force curves on Figure 5.16 a and Figure 5.16 b present a series of spikes which can be fitted to the WLC model. This suggests the existence of a complex three-dimensional geometry, with some thick domains unravelling sequentially as attachment points are broken from retracting the probe. We can extract values of b and L for each of these domains.

The contour length L obtained for each spike corresponds to the length of polymer chain extended as the probe is retracting, which is expected to increase at each unravelling event. The meaning of the persistence length b is more subtle. It

does not directly describe the flexibility of the whole polymer chain, but rather that of globular subunits. Additionally, it has been suggested that for polymer chains, the hierarchical organisation of these subunits, for instance the separation between adjacent globules, influences the value of persistence length [152].

We fitted every spike from each force profile making up each map to the WLC model. The plots in Figure 5.19 are histograms reflecting the distribution of the parameters yielded by this analysis: the spike force (b) as well as the contour (c) and persistence length (d), the measurements were done on a glass substrate at a probe speed of 1 µm.s^{-1} and immediate retraction. A similar analysis on the other substrates at the other speeds measured can be found in Appendix F.1. Figure 5.20 represents the consecutive values of b and L obtained for the first ten curves of the maps from Figure 5.18 a and Figure 5.18 c.

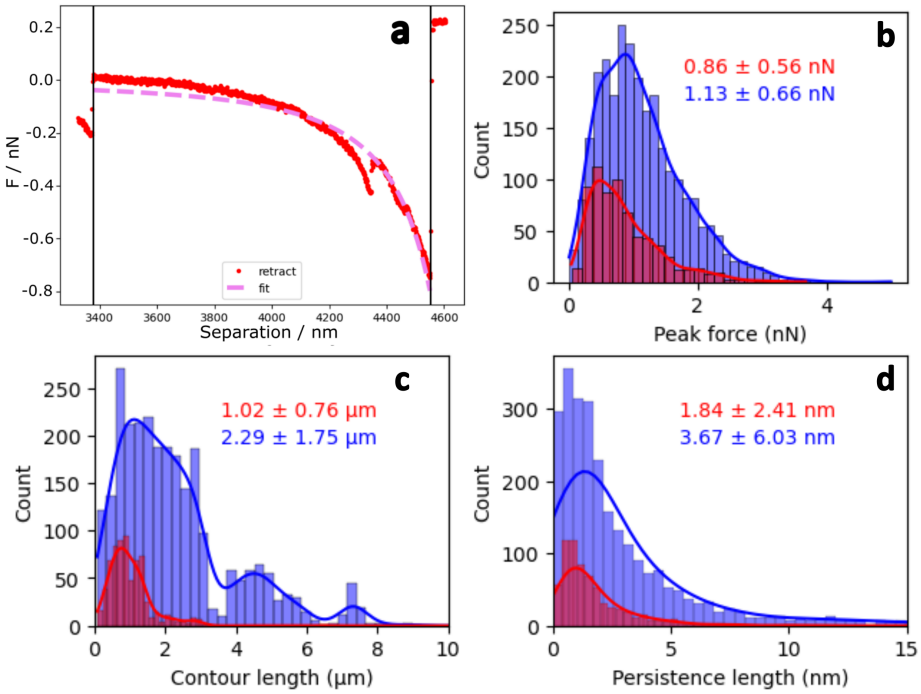

Figure 5.19 *Example WLC fit of a single adhesion spike (a) and histogram representing the distribution of parameters obtained from WLC fits for cohesive Hyaplus (blue) and dispersive Hyadel (red) on glass with a probe speed of 1 µm.s^{-1}: spike adhesion force (b), contour length (c), persistence length (d). The average value and standard deviation are written in the top right corner. Similar figures at the other speeds and substrates can be found in Appendix F.1.*

The number of spikes was generally higher in the case of Hyaplus, as can be seen by the higher count. This was predictable from the OVD's higher molecular weight, as well as its tendency to form a type B profile with multiple individual

spikes, as discussed on Figure 5.18. The individual peak forces had a comparable distribution for both OVDs, albeit slightly higher for Hyaplus. In other words, detaching individual segments of the HA polymer chain requires comparable forces on average, regardless of the adhesive or cohesive classification, which in turn depends on the polymer molecular weight.

The contour length had a wider distribution for Hyaplus, which again makes sense with regard to its higher molecular weight leading to a longer chain. A longer chain has more configurations for segments to attach on the surface of the silica particle, which results in more polydispersity in the contour length determined from the WLC model. One can note that the fitted contour length for either OVD was generally smaller than or equal to the expected contour length at full extension obtained from the calculation previously detailed, and plotted as a dashed line in Figure 5.16. This is likely to reflect that the polymer chains were not necessarily attached to the substrate by their extremity. The presence of three local maxima (2 µm, 4.5 µm and 7.5 µm) in the case of Hyaplus is interesting, and seems to indicate that the HA chain is preferentially attached at certain locations.

In their AFM study about titin, Rief *et al.* observed a clear periodicity of WLC spikes with regard to the probe extension [147]. As a result, the contour length yielded from the model increased by the same amount at each unfolding, which can be linked to the sequence of amino acids expected for each domain. This reflects the systematic packing of the protein into the same 3D structure. There was not a clear periodicity of WLC spikes in our experiment, and in turn the contour length did not increase by the same amount at each detachment, as illustrated on Figure 5.20. This is to be expected, as the local folding of sub-units on HA is likely to be more stochastic than it is for a protein like titin, where the defined sequence of aminoacids leads to a predictable macromolecular configuration. There were however some local maxima for Hyaplus, visible on Figure 5.19 c, which indicates a preferred attachment at certain locations on the polymer coil.

In their titin study, the authors observed a systematic decrease of the persistence length at each domain unfolding. This is a consequence of the protein becoming more flexible as the domains unravelled. Additionally, the spike force increased at each unfolding spike, which they attributed to the domains unravelling in strength order. In our case, the persistence length obtained from the fit fluctuates in a

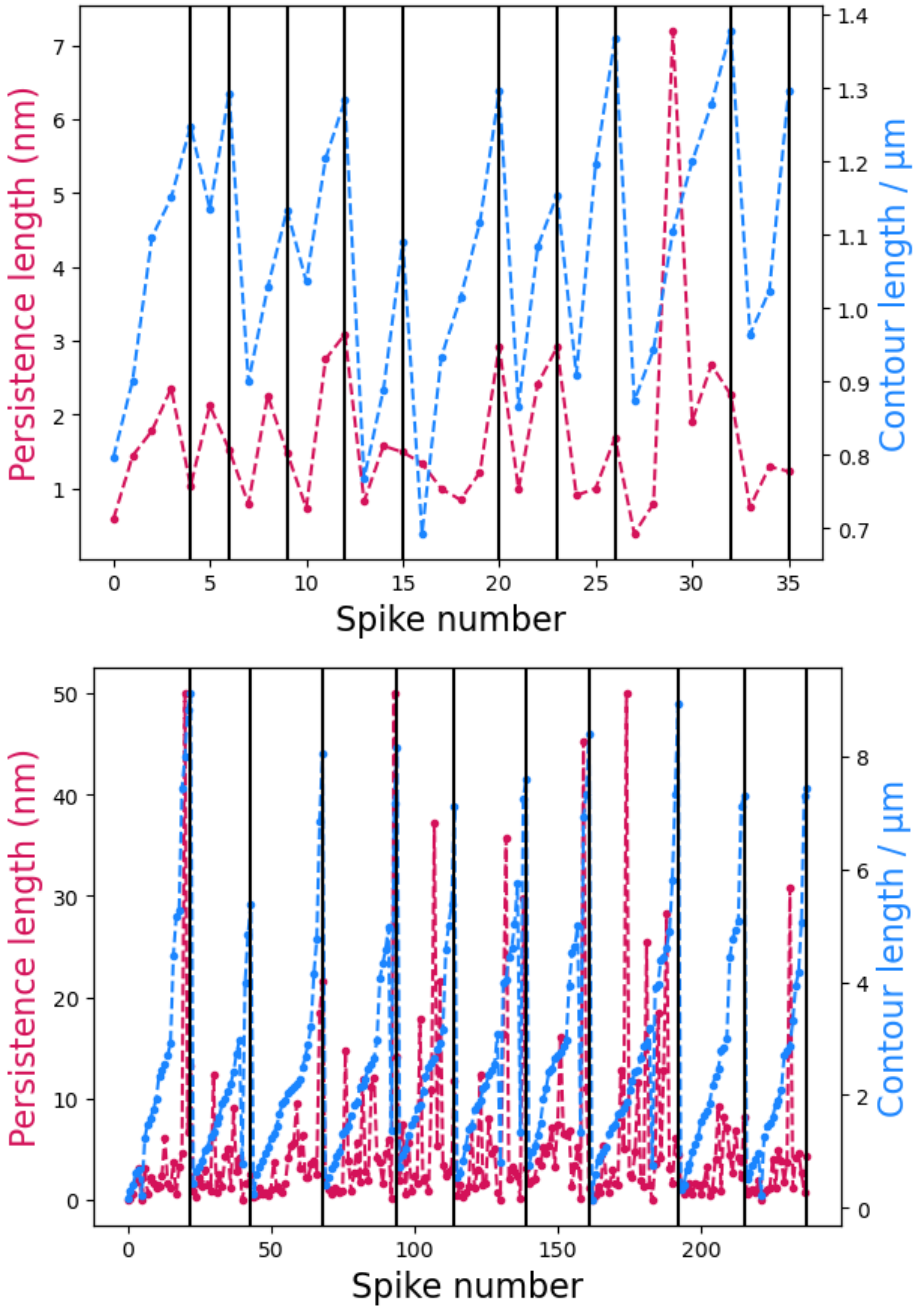

Figure 5.20 *Evolution of the persistence length b (pink) and contour length L (blue) at each consecutive spike for the first ten force curves of the type A Hyadel profile displayed in Figure 5.16 a (upper panel) and the type B Hyaplus profile displayed in Figure 5.16 b (lower panel). Each vertical line corresponds to the next force curve on the map.*

non-monotonic way across the consecutive spikes, as seen on Figure 5.20, and the spike force did not increase at each spike. This shows that the persistence length obtained did not reflect the flexibility of the whole polymer chain, but rather that of a localised structure. It also suggests the domains were not unravelled in a

specific order based on their intrinsic flexibility or strength.

The persistence length observed on Figure 5.19 d was quite low for both OVDs, no more than a few nm on average. That would suggest the polymer chain is very flexible, and any change to a sub-unit conformation only affects the few neighbouring monomer units, leaving the vast majority of the chain undisturbed. This high chain flexibility can be linked back to phacoemulsification, where both classes of OVDs are designed to sustain a significant shear stress during the operation. Small values of persistence length are typically obtained from WLC fits, sometimes even lower than the size of an individual monomer. For the case of HA specifically, coarse-grain modelling studies suggest the persistence length reaches a peak value for a molecular weight above 65 kDa. The limiting value depends on the ionic strength and temperature, and are predicted to be close to 7.5 nm for the conditions used in our system [153]. Persistence length values found in the literature range from 4 to 79 nm, with several studies obtaining results close to 4 nm [146].

The distribution of persistence length observed on Figure 5.19 d also points out some variability in the flexibility of subdomains between OVDs. Hyadel yielded a lower value on average, suggesting a more flexible configuration. The enhanced flexibility of the dispersive OVD allows it to deform and rearrange more effectively under stress, leading to more modes in which energy can be dissipated. This was already suggested with QCM-D measurements in Chapter 4, where the layer of dispersive OVD dissipated more energy than the corresponding layer of cohesive OVD. This characteristic likely contributes to its superior ability to protect the endothelium *in vivo*.

A study by Hanson *et al.* describes polymers as structures composed of a succession of thick globular subunits separated by thin linkers [152].The authors demonstrate that for long linkers, the persistence length of the system is primarily influenced by the linker stiffness, resulting in a flexible polymer. On the contrary, with short linkers, the stiffness is governed by the globular unit, yielding a more rigid or semi-flexible chain. In our study, this interpretation would imply that the small persistence length is due to adjacent folded domains separated by long, flexible linkers. This is reasonable to expect for a polymer coil extended in a good solvent.

The observations discussed in this section remained largely consistent on the measurements performed at various speeds and on different substrates, as shown on the figures in Appendix F.2.

5.4.3 Adhesion Force and Work of Adhesion

In this section, we will unpack the average values of F_{adh} and W_{adh} obtained on the different biomimetic substrates with a range of probe speeds and residence time on the surface. As de Gennes was studying how to translate concepts of polymer physics to cell adhesion, he postulated that the parameter of interest for intrinsic adhesion strength of a material was the energy per unit area G required to separate them [154]. The separation force and energy are related, however the former is dependent upon the thickness of the adhesive layer. To translate W_{adh} into an energy per unit area, we need an estimate of contact area between the polymer and the substrate. The Johnson-Kendall-Roberts (JKR) model is used in adhesion physics to link the pull-off force $F_{pull-off}$ to G using equation 5.1 [155]:

$$F_{pull-off} = \frac{3\pi\ R\ G}{2} \tag{5.1}$$

where R is the contact radius. However, equation 5.1 is only valid if the contact area and the probe displacement follow the JKR interaction potential [156]. The sawtooth type A and type B profiles plotted in Figure 5.16 a and Figure 5.16 b do not possess such a shape. In order to estimate a value of G, we will instead use our measured values of W_{adh}, and use Figure 5.11 b and Figure 5.12 b to estimate the contact area between HA-functionalised silica beads. We obtain a radius of contact of 560 and 540 nm for Hyadel and Hyaplus, respectively, and we use equation 5.2 to calculate G.

$$G = \frac{W_{adh}}{\pi\ R^2} \tag{5.2}$$

Equation 5.2 yields $G = 1.1(10)$ mJ.m^{-2} for Hyadel, and $G = 2.6(9)$ mJ.m^{-2} for Hyaplus. These values are much smaller than those reported for polymer adhesives ($G \approx 75$ J.m^{-2} [157]). Nevertheless, they are of the same order of magnitude as those determined for robust bioadhesive bridging interactions mediated by mussel foot protein [158]. The force profiles clearly indicate that HA molecules act as long connectors between the silica particle and the underlying

substrate. By making an analogy to the role of connector molecules in joining polymer interfaces, de Gennes suggested that the energy could be written as [154]:

$$G \approx \nu \; N \; U \tag{5.3}$$

where ν is the number of chains per unit area, N is the degree of polymerisation of the connector, and U is the energy of interaction between the polymer and the substrate, which we assume to be close to $k_B T$.

In Section 5.3.2, we associated each of the globular structures to a collapsed HA chain. Examining Figures 5.14 and 5.15, one can estimate an area per chain $s^2 = 4 \cdot 10^{-15}$ m^2 for both OVDs, or similarly $\nu = 2 \cdot 10^{14}$ chains.m^{-2}. As discussed in Section 5.4.1, N is about 7600 for Hyaplus and 2600 for Hyadel, and is obtained by dividing the molecular weight of the polymer chain by that of the monomer unit. With equation 5.3, we therefore obtain 3 mJ.m^{-2} for Hyadel and 7 mJ.m^{-2} for Hyaplus, which are in the same order of magnitude as the values calculated from equation 5.2.

Effect of probe speed

The AFM probe speed is an important parameter when considering the implications in phacoemulsification. The OVD and endothelium are subject to a range of shear stresses during the operation, which can originate from the ultrasound-induced flow or the aspiration device. This shear has the potential to induce damage to the endothelium. We can estimate the AFM strain rate by dividing the probe speed by the polymer contour length, yielding values ranging from 0.1 to 4 s^{-1}. Several articles attempted to measure the flow velocity from the ultrasounds produced by the phaco device: Steinert and Schafer measured a mean velocity of 20 mm.s^{-1} [33], whilst Oki found peak velocities ranging from 3.74 to 12.8 mm.s^{-1} depending on the settings used [34]. Given that the anterior chamber is 3 mm deep, the shear rate can be estimated to be between 1 and 7 s^{-1}, so that the AFM-induced strain rate is in the range of interest. It is also similar to the flow-induced shear rate in QCM-D, estimated in Chapter 4 (see Table C.1). One can note that this simple estimate does not take into account the geometry of the anterior chamber and the associated velocity profile, nor does it include the shear stress originating from aspirating the OVDs.

The average F_{adh} and W_{adh} were obtained from triplicates of 8×8 maps for each substrate at five different probe speeds. The results are shown on Figure 5.21, where the error bar corresponds to the standard deviation.

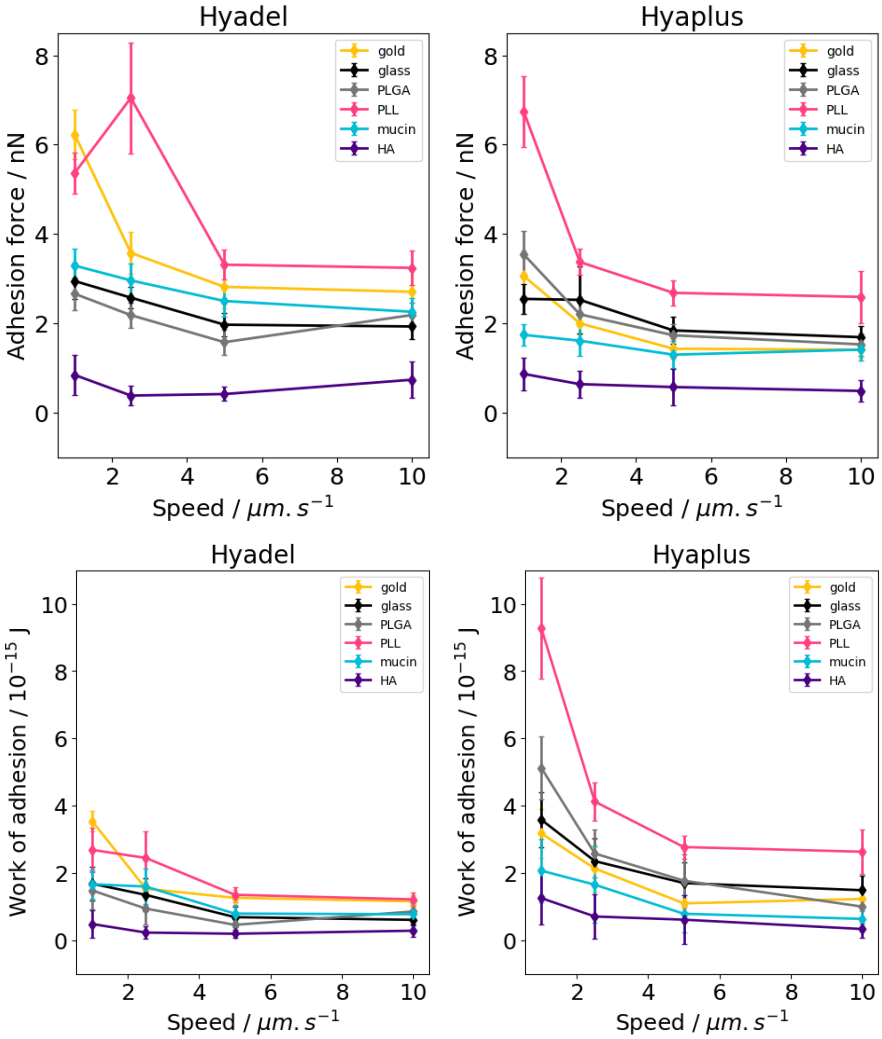

Figure 5.21 *Adhesive force (upper panel) and work of adhesion (lower panel) of OVDs as a function of probe speed for a range of surfaces. Gold (yellow), oxidised glass (black), poly-L-glutamic acid (grey), poly-L-lysine (pink), mucin (blue) and OVD (indigo). The error bars correspond to the standard deviation.*

As seen from Figure 5.21, both F_{adh} and W_{adh} had a tendency to decrease with probe speed, and mostly reached a plateau at 5 µm.s^{-1}, which would correspond to strain rates of 0.7 to 4 s^{-1}. Other studies have observed the same trend, and suggested that an increased repulsive drag force would be exerted on the cantilever at higher speed, whilst the attractive loading force would decrease [159].

F_{adh} had a similar dependence on speed for both OVDs. On the other hand, W_{adh}

displayed a weaker speed dependency for the dispersive Hyadel. We also know from rheology that it is less shear-thinning than its cohesive counterpart [151]. This implies that the polymer has a weaker tendency to rearrange and align with the flow as the shear rate increases. This increased mobility could explain why the dispersive OVD is able to withstand increased stresses compared to the cohesive OVD during phacoemulsification.

Effect of dwelling time

We also tested the effect of dwelling time on the surface by leaving the probe on the substrate for one second before retracting at 2.5 µm.s^{-1}, see Figure 5.22.

For each system, F_{adh} and W_{adh} increased with dwelling time. As the polymer stays in contact with the substrate, it has time to rearrange and make more contact points on the surface, strengthening the interaction, as discussed in Chapter 4. Again, the dispersive OVD, which is less shear-thinning, had a lower W_{adh} dependency on dwelling time.

As discussed in Chapter 1, cataract surgery is typically between 5 and 10 minutes in total. The one second dwelling time measured in this experiment cannot be extrapolated to minutes in a trivial way, however the different slopes observed when plotting W_{adh} against the dwelling time suggests that the measure of adhesion after different dwelling times on the surface merits further investigation. Although this is subject to debate, some studies suggest that a longer operation time increases the risk of endothelial cell loss [17, 160]. This risk has mostly been attributed to the longer exposure to shear stress. As we showed here, a longer dwelling time also leads to a strengthened interaction. This could potentially complicate OVD aspiration, leading the surgeons to use a higher vacuum.

Effect of substrate

As discussed previously, the surface roughness found with AFM imaging for PLL, PLGA and mucin were relatively close (Figure 5.6), which means that any differences in F_{adh} and W_{adh} measured between substrates cannot be attributed to differences in substrate roughness.

The range of W_{adh} obtained for the different substrates was wider for Hyaplus,

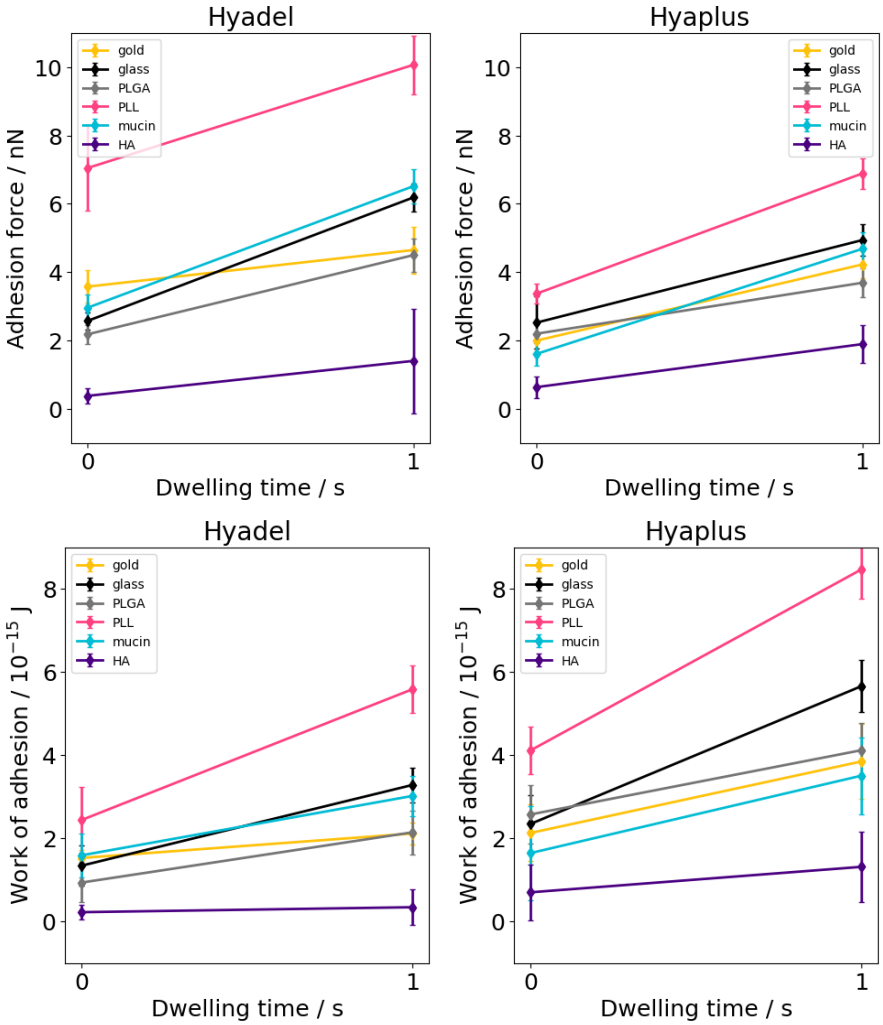

Figure 5.22 *Adhesion force (upper panel) and work of adhesion (lower panel) of OVDs with a range of surfaces as a function of dwelling time on the surface. Gold (yellow), oxidised glass (black), poly-L-glutamic acid (grey), poly-L-lysine (pink), mucin (blue) and OVD (indigo). The error bars correspond to the standard deviation.*

as seen in Figure 5.22. This points towards the defects of the interface exerting an influence, which is a characteristic of adhesive failure at the interface.

Particularly for the case of Hyaplus, an increase in dwell time leads to an increase in W_{adh}. This may be an indication of the emergence of the cohesive character of Hyaplus as entanglements form. The HA-functionalised slide was the one with the lowest adhesion. In addition to the electrostatic repulsion, the long polymer chains attached to the substrate are likely to create a steric barrier, hindering the approach and attachment of the HA attached to the colloidal probe due to unfavourable entropy. The OVD-functionalised substrate was also the least

affected by probe speed. As discussed earlier, using a longer dwelling time may be necessary in order to allow sufficient interaction of polymer coils to allow entanglement. We already start to see an increased F_{adh} after one second on the surface, although the effect remains weak.

The substrate with the highest associated F_{adh} and W_{adh} was consistently PLL, regardless of probe speed or dwelling time. As PLL is positively charged, an electrostatic attraction is expected with the negatively-charged HA. This suggests that HA will have a high affinity for the CD44 and RHAMM receptors, which are both rich in lysine residues. The RHAMM receptors also possess glutamic acid residues, which are important for binding HA. We did not find a particularly strong interaction with PLGA, possibly due to its backbone having a negative charge.

In Chapter 4, we inferred a slightly weaker but not negligible interaction of Hyadel with mucin when compared to a bare gold QCM-D sensor, which we explained by the increased steric hindrance. The results shown on Figure 5.21 suggest this applies to both OVDs. Similar to the HA-HA case, the interaction strength increases with dwell time. As mucin was our model for the glygocalyx, this suggests that HA coils could interact with the viscoelastic cell coating.

From a more general perspective, the different force profiles show that the surface interaction of HA with a range of material found in the eye is far from negligible, which calls for a more careful examination of these interface effects when studying OVDs in phacoemulsification.

Effect of molecular weight: cohesive VS dispersive

Colour plots showing F_{adh} and W_{adh} going from Hyadel to Hyaplus can be found on Figure 5.23.

When looking at the evolution of F_{adh} in Figure 5.23 table as well as F_{adh} at different probe speeds on Figure 5.21, it becomes apparent that the values obtained for either OVD are in the same ballpark regardless of the OVD used. Gold and mucin are an exception to this rule, as F_{adh} experienced a marked decrease with molecular weight. As discussed from the distribution of spike forces shown on Figure 5.19 b, this suggests that the force required to break

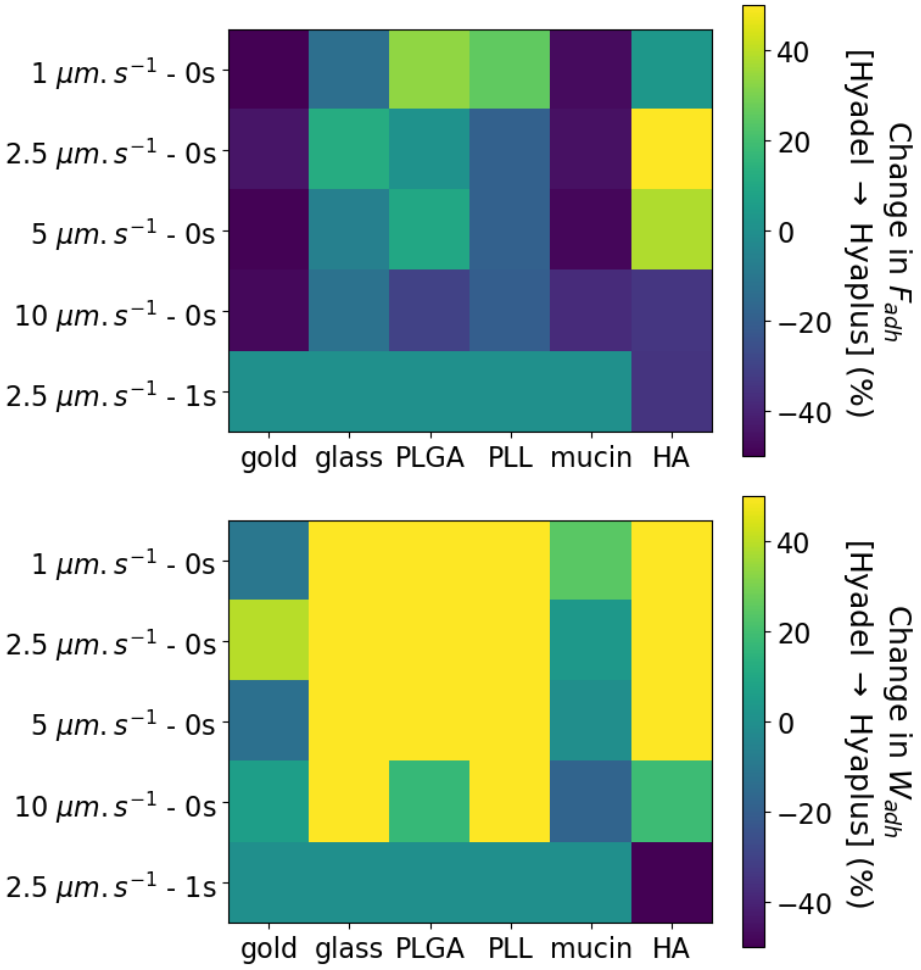

Figure 5.23 *Colour plots summarising the changes in F_{adh} (upper panel) and W_{adh} (lower panel) when going from Hyadel to Hyaplus (increasing Mw) for each substrate and speed.*

single tethering points of the polymer coil to the surface is only weakly affected by the molecular weight. It can also be noted that the results obtained with the one second dwelling time were very close for all substrates, which suggests that the longer the OVD stays on the surface, the closer the values of F_{adh} become.

As for the values of W_{adh}, they are both consistently and significantly higher for Hyaplus, which shows that despite single attachment points having a similar adhesion force, it takes more energy on average to detach the cohesive OVD from the surface when compared to the dispersive OVD. This can be understood from its higher molecular weight, enabling a single polymer coil to create a higher number of anchoring points on the surface. The previous discussion about the preferred type B (specific adhesion) profile also suggests these attachment points are further separated and detached individually. Again, the difference was

somewhat less visible with the longer dwelling time.

5.5 Conclusions

In this chapter, we prepared and characterised biomimetic substrates by adsorbing a range of biopolymers from solution. We also functionalised and characterised silica particles by chemically linking HA from either a cohesive or dispersive OVD. Using these colloids as an AFM probe, we highlighted two main profiles following a sawtooth pattern when pulling off HA from the substrates. These patterns were analysed as sequences of WLC adhesion spikes which could be related to the unravelling of structural domains as one or multiple anchoring points were detached from the substrate. We showed that despite some overlap, the dispersive Hyadel preferably ruptured several anchoring points at the same time (type A), whereas the cohesive Hyaplus had a tendency to sequentially break individual attachment points (type B). These two behaviours agree well with the configurations suggested in Chapter 4, respectively brush-like and collapsed mushroom. The spikes from either OVD displayed a similar force of adhesion, however Hyaplus generated a higher number of spikes, yielding an increased work of adhesion. Removing the cohesive OVD from the endothelium therefore necessitates more energy, which suggests its use causes more damage on aspiration. The dispersive Hyadel also displayed a smaller persistence length, which can be linked to a higher flexibility, and less sensitive to the probe speed, dwelling time and substrate. This reflects its higher ability to withstand shear stress, and points towards a cohesive failure mechanism like the one described by surgeons.

Chapter 6

Conclusions, Implications and Future Work

6.1 Conclusions

Cataract surgeons use Ophthalmic Viscosurgical Devices (OVDs) to maintain volume in the eye, and protect the delicate corneal endothelium from suffering any major cell loss during surgery. Despite the importance at stake, the protection mechanism provided by OVDs remains poorly understood. Most importantly, surface interactions between polymers composing the OVDs and biological interfaces in the eye are typically overlooked.

In Chapter 3, we studied an experimental model for adsorption and subsequent desorption of polymers at solid surfaces using polyvinylpyrrolidone (PVP). Using a combination of Quartz Crystal Microbalance with Dissipation monitoring (QCM-D) and phase modulation ellipsometry, we found that PVP forms ultrathin, rigid layers from highly dilute 1 ppm solutions. The polymers adopt a flat configuration on the sensor surface, making them resistant to desorption during solvent rinsing. As the bulk concentration increases, the polymers form Guiselin brush-like layers, which extend increasingly further into the solution and exhibit a higher coupling with the ambient solvent. These layers partially desorb upon rinsing, and a similar layer to the previous 1 ppm case remains behind, which we describe as a limiting case of undersaturated starved layer. We identified physisorbed mucin layers as a good biomimetic model to estimate how

well these results could be translated into *in vivo* situations.

In Chapter 4, we applied similar experimental procedures to OVD solutions, starting with a highly dilute 1 ppm concentration. Our analysis revealed that hyaluronic acid (HA) assembles as strongly-attached ultrathin flat layers on gold surfaces in this regime. The layer displayed no apparent desorption upon rinsing with solvent, a behaviour which remained consistent even at higher polymer concentrations up to 1000 ppm, unlike PVP. Despite some differences in configuration, the layers formed from dispersive and cohesive OVDs in these two regimes exhibited similar adsorption and desorption behaviour. However, above the entanglement limit, clear differences emerged between the two classes of OVDs. The network of dispersive OVDs appears to consistently break down upon contact with a solid substrate. The polymers rearrange to form layers with a high coupling with the surrounding solvent, which are able to resist desorption upon rinsing. On the other hand, cohesive OVD are able to adsorb without disrupting their entangled polymer network. As a result, desorption of the polymer segments leads to the breaking of surface attachment points rather than network rupture, which can be attributed to an adhesive failure mechanism. These observations remained valid on mucin-coated substrates.

In Chapter 5, we used colloidal probe Atomic Force Microscopy (AFM) to measure the strength of the interaction between HA-coated silica particles and various biomimetic substrates. We identified two types of force profiles following a sawtooth pattern. Our results suggest that pulling off dispersive OVD from solid substrates induces a simultaneous rupture of several tethering points. Conversely, cohesive OVDs are more likely to experience a sequential rupture of individual attachment points, resulting in a higher work of adhesion.

6.2 Implications in Phacoemulsification

These findings have significant implications in the broader context of cataract surgery. QCM-D enabled us to probe the interaction between polymer networks and solid surfaces in solution, while AFM provided insights into the interactions of a reduced number of molecules. Additionally, the layers formed in QCM-D are mostly exposed to a shear stress during rinsing, whereas AFM imposes a normal stress on the HA molecules. In reality, the turbulent flows generated

during cataract surgery put the endothelium through a combination of shear and extensional stresses, which makes them both relevant.

We propose that the reduced endothelial cell loss observed when using dispersive OVDs compared to cohesive OVDs is due to two causes. First, dispersive OVDs offer a superior endothelial protection due to their adsorption mechanism, which results in a higher polymer density at the surface and greater energy dissipation. The second aspect is that cohesive OVDs have the potential to induce more damage to the endothelium upon aspiration, as their bolus aspiration induces a sequential breaking of attachment points.

A previous article proposed that the differences in the removal of cohesive and dispersive OVDs are a result of volume rheology rather than surface interactions [45]. However, their analysis considered much thicker OVD layers - up to several mm - compared to the nanoscale focus of our QCM-D and AFM study. We examined interfacial contributions at a smaller scale, which could induce other effects. Adsorption-entanglement of high molecular weight polymers, like we described with QCM-D in Chapter 4, have been studied in the context of petroleum reservoirs. They offer a method to reduce water permeability by locally decreasing pore size, which results in a pressure build-up [106]. Similarly, the adsorption of HA on ocular structures could induce a local increase in intraocular pressure, as reported by surgeons after phacoemulsification [19].

Our AFM measurements from Chapter 5 yielded values of F_{adh} comprised between 0.4 and 6.7 nN, and W_{adh} comprised between 0.3 and $9.3.10^{-15}$J depending on the OVD, the substrate and the probe speed considered. The adhesion energy of cancer cells to endothelial cells was measured to be between 1 and $8 \cdot 10^{-15}$ J at the probe speeds we used, which lies in the same range [161]. This suggests that an energy transfer of this magnitude has the potential to result in cell detachment. The values of F_{adh} measured between the OVD-functionalised colloidal probe and the biomimetic substrates also indicate that HA can significantly interact with various materials found in the eye cavity. The materials tested possess different surface charges, and both hydrophilic and hydrophobic properties. It follows that such attractive interactions may also occur in an *in vivo* system, and they should not be ignored when studying phacoemulsification.

6.3 Future Directions

In this work, we have clearly established the presence of a specific interaction between HA and substrates functionalised to mimic some structures found on the corneal endothelium. Future research should explore more complex surfaces, such as isolated HA receptors like CD44, or living endothelial cells, in order to provide a sharper understanding of the protection mechanism provided by OVDs, and in particular the dispersive OVDs. Another approach could be to replace our HA-functionalised silica particles with soft gel beads to study the mechanical interaction between HA and biomimetic substrates [162–164].

Additionally, the potential damaging effects of detaching cohesive OVDs independently of the stress resulting from the irrigation/aspiration probe merits further investigation. Whilst most studies compare the number of endothelial cells before and after the phacoemulsification procedure, we suggest counting the cells before OVD injection and after aspiration, in the absence of any additional stress.

It would be interesting to carefully consider the timescales of the effects we highlight in this work in order to see if they can be applied to *in vivo* situations. As discussed in Chapter 1, cataract surgery takes between 5 and 10 minutes for each eye [19], which includes several minutes of phacoemulsification [18, 19, 35] and 10 s to 3.5 minutes of OVD aspiration [26, 28, 40]. Conversely, the QCM-D experiments presented in Chapter 3 and Chapter 4 typically lasted for about an hour. The timescale needed to be long enough for us to depict a meaningful model of polymer adsorption. However, the kinetics of desorption of adsorbed polymer coils are extremely slow, which is why we did not carry on the measurement until thermodynamic equilibrium was reached.

This work could be used as a stepping stone to develop innovative OVD formulations combining the advantages of both cohesive and dispersive classes: efficient endothelial protection, minimal aspiration trauma and easy removal. To do so, one could adjust several parameters such as the polymer composition or the cross-linking density to optimise the efficiency of the OVD.

Appendix A

Uncertainty calculation

When working with the QCM-D models described in Section 2.1.2, we used equation A.1 for error propagation:

$$(\Delta Y)^2 = (\Delta A)^2 \left(\frac{\partial f}{\partial A}\right)^2 \; + \; (\Delta B)^2 \left(\frac{\partial f}{\partial B}\right)^2 \tag{A.1}$$

where A and B are variables contained in the expression of Y, with respective uncertainties ΔA and ΔB. We determined the uncertainty in the sensitivity constant, ΔC_f, with $\Delta N = 1670$ Hz.cm and $\Delta f_0 = 50$ kHz (from manufacturer specifications):

$$(\Delta C_f)^2 = (\Delta f_0)^2 \left(\frac{\partial f}{\partial f_0}\right)^2 \; + \; (\Delta N)^2 \left(\frac{\partial f}{\partial N}\right)^2 \tag{A.2}$$

$$\Delta C_f = \sqrt{(\Delta f_0)^2 \left(\frac{-2\ \rho_Q\ N}{f_0^3}\right)^2 \; + \; (\Delta N)^2 \left(\frac{\rho_Q}{f_0^2}\right)^2} \tag{A.3}$$

yielding $\Delta C_f \; = 0.41$ ng.cm^{-2}.Hz^{-1}. Similarly, the uncertainty in φ in ng.cm^{-2} was determined using $\Delta(\frac{\Delta f_n}{n}) \; = \; \sqrt{2} \; * \; 0.06$ (from manufacturer specifications).

$$\Delta\varphi = \sqrt{\left(\Delta\left(\frac{\Delta f_n}{n}\right)\right)^2 (C_f)^2 + (\Delta C_f)^2 \left(\frac{\Delta f_n}{n}\right)^2} \tag{A.4}$$

On Figure 3.2, we used equation A.5 from the Kanazawa-Gordon model to calculate the shifts in frequency expected from immersing the sensor in distilled water:

$$\Delta f_n = -f_0^{\frac{3}{2}} \sqrt{\frac{\eta_l \rho_l}{\pi \mu_Q \rho_Q}}\, n \tag{A.5}$$

where f_0 is the frequency of the unloaded crystal in air, ρ_l and η_l are the ambient density and viscosity of the liquid, μ_Q and ρ_Q are the shear modulus and density of the crystal.

Using equation A.1, we determined the uncertainty in Δf_n, with $\Delta f_0 = 50$ kHz (from manufacturer specifications):

$$\Delta(\Delta f_n) = \frac{3}{2}\, \Delta f_0\, \sqrt{f_0} \sqrt{\frac{\eta_l \rho_l}{\pi \mu_Q \rho_Q}}\, n \tag{A.6}$$

which can be rearranged into equation A.7.

$$\frac{\Delta(\Delta f_n)}{\Delta f_n} = \frac{3}{2} \frac{\Delta f_0}{f_0} \tag{A.7}$$

Similarly, we determined the dissipation shift at all overtones following equation A.8.

$$\Delta D_n = 2 \sqrt{\frac{f_0}{n}} \sqrt{\frac{\eta_l \rho_l}{\pi \mu_Q \rho_Q}} \tag{A.8}$$

The corresponding uncertainty was then calculated:

$$\Delta D_n = 2 \sqrt{\frac{f_0}{n}}\, \sqrt{\frac{\eta_l \rho_l}{\pi \mu_Q \rho_Q}} \tag{A.9}$$

which can be simplified to equation A.10.

$$\frac{\Delta D_n}{D_n} = \frac{1}{2}\, \frac{\Delta f_0}{f_0} \tag{A.10}$$

Appendix B

Cleaning procedure QCM-D

The QCM-D measurements detailed in Chapter 3 revealed that a layer formed from a 1 ppm solution in distilled water remained adsorbed after rinsing. We used a cleaning protocol where a 2% v/v solution of Hellmanex II was injected in the QCM-D chamber for 30 minutes at 100 µL.min^{-1}, followed by rinsing with distilled water at the same flow rate for 5 hours. As shown on Figure B.1, the values of Δf and ΔD at the end of this procedure were similar to the inverse of the shifts displayed after the adsorption of PVP (Δf_3 = -7 Hz and ΔD_3 = -0.4 ppm), which demonstrates the efficiency of our cleaning protocol.

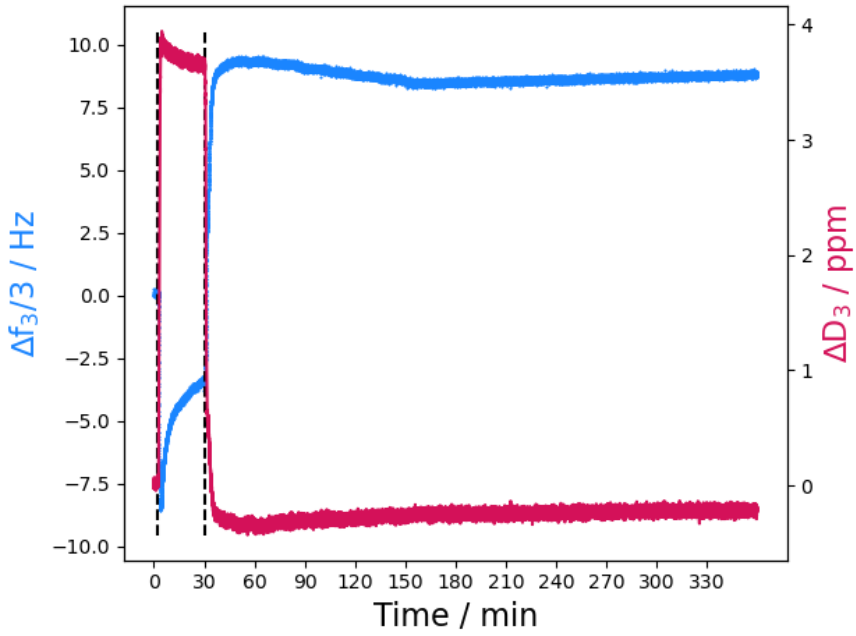

Figure B.1 *Changes in frequency (blue) and dissipation (pink) for the third overtone observed with QCM-D when injecting a 2% Hellmanex II detergent followed by rinsing with distilled water. A PVP layer was initially adsorbed on the quartz surface from a 1 ppm solution, which led to* Δf *= -7 Hz and* ΔD *= -0.4 ppm compared to the bare sensor in distilled water, as in Figure 3.3. This cleaning protocol was efficient to desorb this layer. The dashed lines correspond to the injection of Hellmanex and distilled water, respectively.*

Appendix C

Geometry QCM-D

As can be seen from Figure 2.2, as the fluid flows through the QCM-D it encounters several geometric boundary conditions. The shear rate in the two types of tubing can be calculated as equation C.1:

$$\dot{\gamma} = \frac{4\ Q}{\pi R^3} \tag{C.1}$$

where Q is the flowrate and R is the tube radius. As for the serpentine and the sensor surface, they can be approximated by a rectangle geometry of width w and height h, which yields equation C.2:

$$\dot{\gamma} = \frac{6\ Q}{w\ h^2} \tag{C.2}$$

The shear stress τ in each location was calculated following equation C.3, whilst the dwelling time was calculated with equation C.4:

$$\tau = \dot{\gamma}\ \eta \tag{C.3}$$

$$t = \frac{V}{Q} \tag{C.4}$$

where η is the solution viscosity, and V is the volume. The values of $\dot{\gamma}$, τ and t can be found in Table C.1.

Location	Geometry	Shear rate $\dot{\gamma}$ / s^{-1}	Dwelling time t / s
PTFE tubing	Tube	5	212 (inlet) 159 (outlet)
Serpentine Wall	Cube	15	60
Sensor Surface	Cube	7	24
Tygon pump tubing	Tube	39	103

Table C.1 *Table summarising the shear rate and residence time of OVDs in different parts of the QCM-D setup.*

The viscosity at the different shear rates of interest were estimated from the Carreau-Yasuda predictions obtained from shear rheology, which are plotted in Figure 4.13. The corresponding values of τ and $\dot{\gamma}$ are reported in Table C.2 for Hyadel and Table C.3 for Hyaplus.

Location	Geometry	Shear rate $\dot{\gamma}$ / s^{-1}	Shear Stress τ / $N.m^{-2}$	Viscosity η / Pa.s
PTFE tubing	Tube	5	150	30
Serpentine Wall	Cube	15	270	18
Sensor Surface	Cube	7	182	26
Tygon pump tubing	Tube	39	390	10

Table C.2 *Table summarising the shear rate and residence time of Hyadel in different parts of the QCM-D setup.*

Location	Geometry	Shear rate $\dot{\gamma}$ / s^{-1}	Shear Stress τ / $N.m^{-2}$	Viscosity η / Pa.s
PTFE tubing	Tube	5	125	25
Serpentine Wall	Cube	15	165	11
Sensor Surface	Cube	7	133	19
Tygon pump tubing	Tube	39	195	5

Table C.3 *Table summarising the shear rate and residence time of Hyaplus in different parts of the QCM-D setup.*

Appendix D

Python Codes

D.1 Ellipsometry

The following code was used to fit the ellipsometry data to values of HA layer thickness according to the procedure described in Chapter 2. It was also adapted to the measure of PVP layer thickness by changing the refractive index appropriately.

```
import numpy as np
import matplotlib.pyplot as plt
import pandas as pd
import math
import cmath

#This script aims to determine the HA layer thickness from the measured values
#of Re(r) and Im(r) during in situ adsorption under flow
#The model is as follows: transmission (air, flow cell window (SiO2)),
#reflection (H2O(0), HA (1), gold layer (2), gold substrate(3))
#The experimental values were stored in an Excel file with columns
#labelled Time (s), Re_air, Im_air, Re and Im filled appropriately.
#A similar code was used for PVP by changing the value of the refractive index.

#This version first fits n and k for the bare gold substrate in air.

#Part 0:
#Calculate the values of theta for each medium using snell's law using the values
#of n stored in list_n. Store them in list_theta

def snell(list_theta, list_n, size_model):
    list_theta[0] = 60*np.pi/180
    for i in range(1, size_model-2):
        list_theta[i] = np.arcsin(list_n[i-1]*np.sin(list_theta[i-1])/list_n[i])
```

```
    list_theta[4] = (cmath.asin(list_n[3]*np.sin(list_theta[3])/complex(list_n[4],
        list_k[4]))).real
    list_theta[5] = (cmath.asin(list_n[3]*np.sin(list_theta[3])/complex(list_n[4],
        list_k[4]))).imag

    #beware: we define list_theta [4] as the real part of the complex angle of light
    #at the gold interface. list_theta [5] is the corresponding imaginary part
    return list_theta

#Part 1:
#Determine the p reflection coefficients of each interface
def reflection_coeff_p(list_theta, list_n, size_model):
    rp_H2OHA = (list_n[3]*np.cos(list_theta[2]) - list_n[2]*
        np.cos(list_theta[3]))/(list_n[3]*np.cos(list_theta[2])+list_n[2]*
        np.cos(list_theta[3]))

    rp_HAAu = ((complex(list_n[4], list_k[4])*np.cos(list_theta[3])-list_n[3]*
        cmath.cos(complex(list_theta[4], list_theta[5])))/(complex(list_n[4],
        list_k[4])*np.cos(list_theta[3])+list_n[3]*cmath.cos(complex(list_theta[4],
        list_theta[5]))))

    rp_AuAu = 0

    return (rp_H2OHA, rp_HAAu, rp_AuAu)

#Do the same for the s reflection coefficients
def reflection_coeff_s(list_theta, list_n, size_model):
    rs_H2OHA = (list_n[2]*np.cos(list_theta[2]) - list_n[3]*
        np.cos(list_theta[3]))/(list_n[2]*np.cos(list_theta[2])+list_n[3]*
        np.cos(list_theta[3]))

    rs_HAAu = ((list_n[3]*np.cos(list_theta[3])-complex(list_n[4], list_k[4])*
        cmath.cos(complex(list_theta[4], list_theta[5])))/((list_n[3]*
        np.cos(list_theta[3])+complex(list_n[4], list_k[4])*
        cmath.cos(complex(list_theta[4], list_theta[5]))))

    rs_AuAu = 0

    return(rs_H2OHA, rs_HAAu, rs_AuAu)

#Part 2:
#Determine the p transmission coefficients of each interface

def transmission_coeff_p(list_theta, list_n):
    tp_ASiO2 =  2*list_n[0]*np.cos(list_theta[0])/(list_n[1]*
        np.cos(list_theta[0])+list_n[0]*np.cos(list_theta[1]))
    tp_SiH2O =  2*list_n[1]*np.cos(list_theta[1])/(list_n[2]*
        np.cos(list_theta[1])+list_n[1]*np.cos(list_theta[2]))
    tp_H2OSiO2 =  2*list_n[2]*np.cos(list_theta[2])/(list_n[1]*
        np.cos(list_theta[2])+list_n[2]*np.cos(list_theta[1]))
    tp_SiO2A =  2*list_n[1]*np.cos(list_theta[1])/(list_n[0]*
        np.cos(list_theta[1])+list_n[1]*np.cos(list_theta[0]))

    return (tp_ASiO2, tp_SiH2O, tp_H2OSiO2, tp_SiO2A)

#Do the same for the s transmission coefficients
def transmission_coeff_s(list_theta, list_n):
```

```
    ts_ASiO2 =  2*list_n[0]*np.cos(list_theta[0])/(list_n[0]*
        np.cos(list_theta[0])+list_n[1]*np.cos(list_theta[1]))
    ts_SiH2O =  2*list_n[1]*np.cos(list_theta[1])/(list_n[1]*
        np.cos(list_theta[1])+list_n[2]*np.cos(list_theta[2]))
    ts_H2OSiO2 =  2*list_n[2]*np.cos(list_theta[2])/(list_n[2]*
        np.cos(list_theta[2])+list_n[1]*np.cos(list_theta[1]))
    ts_SiO2A =  2*list_n[1]*np.cos(list_theta[1])/(list_n[1]*
        np.cos(list_theta[1])+list_n[0]*np.cos(list_theta[0]))

    return (ts_ASiO2, ts_SiH2O, ts_H2OSiO2, ts_SiO2A)

#Part 3:
#Determine the phase shift
def phase_shift(list_n, n_HA, d_HA, d_Au, list_theta, list_k):
    wavelength = 632.8 #wavelength of the laser in nm

    delta_Au = 0
    delta_HA = (2*np.pi/wavelength)*(n_HA)*d_HA*np.cos(list_theta[3])

    return (delta_Au, delta_HA)

#Rouard method: the effective reflection coeff can be approximated as a surface
#with these properties.
def rouard(r_H2OHA, r_HAAu, r_AuAu, delta_HA, delta_Au):
    num = ((r_H2OHA + r_HAAu*np.exp(complex(0, -2)*delta_HA))+(r_AuAu*
        np.exp(complex(0, -2)*(delta_HA+delta_Au)))+r_H2OHA*r_HAAu*r_AuAu*
        np.exp(complex(0,-2)*delta_HA))

    den = (1+r_H2OHA*r_HAAu*np.exp(complex(0, -2)*delta_HA)+(r_H2OHA*r_AuAu*
        np.exp(complex(0,-2)*(delta_Au+delta_HA)))+(r_HAAu*r_AuAu*
        np.exp(complex(0,-2)*delta_Au)))

    overall_R = num/den
    return overall_R

def get_theo_value(d_HA, n_layer, list_n, list_theta, size_model):
    snell(list_theta, list_n, size_model)

    list_n[3] = n_layer

    (rp_H2OHA, rp_HAAu, rp_AuAu) = reflection_coeff_p(list_theta, list_n, size_model)
    (rs_H2OHA, rs_HAAu, rs_AuAu) = reflection_coeff_s(list_theta, list_n, size_model)

    (delta_Au, delta_HA) = phase_shift(list_n, n_layer, d_HA, d_Au, list_theta, list_k)

    #Rouard method

    overall_Rp = rouard(rp_H2OHA, rp_HAAu, rp_AuAu, delta_HA, delta_Au)
    overall_Rs = rouard(rs_H2OHA, rs_HAAu, rs_AuAu, delta_HA, delta_Au)

    #predict Im(r) and Re(r)
    re_calc = (overall_Rp/overall_Rs).real
    im_calc = (overall_Rp/overall_Rs).imag

    return (abs(re_calc), abs(im_calc))

def get_data_time(list_time, sheet, size_sheet):
```

```
    for i in range(size_sheet-1):
        list_time[i] = sheet['Time (s)'].iloc[i]
    return (list_time_exp)

#We divide the real part of the signal by 1.445 to normalise it from the refractive index
#of the glass window.
def get_data_re(list_re_air, list_re_exp, sheet, size_sheet):
    for i in range(size_sheet-1):
        list_re_air[i] = (sheet['Re_air'].iloc[i])/1.445
        list_re_exp[i] = (sheet['Re'].iloc[i])/1.445
    return list_re_air, list_re_exp

def get_data_im(list_im_air, list_im_exp, sheet, size_sheet):
    for i in range(size_sheet-1):
        list_im_air[i] = (sheet['Im_air'].iloc[i])
        list_im_exp[i] = sheet['Im'].iloc[i]
    return list_im_air, list_im_exp

if __name__ == "__main__":

    #step 0: retrieve data
    #open sheet and store everything in sheet
    sheet = pd.read_excel("~/Desktop/file.xlsx", sheet_name='sheet')
    size_sheet = len(sheet)-1

    list_d = [-1, 2*10**6, -1, 0, 8000, -1] #layer thicknesses in nm. -1 = infinite
    list_time_exp = np.zeros(size_sheet)

    d_Au = list_d[4]
    d_HA = list_d[3]

    list_re_air = np.zeros(size_sheet)
    list_im_air = np.zeros(size_sheet)
    list_re_exp = np.zeros(size_sheet)
    list_im_exp = np.zeros(size_sheet)

    #-------------------------retrieve data from Excel ------------------
    get_data_time (list_time_exp, sheet, size_sheet)
    get_data_re (list_re_air, list_re_exp, sheet, size_sheet)
    get_data_im (list_im_air, list_im_exp, sheet, size_sheet)

    print('list_re_air[0] is ', list_re_air[0])

    d_HA_sol = np.zeros(size_sheet)
    n_layer_sol = np.zeros(size_sheet)

    #--------------generate_values for the parameters to be fitted--------------
    n_gold_range = np.linspace(0.1, 0.25, 50)
    k_gold_range = np.linspace(-3.1, -3.2, 50)

    diff_from_exp_im = np.zeros((len(n_gold_range), len(k_gold_range)))
    diff_from_exp_re = np.zeros((len(n_gold_range), len(k_gold_range)))

    d_HA_range = np.linspace(0, 3, 100).astype(float)
    n_layer_range = np.linspace(1.563, 1.563, 1).astype(float)

    min_diff = 3000
```

```
min_diff_re = 3000
min_diff_im = 3000

#--------------step 1: fit the data in air to (n, k) for gold -----------------
size_model = 4
list_n = [1, 1.47, 1, 0.166]
list_k = [0, 0, 0, -3.15]

#-----------------get theta_gold from Snell's law----------------------------
theta_air = 60*np.pi/180
theta_window = np.arcsin(list_n[0]*np.sin(theta_air)/list_n[1])

for i in range(len(n_gold_range)):
    for j in range(len(k_gold_range)):
        theta_gold = cmath.asin(list_n[2]*np.sin(theta_air)/complex(n_gold_range[i],
            k_gold_range[j]))

        #---------------get rp and rs at air/gold interface-----------------
        rp_AirGold = ((complex(n_gold_range[i], k_gold_range[j])*np.cos(theta_air))
            -(list_n[2]*cmath.cos(theta_gold)))/((complex(n_gold_range[i],
            k_gold_range[j])*np.cos(theta_air))+list_n[2]*cmath.cos(theta_gold))
        rs_AirGold = (list_n[2]*np.cos(theta_air)-complex(n_gold_range[i],
            k_gold_range[j])*cmath.cos(theta_gold))/(list_n[2]*np.cos(theta_air)
            +complex(n_gold_range[j], k_gold_range[j])*cmath.cos(theta_gold))

        #--------------------get the theoretical values----------------------
        re_calc = abs((rp_AirGold/rs_AirGold).real)
        im_calc = abs((rp_AirGold/rs_AirGold).imag)

        #---------compare with experiment and select the best value---------
        diff_from_exp_re[i,j] = abs(re_calc-list_re_air[0])

        if diff_from_exp_re[i,j] <= min_diff:

            min_diff_re = diff_from_exp_re[i, j]
            min_diff_ind_re_k = j
            min_diff_ind_re_n = i

            min_diff = min_diff_re
            re_val = re_calc
            im_val = im_calc

n_gold_sol = n_gold_range[min_diff_ind_re_n]
k_gold_sol = k_gold_range[min_diff_ind_re_k]

print('air : the best solution is ', complex(n_gold_sol, k_gold_sol))
print('it gives rho = ', complex(re_val, im_val))
print('the difference is ', min_diff)

#------step 2: fit the OVD adsorption data to (n, d) for the layer --------

min_diff = 3000
min_diff_re = 3000
min_diff_im = 3000

size_model = 6
list_theta = np.zeros(size_model)
```

```
list_n = [1, 1.47, 1.33, 1.563, n_gold_sol, n_gold_sol]
list_k = [0, 0, 0, 0.001, k_gold_sol, k_gold_sol]

min_diff_sol_re = None
min_diff_sol_im = None
tmp = None
diff_from_exp_im = np.zeros(len(d_HA_range))
diff_from_exp_re = np.zeros(len(n_layer_range))
min_diff_ind_re = 0
min_diff_ind_im = 0

re_calc0, im_calc0 = get_theo_value(0, 1.5, list_n, list_theta, size_model)
offset_value_im = im_calc0 - list_im_exp[0]
offset_value_re = re_calc0 - list_re_exp[0]


print('initial value of im =', list_im_exp[0])
print('im_calc0 =', im_calc0)
print('offset_value_im =', offset_value_im)
print('re_calc0 =', re_calc0)
print('offset_value_re =', offset_value_re)

for k in range(len(sheet)-1):
    min_diff_re = 3000
    min_diff_im = 3000
    min_diff = 3000

    for i in range(len(d_HA_range)):
        for j in range(len(n_layer_range)):
            re_calc, im_calc = get_theo_value(d_HA_range[i], 1.563, list_n,
                list_theta, size_model)
            diff_from_exp_im[i] = abs(im_calc-(list_im_exp[k]+offset_value_im))
            diff_from_exp_re[j] = abs(re_calc-(list_re_exp[k]+offset_value_re))
            dist = np.sqrt(diff_from_exp_im[i]**2 + diff_from_exp_re[j]**2)

            if dist <= min_diff:

                min_diff_im = diff_from_exp_im[i]
                min_diff_ind_im = i
                min_diff_re = diff_from_exp_re[j]
                min_diff_ind_re = j
                min_diff = dist

    d_HA_sol[k] = d_HA_range[min_diff_ind_im]

#make a figure y=f(x)
fig, ax1 = plt.subplots()

#plot h = f(t)
ax1.plot(list_time_exp, d_HA_sol, color='black',  linestyle='none', marker='v',
    markersize=6, label='Layer thickness h / nm')

print('done')
```

D.2 Worm-Like Chain

```
# This script sequentially opens text files which contain AFM force curve data
# exported from JPKSPM Data Processing.
# The files contain descriptive lines starting with a #, followed by 3 columns:
# "Vertical Tip Position" "Vertical Deflection" and "Height (measured)"
# The files are first sorted by number to reconstruct the geometry of the 64x64 force map
# All force spikes are plotted sequentially with the corresponding WLC fit
# After a file has been completely analysed, another plot contains the values of
# persistence length b and contour length L obtained for the sequential spikes.

#Step 0: import libraries
import sys
import numpy as np
import matplotlib.pyplot as plt
import pandas as pd
import scipy.optimize as opti
import os
import scipy
import glob
import gc
from IPython.display import Audio

def read_text_file (file_path):
    data_AFM = pd.read_csv(file_path, sep=" ", on_bad_lines='skip', names=["d(m)", "F(N)",
        "N/A"])
    return data_AFM

def find_index_max(nb_values, index_end_liste):
    liste_diff = np.diff(nb_values)
    for i in range(len(nb_values)-1):
        if liste_diff[i] == liste_diff.max():
            index_end_liste = i
    return index_end_liste

def get_numerical_data(size, nb_values, data_AFM):
    for i in range(size):
        if (data_AFM['d(m)'].iloc[i])[0] != "#":
            nb_values.append(i)
    return nb_values

def fill_lists(nb_values, index_end_liste, diff, data_AFM, d_extend, d_retract, F_extend,
    F_retract):

    for i in range(len(nb_values)):
        if i < index_end_liste:
            d_extend[i] = float(data_AFM['d(m)'].iloc[nb_values[i]])*10**9 #nm
            F_extend[i] = float(data_AFM['F(N)'].iloc[nb_values[i]])*10**9 #nN
            diff = i

        else:
            d_retract[i-diff-1] = float(data_AFM['d(m)'].iloc[nb_values[i]])*10**9 #nm
            F_retract[i-diff-1] = float(data_AFM['F(N)'].iloc[nb_values[i]])*10**9 #nN

    return d_extend, F_extend, d_retract, F_retract
```

```
def get_values_density_plot(F_retract, d_retract, adhesion_event_f, adhesion_event_d):
    #look for negative peaks greater than -0.2 mN/m in F_retract. The function returns
    #the indexes.
    #we use np.negative(F_retract) because the function looks for maxima.
    peaks, _  = (scipy.signal.find_peaks(np.negative(F_retract), height=0,
        prominence = (0.2)))

    adhesion_event_f.extend(F_retract[peaks])
    adhesion_event_d.extend(d_retract[peaks])
    number_adhesion_events.append(len(peaks))
    return peaks

def fit(x, b, L):
    kBT = 295*1.380649*10**-23
    value = ((kBT*10**18)/b) * (0.25*(1-x/L)**-2 - 0.25 + x/L)
    return value

def get_contact_point(f_retract, peaks):
    contact_point=0
    print(peaks)
    if len(peaks) != 0:
        while f_retract[contact_point] < 0 and contact_point < peaks[0]:
            contact_point = contact_point+1
    return contact_point

#Return the fitting parameters and the covalence matrix
def get_fitting_parameters(fit, d_retract, f_retract, ind_min, ind_max, bound_min_b,
    bound_max_b, bound_min_L, bound_max_L, contact_point):
    #ind_min is the contact_point
    size = ind_max-ind_min
    liste_d_fit = np.zeros(size)
    liste_f_fit = np.zeros(size)
    j=0

    #this crops the data to the part we want to fit
    for i in range(ind_min, ind_max):
        liste_d_fit[j] = d_retract[i]
        liste_f_fit[j] = f_retract[i]
        j=j+1

    #first variable is b (persistence length), second variable is L (contour length)
    (var, M_cov) = opti.curve_fit(fit, liste_d_fit, liste_f_fit,
        maxfev=500000000, bounds = ([bound_min_b, bound_min_L], [bound_max_b,
        bound_max_L]))

    #var is a liste of the fitted parameters (a, b...) and M_cov is the estimated
    #covariance of var.
    #The diagonals provide the variance of the parameter estimate.
    return (var, M_cov)

#Calculate y_theo with the values of fitting parameters
def compute_fit_data(y_theo, liste_x, b, L, start_ind, peak_ind):
    for i in range(peak_ind):
        if i<start_ind:
            y_theo[i] = None
        else:
```

```
            y_theo[i] = fit(liste_x[i], b, L)

    return y_theo

def fix_initial_offset(F_retract, start_ind, peak_ind):
    length = int((peak_ind - start_ind)/4)
    offset = np.average(F_retract[start_ind:start_ind+length])
    print('offset is ', offset)

    for i in range(peak_ind-start_ind):
        F_retract[start_ind+i] = F_retract[start_ind+i] - offset
    return -F_retract

def find_start_ind(F_retract, peak_ind, d_retract, contact_point):
    start_ind = peak_ind
    while abs(F_retract[start_ind]-F_retract[start_ind-1]) < 0.1 and
        start_ind > contact_point:
        start_ind = start_ind-1
    return start_ind

def play_sound():
    sound_file = './sound.wav'
    display(Audio(sound_file, autoplay=True))

if __name__ == "__main__":

    #path = #include the path to a file which contains all 64 force maps here
    index_end_liste = 0

    diff = 0
    adhesion_event_f = []
    adhesion_event_d = []
    number_adhesion_events = []
    diff_list_total = []
    area_total = []
    y_list = []
    adhesion_values = []
    contact_point = 0
    b_persistence_length = []
    L_contour_length = []
    new_plot = []
    peaks_values = []

    last_b_persistence_length = []
    last_L_contour_length = []
    last_peaks_value = []

    peak_ind = 0

    #sort files by time of modification
    file_list = list(filter(os.path.isfile, glob.glob(path + "\*")))
    file_list.sort(key=os.path.getmtime)

    #Step 1: open text files
    for file in file_list:
        if file.endswith(".txt"):
            file_path = f"{file}"
```

```
        print(file_path)

        data_AFM = read_text_file(file_path)
        size_file = len(data_AFM)
        nb_values = []

        #Step 2: import numerical data from the text file
        nb_values = get_numerical_data(size_file, nb_values, data_AFM)

        d_extend = np.array([None]*len(nb_values)).astype(np.double)
        F_extend = np.array([None]*len(nb_values)).astype(np.double)
        d_retract = np.array([None]*len(nb_values)).astype(np.double)
        F_retract = np.array([None]*len(nb_values)).astype(np.double)

        #Step 3: retrieve the index where we go from extend to retract
        index_end_liste = find_index_max(nb_values, index_end_liste)

        #Step 4: fill both lists with relevant data
        d_extend, F_extend, d_retract, F_retract = fill_lists(nb_values,
            index_end_liste, diff, data_AFM, d_extend, d_retract, F_extend, F_retract)

        #Step 5: look for all force spikes in a file
        peaks = get_values_density_plot (F_retract, d_retract,
            adhesion_event_f, adhesion_event_d)
        print('en cours, file = ', file_path)

    #-----------Step 6: fit the peaks to WLC model--------------------
        #first we look for the contact point
        contact_point = get_contact_point(-F_retract, peaks)

        for i in range(len(peaks)):
            #then we look for start_ind at each spike, which is where the spike starts.

            peak_ind = peaks[i]
            print('peak_ind = ', peak_ind)
            start_ind = find_start_ind(-F_retract, peak_ind, d_retract, contact_point)
            print('start_ind = ', start_ind)

            #a spike is only considered valid if it contains 50 data points

            if peak_ind - start_ind > 50:

                #corrects the offset and calculates the values of the WLC fit
                F_retract = fix_initial_offset(-F_retract, start_ind, peak_ind)
                (var, M_cov) = get_fitting_parameters(fit, d_retract, -F_retract,
                    start_ind, peak_ind, 0, 50, 0, 15000, contact_point)
                y_theo = np.zeros(peak_ind)
                y_theo = compute_fit_data(y_theo, d_retract, var[0], var[1],
                    start_ind, peak_ind)

                #the fit is only considered valid is the maximum force is less than
                #10 nN and if the amplitude is at least 0.03 nN.

                if np.nanmax(y_theo) < 10 and np.nanmax(y_theo) - np.nanmin(y_theo)
                    > 0.03:

                    print('b, L = ', var)
```

```
                b_persistence_length.append(var[0])
                L_contour_length.append(var[1]/1000)
                print('Mcov = ', M_cov)
                peaks_values.append(-F_retract[peak_ind])

                #plots the portion of the force curve which is a spike and the
                #corresponding WLC fit

                fig, ax1 = plt.subplots()

                d_extend_mask = np.isfinite(d_extend)
                d_retract_mask = np.isfinite(d_retract)
                #masks are used to ignore any NaN data

                ax1.plot(d_retract[start_ind-50:peak_ind+50],
                    F_retract[start_ind-50:peak_ind+50], color = 'red',
                    marker = '.', linestyle = 'None', label = "retract")
                ax1.legend()
                ax1.set_xlabel("Separation d / nm")

                ax1.set_ylabel("F / nN")

                ax1.plot(d_retract[start_ind:peak_ind],
                    -y_theo[start_ind:peak_ind], color = 'violet',
                    linestyle = '--', linewidth = 4, label = 'fit')
                ax1.axvline(x = d_retract[start_ind], color = 'black')
                ax1.axvline(x = d_retract[peak_ind], color = 'black')
                ax1.legend()
                plt.show()

                #We clear variables to avoid crash

                del ax1
                del d_extend_mask
                del d_retract_mask

            del var
            del M_cov
            del y_theo

    #we plot the successive values of {b, L} for each peak of each plot
    if b_persistence_length:

        last_b_persistence_length.append(b_persistence_length[-1])
        last_L_contour_length.append(L_contour_length[-1])
        last_peaks_value.append(peaks_values[-1])

        x = range(len(b_persistence_length))
        fig, ax2 = plt.subplots()

        ax2.plot(x, b_persistence_length, color = '#D41159', marker = '.',
            linestyle = '--', label = "Persistence length / nm")
        ax2.set_ylabel('Persistence length (nm)', fontsize = 16,
            color = '#D41159')
        ax2.set_xlabel('Spike number', fontsize = 16, color = 'black')
        ax3 = ax2.twinx()
        ax3.plot(x, L_contour_length, color = '#1A85FF', marker = '.',
```

```
                linestyle = '--', label = "Contour length / $\mu$ m")
            ax3.set_ylabel('Contour length / $\mu$ m', fontsize = 16,
                color = '#1A85FF')
            new_plot.append(x[-1])

        else:
            print('It looks like there is no fit')

        plt.show()

        del data_AFM
        del size_file
        del nb_values
        del d_extend
        del F_extend
        del d_retract
        del F_retract
        del peaks
        del contact_point

        del fig
        del ax2
        del ax3
        del x

del file_path
del index_end_liste
del diff
del adhesion_event_f
del adhesion_event_d
del number_adhesion_events
del diff_list_total
del area_total
del y_list
del adhesion_values
del b_persistence_length
del L_contour_length
del new_plot
del peaks_values
del file_list

del last_b_persistence_length
del last_L_contour_length
del last_peaks_value

play_sound()

#This resets all variables
%reset out
gc.collect()

print('done')
```

Appendix E

Voinova fits

In Chapter 4, we used the Biolin Dfind software to fit experimental values of Δf and ΔD measured with QCM-D to the Voinova model detailed in Section 2.1.2. This yielded values of layer thickness h_{layer}, viscosity η_{layer} and elastic modulus μ_{layer}. The fit was obtained from the 3rd, 5th, 7, 9th and 11th overtones, but we only present the 3rd and 11th in the following figures for clarity. The input parameters for mucin were layer density $\rho_{layer} = 1050$ kg.m^{-3}, whilst the PBS density and viscosity were set to $\rho_{fluid} = 1006$ kg.m^{-3} and $\eta_{fluid} = 1.03$ mPa.s, respectively. For the OVDs, we used $\rho_{layer} = 1000$ kg.m^{-3}.

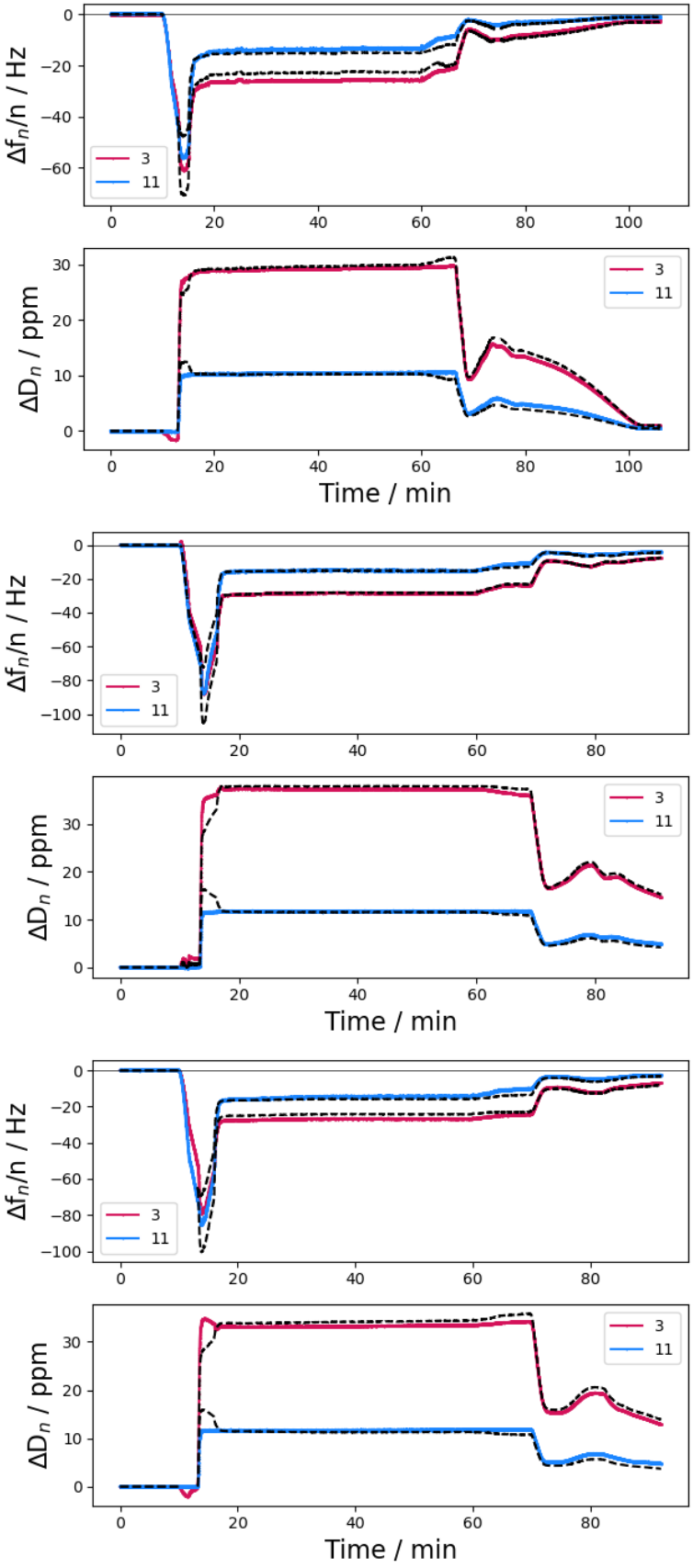

Figure E.1 *Changes in frequency (upper panel) and dissipation (lower panel) for the 3rd (pink) and 11th overtone (blue) observed with QCM-D when injecting a 15000 ppm solution of Hyadel in PBS. The Biolin Dfind software was used to fit the experimental data to the Voinova model for viscoelastic layers (dashed line).*

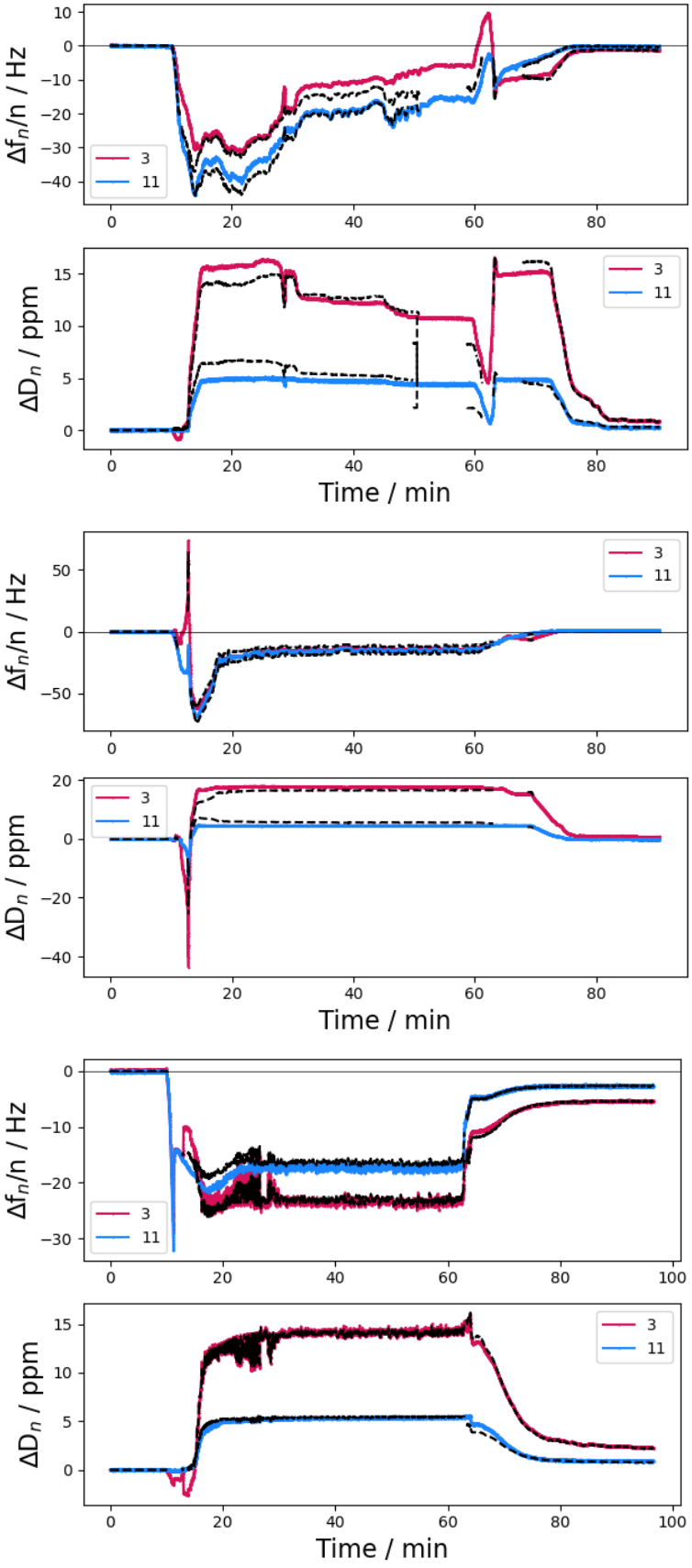

Figure E.2 *Changes in frequency (upper panel) and dissipation (lower panel) for the 3rd (pink) and 11th overtone (blue) observed with QCM-D when injecting a 25 ppm solution of mucin in PBS. The Biolin Dfind software was used to fit the experimental data to the Voinova model for viscoelastic layers (dashed line).*

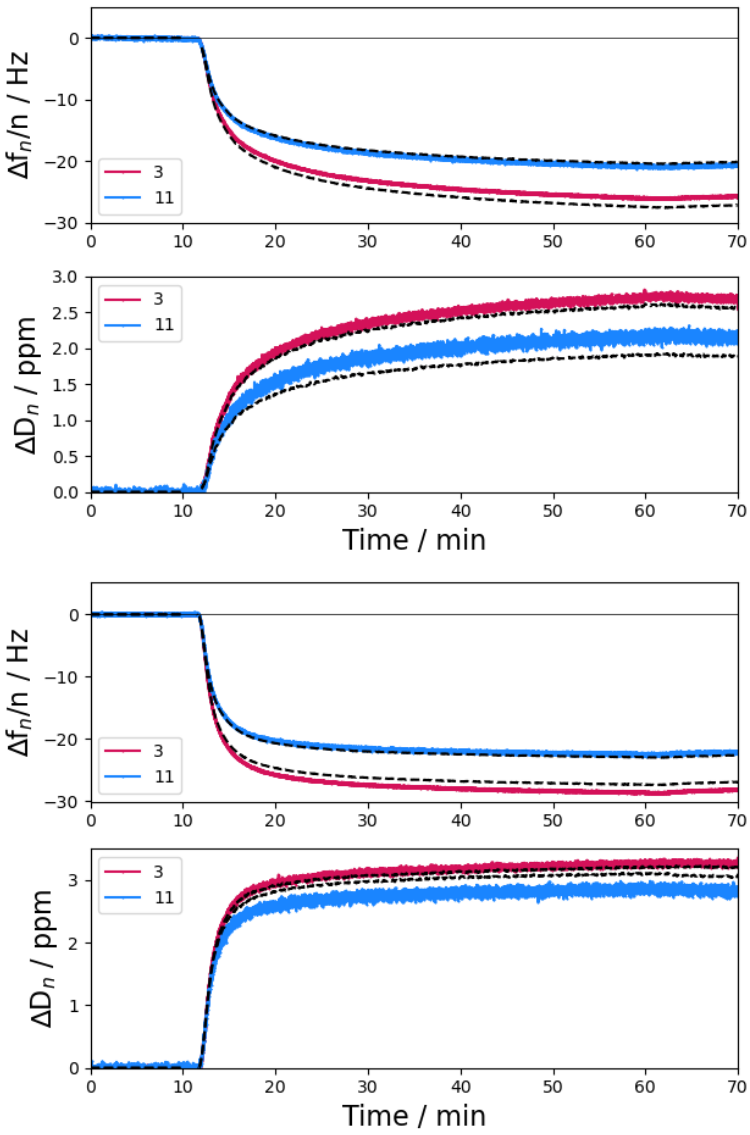

Figure E.3 *Changes in frequency (upper panel) and dissipation (lower panel) for the 3rd (pink) and 11th overtone (blue) observed with QCM-D when injecting a 7500 ppm solution of Hyaplus in PBS. The Biolin Dfind software was used to fit the experimental data to the Voinova model for viscoelastic layers (dashed line).*

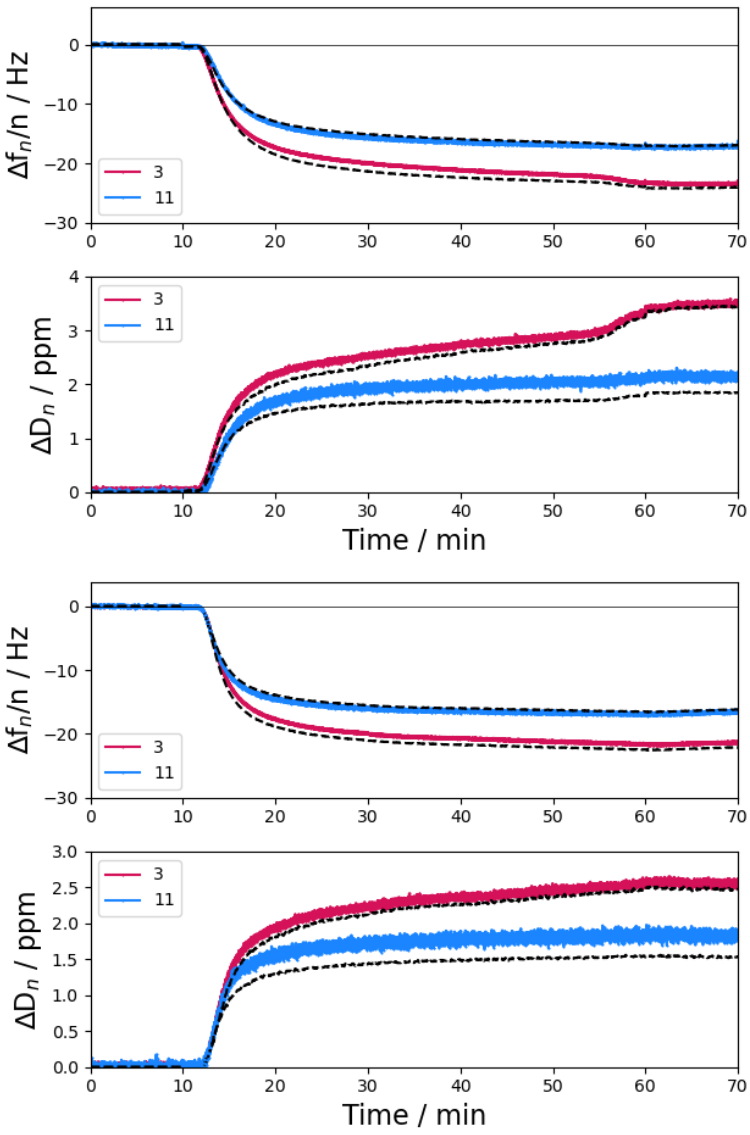

Figure E.4 *Changes in frequency (upper panel) and dissipation (lower panel) for the 3rd (pink) and 11th overtone (blue) observed with QCM-D when injecting a 25 ppm solution of mucin in PBS. The Biolin Dfind software was used to fit the experimental data to the Voinova model for viscoelastic layers (dashed line). A 7500 ppm Hyaplus solution was injected afterwards, as shown on Figure 4.17.*

Appendix F

Worm-like Chain Fits

In Chapter 5, we presented histograms to illustrate the distribution of parameters obtained from fitting individual spikes to the WLC model (see Figure 5.19). The parameters were the peak force, the contour length L and the persistence length b. b and L were fitted with respect to equation 2.20 using the function scipy.optimize.curve_fit, which uses non-linear least squares fit. These measurements were conducted using a glass substrate with a probe speed of 1 µm.s^{-1}. In Section F.1, we present a similar analysis performed at all the speeds of interest (1, 2.5, 5 and 10 µm.s^{-1}) as well as with a 1 s dwelling time on the surface at 2.5 µm.s^{-1}, and on the other substrates (gold, mucin, PLGA, PLL and HA). In Section F.2, we plot the average values of the output parameters against the probe speed on the surface for each substrate, taking into account the dwelling time on the surface.

F.1 Histograms

F.1.1 Glass

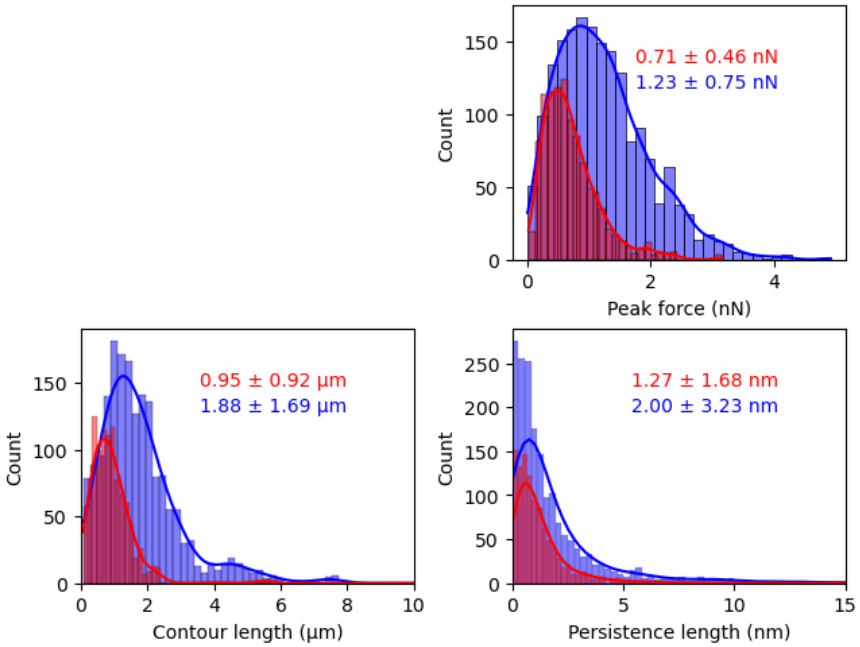

Figure F.1 *Histograms representing the distribution of spike adhesion force (upper right panel), contour length (lower left panel) and persistence length (lower right panel) obtained from WLC fits for cohesive Hyaplus (blue) and dispersive Hyadel (red) on glass with a probe speed of 2.5 $\mu m.s^{-1}$.*

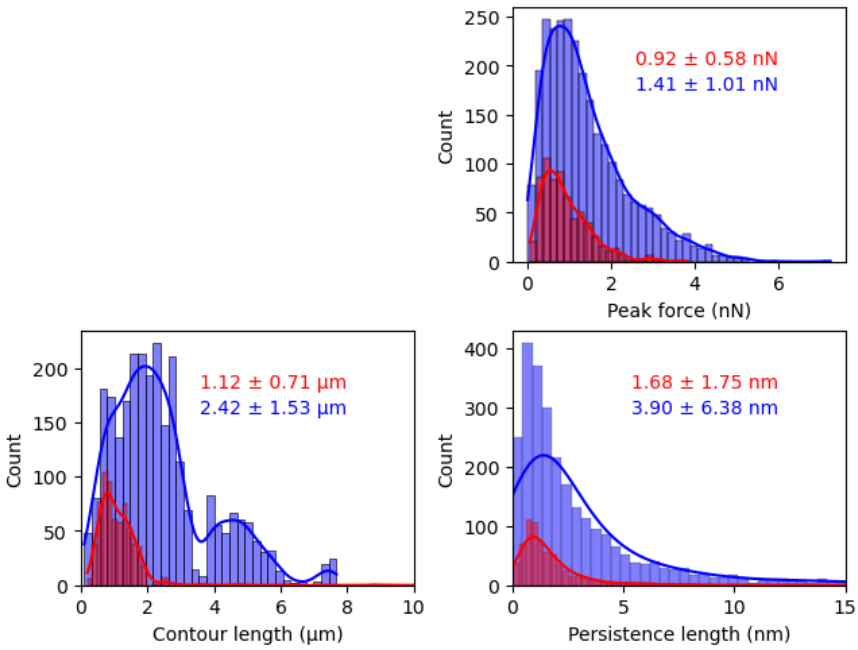

Figure F.2 *Histograms representing the distribution of spike adhesion force (upper right panel), contour length (lower left panel) and persistence length (lower right panel) obtained from WLC fits for cohesive Hyaplus (blue) and dispersive Hyadel (red) on glass with a probe speed of 2.5 µm.s^{-1} and a 1 s residence time on the surface.*

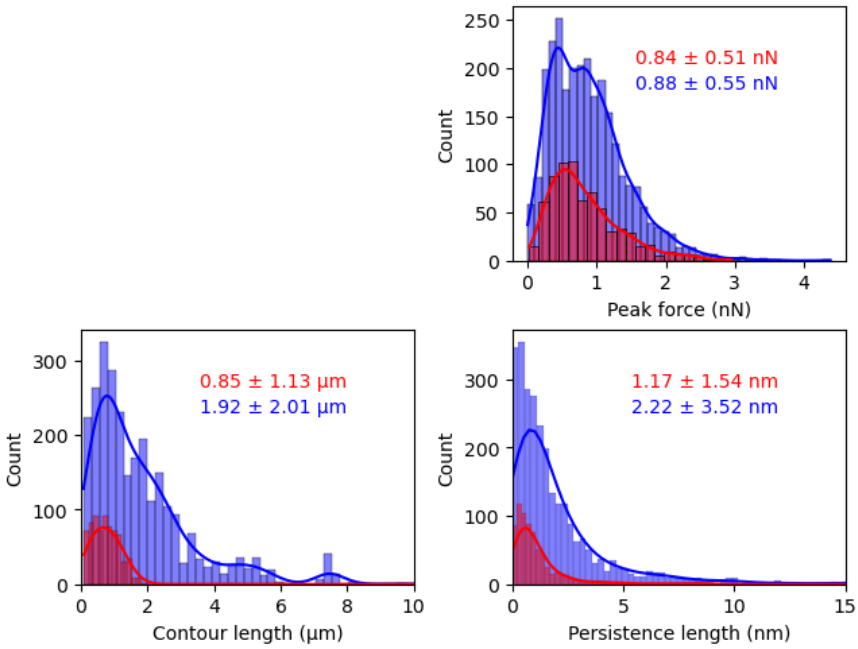

Figure F.3 *Histograms representing the distribution of spike adhesion force (upper right panel), contour length (lower left panel) and persistence length (lower right panel) obtained from WLC fits for cohesive Hyaplus (blue) and dispersive Hyadel (red) on glass with a probe speed of 5 µm.s^{-1}.*

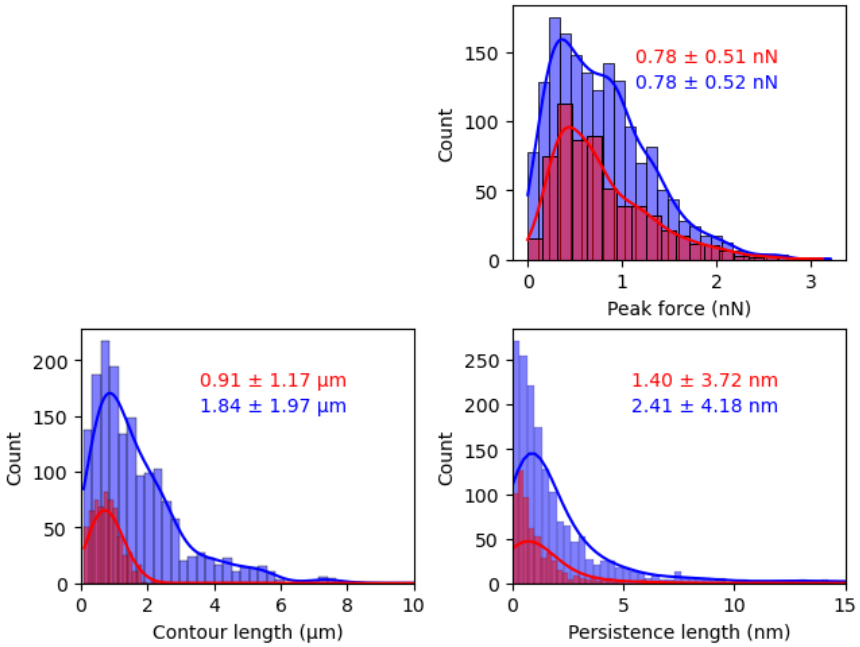

Figure F.4 *Histograms representing the distribution of spike adhesion force (upper right panel), contour length (lower left panel) and persistence length (lower right panel) obtained from WLC fits for cohesive Hyaplus (blue) and dispersive Hyadel (red) on glass with a probe speed of 10 $\mu m.s^{-1}$.*

F.1.2 Gold

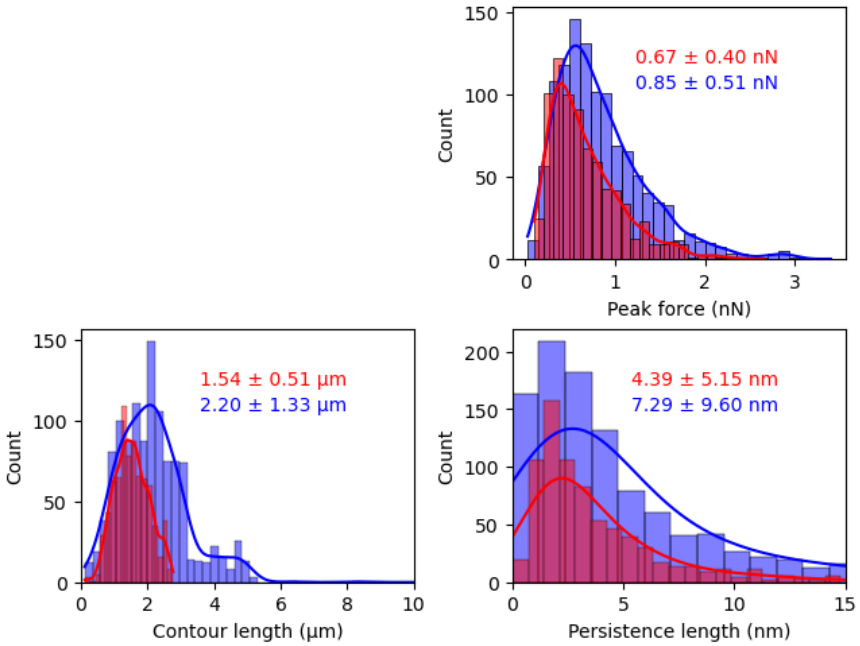

Figure F.5 *Histograms representing the distribution of spike adhesion force (upper right panel), contour length (lower left panel) and persistence length (lower right panel) obtained from WLC fits for cohesive Hyaplus (blue) and dispersive Hyadel (red) on gold with a probe speed of 1 $\mu m.s^{-1}$.*

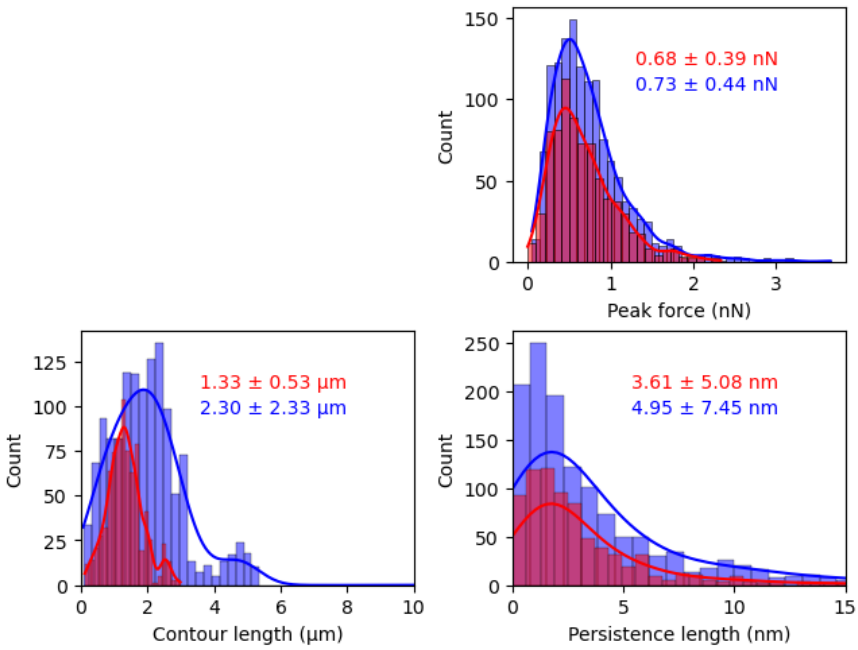

Figure F.6 *Histograms representing the distribution of spike adhesion force (upper right panel), contour length (lower left panel) and persistence length (lower right panel) obtained from WLC fits for cohesive Hyaplus (blue) and dispersive Hyadel (red) on gold with a probe speed of 2.5 µm.s^{-1}.*

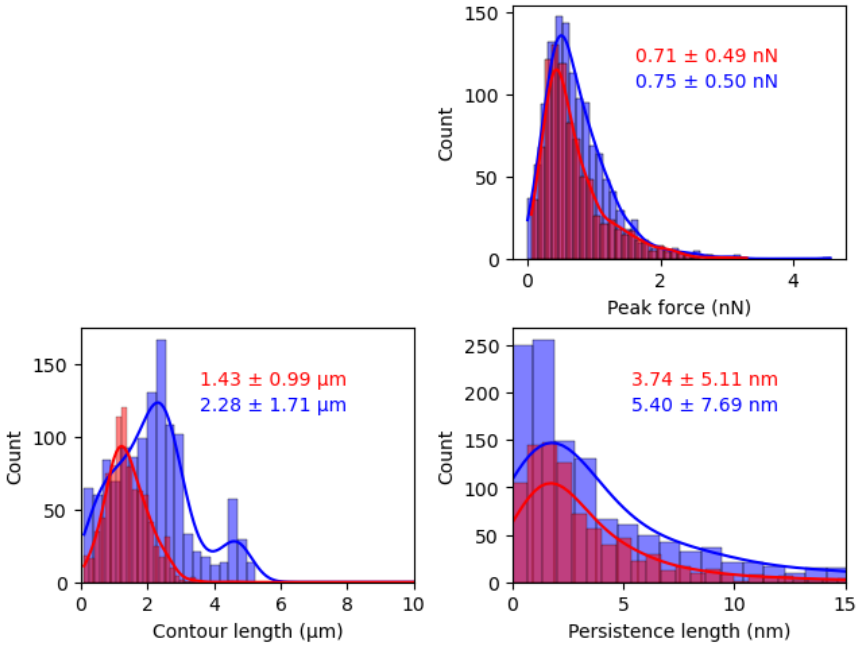

Figure F.7 *Histograms representing the distribution of spike adhesion force (upper right panel), contour length (lower left panel) and persistence length (lower right panel) obtained from WLC fits for cohesive Hyaplus (blue) and dispersive Hyadel (red) on gold with a probe speed of 2.5 µm.s^{-1} and a 1 s residence time on the surface.*

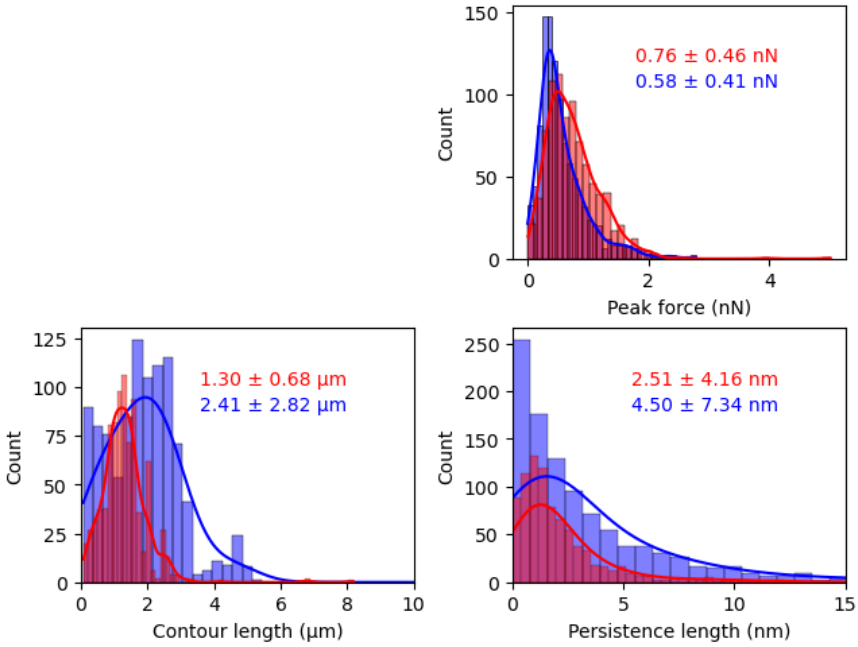

Figure F.8 *Histograms representing the distribution of spike adhesion force (upper right panel), contour length (lower left panel) and persistence length (lower right panel) obtained from WLC fits for cohesive Hyaplus (blue) and dispersive Hyadel (red) on gold with a probe speed of 5 µm.s^{-1}.*

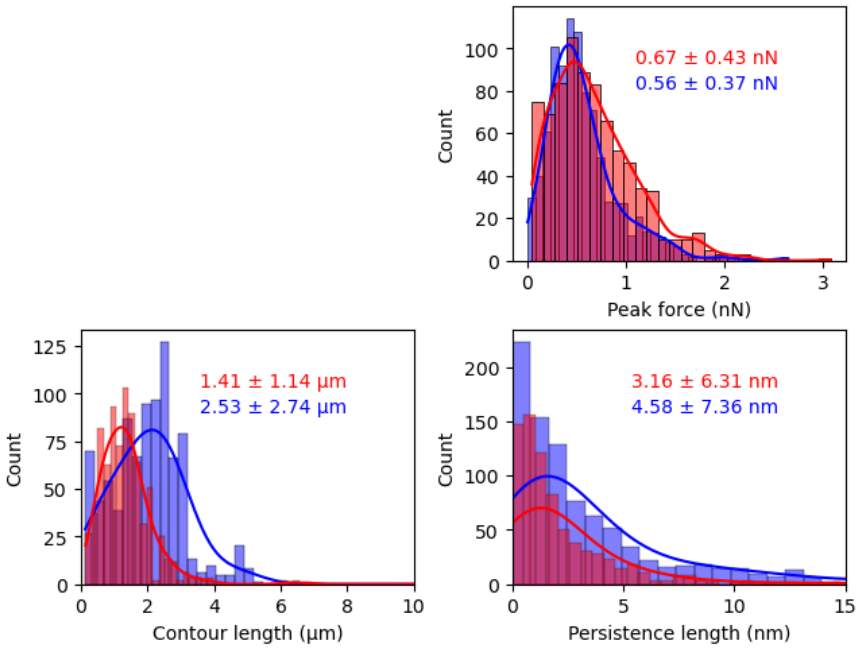

Figure F.9 *Histograms representing the distribution of spike adhesion force (upper right panel), contour length (lower left panel) and persistence length (lower right panel) obtained from WLC fits for cohesive Hyaplus (blue) and dispersive Hyadel (red) on gold with a probe speed of 10 µm.s^{-1}.*

F.1.3 Mucin

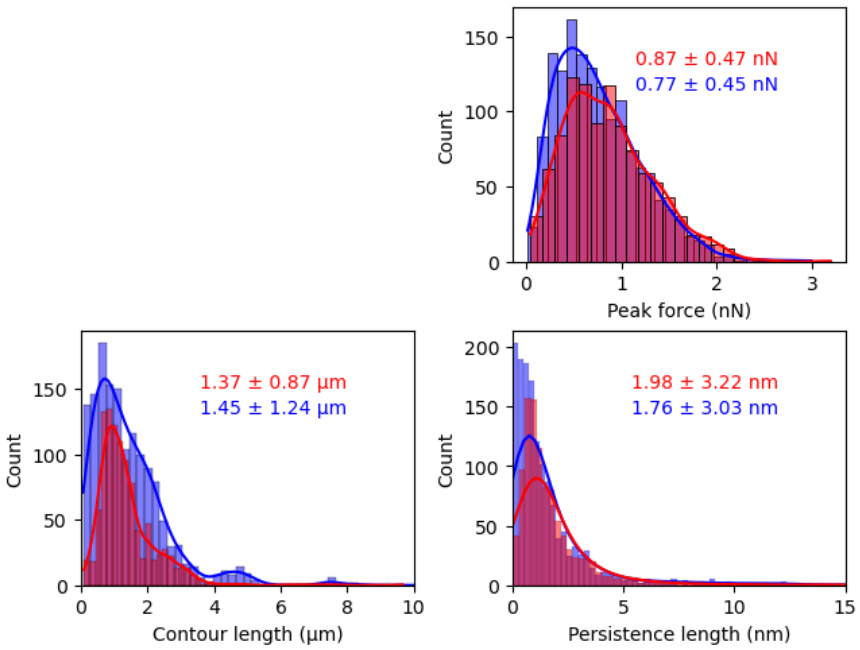

Figure F.10 *Histograms representing the distribution of spike adhesion force (upper right panel), contour length (lower left panel) and persistence length (lower right panel) obtained from WLC fits for cohesive Hyaplus (blue) and dispersive Hyadel (red) on mucin with a probe speed of 1 $\mu m.s^{-1}$.*

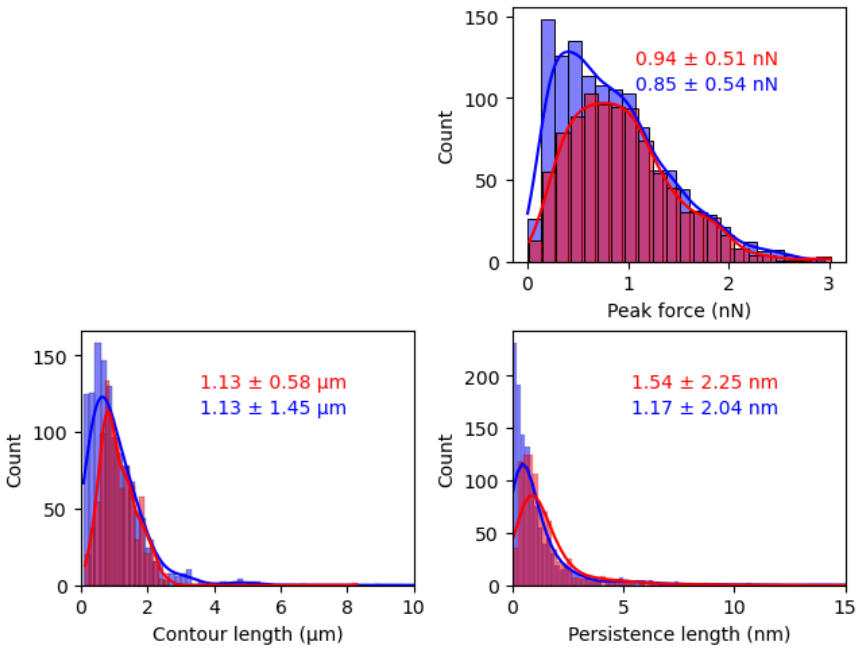

Figure F.11 *Histograms representing the distribution of spike adhesion force (upper right panel), contour length (lower left panel) and persistence length (lower right panel) obtained from WLC fits for cohesive Hyaplus (blue) and dispersive Hyadel (red) on mucin with a probe speed of 2.5 µm.s^{-1}.*

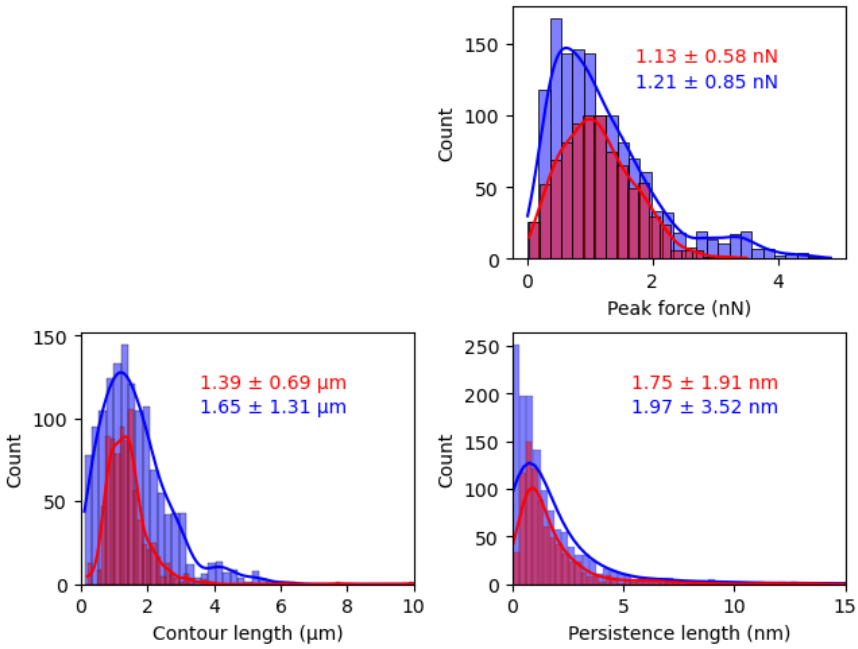

Figure F.12 *Histograms representing the distribution of spike adhesion force (upper right panel), contour length (lower left panel) and persistence length (lower right panel) obtained from WLC fits for cohesive Hyaplus (blue) and dispersive Hyadel (red) on mucin with a probe speed of 2.5 µm.s^{-1} and a 1 s residence time on the surface.*

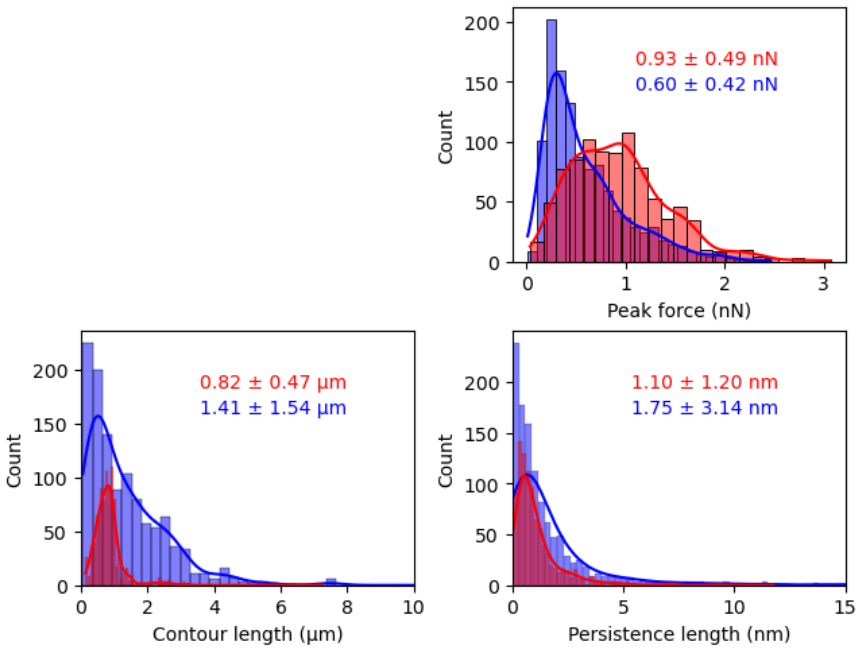

Figure F.13 *Histograms representing the distribution of spike adhesion force (upper right panel), contour length (lower left panel) and persistence length (lower right panel) obtained from WLC fits for cohesive Hyaplus (blue) and dispersive Hyadel (red) on mucin with a probe speed of 5 $\mu m.s^{-1}$.*

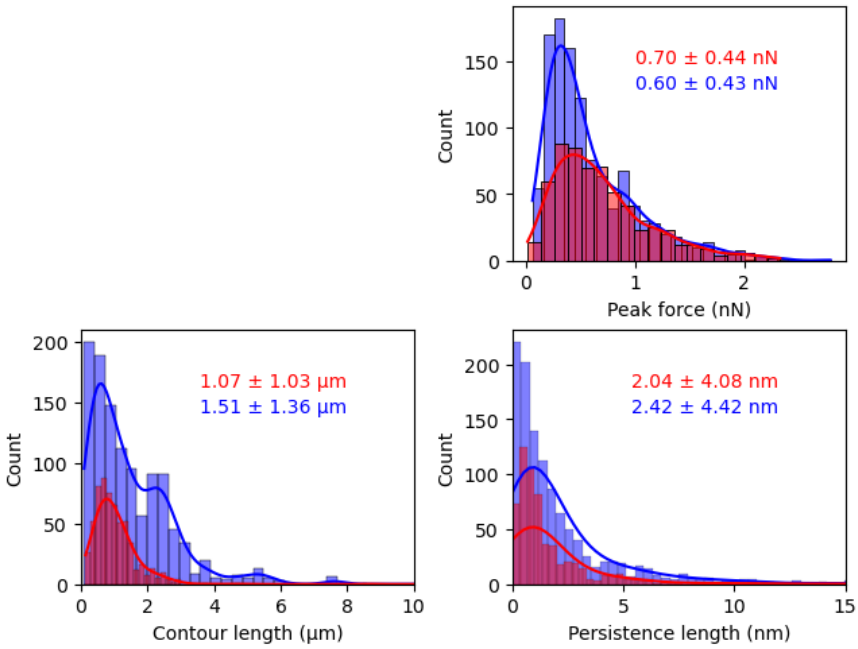

Figure F.14 *Histograms representing the distribution of spike adhesion force (upper right panel), contour length (lower left panel) and persistence length (lower right panel) obtained from WLC fits for cohesive Hyaplus (blue) and dispersive Hyadel (red) on mucin with a probe speed of 10 $\mu m.s^{-1}$.*

F.1.4 PLGA

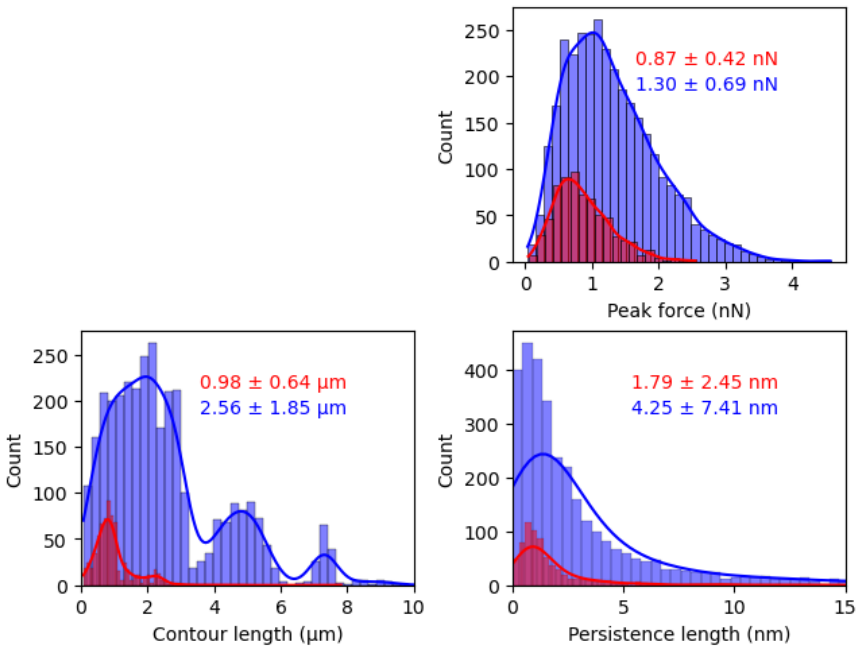

Figure F.15 *Histograms representing the distribution of spike adhesion force (upper right panel), contour length (lower left panel) and persistence length (lower right panel) obtained from WLC fits for cohesive Hyaplus (blue) and dispersive Hyadel (red) on PLGA with a probe speed of 1 $\mu m.s^{-1}$.*

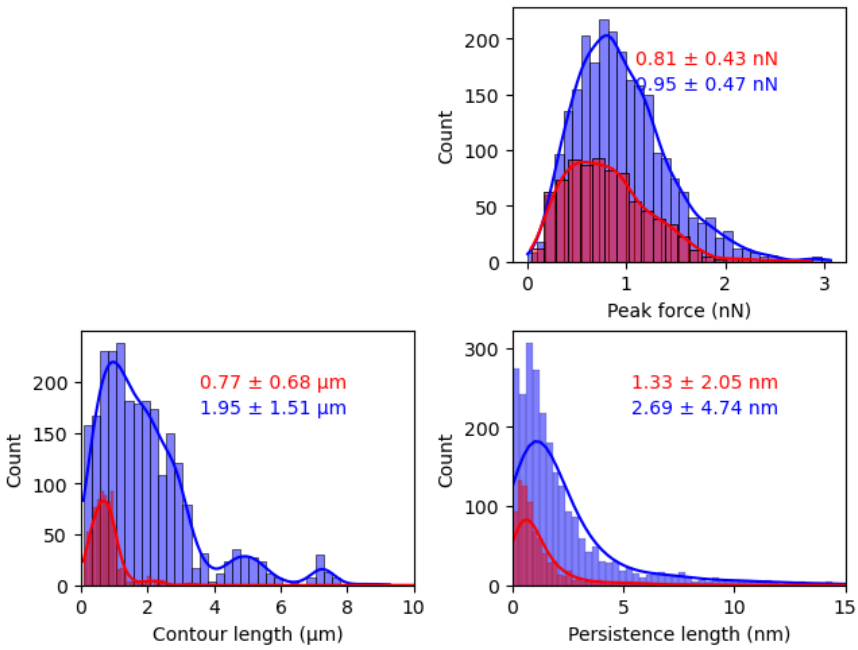

Figure F.16 *Histograms representing the distribution of spike adhesion force (upper right panel), contour length (lower left panel) and persistence length (lower right panel) obtained from WLC fits for cohesive Hyaplus (blue) and dispersive Hyadel (red) on PLGA with a probe speed of 2.5 µm.s^{-1}.*

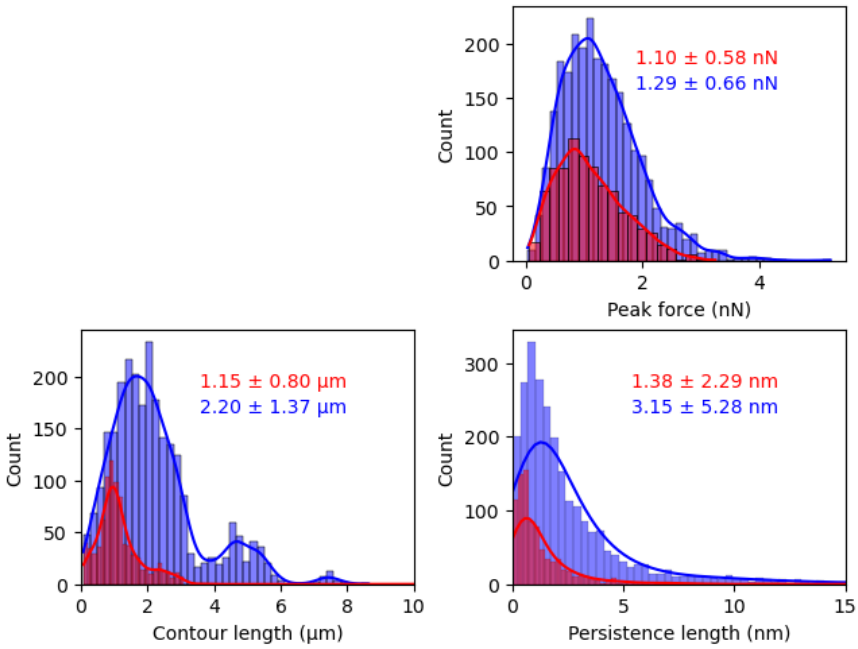

Figure F.17 *Histograms representing the distribution of spike adhesion force (upper right panel), contour length (lower left panel) and persistence length (lower right panel) obtained from WLC fits for cohesive Hyaplus (blue) and dispersive Hyadel (red) on PLGA with a probe speed of 2.5 µm.s^{-1} and a 1 s residence time on the surface.*

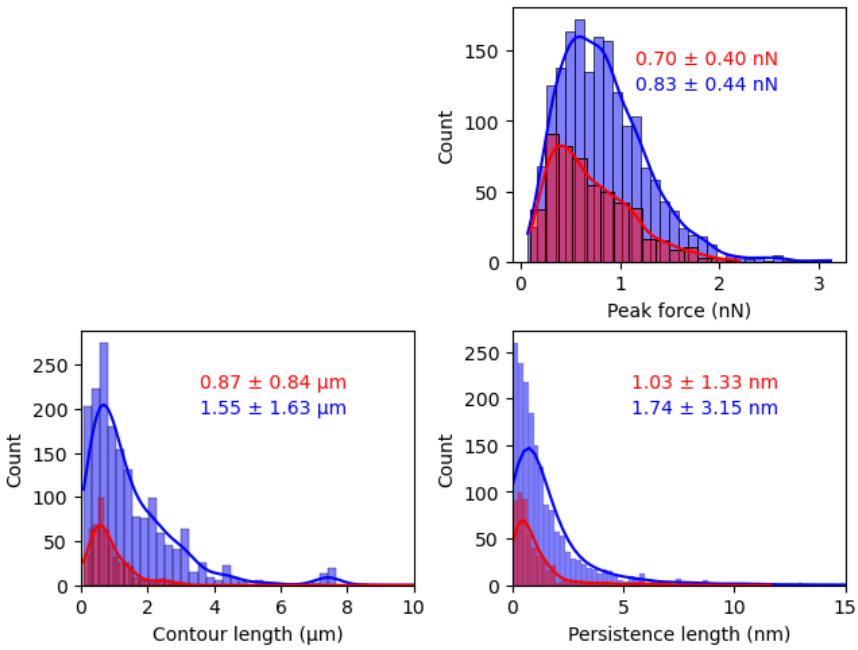

Figure F.18 *Histograms representing the distribution of spike adhesion force (upper right panel), contour length (lower left panel) and persistence length (lower right panel) obtained from WLC fits for cohesive Hyaplus (blue) and dispersive Hyadel (red) on PLGA with a probe speed of 5 $\mu m.s^{-1}$.*

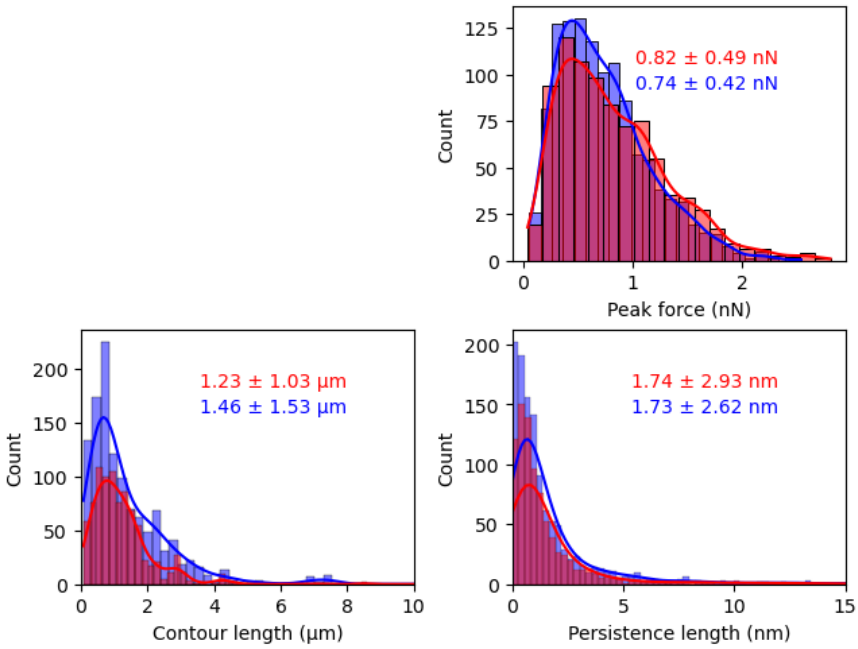

Figure F.19 *Histograms representing the distribution of spike adhesion force (upper right panel), contour length (lower left panel) and persistence length (lower right panel) obtained from WLC fits for cohesive Hyaplus (blue) and dispersive Hyadel (red) on PLGA with a probe speed of 10 $\mu m.s^{-1}$.*

F.1.5 PLL

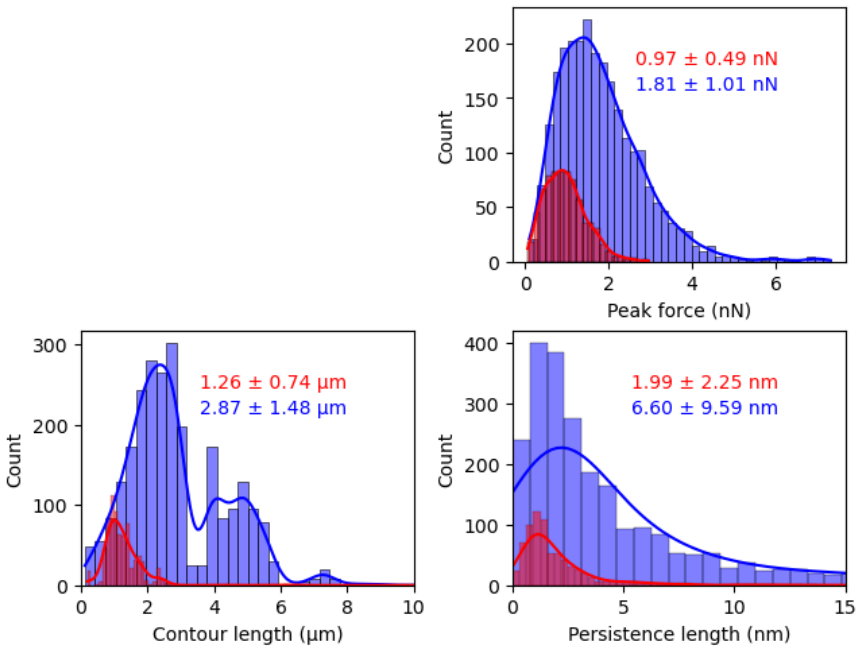

Figure F.20 *Histograms representing the distribution of spike adhesion force (upper right panel), contour length (lower left panel) and persistence length (lower right panel) obtained from WLC fits for cohesive Hyaplus (blue) and dispersive Hyadel (red) on PLL with a probe speed of 1 $\mu m.s^{-1}$.*

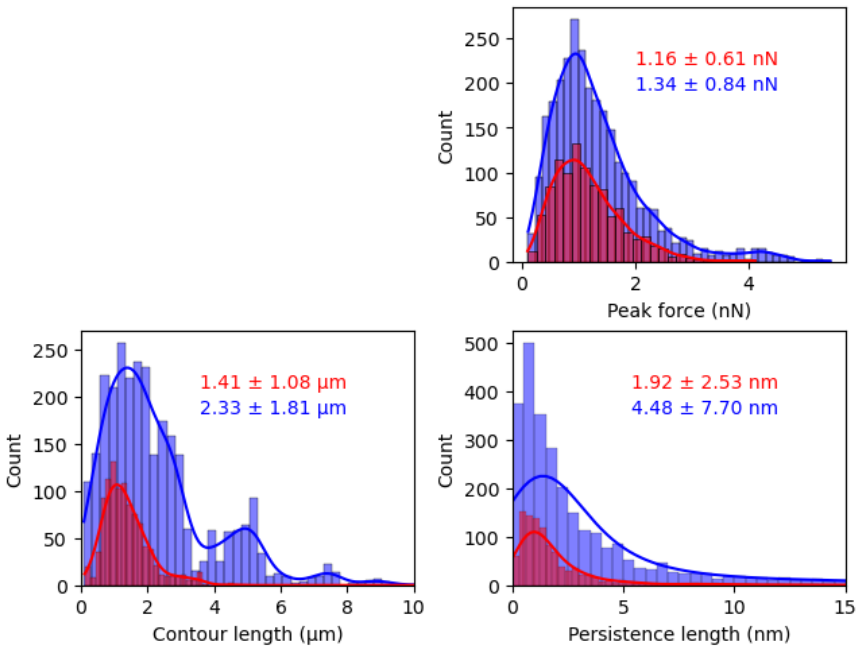

Figure F.21 *Histograms representing the distribution of spike adhesion force (upper right panel), contour length (lower left panel) and persistence length (lower right panel) obtained from WLC fits for cohesive Hyaplus (blue) and dispersive Hyadel (red) on PLL with a probe speed of 2.5 µm.s^{-1}.*

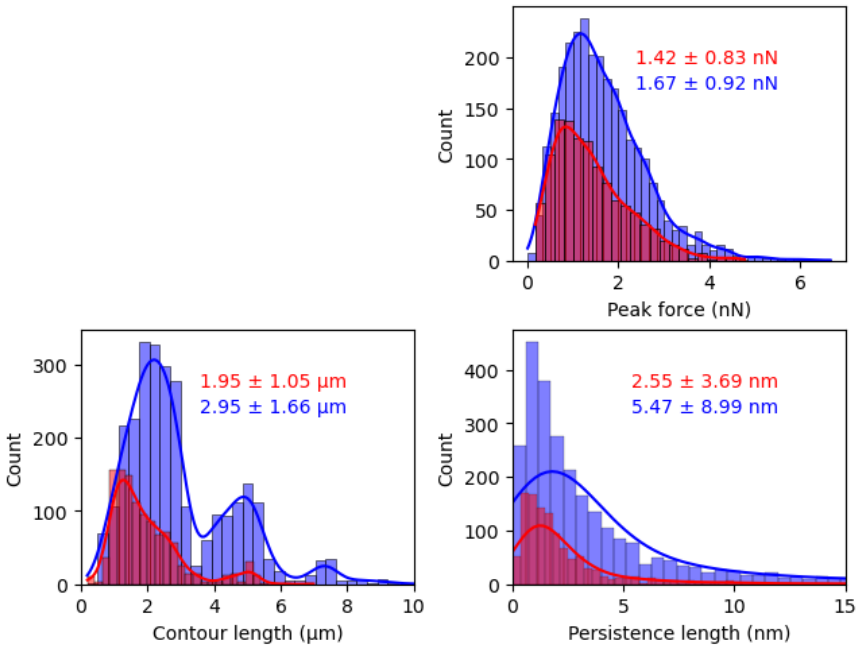

Figure F.22 *Histograms representing the distribution of spike adhesion force (upper right panel), contour length (lower left panel) and persistence length (lower right panel) obtained from WLC fits for cohesive Hyaplus (blue) and dispersive Hyadel (red) on PLL with a probe speed of 2.5 µm.s^{-1} and a 1 s residence time on the surface.*

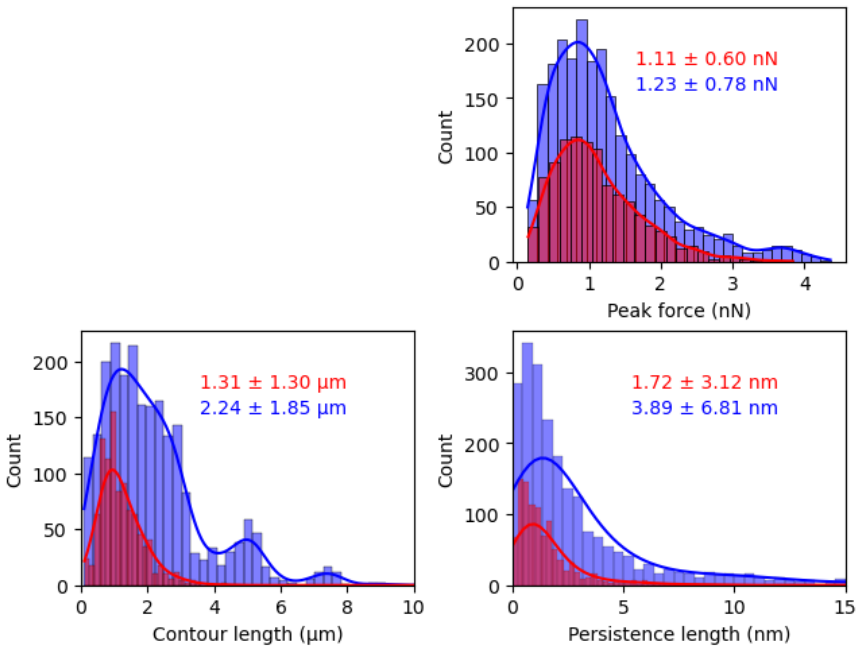

Figure F.23 *Histograms representing the distribution of spike adhesion force (upper right panel), contour length (lower left panel) and persistence length (lower right panel) obtained from WLC fits for cohesive Hyaplus (blue) and dispersive Hyadel (red) on PLL with a probe speed of 5 $\mu m.s^{-1}$.*

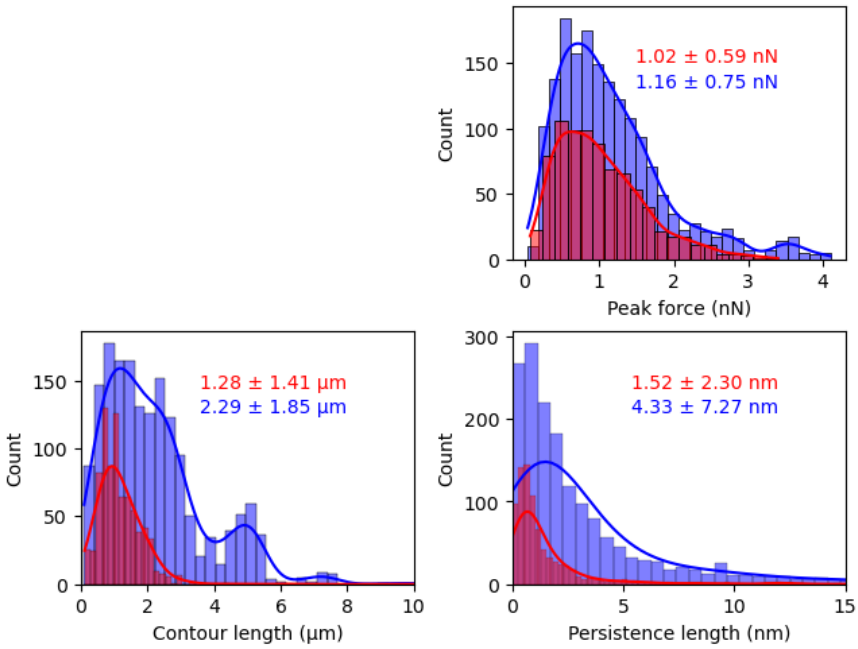

Figure F.24 *Histograms representing the distribution of spike adhesion force (upper right panel), contour length (lower left panel) and persistence length (lower right panel) obtained from WLC fits for cohesive Hyaplus (blue) and dispersive Hyadel (red) on PLL with a probe speed of 10 $\mu m.s^{-1}$.*

F.1.6 HA

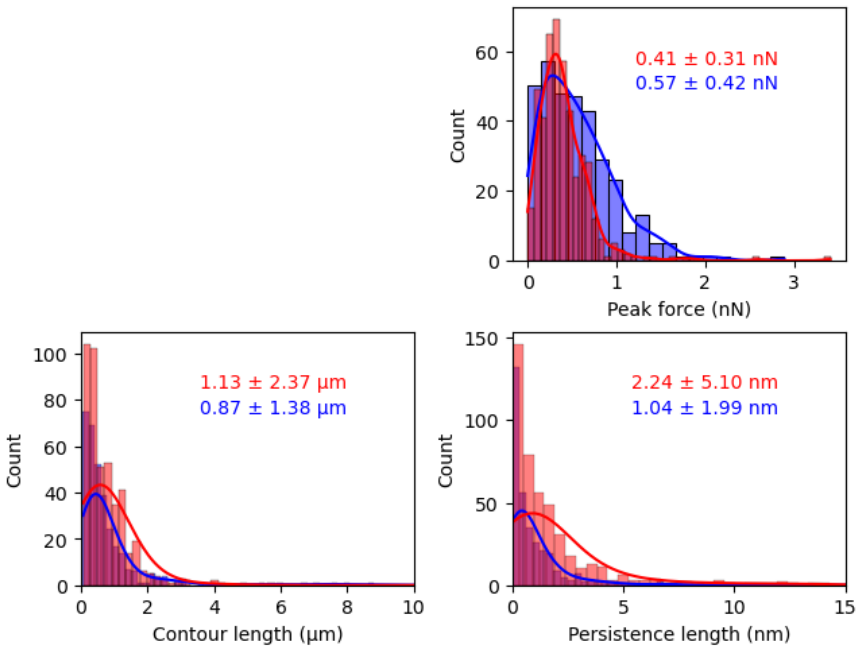

Figure F.25 *Histograms representing the distribution of spike adhesion force (upper right panel), contour length (lower left panel) and persistence length (lower right panel) obtained from WLC fits for cohesive Hyaplus (blue) and dispersive Hyadel (red) on HA with a probe speed of 1 µm.s^{-1}.*

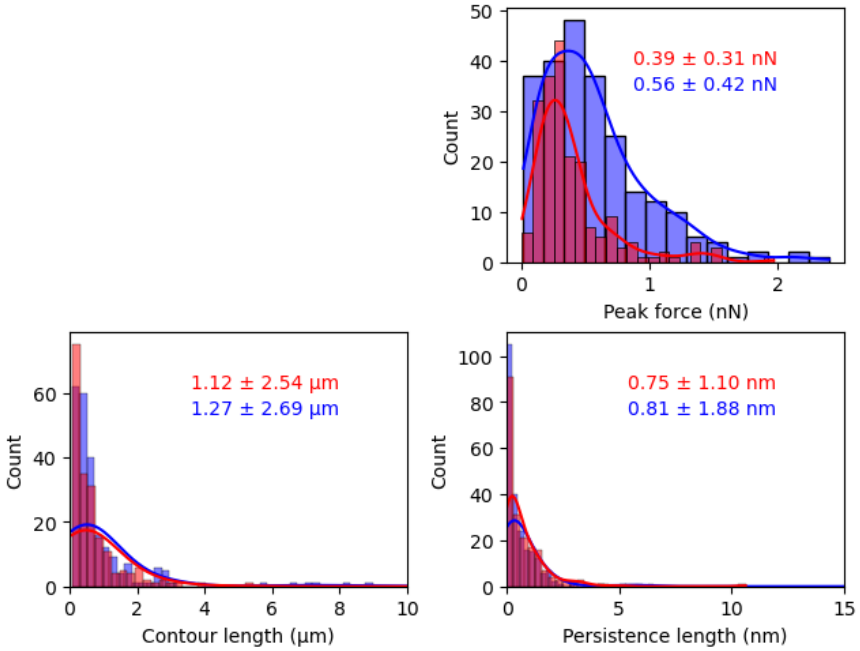

Figure F.26 *Histograms representing the distribution of spike adhesion force (upper right panel), contour length (lower left panel) and persistence length (lower right panel) obtained from WLC fits for cohesive Hyaplus (blue) and dispersive Hyadel (red) on HA with a probe speed of 2.5 µm.s^{-1}.*

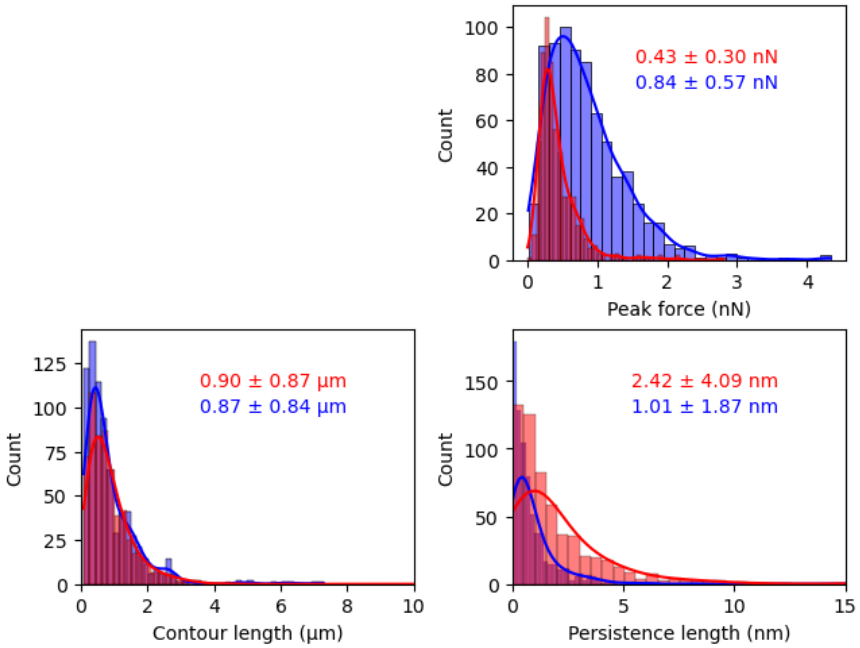

Figure F.27 *Histograms representing the distribution of spike adhesion force (upper right panel), contour length (lower left panel) and persistence length (lower right panel) obtained from WLC fits for cohesive Hyaplus (blue) and dispersive Hyadel (red) on HA with a probe speed of 2.5 µm.s^{-1} and a 1 s residence time on the surface.*

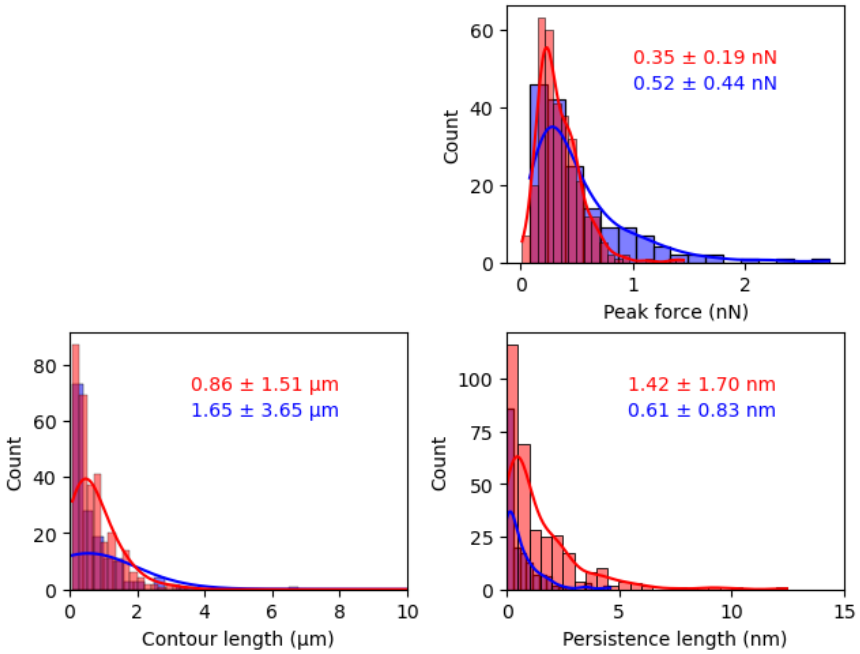

Figure F.28 *Histograms representing the distribution of spike adhesion force (upper right panel), contour length (lower left panel) and persistence length (lower right panel) obtained from WLC fits for cohesive Hyaplus (blue) and dispersive Hyadel (red) on HA with a probe speed of 5 µm.s^{-1}.*

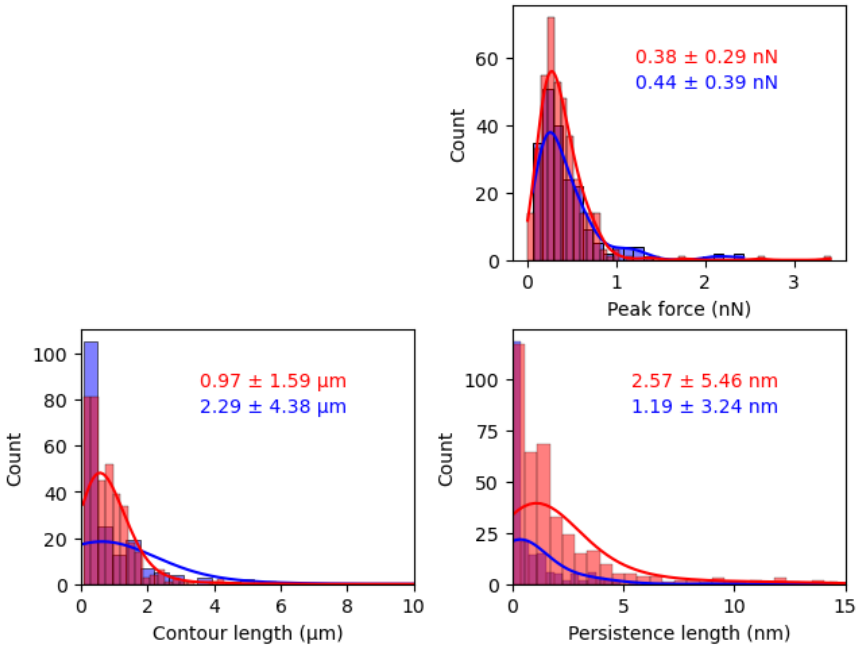

Figure F.29 *Histograms representing the distribution of spike adhesion force (upper right panel), contour length (lower left panel) and persistence length (lower right panel) obtained from WLC fits for cohesive Hyaplus (blue) and dispersive Hyadel (red) on HA with a probe speed of 10 µm.s^{-1}.*

F.2 Dependence on Probe Speed and Dwelling Time

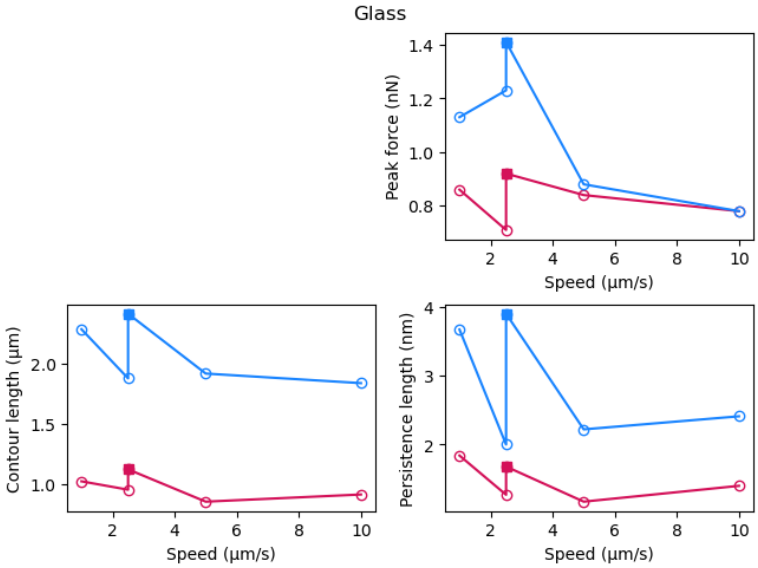

Figure F.30 *Evolution of the average spike adhesion force (upper right panel), contour length (lower left panel) and persistence length (lower right panel) obtained from WLC fits on glass for cohesive Hyaplus (blue) and dispersive Hyadel (pink) with respect to probe speed. The empty symbols correspond to immediate probe retraction, and the filled symbols correspond to a 1 s dwelling time on the surface.*

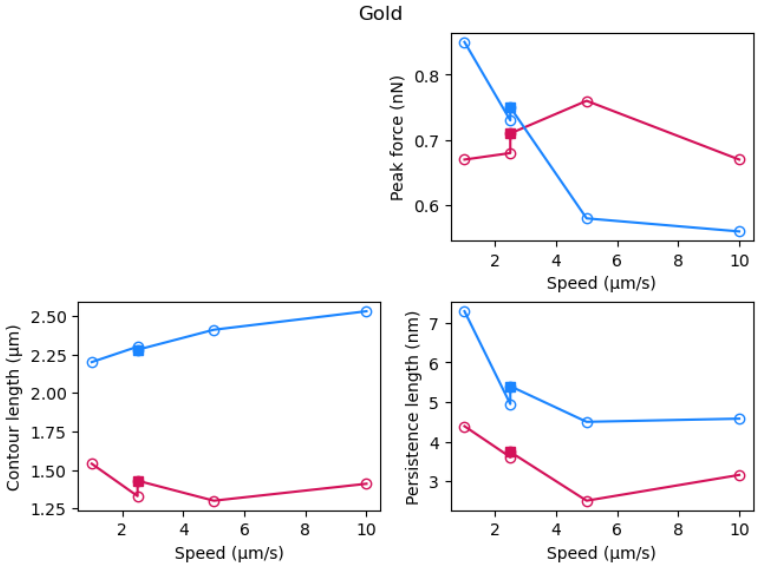

Figure F.31 *Evolution of the average spike adhesion force (upper right panel), contour length (lower left panel) and persistence length (lower right panel) obtained from WLC fits on gold for cohesive Hyaplus (blue) and dispersive Hyadel (pink) with respect to probe speed. The empty symbols correspond to immediate probe retraction, and the filled symbols correspond to a 1 s dwelling time on the surface.*

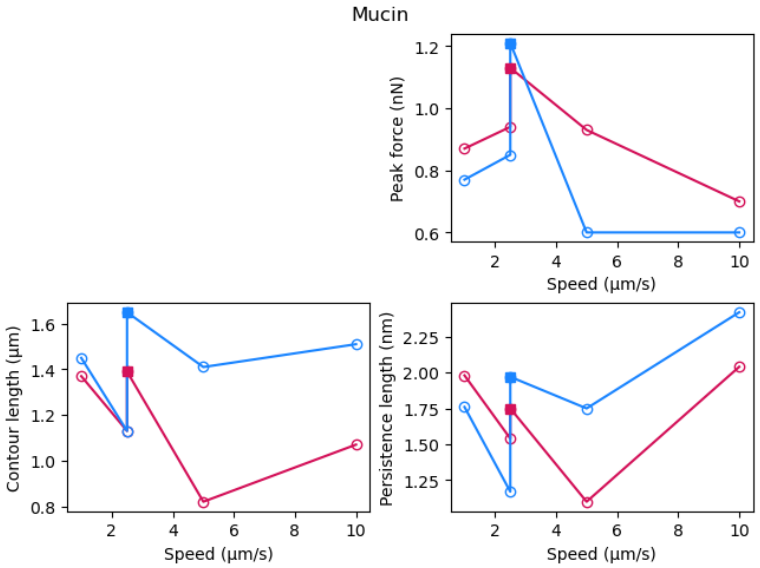

Figure F.32 *Evolution of the average spike adhesion force (upper right panel), contour length (lower left panel) and persistence length (lower right panel) obtained from WLC fits on mucin for cohesive Hyaplus (blue) and dispersive Hyadel (pink) with respect to probe speed. The empty symbols correspond to immediate probe retraction, and the filled symbols correspond to a 1 s dwelling time on the surface.*

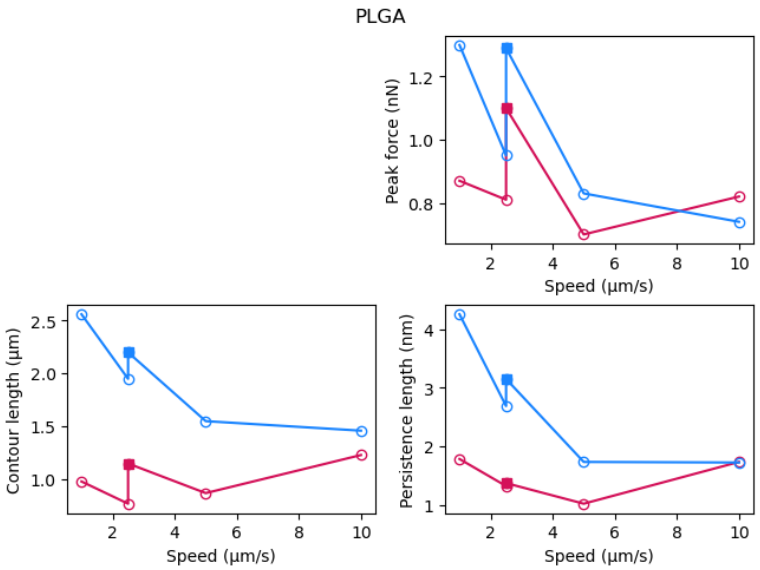

Figure F.33 *Evolution of the average spike adhesion force (upper right panel), contour length (lower left panel) and persistence length (lower right panel) obtained from WLC fits on PLGA for cohesive Hyaplus (blue) and dispersive Hyadel (pink) with respect to probe speed. The empty symbols correspond to immediate probe retraction, and the filled symbols correspond to a 1 s dwelling time on the surface.*

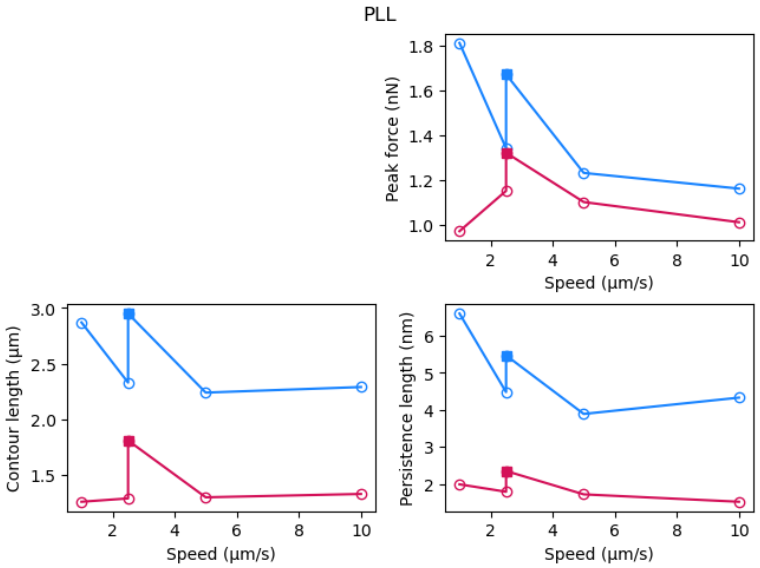

Figure F.34 *Evolution of the average spike adhesion force (upper right panel), contour length (lower left panel) and persistence length (lower right panel) obtained from WLC fits on PLL for cohesive Hyaplus (blue) and dispersive Hyadel (pink) with respect to probe speed. The empty symbols correspond to immediate probe retraction, and the filled symbols correspond to a 1 s dwelling time on the surface.*

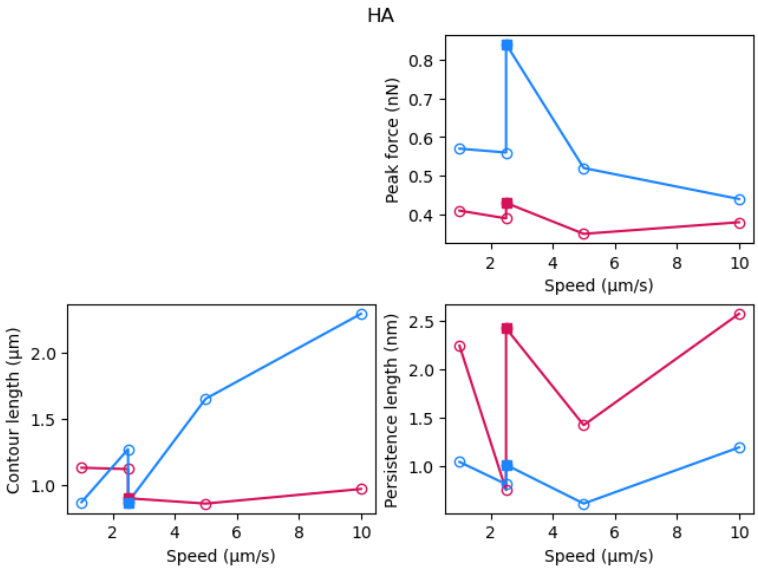

Figure F.35 *Evolution of the average spike adhesion force (upper right panel), contour length (lower left panel) and persistence length (lower right panel) obtained from WLC fits on HA for cohesive Hyaplus (blue) and dispersive Hyadel (pink) with respect to probe speed. The empty symbols correspond to immediate probe retraction, and the filled symbols correspond to a 1 s dwelling time on the surface.*

Bibliography

[1] Tommaso Rossi, Mario R. Romano, Danilo Iannetta, Vito Romano, Luca Gualdi, Isabella D'Agostino, and Guido Ripandelli. Cataract surgery practice patterns worldwide: A survey. *BMJ Open Ophthalmology*, 6(1):e000464, January 2021. ISSN 2397-3269. doi: 10.1136/bmjophth-2020-000464.

[2] Dennis Lam, Srinivas K. Rao, Vineet Ratra, Yizhi Liu, Paul Mitchell, Jonathan King, Marie-José Tassignon, Jost Jonas, Chi P. Pang, and David F. Chang. Cataract. *Nat Rev Dis Primers*, 1(1):1–15, June 2015. ISSN 2056-676X. doi: 10.1038/nrdp.2015.14.

[3] Manik Goel, Renata G Picciani, Richard K Lee, and Sanjoy K Bhattacharya. Aqueous Humor Dynamics: A Review. *Open Ophthalmol J*, 4:52–59, September 2010. ISSN 1874-3641. doi: 10.2174/1874364101004010052.

[4] Mittanamalli S. Sridhar. Anatomy of cornea and ocular surface. *Indian J Ophthalmol*, 66(2):190–194, February 2018. ISSN 1998-3689. doi: 10.4103/ijo.IJO_646_17.

[5] Parker E. Ludwig, Michael J. Lopez, and Karlin E. Sevensma. Anatomy, Head and Neck, Eye Cornea. In *StatPearls*. StatPearls Publishing, Treasure Island (FL), 2024.

[6] Nancy C Joyce. Proliferative capacity of the corneal endothelium. *Progress in Retinal and Eye Research*, 22(3):359–389, May 2003. ISSN 1350-9462. doi: 10.1016/S1350-9462(02)00065-4.

[7] S. J. Tuft and D. J. Coster. The corneal endothelium. *Eye (London, England)*, 4 (Pt 3):389–424, 1990. ISSN 0950-222X. doi: 10.1038/eye.1990.53.

[8] Zhiguo He, Nelly Campolmi, Philippe Gain, Binh Minh Ha Thi, Jean-Marc Dumollard, Sébastien Duband, Michel Peoc'h, Simone Piselli, Olivier Garraud, and Gilles Thuret. Revisited microanatomy of the corneal endothelial periphery: New evidence for continuous centripetal migration of endothelial cells in humans. *Stem Cells*, 30(11):2523–2534, November 2012. ISSN 1549-4918. doi: 10.1002/stem.1212.

[9] Angela Y. Chang and Boonkit Purt. Biochemistry, Tear Film. In *StatPearls*. StatPearls Publishing, Treasure Island (FL), 2024.

[10] Chen-Yuan Charlie Yang, Tiffany Huynh, Mark Johnson, and Haiyan Gong. Endothelial glycocalyx layer in the aqueous outflow pathway of bovine and human eyes. *Experimental Eye Research*, 128:27–33, November 2014. ISSN 0014-4835. doi: 10.1016/j.exer.2014.08.015.

[11] Ilene K. Gipson and Pablo Argüeso. Role of mucins in the function of the corneal and conjunctival epithelia. *Int Rev Cytol*, 231:1–49, 2003. ISSN 0074-7696. doi: 10.1016/s0074-7696(03)31001-0.

[12] J. a. P. Gomes, R. Amankwah, A. Powell-Richards, and H. S. Dua. Sodium hyaluronate (hyaluronic acid) promotes migration of human corneal epithelial cells in vitro. *British Journal of Ophthalmology*, 88(6):821–825, June 2004. ISSN 0007-1161, 1468-2079. doi: 10.1136/bjo.2003.027573.

[13] Mary K. Cowman and Eva A. Turley. Functional organization of extracellular hyaluronan, CD44, and RHAMM. *Proteoglycan Research*, 1 (2):e4, 2023. ISSN 2832-3556. doi: 10.1002/pgr2.4.

[14] Kendrick M. Wang, Albert S. Jun, John G. Ladas, and Uday Devgan. Phacoemulsification: Principles and Techniques. In *Albert and Jakobiec's Principles and Practice of Ophthalmology: Fourth Edition*, pages 1467–1489. Springer International Publishing, January 2022. doi: 10.1007/978-3-030-42634-7_191.

[15] N. Ray-Chaudhuri, G.M. Voros, S. Sutherland, and F.C. Figueiredo. Comparison of the effect of sodium hyaluronate (ophthalin®) and hydroxypropylmethylcellulose (HPMC-ophtal®) on corneal endothelium, central corneal thickness, and intraocular pressure after phacoemulsification. *European Journal of Ophthalmology*, 16(2):239–246, 2006. doi: 10.1177/112067210601600208.

[16] Hyung Bin Hwang, Byul Lyu, Hye Bin Yim, and Na Young Lee. Endothelial Cell Loss after Phacoemulsification according to Different Anterior Chamber Depths. *J Ophthalmol*, 2015, 2015. ISSN 2090-004X. doi: 10.1155/2015/210716.

[17] Tony Walkow, Norbert Anders, and Sonja Klebe. Endothelial cell loss after phacoemulsification: Relation to preoperative and intraoperative parameters. *Journal of Cataract & Refractive Surgery*, 26(5):727, May 2000. ISSN 0886-3350. doi: 10.1016/S0886-3350(99)00462-9.

[18] Tina Wong, Melanie Hingorani, and Vincent Lee. Phacoemulsification time and power requirements in phaco chop and divide and conquer nucleofractis techniques11None of the authors has a financial or proprietary interest in any material or method mentioned. *Journal of Cataract & Refractive Surgery*, 26(9):1374–1378, September 2000. ISSN 0886-3350. doi: 10.1016/S0886-3350(00)00538-1.

[19] Stephan D Schulze, Thomas Bertelmann, Irena Manojlovic, Stefan Bodanowitz, Sebastian Irle, and Walter Sekundo. Changes in corneal endothelium cell characteristics after cataract surgery with and without use of viscoelastic substances during intraocular lens implantation. *Clin Ophthalmol*, 9:2073–2080, November 2015. ISSN 1177-5467. doi: 10.2147/OPTH.S90628.

[20] Åke S. Holmberg and Bo T. Philipson. Sodium Hyaluronate in Cataract Surgery: II. Report on the Use of Healon® in Extracapsular Cataract Surgery Using Phacoemulsification. *Ophthalmology*, 91(1):53–59, January 1984. ISSN 0161-6420. doi: 10.1016/S0161-6420(84)34340-8.

[21] Karl Meyer and John W. Palmer. The Polysaccharide of the Vitreous Humor. *J. Biol. Chem.*, 107(3):629–634, December 1934. ISSN 0021-9258, 1083-351X.

[22] J. W. Kuo and G. D. Prestwich. 2.214 - Hyaluronic Acid. In Paul Ducheyne, editor, *Comprehensive Biomaterials*, pages 239–259. Elsevier, Oxford, January 2011. ISBN 978-0-08-055294-1. doi: 10.1016/B978-0-08-055294-1.00073-8.

[23] Ulf Stenevi, Todd Gwin, Anders Harfstrand, and David Apple. Demonstration of Hyaluronic Acid Binding to Corneal Endothelial Cells in Human Eye-Bank Eyes. *European journal of Implant and Refractive Surgery*, 5(4):228–232, December 1993. ISSN 0955-3681. doi: 10.1016/S0955-3681(13)80162-1.

[24] K. Madsen, M. Schenholm, G. Jahnke, and A. Tengblad. Hyaluronate binding to intact corneas and cultured endothelial cells. *Invest. Ophthalmol. Vis. Sci.*, 30(10):2132–2137, October 1989. ISSN 0146-0404.

[25] H. Burkhard Dick, Frank Krummenauer, Albert J Augustin, Tadeusz Pakula, and Norbert Pfeiffer. Healon5 viscoadaptive formulation: Comparison to Healon and Healon GV11None of the authors has a financial or proprietary interest in any material or method mentioned. *Journal of Cataract & Refractive Surgery*, 27(2):320–326, February 2001. ISSN 0886-3350. doi: 10.1016/S0886-3350(00)00482-X.

[26] Gerd U. Auffarth, Mike P. Holzer, Nithi Visessook, David J. Apple, and Hans E. Völcker. Removal times for a dispersive and a cohesive ophthalmic viscosurgical device correlated with intraocular lens material. *Journal of Cataract & Refractive Surgery*, 30(11):2410–2414, November 2004. ISSN 0886-3350. doi: 10.1016/j.jcrs.2004.03.039.

[27] Eric J Linebarger, David R Hardten, Gaurav K Shah, and Richard L Lindstrom. Phacoemulsification and Modern Cataract Surgery. *Survey of Ophthalmology*, 44(2):123–147, September 1999. ISSN 0039-6257. doi: 10.1016/S0039-6257(99)00085-5.

[28] Ehud I. Assia, David J. Apple, Edward S. Lim, Robin C. Morgan, and Julie C. Tsai. Removal of viscoelastic materials after experimental cataract surgery in vitro. *Journal of Cataract & Refractive Surgery*, 18(1):3–6, January 1992. ISSN 0886-3350. doi: 10.1016/S0886-3350(13)80376-8.

[29] Hiroko Bissen-Miyajima. In vitro behavior of ophthalmic viscosurgical devices during phacoemulsification. *J Cataract Refract Surg*, 32(6):1026–1031, June 2006. ISSN 0886-3350. doi: 10.1016/j.jcrs.2006.02.039.

[30] Andreas F. Borkenstein, Eva-Maria Borkenstein, and Boris Malyugin. Ophthalmic Viscosurgical Devices (OVDs) in Challenging Cases: A Review. *Ophthalmology and Therapy*, 10(4):831–843, December 2021. ISSN 2193-6528. doi: 10.1007/s40123-021-00403-9.

[31] Steve A. Arshinoff. Dispersive-cohesive viscoelastic soft shell technique. *Journal of Cataract & Refractive Surgery*, 25(2):167–173, February 1999. ISSN 0886-3350. doi: 10.1016/S0886-3350(99)80121-7.

[32] ZEISS OVDs - ophthalmic viscosurgical devices. URL `https://www.zeiss.com/meditec/en/products/iols/ovds.html`.

[33] Roger F. Steinert and Mark E. Schafer. Ultrasonic-generated fluid velocity with Sovereign WhiteStar micropulse and continuous phacoemulsification. *Journal of Cataract & Refractive Surgery*, 32(2):284–287, February 2006. ISSN 0886-3350. doi: 10.1016/j.jcrs.2005.09.025.

[34] Kotaro Oki. Measuring rectilinear flow within the anterior chamber in phacoemulsification procedures. *Journal of Cataract & Refractive Surgery*, 30(8):1759–1767, August 2004. ISSN 0886-3350. doi: 10.1016/j.jcrs.2003.12.035.

[35] G. Pirazzoli, D. D'Eliseo, M. Ziosi, and R. Acciarri. Effects of phacoemulsification time on the corneal endothelium using phacofracture and phaco chop techniques. *Journal of Cataract & Refractive Surgery*, 22(7):967–969, September 1996. ISSN 0886-3350. doi: 10.1016/S0886-3350(96)80200-8.

[36] S. Milazzo, P. Laurans, and P. Turut. Phacoémulsification. *EMC - Ophtalmologie*, 2(2):77–102, May 2005. ISSN 1762-584X. doi: 10.1016/j.emcop.2004.12.001.

[37] Ho Young Lee, Yoon Jung Choy, and Jong Seok Park. Comparison of OVD and BSS for Maintaining the Anterior Chamber during IOL Implantation. *Korean J Ophthalmol*, 25(1):15–21, February 2011. ISSN 1011-8942. doi: 10.3341/kjo.2011.25.1.15.

[38] Berenike C. Kunzmann, Daniel A. Wenzel, Karl U. Bartz-Schmidt, Martin S. Spitzer, and Maximilian Schultheiss. Effects of ultrasound energy on the porcine corneal endothelium – Establishment of a

phacoemulsification damage model. *Acta Ophthalmologica*, 98(2):e155–e160, 2020. ISSN 1755-3768. doi: 10.1111/aos.14235.

[39] Arisa Mitani, Takashi Suzuki, Yoshitaka Tasaka, Takahiro Uda, Yukako Hiramatsu, Shiro Kawasaki, and Yuichi Ohashi. Evaluation of a new method of irrigation and aspiration for removal of ophthalmic viscoelastic device during cataract surgery in a porcine model. *BMC Ophthalmol*, 14, November 2014. ISSN 1471-2415. doi: 10.1186/1471-2415-14-129.

[40] T Oshika, F Okamoto, Y Kaji, T Hiraoka, T Kiuchi, M Sato, and K Kawana. Retention and removal of a new viscous dispersive ophthalmic viscosurgical device during cataract surgery in animal eyes. *Br J Ophthalmol*, 90(4):485–487, April 2006. ISSN 0007-1161. doi: 10.1136/bjo.2005.085969.

[41] Muge Coban-Karatas, Selcuk Sizmaz, Rana Altan-Yaycioglu, Handan Canan, and Yonca Aydin Akova. Risk factors for intraocular pressure rise following phacoemulsification. *Indian J Ophthalmol*, 61(3):115–118, March 2013. ISSN 0301-4738. doi: 10.4103/0301-4738.99997.

[42] Daniel K. Sunderland and Amit Sapra. Physiology, Aqueous Humor Circulation. In *StatPearls*. StatPearls Publishing, Treasure Island (FL), 2024.

[43] Florian T. A. Kretz, Il-Joo Limberger, and Gerd U. Auffarth. Corneal endothelial cell coating during phacoemulsification using a new dispersive hyaluronic acid ophthalmic viscosurgical device. *Journal of Cataract & Refractive Surgery*, 40(11):1879–1884, November 2014. ISSN 0886-3350. doi: 10.1016/j.jcrs.2014.04.025.

[44] Frederick H. Silver, Joseph LiBrizzi, George Pins, Ming-Che Wang, and Dominick Benedetto. Physical properties of hyaluronic acid and hydroxypropylmethylcellulose in solution: Evaluation of coating ability. *Journal of Applied Biomaterials*, 5(1):89–98, 1994. ISSN 1549-9316. doi: 10.1002/jab.770050111.

[45] Melanie Wüst, Philipp Matten, Magdalena Nenning, and Oliver Findl. Thickness of the Protective Layers of Different Ophthalmic Viscosurgical Devices During Lens Surgery in a Porcine Model. *Translational Vision Science & Technology*, 11(2):28, February 2022. ISSN 2164-2591. doi: 10.1167/tvst.11.2.28.

[46] Timur Mert Yildirim, Gerd U. Auffarth, Hyeck-Soo Son, Ramin Khoramnia, Donald John Munro, and Patrick R. Merz. Dispersive viscosurgical devices demonstrate greater efficacy in protecting corneal endothelium in vitro. *BMJ Open Ophthalmology*, 4(1):e000227, February 2019. ISSN 2397-3269. doi: 10.1136/bmjophth-2018-000227.

[47] Gerd U. Auffarth, Florian N. Auerbach, Tanja Rabsilber, José A. Gegúndez, Ricardo Cuiña, Yves Renard, Paolo Vinciguerra, Fabrizio Camesasca, Francoise Van Cauwenberge, Thierry Amzallag, Gysbert Van Setten, and Mike P. Holzer. Comparison of the performance and safety of 2 ophthalmic viscosurgical devices in cataract surgery. *Journal of Cataract & Refractive Surgery*, 43(1):87–94, January 2017. ISSN 0886-3350. doi: 10.1016/j.jcrs.2016.10.025.

[48] Weidong Zeng, Qi Li, Tao Wan, Cui Liu, Wenhui Pan, Zushuai Wu, Guoguang Zhang, Jingtong Pan, Mengyao Qin, Yuanyuan Lin, Chuanbin Wu, and Yuehong Xu. Hyaluronic acid-coated niosomes facilitate tacrolimus ocular delivery: Mucoadhesion, precorneal retention, aqueous humor pharmacokinetics, and transcorneal permeability. *Colloids and Surfaces B: Biointerfaces*, 141:28–35, May 2016. ISSN 0927-7765. doi: 10.1016/j.colsurfb.2016.01.014.

[49] Günter Sauerbrey. Verwendung von Schwingquarzen zur Wägung dünner Schichten und zur Mikrowägung. *Z. Physik*, 155(2):206–222, April 1959. doi: 10.1007/BF01337937.

[50] K Keiji Kanazawa and Joseph G Gordon. The oscillation frequency of a quartz resonator in contact with liquid. *Analytica Chimica Acta*, 175:99–105, January 1985. ISSN 0003-2670. doi: 10.1016/S0003-2670(00)82721-X.

[51] Ilya Reviakine, Diethelm Johannsmann, and Ralf P. Richter. Hearing What You Cannot See and Visualizing What You Hear: Interpreting Quartz Crystal Microbalance Data from Solvated Interfaces. *Anal. Chem.*, 83(23):8838–8848, December 2011. ISSN 0003-2700. doi: 10.1021/ac201778h.

[52] M. V. Voinova, M. Rodahl, M. Jonson, and B. Kasemo. Viscoelastic acoustic response of layered polymer films at fluid-solid interfaces: Continuum mechanics approach. *Phys. Scr.*, 59(5):391–396, May 1999. ISSN 0031-8949, 1402-4896. doi: 10.1238/Physica.Regular.059a00391.

[53] Pierre Lecaruyer, Emmanuel Maillart, Michael Canva, and Jannick Rolland. Generalization of the Rouard method to an absorbing thin-film stack and application to surface plasmon resonance. *Appl. Opt., AO*, 45(33):8419–8423, November 2006. ISSN 2155-3165. doi: 10.1364/AO.45.008419.

[54] Rafael Tadmor, Nianhuan Chen, and Jacob N. Israelachvili. Thin film rheology and lubricity of hyaluronic acid solutions at a normal physiological concentration. *Journal of Biomedical Materials Research*, 61(4):514–523, 2002. ISSN 1097-4636. doi: 10.1002/jbm.10215.

[55] Hans-Jürgen Butt, Brunero Cappella, and Michael Kappl. Force measurements with the atomic force microscope: Technique, interpretation and applications. *Surface Science Reports*, 59(1):1–152, October 2005. ISSN 0167-5729. doi: 10.1016/j.surfrep.2005.08.003.

[56] John E. Sader, James W. M. Chon, and Paul Mulvaney. Calibration of rectangular atomic force microscope cantilevers. *Review of Scientific Instruments*, 70(10):3967–3969, October 1999. ISSN 0034-6748. doi: 10.1063/1.1150021.

[57] Lei Jiang, Simon Titmuss, Andrew Cowley, and Jacob Klein. Direct measurement of forces between cell-coating polymers and chiral crystal surfaces: The enantioselectivity of hyaluronan. *Soft Matter*, 4(7):1521–1530, 2008. doi: 10.1039/B717940E.

[58] Jacob N. Israelachvili. Chapter 16 - Steric (Polymer-Mediated) and Thermal Fluctuation Forces. In Jacob N. Israelachvili, editor, *Intermolecular and Surface Forces (Third Edition)*, pages 381–413. Academic Press, San Diego, January 2011. ISBN 978-0-12-375182-9. doi: 10.1016/B978-0-12-375182-9.10016-8.

[59] Jörg Baschnagel, Hendrik Meyer, Joachim Wittmer, Igor Kulić, Hervé Mohrbach, Falko Ziebert, Gi-Moon Nam, Nam-Kyung Lee, and Albert Johner. Semiflexible Chains at Surfaces: Worm-Like Chains and beyond. *Polymers*, 8(8):286, August 2016. ISSN 2073-4360. doi: 10.3390/polym8080286.

[60] Goerg H. Michler and Werner Lebek. Electron microscopy of polymers. In *Polymer Morphology*, pages 37–53. John Wiley & Sons, Ltd, 2016. ISBN 978-1-118-89275-6.

[61] M. Kannan. Scanning Electron Microscopy: Principle, Components and Applications. In *A Textbook on Fundamentals and Applications of Nanotechnology*, pages 81–92. Daya Publishing House A Division of Astral International, March 2018. ISBN 978-93-5124-932-0.

[62] Kalsoom Akhtar, Shahid Ali Khan, Sher Bahadar Khan, and Abdullah M. Asiri. Scanning Electron Microscopy: Principle and Applications in Nanomaterials Characterization. In Surender Kumar Sharma, editor, *Handbook of Materials Characterization*, pages 113–145. Springer International Publishing, Cham, 2018. ISBN 978-3-319-92955-2. doi: 10.1007/978-3-319-92955-2_4.

[63] Rebecca F. Thompson, Matt Walker, C. Alistair Siebert, Stephen P. Muench, and Neil A. Ranson. An introduction to sample preparation and imaging by cryo-electron microscopy for structural biology. *Methods*, 100:3–15, May 2016. ISSN 1046-2023. doi: 10.1016/j.ymeth.2016.02.017.

[64] Xu Benjin and Liu Ling. Developments, applications, and prospects of cryo-electron microscopy. *Protein Science*, 29(4):872–882, 2020. doi: 10.1002/pro.3805.

[65] Cagatay Karaca, Mustafa Ozkose, Metin Unlu, Duygu Gulmez Sevim, and Ertugrul Mirza. COMPARISON OF CORNEAL WETTING PROPERTIES OF DIFFERENT DISPERSIVE OPHTHALMIC VISCOSURGICAL

DEVICES: An Optical Coherence Tomography Study. *RETINA*, 38 (11):2137, November 2018. ISSN 0275-004X. doi: 10.1097/IAE.0000000000001854.

[66] Walter Petroll, Masoud Jafari, Stephen Lane, James Jester, and Harrison Cavanagh. Quantitative assessment of ophthalmic viscosurgical device retention using in vivo confocal microscopy. *Journal of cataract and refractive surgery*, 31:2363–8, December 2005. doi: 10.1016/j.jcrs.2005.05.032.

[67] Takao Tanaka, Keisuke Kimura, and Masahiko Usui. Adhesive retention of sodium hyaluronate ophthalmic viscosurgical devices in an acrylic tube model and in porcine-eye corneal endothelium with different irrigation rates. *Journal of Cataract & Refractive Surgery*, 35(11):2008–2013, November 2009. ISSN 0886-3350. doi: 10.1016/j.jcrs.2009.05.051.

[68] Kenichi Sakai. Quartz Crystal Microbalance with Dissipation Monitoring (QCM-D). In Masahiko Abe, editor, *Measurement Techniques and Practices of Colloid and Interface Phenomena*, pages 45–50. Springer, Singapore, 2019. ISBN 9789811359316. doi: 10.1007/978-981-13-5931-6_7.

[69] Katarzyna Kubiak, Zbigniew Adamczyk, and Monika Wasilewska. Mechanisms of fibrinogen adsorption at the silica substrate determined by QCM-D measurements. *Journal of Colloid and Interface Science*, 457:378–387, November 2015. ISSN 0021-9797. doi: 10.1016/j.jcis.2015.07.009.

[70] Hanh T. M. Phan, Shannon Bartelt-Hunt, Keith B. Rodenhausen, Mathias Schubert, and Jason C. Bartz. Investigation of Bovine Serum Albumin (BSA) Attachment onto Self-Assembled Monolayers (SAMs) Using Combinatorial Quartz Crystal Microbalance with Dissipation (QCM-D) and Spectroscopic Ellipsometry (SE). *PLOS ONE*, 10(10):e0141282, October 2015. ISSN 1932-6203. doi: 10.1371/journal.pone.0141282.

[71] Jagoba Iturri Ramos and Sergio E. Moya. Effect of the Density of ATRP Thiol Initiators in the Yield and Water Content of Grafted-From PMETAC Brushes. A Study by Means of QCM-D and Spectroscopic Ellipsometry Combined in a Single Device. *Macromolecular Chemistry and Physics*, 213 (5):549–556, 2012. ISSN 1521-3935. doi: 10.1002/macp.201100501.

[72] Kai Yu, Chris Hodges, Simon Biggs, Olivier J. Cayre, and David Harbottle. Polymer Molecular Weight Dependence on Lubricating Particle–Particle Interactions. *Ind. Eng. Chem. Res.*, 57(6):2131–2138, February 2018. ISSN 0888-5885. doi: 10.1021/acs.iecr.7b04609.

[73] Katarzyna Lewandowska and Marta Szulc. Characterisation of Hyaluronic Acid Blends Modified by Poly(N-Vinylpyrrolidone). *Molecules*, 26(17):5233, January 2021. ISSN 1420-3049. doi: 10.3390/molecules26175233.

[74] Marco Contardi, Debora Russo, Giulia Suarato, José A. Heredia-Guerrero, Luca Ceseracciu, Ilaria Penna, Natasha Margaroli, Maria Summa, Raffaele Spanò, Giovanni Tassistro, Luigi Vezzulli, Tiziano Bandiera, Rosalia Bertorelli, Athanassia Athanassiou, and Ilker S. Bayer. Polyvinylpyrrolidone/hyaluronic acid-based bilayer constructs for sequential delivery of cutaneous antiseptic and antibiotic. *Chemical Engineering Journal*, 358:912–923, February 2019. ISSN 1385-8947. doi: 10.1016/j.cej.2018.10.048.

[75] Olof Sterner, Chrysanthi Karageorgaki, Massimiliano Zürcher, Stefan Zürcher, Charles W. Scales, Zohra Fadli, Nicholas D. Spencer, and Samuele G. P. Tosatti. Reducing Friction in the Eye: A Comparative Study of Lubrication by Surface-Anchored Synthetic and Natural Ocular Mucin Analogues. *ACS Appl. Mater. Interfaces*, 9(23):20150–20160, June 2017. ISSN 1944-8244. doi: 10.1021/acsami.6b16425.

[76] Furqan A. Maulvi, Pooja J. Patel, Parth D. Soni, Ankita R. Desai, Ditixa T. Desai, Manish R. Shukla, Ketan M. Ranch, Shailesh A. Shah, and Dinesh O. Shah. Novel Poly(vinylpyrrolidone)-Coated Silicone Contact Lenses to Improve Tear Volume During Lens Wear: In Vitro and In Vivo Studies. *ACS Omega*, 5(29):18148–18154, July 2020. doi: 10.1021/acsomega.0c01764.

[77] Moez Guettari, Amal Belaidi, Stéphane Abel, and Tahar Tajouri. Polyvinylpyrrolidone Behavior in Water/Ethanol Mixed Solvents: Comparison of Modeling Predictions with Experimental Results. *J Solution Chem*, 46(7):1404–1417, July 2017. ISSN 1572-8927. doi: 10.1007/s10953-017-0649-0.

[78] Michael Rubinstein and Ralph H Colby. Polymer solutions. In Michael Rubinstein and Ralph H Colby, editors, *Polymer Physics*, page 0. Oxford University Press, June 2003. ISBN 978-0-19-852059-7. doi: 10.1093/oso/9780198520597.003.0005. URL `https://doi.org/10.1093/oso/9780198520597.003.0005`.

[79] E. K. Kim, S. M. Cristol, H. L. Kim, S. J. Kang, J. W. Park, and H. F. Edelhauser. The mucinous layer of corneal endothelial cells. *Yonsei Med J*, 41(5):651–656, October 2000. ISSN 0513-5796. doi: 10.3349/ymj.2000.41.5.651.

[80] Rama Bansil and Bradley S. Turner. The biology of mucus: Composition, synthesis and organization. *Adv Drug Deliv Rev*, 124:3–15, January 2018. ISSN 1872-8294. doi: 10.1016/j.addr.2017.09.023.

[81] Jasmim Leal, Hugh D. C. Smyth, and Debadyuti Ghosh. Physicochemical properties of mucus and their impact on transmucosal drug delivery. *Int J Pharm*, 532(1):555–572, October 2017. ISSN 0378-5173. doi: 10.1016/j.ijpharm.2017.09.018.

[82] Seung Eun Jung, Kyoung Yul Seo, Hyun Kim, Hyung-Lae Kim, In-Hyuk Chung, and Eung Kweon Kim. Expression of MUC1 on Corneal Endothelium of Human. *Cornea*, 21(7):691, October 2002. ISSN 0277-3740.

[83] A. N. Semenov and J.-F. Joanny. Kinetics of Adsorption of Linear Homopolymers onto Flat Surfaces: Rouse Dynamics. *J. Phys. II France*, 5(6):859–876, June 1995. ISSN 1155-4312, 1286-4870. doi: 10.1051/jp2:1995169.

[84] B. O'Shaughnessy and D. Vavylonis. Irreversible adsorption from dilute polymer solutions. *Eur. Phys. J. E*, 11(3):213–230, July 2003. ISSN 1292-895X. doi: 10.1140/epje/i2003-10015-9.

[85] Walter J. Weber and J. Carrell Morris. Kinetics of Adsorption on Carbon from Solution. *Journal of the Sanitary Engineering Division*, 89(2):31–59, April 1963. doi: 10.1061/JSEDAI.0000430.

[86] P. G. De Gennes. Polymer solutions near an interface. Adsorption and depletion layers. *Macromolecules*, 14(6):1637–1644, November 1981. ISSN 0024-9297. doi: 10.1021/ma50007a007.

[87] Leonid K. Filippov. Adsorption, Desorption, and Exchange Kinetics of Mixtures on Planar Surfaces. *Journal of Colloid and Interface Science*, 181 (1):232–251, July 1996. ISSN 0021-9797. doi: 10.1006/jcis.1996.0375.

[88] J. F. Douglas, H. E. Johnson, and S. Granick. A simple kinetic model of polymer adsorption and desorption. *Science (New York, N.Y.)*, 262(5142): 2010–2012, December 1993. ISSN 0036-8075. doi: 10.1126/science.262.5142.2010.

[89] A. N. Semenov and J.-F. Joanny. Structure of Adsorbed Polymer Layers: Loops and Tails. *EPL*, 29(4):279, February 1995. ISSN 0295-5075. doi: 10.1209/0295-5075/29/4/002.

[90] P. G. de Gennes. Polymers at an interface; a simplified view. *Advances in Colloid and Interface Science*, 27(3):189–209, July 1987. ISSN 0001-8686. doi: 10.1016/0001-8686(87)85003-0.

[91] Kunio Furusawa, Kyogo Yamashita, and Kazuhiko Konno. Adsorption of monodisperse polystyrene onto porous glass. I. preference adsorption and displacement of high-molecular-weight species. *Journal of Colloid and Interface Science*, 86(1):35–42, March 1982. ISSN 0021-9797. doi: 10.1016/0021-9797(82)90038-8. URL `https://www.sciencedirect.com/science/article/pii/0021979782900388`.

[92] M.A. Cohen Stuart, J.M.H.M. Scheutjens, and G.J. Fleer. POLYDISPERSITY EFFECTS AND THE INTERPRETATION OF POLYMER ADSORPTION ISOTHERMS. *Journal of polymer science. Part A-2, Polymer physics*, 18(3):559–573, 1980.

[93] Vincent A. Martinez, Jana Schwarz-Linek, Mathias Reufer, Laurence G. Wilson, Alexander N. Morozov, and Wilson C. K. Poon. Flagellated bacterial motility in polymer solutions. *Proceedings of the National Academy of Sciences*, 111(50):17771–17776, December 2014. doi: 10.1073/pnas.1415460111.

[94] Marcus Hildebrandt, Eui-young Shin, Suan Yang, Wael Ali, Sedakat Altinpinar, and Jochen S. Gutmann. Investigation of Roughness Correlation in Polymer Brushes via X-ray Scattering. *Polymers*, 12(9): 2101, September 2020. ISSN 2073-4360. doi: 10.3390/polym12092101.

[95] O. Guiselin. Irreversible Adsorption of a Concentrated Polymer Solution. *EPL*, 17(3):225, January 1992. ISSN 0295-5075. doi: 10.1209/0295-5075/17/3/007.

[96] Yukari Oda, Daisuke Kawaguchi, Yuma Morimitsu, Satoru Yamamoto, and Keiji Tanaka. Direct observation of morphological transition for an adsorbed single polymer chain. *Sci Rep*, 10:20914, December 2020. ISSN 2045-2322. doi: 10.1038/s41598-020-77761-0.

[97] Sejin Oh, Matthew Wilcox, Jeffrey P. Pearson, and Salvador Borrós. Optimal design for studying mucoadhesive polymers interaction with gastric mucin using a quartz crystal microbalance with dissipation (QCM-D): Comparison of two different mucin origins. *Eur J Pharm Biopharm*, 96: 477–483, October 2015. ISSN 1873-3441. doi: 10.1016/j.ejpb.2015.08.002.

[98] Feng Wan, Mikkel Herzberg, Zheng Huang, Tue Hassenkam, and Hanne M. Nielsen. A free-floating mucin layer to investigate the effect of the local microenvironment in lungs on mucin-nanoparticle interactions. *Acta Biomaterialia*, 104:115–123, March 2020. ISSN 1742-7061. doi: 10.1016/j.actbio.2020.01.014.

[99] Daniele Tognetto, Paolo Cecchini, Rossella D'Aloisio, and Romano Lapasin. Mixed polymeric systems: New ophthalmic viscosurgical device created by mixing commercially available devices. *Journal of Cataract & Refractive Surgery*, 43(1):109–114, January 2017. ISSN 0886-3350. doi: 10.1016/j.jcrs.2016.11.035.

[100] Francesco Del Giudice, Simon J. Haward, and Amy Q. Shen. Relaxation time of dilute polymer solutions: A microfluidic approach. *Journal of Rheology*, 61(2):327–337, March 2017. ISSN 0148-6055. doi: 10.1122/1.4975933.

[101] J E Scott, C Cummings, A Brass, and Y Chen. Secondary and tertiary structures of hyaluronan in aqueous solution, investigated by rotary shadowing-electron microscopy and computer simulation. Hyaluronan is a very efficient network-forming polymer. *Biochem J*, 274(Pt 3):699–705, March 1991. ISSN 0264-6021.

[102] Mary K. Cowman, Hong-Gee Lee, Kathryn L. Schwertfeger, James B. McCarthy, and Eva A. Turley. The Content and Size of Hyaluronan in Biological Fluids and Tissues. *Front. Immunol.*, 6, June 2015. ISSN 1664-3224. doi: 10.3389/fimmu.2015.00261.

[103] Wendy E. Krause, Enrico G. Bellomo, and Ralph H. Colby. Rheology of Sodium Hyaluronate under Physiological Conditions. *Biomacromolecules*, 2(1):65–69, March 2001. ISSN 1525-7797. doi: 10.1021/bm0055798.

[104] Amol Bansal, Hrishikesh Amin, and R Rekha. Correlation of aqueous humor electrolytes with serum electrolytes in cataract patients. *Indian J Ophthalmol*, 69(10):2675–2677, October 2021. ISSN 0301-4738. doi: 10.4103/ijo.IJO_20_21.

[105] J. F. Douglas, H. E. Johnson, and S. Granick. A simple kinetic model of polymer adsorption and desorption. *Science*, 262(5142):2010–2012, December 1993. ISSN 0036-8075. doi: 10.1126/science.262.5142.2010.

[106] C. A. Grattoni, P. F. Luckham, X. D. Jing, L. Norman, and R. W. Zimmerman. Polymers as relative permeability modifiers: Adsorption and the dynamic formation of thick polyacrylamide layers. *Journal of Petroleum Science and Engineering*, 45(3):233–245, December 2004. ISSN 0920-4105. doi: 10.1016/j.petrol.2004.07.002.

[107] Eseosa M. Ekanem, Maja Rücker, Sherifat Yesufu-Rufai, Catherine Spurin, Nicholas Ooi, Apostolos Georgiadis, Steffen Berg, and Paul F. Luckham. Novel adsorption mechanisms identified for polymer retention in carbonate rocks. *JCIS Open*, 4:100026, December 2021. ISSN 2666-934X. doi: 10.1016/j.jciso.2021.100026.

[108] Naoyuki Ishida and Simon Biggs. Salt-Induced Structural Behavior for Poly(N-isopropylacryamide) Grafted onto Solid Surface Observed Directly by AFM and QCM-D. *Macromolecules*, 40(25):9045–9052, December 2007. ISSN 0024-9297. doi: 10.1021/ma071878e.

[109] Hyaltech report. Technical Report PDP008-DEV-FR3-001, Hyaltech, 2020.

[110] Michael Rubinstein and Ralph H Colby. Polymer solutions. In Michael Rubinstein and Ralph H Colby, editors, *Polymer Physics*, page 0. Oxford University Press, June 2003. ISBN 978-0-19-852059-7. doi: 10.1093/oso/9780198520597.003.0005.

[111] Raniero Mendichi, Ladislav Šoltés, and Alberto Giacometti Schieroni. Evaluation of Radius of Gyration and Intrinsic Viscosity Molar Mass Dependence and Stiffness of Hyaluronan. *Biomacromolecules*, 4(6):1805–1810, November 2003. ISSN 1525-7797. doi: 10.1021/bm0342178.

[112] Karin Glasmästar, Charlotte Larsson, Fredrik Höök, and Bengt Kasemo. Protein Adsorption on Supported Phospholipid Bilayers. *Journal of Colloid*

and Interface Science, 246(1):40–47, February 2002. ISSN 0021-9797. doi: 10.1006/jcis.2001.8060.

[113] Erik Reimhult, Fredrik Höök, and Bengt Kasemo. Intact Vesicle Adsorption and Supported Biomembrane Formation from Vesicles in Solution Influence of Surface Chemistry, Vesicle Size, Temperature, and Osmotic Pressure. *Langmuir*, 19(5):1681–1691, March 2003. ISSN 0743-7463. doi: 10.1021/la0263920.

[114] Guangming Liu, Lifeng Yan, Xi Chen, and Guangzhao Zhang. Study of the kinetics of mushroom-to-brush transition of charged polymer chains. *Polymer*, 47(9):3157–3163, April 2006. ISSN 0032-3861. doi: 10.1016/j.polymer.2006.02.091.

[115] J. Kou, D. Tao, and G. Xu. Fatty acid collectors for phosphate flotation and their adsorption behavior using QCM-D. *International Journal of Mineral Processing*, 95(1):1–9, July 2010. ISSN 0301-7516. doi: 10.1016/j.minpro.2010.03.001.

[116] Katherine Vorvolakos, Irada S Isayeva, Hoan-My Do Luu, Dinesh V Patwardhan, and Steven K Pollack. Ionically cross-linked hyaluronic acid: Wetting, lubrication, and viscoelasticity of a modified adhesion barrier gel. *Med Devices (Auckl)*, 4:1–10, December 2010. ISSN 1179-1470. doi: 10.2147/MDER.S13962.

[117] Lei Jiang, Guihua Liu, Hanyun Liu, Juan Han, Zhibin Liu, and Hongchao Ma. Molecular weight impact on the mechanical forces between hyaluronan and its receptor. *Carbohydrate Polymers*, 197:326–336, October 2018. ISSN 0144-8617. doi: 10.1016/j.carbpol.2018.06.015.

[118] Bieke Vanslembrouck, Jian-hua Chen, Carolyn Larabell, and Jolanda van Hengel. Microscopic Visualization of Cell-Cell Adhesion Complexes at Micro and Nanoscale. *Front. Cell Dev. Biol.*, 10, April 2022. ISSN 2296-634X. doi: 10.3389/fcell.2022.819534.

[119] Fengyuan Yu, Fei Zhang, Tu Luan, Zinan Zhang, and Hongbin Zhang. Rheological studies of hyaluronan solutions based on the scaling law and constitutive models. *Polymer*, 55(1):295–301, January 2014. ISSN 0032-3861. doi: 10.1016/j.polymer.2013.11.047. URL `https://www.sciencedirect.com/science/article/pii/S0032386113010987`.

[120] Paige N. Wiecinski, Kevin M. Metz, Andrew N. Mangham, Kurt H. Jacobson, Robert J. Hamers, and Joel A. Pedersen. Gastrointestinal biodurability of engineered nanoparticles: Development of an in vitro assay. *Nanotoxicology*, 3(3):202–214, January 2009. ISSN 1743-5390. doi: 10.1080/17435390902859556.

[121] Jonathan P. Celli, Bradley S. Turner, Nezam H. Afdhal, Randy H. Ewoldt, Gareth H. McKinley, Rama Bansil, and Shyamsunder Erramilli.

Rheology of Gastric Mucin Exhibits a pH Dependent Sol Gel Transition. *Biomacromolecules*, 8(5):1580–1586, May 2007. ISSN 1525-7797. doi: 10.1021/bm0609691.

[122] Yunsoo Choi, Hung-Vu Tran, and T. Randall Lee. Self-Assembled Monolayer Coatings on Gold and Silica Surfaces for Antifouling Applications: A Review. *Coatings*, 12(10):1462, October 2022. ISSN 2079-6412. doi: 10.3390/coatings12101462.

[123] Emanuele Ostuni, Robert G. Chapman, Michael N. Liang, Gloria Meluleni, Gerald Pier, Donald E. Ingber, and George M. Whitesides. Self-Assembled Monolayers That Resist the Adsorption of Proteins and the Adhesion of Bacterial and Mammalian Cells. *Langmuir*, 17(20):6336–6343, October 2001. ISSN 0743-7463. doi: 10.1021/la010552a.

[124] Min Soo Lim, Ke Feng, Xinqi Chen, Nianqiang Wu, Aparna Raman, Joshua Nightingale, Ellen S. Gawalt, Dimitris Korakakis, Larry A. Hornak, and Aaron T. Timperman. Adsorption and Desorption of Stearic Acid Self-Assembled Monolayers on Aluminum Oxide. *Langmuir*, 23(5):2444–2452, February 2007. ISSN 0743-7463. doi: 10.1021/la061914n.

[125] Steve A. Arshinoff and Masoud Jafari. New classification of ophthalmic viscosurgical devices—2005. *Journal of Cataract & Refractive Surgery*, 31 (11):2167–2171, November 2005. ISSN 0886-3350. doi: 10.1016/j.jcrs.2005.08.056.

[126] Satish S Modi, James A Davison, and Tom Walters. Safety, efficacy, and intraoperative characteristics of DisCoVisc and Healon ophthalmic viscosurgical devices for cataract surgery. *Clinical Ophthalmology*, 5:1381–1389, September 2011. ISSN 1177-5467. doi: 10.2147/OPTH.S22243.

[127] Mark Packer, Mitchell Shultz, James Loden, and George Lau. Safety and effectiveness comparison of a new cohesive ophthalmic viscosurgical device. *Journal of Cataract & Refractive Surgery*, 49(8):804, August 2023. ISSN 0886-3350. doi: 10.1097/j.jcrs.0000000000001201.

[128] Brian Button, Henry P. Goodell, Eyad Atieh, Yu-Cheng Chen, Robert Williams, Siddharth Shenoy, Elijah Lackey, Nathan T. Shenkute, Li-Heng Cai, Robert G. Dennis, Richard C. Boucher, and Michael Rubinstein. Roles of mucus adhesion and cohesion in cough clearance. *Proceedings of the National Academy of Sciences*, 115(49):12501–12506, December 2018. doi: 10.1073/pnas.1811787115.

[129] Hong Zhang, Wensheng Cai, and Xueguang Shao. Regulation of aquaporin-3 water permeability by hyaluronan. *Phys. Chem. Chem. Phys.*, 23(45): 25706–25711, November 2021. ISSN 1463-9084. doi: 10.1039/D1CP02867G.

[130] D. Liu, T. Liu, and M. S. Sy. Identification of two regions in the cytoplasmic domain of CD44 through which PMA, calcium, and foskolin differentially

regulate the binding of CD44 to hyaluronic acid. *Cell Immunol*, 190(2): 132–140, December 1998. ISSN 0008-8749. doi: 10.1006/cimm.1998.1397.

[131] Masami Lintuluoto, Yota Horioka, Saki Hongo, Juha Mikael Lintuluoto, and Yoshifumi Fukunishi. Molecular Dynamics Simulation Study on Allosteric Regulation of CD44-Hyaluronan Binding as a Force Sensing Mechanism. *ACS Omega*, 6(12):8045–8055, March 2021. doi: 10.1021/acsomega.0c05502.

[132] Natalia P. Akentieva and Alexey F. Topunov. RHAMM-Target Peptides as Molecular Imaging Probes for the Imaging of RHAMM-Expressing Cancer Cells. *Biointerface Res Appl Chem*, 12(1):2–24, April 2021. ISSN 2069-5837. doi: 10.33263/BRIAC121.002024.

[133] Paul A. Knepper, Steven Covici, James R. Fadel, Chandra S. K. Mayanil, and Robert Ritch. Surface-Tension Properties of Hyaluronic Acid. *Journal of Glaucoma*, 4(3):194, June 1995. ISSN 1057-0829.

[134] Walkiria Ribeiro, José Luis Mata, and Benilde Saramago. Effect of concentration and temperature on surface tension of sodium hyaluronate saline solutions. *Langmuir*, 23(13):7014–7017, June 2007. ISSN 0743-7463. doi: 10.1021/la700269k.

[135] Frederick H. Silver, Joseph J. LiBrizzi, and Dominick Benedetto. Physical properties of model viscoelastic materials. *Journal of Applied Biomaterials*, 5(3):227–234, 1994. ISSN 1549-9316. doi: 10.1002/jab.770050308.

[136] Carolyn J. Moll, Giulia Giubertoni, Lennard van Buren, Jan Versluis, Gijsje H. Koenderink, and Huib J. Bakker. Molecular Structure and Surface Accumulation Dynamics of Hyaluronan at the Water–Air Interface. *Macromolecules*, 54(18):8655–8663, September 2021. ISSN 0024-9297. doi: 10.1021/acs.macromol.1c00366.

[137] H. Yim, M. S. Kent, A. Matheson, M. J. Stevens, R. Ivkov, S. Satija, J. Majewski, and G. S. Smith. Adsorption of Sodium Poly(styrenesulfonate) to the Air Surface of Water by Neutron and X-ray Reflectivity and Surface Tension Measurements: Polymer Concentration Dependence. *Macromolecules*, 35(26):9737–9747, December 2002. ISSN 0024-9297. doi: 10.1021/ma0200468.

[138] Frank J. Holly and Michael A. Lemp. Wettability and wetting of corneal epithelium. *Experimental Eye Research*, 11(2):239–250, March 1971. ISSN 0014-4835. doi: 10.1016/S0014-4835(71)80028-3.

[139] Katherine Vorvolakos, James C. Coburn, and David M. Saylor. Dynamic interfacial behavior of viscoelastic aqueous hyaluronic acid: Effects of molecular weight, concentration and interfacial velocity. *Soft Matter*, 10 (13):2304–2312, March 2014. ISSN 1744-6848. doi: 10.1039/C3SM52372A.

[140] Petr Snetkov, Kseniia Zakharova, Svetlana Morozkina, Roman Olekhnovich, and Mayya Uspenskaya. Hyaluronic Acid: The Influence of Molecular Weight on Structural, Physical, Physico-Chemical, and Degradable Properties of Biopolymer. *Polymers*, 12(8):1800, August 2020. ISSN 2073-4360. doi: 10.3390/polym12081800.

[141] Elaine T Vandenberg, Lars Bertilsson, Bo Liedberg, Kajsa Uvdal, Ragnar Erlandsson, Hans Elwing, and Ingemar Lundström. Structure of 3-aminopropyl triethoxy silane on silicon oxide. *Journal of Colloid and Interface Science*, 147(1):103–118, November 1991. ISSN 0021-9797. doi: 10.1016/0021-9797(91)90139-Y.

[142] Maroua Ben Haddada, Juliette Blanchard, Sandra Casale, Jean-Marc Krafft, Anne Vallée, Christophe Méthivier, and Souhir Boujday. Optimizing the immobilization of gold nanoparticles on functionalized silicon surfaces: Amine- vs thiol-terminated silane. *Gold Bull*, 46(4):335–341, December 2013. ISSN 2190-7579. doi: 10.1007/s13404-013-0120-y.

[143] Derek Marsh, Rosa Bartucci, and Luigi Sportelli. Lipid membranes with grafted polymers: Physicochemical aspects. *Biochimica et Biophysica Acta (BBA) - Biomembranes*, 1615(1):33–59, September 2003. ISSN 0005-2736. doi: 10.1016/S0005-2736(03)00197-4.

[144] Ana Violeta Girão, Gianvito Caputo, and Marta C. Ferro. Chapter 6 - Application of Scanning Electron Microscopy–Energy Dispersive X-Ray Spectroscopy (SEM-EDS). In Teresa A. P. Rocha-Santos and Armando C. Duarte, editors, *Comprehensive Analytical Chemistry*, volume 75 of *Characterization and Analysis of Microplastics*, pages 153–168. Elsevier, January 2017. doi: 10.1016/bs.coac.2016.10.002.

[145] Robyn Aston, Kim Sewell, Travis Klein, Gwen Lawrie, and Lisbeth Grøndahl. Evaluation of the impact of freezing preparation techniques on the characterisation of alginate hydrogels by cryo-SEM. *European Polymer Journal*, 82:1–15, September 2016. ISSN 0014-3057. doi: 10.1016/j.eurpolymj.2016.06.025.

[146] Evgeniy V. Dubrovin, Nikolay A. Barinov, Dmitry A. Ivanov, and Dmitry V. Klinov. Single-molecule AFM study of hyaluronic acid softening in electrolyte solutions. *Carbohydrate Polymers*, 303:120472, March 2023. ISSN 0144-8617. doi: 10.1016/j.carbpol.2022.120472.

[147] Matthias Rief, Mathias Gautel, Filipp Oesterhelt, Julio M. Fernandez, and Hermann E. Gaub. Reversible Unfolding of Individual Titin Immunoglobulin Domains by AFM. *Science*, 276(5315):1109–1112, May 1997. doi: 10.1126/science.276.5315.1109.

[148] Thorsten Hugel and Markus Seitz. The Study of Molecular Interactions by AFM Force Spectroscopy. *Macromolecular Rapid Communications*, 22(13):989–1016, 2001. ISSN 1521-3927. doi: 10.1002/1521-3927(20010901)22:13⟨989::AID-MARC989⟩3.0.CO;2-D.

[149] C. Friedsam, H. E. Gaub, and R. R. Netz. Probing surfaces with single-polymer atomic force microscope experiments. *Biointerphases*, 1(1):MR1, March 2006. ISSN 1559-4106. doi: 10.1116/1.2171996.

[150] Jin Hau Lew, Omar K. Matar, Erich A. Müller, Paul F. Luckham, Adrielle Sousa Santos, and Maung Maung Myo Thant. Atomic Force Microscopy of Hydrolysed Polyacrylamide Adsorption onto Calcium Carbonate. *Polymers*, 15(20):4037, January 2023. ISSN 2073-4360. doi: 10.3390/polym15204037.

[151] Matthew Reeves, Andreia Silva, Ben Robertson, and Alexander Morozov. Optimizing the flow behaviour of opthalmic viscosurgical devices (OVDs) for use during surgery. Technical report, Edinburgh Complex Fluids Partnership, 2020.

[152] Benjamin S. Hanson, David Head, and Lorna Dougan. The hierarchical emergence of worm-like chain behaviour from globular domain polymer chains. *Soft Matter*, 15(43):8778–8789, November 2019. ISSN 1744-6848. doi: 10.1039/C9SM01656B.

[153] Mark Bathe, Gregory C. Rutledge, Alan J. Grodzinsky, and Bruce Tidor. A Coarse-Grained Molecular Model for Glycosaminoglycans: Application to Chondroitin, Chondroitin Sulfate, and Hyaluronic Acid. *Biophysical Journal*, 88(6):3870–3887, June 2005. ISSN 00063495. doi: 10.1529/biophysj.104.058800.

[154] Pierre Nassoy. An Approach to Cell Adhesion Inspired from Polymer Physics. In *P.G. De Gennes' Impact on Science ? Volume II*, volume Volume 19 of *Series on Directions in Condensed Matter Physics*, pages 127–138. World Scientific Publishing Company, July 2009. ISBN 978-981-4280-63-1. doi: 10.1142/9789814280648_0014.

[155] Dmitrii Sychev, Simon Schubotz, Quinn A. Besford, Andreas Fery, and Günter K. Auernhammer. Critical analysis of adhesion work measurements from AFM-based techniques for soft contact. *Journal of Colloid and Interface Science*, 642:216–226, July 2023. ISSN 0021-9797. doi: 10.1016/j.jcis.2023.03.139.

[156] Jacob N. Israelachvili. *Intermolecular and Surface Forces*. Academic Press, July 2011. ISBN 978-0-12-391933-5.

[157] Cyprien Gay. Stickiness—Some Fundamentals of Adhesion1. *Integrative and Comparative Biology*, 42(6):1123–1126, December 2002. ISSN 1540-7063. doi: 10.1093/icb/42.6.1123.

[158] Hongbo Zeng, Dong Soo Hwang, Jacob N. Israelachvili, and J. Herbert Waite. Strong reversible Fe3+-mediated bridging between dopa-containing protein films in water. *Proc Natl Acad Sci U S A*, 107(29):12850–12853, July 2010. ISSN 1091-6490. doi: 10.1073/pnas.1007416107.

[159] Younghun Kim, Young In Yang, Inhee Choi, and Jongheop Yi. Dependence of approaching velocity on the force-distance curve in AFM analysis. *Korean J. Chem. Eng.*, 27(1):324–327, January 2010. ISSN 1975-7220. doi: 10.1007/s11814-009-0314-4.

[160] Paul D O'Brien, Patricia Fitzpatrick, Dara J Kilmartin, and Stephen Beatty. Risk factors for endothelial cell loss after phacoemulsification surgery by a junior resident. *Journal of Cataract & Refractive Surgery*, 30(4):839–843, April 2004. ISSN 0886-3350. doi: 10.1016/S0886-3350(03)00648-5.

[161] Valérie M. Laurent, Alain Duperray, Vinoth Sundar Rajan, and Claude Verdier. Atomic Force Microscopy Reveals a Role for Endothelial Cell ICAM-1 Expression in Bladder Cancer Cell Adherence. *PLOS ONE*, 9(5):e98034, May 2014. ISSN 1932-6203. doi: 10.1371/journal.pone.0098034.

[162] Sema Ekici, Pinar Ilgin, Sultan Butun, and Nurettin Sahiner. Hyaluronic acid hydrogel particles with tunable charges as potential drug delivery devices. *Carbohydrate Polymers*, 84(4):1306–1313, April 2011. ISSN 0144-8617. doi: 10.1016/j.carbpol.2011.01.028.

[163] Andrew Marais, Samuel Pendergraph, and Lars Wågberg. Nanometer-Thick Hyaluronic Acid Self-Assemblies with Strong Adhesive Properties. *ACS Appl. Mater. Interfaces*, 7(28):15143–15147, July 2015. ISSN 1944-8244. doi: 10.1021/acsami.5b03760.

[164] Steve Martin, Hanqing Wang, Tino Rathke, Ulf Anderegg, Stephanie Möller, Matthias Schnabelrauch, Tilo Pompe, and Stephan Schmidt. Polymer hydrogel particles as biocompatible AFM probes to study CD44/hyaluronic acid interactions on cells. *Polymer*, 102:342–349, October 2016. ISSN 0032-3861. doi: 10.1016/j.polymer.2016.02.019.